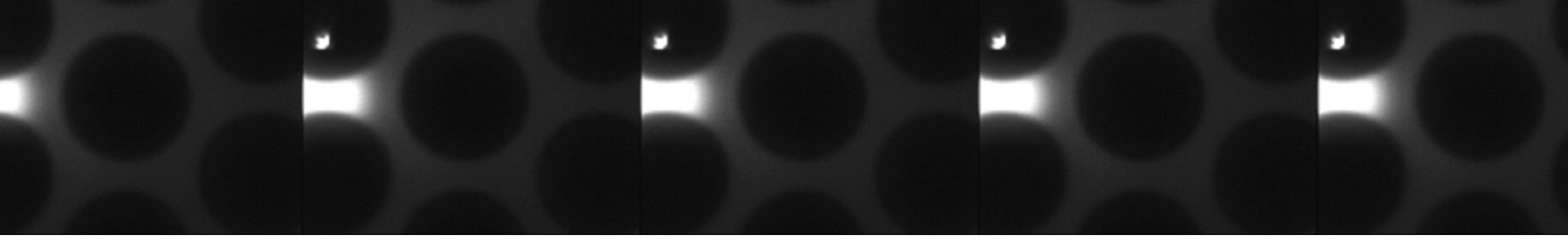

Design and Characterization of Microfabricated On-Chip HPLC Columns

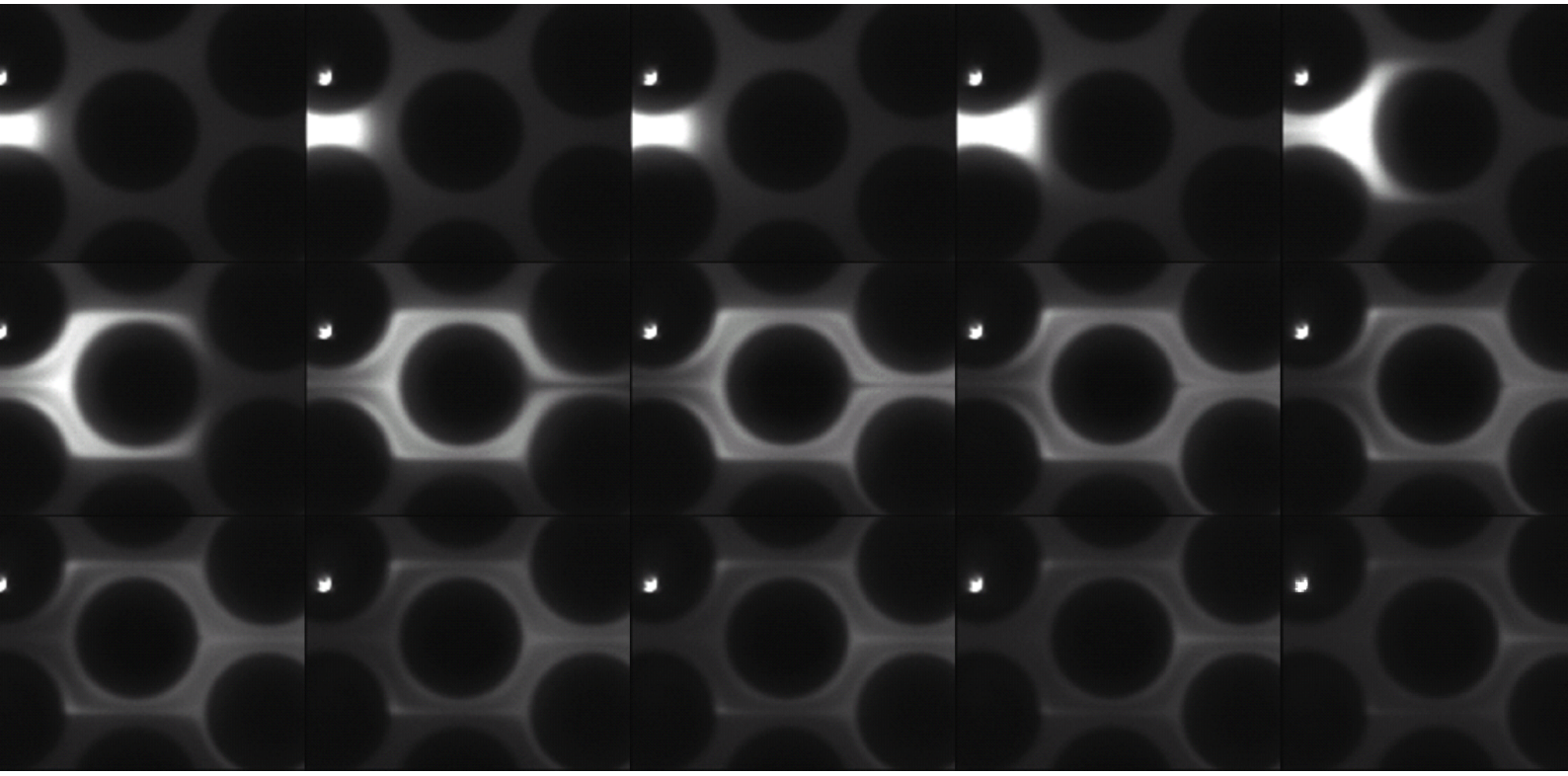

Selm De Bruyne

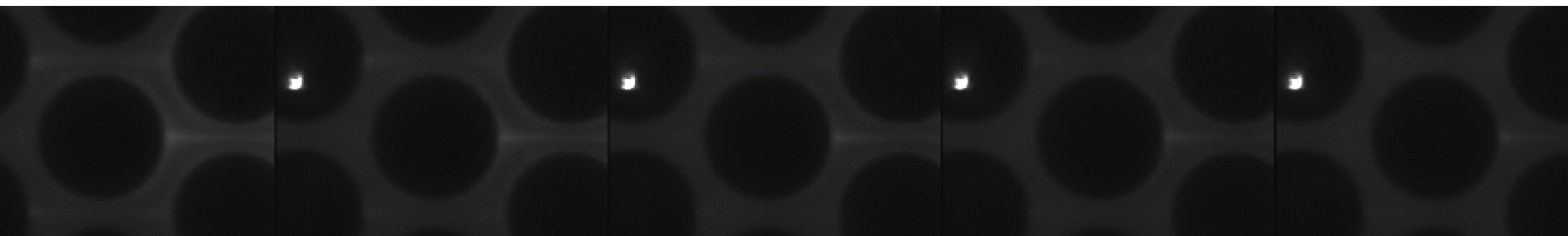

Design and Characterization of Microfabricated On-Chip HPLC Columns

Selm De Bruyne

Vrije Universiteit Brussel

UNIVERSITY OF TWENTE.

MESA+
INSTITUTE FOR NANOTECHNOLOGY

This thesis was made in the frame of a cotutelle agreement between the Vrije Universiteit Brussel (Brussels, Belgium) and The University of Twente (Enschede, The Netherlands). The work in this thesis was carried out at the MESA+ Institute for Nanotechnology and at the Mesoscale Chemical Systems group of the Faculty of Science and Technology at the University of Twente and at the Department of Chemical Engineering of the Faculty of Engineering at the Vrije Universiteit Brussel.

Nederlandse titel:

Ontwerp en Karakterisatie van Microfabricated On-Chip HPLC-kolommen

Graduation Committee:

Chairman and Secretary:

Prof.dr. Gerard van der Steenhoven	Universiteit Twente

Promotors:

Prof.dr. Han J.G.E. Gardeniers	Universiteit Twente
Prod.dr.ir. Gert Desmet	Vrije Universiteit Brussel

Referee and copromotor

Dr.ir. Wim De Malsche	Vrije Universiteit Brussel

Members:

Prof.dr.ir. Rob G.H. Lammertink	Universiteit Twente
Prof.dr.ir. Jurriaan Huskens	Universiteit Twente
Prof.dr. Govert W. Somsen	Vrije Universiteit Amsterdam
Prof.dr.ir. Gijs J.M. Krijnen	Universiteit Twente
Prof.dr. Jan C.T. Eijkel	Universiteit Twente

Front cover: radial dispersion experiment

Back cover: Etching machine hinting at me I should do some skating.

Design and Characterization of Microfabricated On-Chip HPLC Columns

ISBN 978-90-365-3562-5

DOI 10.3990/1.9789036535625

URL http://dx.doi.org/10.3990/1.9789036535625

Printed by Gildeprint Drukkerijen, Enschede, The Netherlands

DESIGN AND CHARACTERIZATION OF MICROFABRICATED ON-CHIP HPLC COLUMNS

DISSERTATION

to obtain
the degree of doctor at the University of Twente
on the authority of the rector magnificus,
prof.dr. H. Brinksma,
on account of the decision of the graduation committee,
to be publicly defended on
Friday, 25 October 2013 at 12:45

by

Selm De Bruyne

born on 3 September, 1982
in Wilrijk, Belgium

You can strive for perfection...
and sometimes that makes you a miserable son of a bitch

Jimmy Dean, Sausage king and singer, 1928-2010

Table of Contents

Chapter 1

Project Aim & Thesis Outline

The aim of the present thesis was to explore the possibilities of the state-of-the-art in the micro-machining of silicon and glass to develop novel structures enabling faster and more efficient chromatographic separations, as well as to develop novel devices enabling the in-situ analysis of the flow and dispersion phenomena occurring in liquid chromatographic systems. The latter is needed as the current theoretical modeling of the performance of liquid chromatographic systems is lacking some initial pieces of information, for example on the correlation between the radial dispersion and the fluid velocity and diffusivity.

After an introduction (**Chapter 2**) on the theory of chromatography and on the many possibilities of advanced microfabrication methods, an overview is given of the many new microfabrication procedures (**Chapter 3**) that have been developed in the frame of this thesis, and that have been used in the present thesis, but also in the work of other PhD students and post doctoral workers of the department (Veronica Fekete, Hamed Eghbali, Jef Op de Beeck, Wim de Malsche).

Chapter 4 describes the details and the achieved measurement accuracy of the dedicated optical set-up that has been built to study the radial dispersion in the pillar array columns, used as a 2-D representation of the reality of 3-D packed bed columns. The detailed analysis

of the results is subsequently discussed in **Chapter 5**, where the collected experimental data could be used to invalidate the classic model for dispersion.

In **Chapter 6**, the speed limits of liquid chromatography have been explored by performing separation in nanochannels as thin as 45 nm. Due to the enhanced mass transfer at this scale, and due to the use of the shear-driven flow principle, a new record in terms of efficiency per time could be achieved.

In **Chapter 7**, another record (achieving 1million theoretical plates in the shortest possible time) was realized using a 3m long microfabricated pillar array column, which clearly offered a uniform performance over its entire length. With this column 1 million theoretical plates could be achieved in 20minutes, which is as much as an order of magnitude faster than the previous record.

Last but not least, it has been attempted in **Chapter 8** to increase the loadability of a 3 x 3 cm long pillar array column by coating the pillars with a meso-porous silica layer with a thickness of 300 nm. The achievable separation performance was investigated by coupling the porous-shell pillar array column to a capillary LC instrument and evaluated by conducting gradient elution separations of digests of cytochrome c and bovine serum albumine yielding peak capacities of 150 nearly independent of the flow rate.

Chapter 2

Introduction

2.1. Chromatography & Column performance

Chromatography, a combination of the Greek words “chromatos” (colour) and “graphein” (to write), is the collective term for separation techniques that are achieved by distributing the components in a mixture between two phases, a stationary phase and a mobile phase. Because the various components inside the mixture exhibit different affinities towards the different phases, they will travel at different speeds, causing them to separate. Components with a strong affinity for the stationary phase will be retained longer in the system compared to components with a weak affinity with the stationary phase.

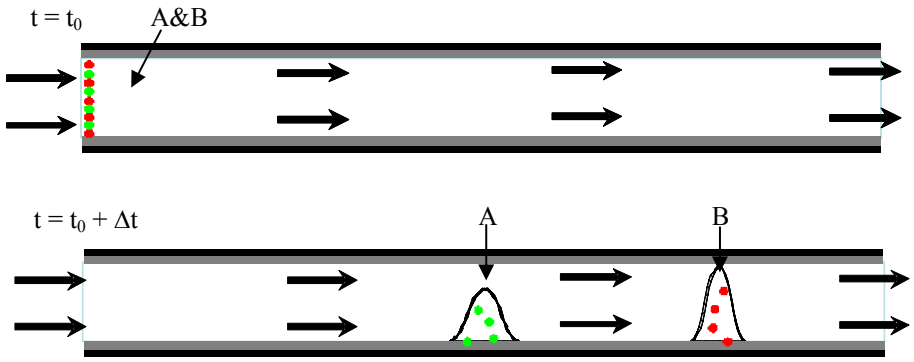

Figure 2.1. Principle of a chromatographic separation. Component A, which has a bigger affinity for the stationary phase than component B, will migrate more slowly through the column.

The different categories of chromatography can be divided into many sub-classes of separation techniques based on selectivity mechanism (e.g. size exclusion, affinity), bed shape (column vs. planar chromatography), mobile phase phases (gas vs. liquid chromatography) and stationary phases (e.g. solid, immobilized liquid).

The invention of chromatography was done by Michael Tswett, who reported in 1906 the separation of plant pigments in a liquid adsorption column with calcium carbonate as stationary phase or adsorbent and a petrol-ether/ethanol mixture as mobile phase or eluent. He noticed a separation of different color bands that were moving through the column at different velocities, hence “chromato-graphein” [1]. The discovery of Tswett remained unused for a long time until Edgar Lederer at the university of Heidelberg reported the separation of carotenoids in egg yolk in 1931 [2]. Shortly after, the technique gained more interest and importance as a valid analytical separation technique. In the 1940’s and 50’s, gas chromatography and planar chromatography were the most popular techniques due to the low analysis time and ease of execution while yielding acceptable efficiencies compared to LC which required sophisticated column technology [3].

However, since the early 60's, there was an increasing demand for more powerful separation techniques that were capable of rapidly separating non-volatile compounds like biomolecules. This prompted researchers like Horvath [4], Huber [5] and Kirkland [6] to build equipment allowing the use of high pressures which would yield higher mobile phase velocities and faster separations. Their efforts eventually led to the development of a technique that had many design aspects in common with gas chromatography, but used liquid as the mobile phase and which was capable of separating complex biological mixtures. This technique has evolved to what is known today as "High Performance Liquid Chromatography", or HPLC, and has undergone a long path of improvements over the years. HPLC is now routinely used in many laboratories and columns containing particles of 3-5 μm operating at pressures of 400 bars and above are commonly used. Nowadays, HPLC is the dominant analytical separation tool, due to the ease of sample preparation and the broader range of samples that can be dealt with.

2.2. Theory of Chromatography

The chromatographic separation of a mixture can be considered a combination of two effects occurring simultaneously. The first effect can be described by thermodynamics and is related to the interaction effects of the analyte with the different phases inside the column. The second effect is more related to the kinetical mechanics associated with adsorption-desorption kinetics as well as the hydrodynamics or motion of analytes through the system [7].

2.2.1. Thermodynamics of chromatography

The phase retention factor k' of a compound is the ratio of molecules N_s that are at any time present in the stationary phase to the number of molecules N_m that are in the mobile phase:

$$k' = \frac{N_s}{N_m} \qquad (2.1)$$

The number of molecules in the stationary and mobile phase can be related to their respective concentration C'_m and C'_s:

$$k' = \frac{C'_s . V_s}{C'_m . V_m} \qquad (2.2)$$

Where V_m and V_s represent the volumes of the mobile and stationary phases respectively. The ratio of the concentration C'_s to C'_m is the partition coefficient K:

$$K = \frac{C'_s}{C'_m} \qquad (2.3)$$

The phase retention factor can also be expressed as a function of time. It describes how much longer the retention time, t_r, is of a specific component with respect to the retention time of a non-retaining component, which is also often referred to as the dead-time of a column (t_0).

$$k' = \frac{t_r - t_0}{t_0} \tag{2.4}$$

When porous layers are incorporated in the chromatographic system, another retention factor is defined: the zone retention factor (k''). This factor is the ratio of the time that molecules spend in the porous material (t_{por}), either adsorbed to the stationary phase or diffusing in the stationary mobile phase within the pore, over the dead-time.

$$k'' = \frac{t_r - t_0}{t_0} = \frac{t_{por}}{t_0} \tag{2.5}$$

Even molecules with no special affinity to the stationary phase (k'=0) will spend a certain amount of time in the porous material (k''≠0) if the pores are accessible.

2.2.2. Hydrodynamics in chromatography

In the early days of chromatography, the most common separation technique was distillation. For this reason, many concepts which describe the efficiency of separation in a chromatographic system, were borrowed from distillation technology. In 1941, Martin and Synge introduced the concept of the height equivalent to a theoretical plate (HETP) which allowed evaluating a chromatographic process in a simple mathematical way (Eq. (2.6)). In analogy with distillation, they assumed that in each "plate" the analyte achieved equilibrium between the stationary and mobile phase [8], and that the plate height (H) was related to the time-related peak standard deviation (σ_t), retention time (t_r) and the column length (L) as:

$$H = \left(\frac{\sigma_t}{t_r}\right)^2 .L \tag{2.6}$$

Last equation can also be expressed in the spatial domain which describes that the plate height is a measure of peak broadening on a certain distance.

$$H = \frac{d\sigma_x^2}{dL} \tag{2.7}$$

The amount of "plates" (N) which a column with a specific length (L) can yield is now easily derived by taking the ratio of column length to plate height:

$$N = \frac{L}{H} \tag{2.8}$$

Despite being an elegant concept, the plate height did not explain how some parameters, like column geometry or different properties of stationary phase, are related to the overall peak dispersion.

2.3. Plate height equations

2.3.1. The van Deemter equation

Van Deemter et al. made a model [9] that describes the plate height as a function of the mobile phase velocity (see Figure 2.2):

$$H = A + \frac{B}{u_0} + C.u_0 \qquad (2.9)$$

u_0 is the unretained species velocity while A, B and C are constants that are determined by the geometry inside the column and by the physico-chemical parameters of the analytes and the mobile and stationary phase.

In this equation, the first term (A-term) is independent of the velocity inside the system and is a measure for the dispersive contribution of tortuous multiple flow paths inside the system (or Eddy diffusion as van Deemter et al. called it). This A-term adds a fixed value to the plate height and can be considered as being representative for the systems disorder or heterogeneity. In consequence, open tubular system, which are often used in GC, will have no contribution of the A term since all flow paths are identical. For packed beds, the A-term can be expressed as a function of the particle diameter (d_p) and a geometrical factor (λ).

$$A = \lambda.d_p \qquad (2.10)$$

The second term in the equation, the so called B-term, describes the molecular diffusion in the axial direction and is inversely proportional to the velocity. It can be described as a function of an obstruction factor (γ) and the molecular diffusion constant (D_m):

$$B = 2.\gamma.D_m \qquad (2.11)$$

The last term, the so-called C-term, expresses the resistance to mass transfer between stationary and mobile phase, which includes adsorption and desorption kinetics but also mass transfer inside the particle. Due to these slow kinetics, the partition equilibrium between stationary and mobile phase is never perfectly achieved. The C-term is proportional to the mobile phase velocity since at higher mobile phase velocities, the inequilibrium between stationary and mobile phase will become worse and lead to more band broadening and an increased plate height. Two major contributions to the resistance to mass transfer can be

distinguished: the mass transfer in the mobile phase and the mass transfer in the stationary phase

$$C = c_s' \frac{k''}{(k''+1)^2} \frac{d_f^2}{D_s} + c_m' \frac{k''^2}{(k''+1)^2} \frac{d_p^2}{D_m} \qquad (2.12)$$

wherein c'_s and c'_m are van Deemter constants, d_f is the film thickness of the stationary phase, D_s and D_m are the diffusion constants of the stationary and mobile phase respectively, k" is the zone retention factor (Eq. (2.5)).

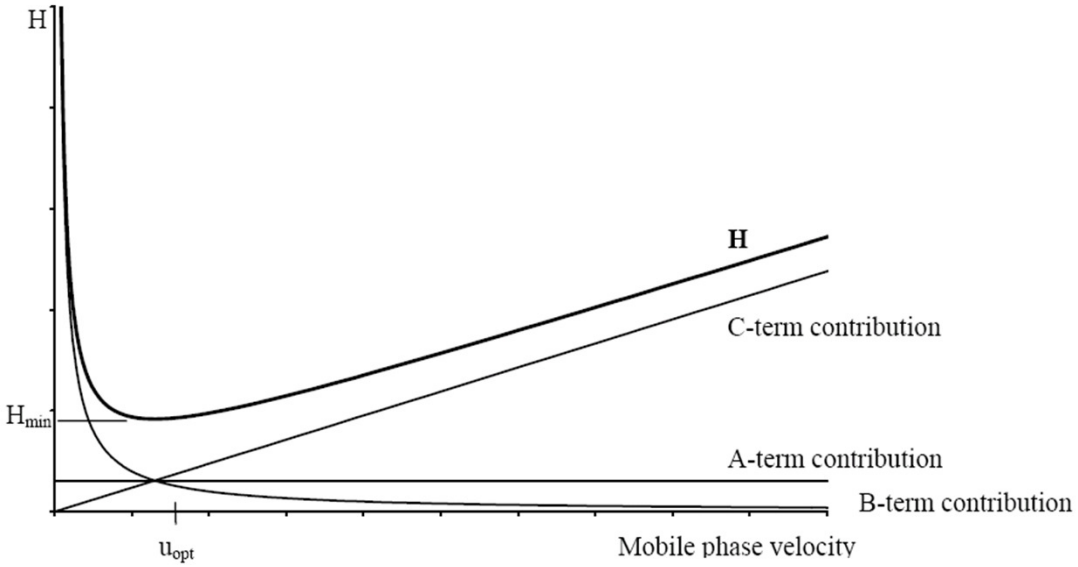

Figure 2.2. Graphical representation of the van Deemter equation. The different contributions are depicted individually.

One conclusion that can be made at this point is that the A-term is proportional to d_p and the C-term with d_p^2. Hence, downscaling the dimensions inside chromatographic systems will decrease the plate height and increase the performance.

2.3.2. The Giddings equation

The van Deemter equation displays an important irregularity, namely that in the case of a zero mobile phase velocity, the A-term still adds a non-zero finite contribution to the band broadening. In his coupling theory [7,10], Giddings argues that eddy dispersion and the C_m term cannot be regarded to be independent, but rather are coupled to each other. In the Giddings equation, the tortuous flow around the particles and the slow mass transfer affect the band broadening rather in parallel and not in series like in the van Deemter equation.

$$H = \left(\frac{1}{A} + \frac{1}{C_m . u_0} \right)^{-1} + \frac{B}{u_0} + C_s . u_0 \qquad (2.13)$$

The original A-term of the van Deemter equation now has become velocity dependent. For very low velocities this term tends to be zero, which is in agreement with the fact that at zero mobile phase velocity the mobile phase dispersion can only be due to molecular diffusion.

2.3.3. The Knox equation

In 1969, Knox proposed a simplified empirical version of the Giddings equation [11] which eases the comparison of performance between different columns with particles of different sizes. In order to compare different column efficiencies, Knox made use of reduced parameters as proposed by Giddings [7],

$$h = \frac{H}{d_p} \tag{2.14}$$

$$\nu = \frac{u_0 . d_p}{D_m} \tag{2.15}$$

Using these reduced parameters, Knox proposed an equation in which he assigned a power dependence on the reduced phase velocity to account for the band broadening due to the cooperative effects of eddy diffusion and transverse diffusion [11].

$$h = a.\nu^n + \frac{b}{\nu} + c.\nu \tag{2.16}$$

When comparing the different models, the Giddings equation represents best the description of a packed bed column [12], although the van Deemter equation is still the most widely used especially for columns working around the optimum mobile phase velocity, mostly due to its simplicity [13,14]. Only at reduced velocities higher than 20, a significant difference between the van Deemter equation and the other ones becomes apparent. Since the Knox equation is obtained by curve fitting of experimental data and not based on a theoretical derivation, its use is limited in column design but is valuable for column measurements and comparisons of column quality [15].

2.4. Selectivity and Resolution

In order to achieve a chromatographic separation of two components in a mixture, the different compounds need to be retained differently by the stationary phase. Selectivity (α) is the ability of a chromatographic system to separate two different analytes and is defined as the ratio of the corresponding retention factors (k'_1 and k'_2).

$$\alpha = \frac{k'_2}{k'_1} \tag{2.17}$$

The selectivity is dependent on the chemistry of the stationary phase and analytes but is independent of the column performance. However, selectivity is not the only characteristic that determines whether a mixture can be separated on a particular column or not. Besides being selective, the column also needs to generate enough theoretical plates in order to resolve the different peaks.

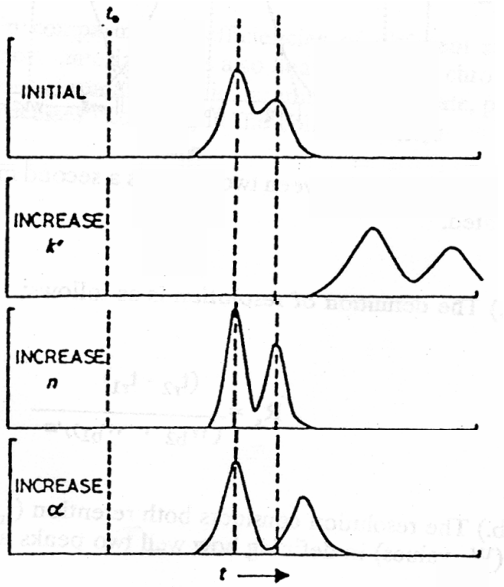

Figure 2.3. Influence of the phase retention factor (k'), plate number (N), and selectivity (α) on the resolution of a separation. Figure taken from [16].

Both criteria can be combined into the resolution parameter, which is an easy measure of the separation quality of a column to separate two different analytes into two different peaks. The resolution of a separation (R_S) is the ratio of the distance between the peaks to their average peak width [12].

$$R_s = \frac{\left(t_{r,2} - t_{r,1}\right)}{\frac{1}{2}\left(w_{t,1} + w_{t,2}\right)} \qquad (2.18)$$

Wherein $t_{r,1}$ and $t_{r,2}$ are the retention times of two resolving peaks and $w_{t,1}$ and $w_{t,2}$ their corresponding peak widths.

The relative difference in retention times depends on the selectivity while the peak widths depend on the column performance. By combining the equations of retention, selectivity and efficiency and assuming both peaks to be Gaussian, an alternative equation for resolution is obtained [17].

$$R_s = \frac{\sqrt{N}}{4}\frac{k'_2}{1+k'_2}\frac{\alpha-1}{\alpha} \qquad (2.19)$$

Wherein N is the plate number of the column, α the selectivity between the two peaks and k'_2 the retention factor of the second peak.

2.5. Novel Column formats and trends

2.5.1. Packed Columns

Over the last few decades, HPLC has gone through huge advancements and has played a major factor in the revolutionizing analysis of chemical and biochemical samples. In the early days of chromatography, the packing materials of the columns were made of limestone, silica gel, hydroxyapatite and diatomic earth. The packing, and the large grain size of the irregularly shaped particles was very irreproducible. The separation power of these early columns was limited due to the choice of materials together with the unawareness of the importance of packing, size and shape control. In an attempt to enhance the mass transfer, porous-shell silica particles were developed during the 1940's to 60's which increased the separation power considerably.

With the development of plate height models, Knox and Saleem [18] reported in 1969 that reducing particle diameters and using elevated pressures would lead to a great improvement in separation efficiency, which explains the race of manufacturers to develop smaller sized particles still today. At the same time, great advances were also made on the development of porous silica particles with low impurities. These B-type silica's were produced in a reproducible way and showed to have better selectivity characteristics, which made them the preferred choice until now as stationary phase [19]. Since then many advances were made which were very substantial since the introduction of HPLC, but were always incremental. Particle diameters have been reduced to 1 µm and have been tested successfully by Jorgensen et al [20,21], but required a extremely high backpressure of 7500 bar.

Latest trends in the field of column chromatography are situated in miniaturization of the complete chromatography system. The major motivation of this trend is the better separation characteristics in terms of efficiency and separation speed but also has ecological advantages since less mobile phase is needed and reduced sample volume gives additional benefits [19].

Recently, Ultra Performance Liquid Chromatography (UPLC), has been introduced which uses sub-2µm particles in short columns (30-80 mm) at elevated pressures (ca. 1000 bar) and

can be considered the "state of the art"-technology in liquid chromatography [22]. These columns have a balance between particle size, column length and pressure which makes it possible to do high throughput analysis without sacrificing efficiency [23].

In an attempt to moderate the high pressures needed, High Temperature HPLC (HTLC) was introduced. By increasing the temperature, the mobile phase viscosity is reduced so higher velocities can be obtained without increasing the pressure [24–26]. Since another parameter is added into the mix, new technical problems arise which limit the effectiveness of working at elevated temperatures. The mobile phase has to be preheated to the column temperature and the effluent has to be cooled down to ambient temperatures before entering the detector. These actions require additional tubing lengths and add additional volume and pressure drops which will be pernicious for the increased separation efficiency of the heated column and limit the achievable separation efficiency and speed.

Also Halo HPLC columns based on the porous shell particle technology (or fused core technology) originally introduced by Kirkland have been a "hot topic" in the HPLC world more recently [27]. These particles have a solid core of 1.7 μm surrounded by a porous layer of 0.5 μm while they have a very narrow size distribution compared to other commercially available particles. Due to these properties, these columns show extremely good mass transfer characteristics as well as plate heights [23] and are often used in UPLC™ systems.

2.5.2. Monoliths

A disadvantage of the particulate column is that the required backpressure of a column increases with the second power of the decreasing particle diameter according to Poiseuille's law for packed columns.

$$\Delta P = \frac{\phi.u.\eta.L}{d_p^2} \qquad (2.20)$$

The most advanced commercially available LC pumps can yield 1300 bar while maintaining a stable flow (Shimadzu Nexera, Shimadzu Corporation, Kyoto, Japan). Since decreasing the particle diameter also shifts the optimal velocity to higher values [18], this means that a further decrease of particle diameter would yield very few additional benefits due to pump limitations. A fundamental way to overcome these limitations is to use another packing material such as monoliths.

Monoliths have been introduced since the late 1980's-mid 90's as a solution to this problem. These materials have a continuous porous skeleton with wide flow-through-pores that can be considered as a single large "particle" that fills the entire column. This emerging technology looks very promising since the average sizes of both the pores and monolithic skeleton can be controlled by the preparation of the monolith. Due to the many parameters involved in the preparation, a wide variety of possibilities has yet to be explored. Another major advantage of monoliths is that the preparation can be done in-situ and thus the packing of silica particles is circumvented. This research can be divided into two main categories, silica monoliths and polymer monoliths [28].

Silica monolithic columns are prepared using the classical sol-gel process. Silane compounds such as tetramethoxysilane (TMOS) or tetraethoxysilane (TEOS) are polycondensated in the presence of a porogen such as polyacrylic acid (HPAA) or polyethylene dioxide (PEO) [29]. The concentration of the porogen has a huge influence on the morphology of the skeleton. As the condensation reaction evolves, a phase separation of the reaction products occurs and the skeleton is formed. After the phase separation, the monolith is dried and aged [30]. An additional hydrothermal treatment can be done to increase the surface area and mesopore volume of the skeleton [31]. After this step, the resulting monolith has a bimodal structure of large through-pores (1-3 μm) providing a high permeability, and mesopores in the skeleton (10-25 nm) providing a high surface area. Finally, the monolith can be coated with (typically) C18 though a derivatization step which makes the final column suitable for reversed-phase applications [32].

Polymeric monoliths can be prepared from a mixture of monomers (e.g. styrene, divinylbenzene, methacrylate, acrylamide), a cross-linker, an initiator and a porogen. Due to the large variety of monomers, the chemistry of these polymeric monoliths is very diverse and can be tuned by adding reactive functionalities to accomplish different stationary phases [31,33]. These monoliths are prepared *in situ* in a plastic or stainless steel tube and the polymerization reaction is initiated either thermally or by irradiation with UV-light [28]. Polymeric monoliths have a morphology that is quite different compared to silica monoliths (see Figure 2.4) and instead of a skeleton with through-pores, they have a "cauliflower" structure of little organized microglobules with large through-pores (ca. 0.5-1 μm) [34,35].

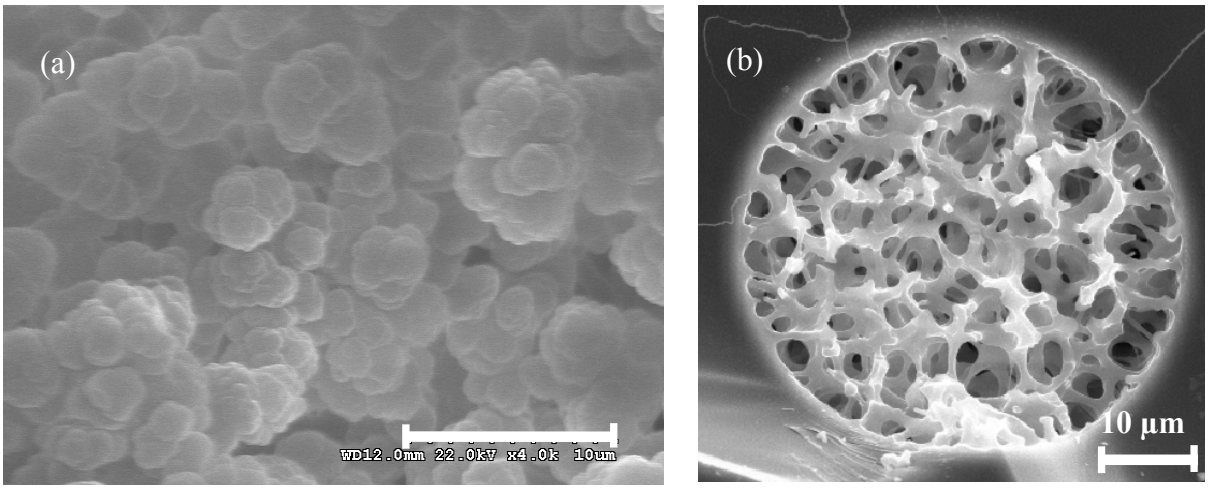

Figure 2.4. SEM-images of (a) a polymer monolith and (b) a silica monolith (reproduced from [36]).

2.5.3. Lab on a chip and on-chip liquid chromatography

As already pointed out in §2.5.1, the main motivation for miniaturization was to enhance the separation power rather than reducing the size. Reducing the distances for mass transfer processes will lower the C-term in the Van Deemter equation (Eq. 2.9.) since the time needed for diffusion scales with the second power of the distance. The first on-chip liquid chromatograph was reported by Manz et al. in 1990 [37]. He used a 5 x 5 mm silicon chip containing an open tubular column and a conductometric detector. Even though the separation power of the chromatograph was never demonstrated, his work is still considered a benchmark as the concept of a micro-Total-Analysis-System (or shortly µTAS) was also introduced in the same study. µTAS or "lab on a chip" is an analysis device which contains all the components needed for an analysis: injector, sample pre-treatment, separation and detection. During the late 1980's, early 90's, several microfluidic structures, such as microvalves [38] and micropumps [39] had been fabricated using silicon micromachining technology. These could provide the control for the complex microfluidic actions required to operate the LC chip presented by Manz et al. Despite that the concept was presented in 1990, it was not the first study which incorporated all the parts of a chemical analysis system in a silicon wafer. In 1973, Terry and co-workers proposed a gas chromatograph integrated in a silicon wafer containing a sample injector, column, and a clamped thermal conductivity detector which was fabricated on a different silicon wafer [40].

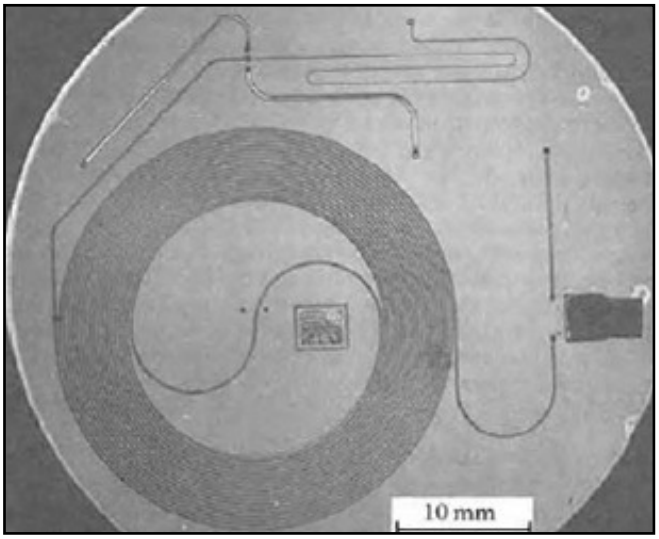

Figure 2.5. The first "lab-on-a-chip" made by Terry et al. (picture taken from [40])

Unfortunately the separation power of the device was poor compared to the standard columns of those days which explains the disinterest of the scientific world, as it took another 10 years before this field was explored again by Manz et al.

In the years after the introduction of the μTAS concept, the field of the lab on a chip was further explored using electrokinetic flow driving techniques introduced by the Harrison [41] and Ramsey [42] groups. The idea of electrokinetic separation has since then evolved into an extremely prolific field of academic research. On the other hand, the direct transfer of the conventional pressure driven liquid chromatography to a chip based platform was pursued by only very few groups. This can be explained by the technical difficulties experienced when applying high pressures to these microchannels. Generating and controlling microfluidic flows could be easier accomplished using electrokinetics compared to using pressure as driving force due to high backpressures required to generate a flow through a microchannel (Eq.2.20). Due to the diversity of technical difficulties that have to be overcome in the development of fully integrated HPLC chips, most research and development efforts have focused on hybrid LC systems that combine on-chip components with off-chip components. The major challenging aspect of creating a fully integrated HPLC chip is the incorporation of a high pressure pump. The more advanced HPLC pumps used for capillary HPLC and UPLC can deliver pressures up to 1300 bar (Shimadzu Nexera, Shimadzu corporation, Kyoto, Japan) and are also typically used for chip-based HPLC systems as an off-chip component. While the design of these pumps can be scaled down and be microfabricated on wafer level [43–45], their applicability to on-chip HPLC have not been demonstrated yet. Other components like

injectors have been included on-chip and actually directly improve the analytical performance of the device due to the technical difficulties related to connecting off-chip and on-chip components and their resulting dead volumes [46]. Reducing dead volumes in an HPLC system between injector, column and detector always increases the performance of the system. These on-chip injectors are valveless and require an off-chip pressure controller for each microfluidic connection which is also the major drawback of these injectors. The control of the pressures on the in- and outlets of both injector and column have to be done with uttermost precision in order to produce reproducible injections. Gas inclusions or particle contamination between the injector and off-chip pressure controller greatly reduce the reliability of this system.

Including the detector on the chip will improve the performance of the system by minimizing the extra column band broadening. However the performance of the system also depends on the availability of a suitable sample detection technique which tends to be more cumbersome for miniaturized systems. Upon downscaling the column, the amount of sample eluted from these miniaturized columns will decrease and will pose problems in terms of sensitivity and spatial resolution. Optical absorption detectors, which are commonly used in conventional HPLC, have the disadvantage that the sensitivity scales with the available optical path length. Another requirement is that the detector volume is only a fraction of the eluting sample in order to get enough data points per eluting sample peak and for this reason, optical detectors become less suitable with the decreasing column volume. In order to compensate the loss in optical path and sensitivity, several solutions have been reported which make use of a multiple optical path [47] or an optical cavity [48]. Electrochemical [49] and electrical impedance detectors [50] are more amenable to miniaturization and integration since they rely less on off-chip components as they take advantage of micro-patterned planar electrodes. These have been successfully integrated in microfluidic systems and their sensitivity has gone to zeptogram level [51]. Less amenable, but more promising is the coupling of these microfluidic devices with mass spectroscopy. This has lately been the focus of a lot of research [52–55]. Mass spectroscopy is a very powerful detection and identification tool and provided that the interface between the chip and MS is designed properly, post-column band broadening is minimized. The Agilent HPLC chip [54] is a notable example of this detection approach that has been commercialized and had significant practical impact [50,56,57] (see also §2.5.5).

2.5.4. Pillar array columns

Instead of "implementing" already existing column formats onto a microchip, Regnier and co-workers explored the possibilities of microfabrication and created a microfabricated pillar array, or the so called "collocated monolithic support structure" (COMOSS) as Regnier introduced this, a regular array of posts with identical size and shape and equally distributed over the area of a larger channel, thus mimicking a perfectly ordered packed bed [58,59]. With this approach, he took advantage of the improved separation kinetics of miniaturized systems but more importantly, he introduced an ordering in the stationary phase support to improve the column efficiency. As Knox stated [60], the major cause of the efficiency limits in modern HPLC is the band dispersion occurring because of the poor structural homogeneity of the stationary phase support such as the random arrangement of particles in a packed bed inside a column or the random structure of monoliths.

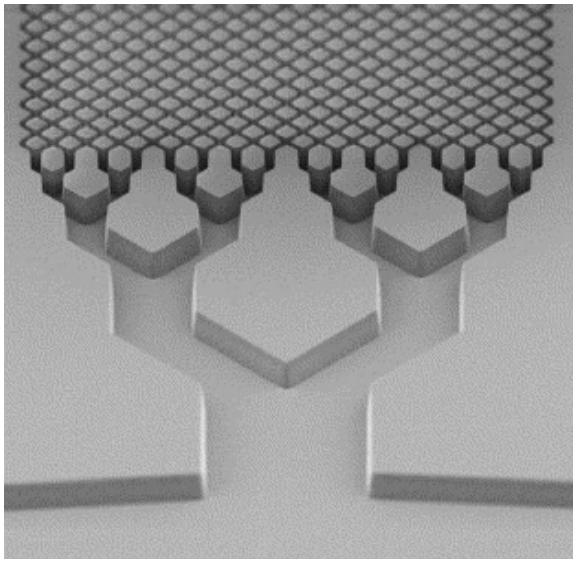

Figure 2.6. SEM-image of the first pillar array column made by Regnier et al. (Reproduced from [58]).

Using CHF_3-based chemistry, Regnier and co-workers etched a packed bed anisotropically directly into a quartz wafer creating microfluidic channels as well as a stationary phase support. The created channels were explored using capillary electro-chromatography (CEC) techniques and not with pressure-driven techniques. This was mainly due to the ease of applying an electrical gradient compared to a pressure gradient over the channel, but also due to mechanical problems occurring in pressure driven mode. The cover glass on top of the pillar array was only bonded effectively with the side walls of the channel and not the top of the pillars. When applying pressure, a gap was formed between the ceiling glass and the top of the pillars creating either a preferential flow path or a dead volume which both result in

additional band broadening. Another advantage of CEC is that the electro-driven flow is less sensitive compared to the pressure-driven flow to local differences in pillar size, which were unavoidable due to the microfabrication techniques available at the time. The preference to evaluate these channels with an electro-driven flow also explains the preference of electrically insulating quartz over semiconducting silicon as substrate material, besides the chemical similarity of the quartz microstructures with the silica particles used in conventional HPLC.

The chemical engineering department of the Vrije Universiteit Brussels picked up the idea, and started with computational fluid dynamics (CFD) simulations to characterize the novel column format and its limitations when used in pressure driven chromatography. Gzil estimated plate heights for these columns [61], which were confirmed by band broadening experiments on non-porous pillars under non-retentive conditions performed by de Pra et al. [62]. De Malsche et al. carried out a reversed-phase separation in pillar array columns with non-porous [63] and porous pillars [63,64] under pressure driven LC conditions. Eghbali et al. separated a realistic sample on the same column and was able to separate up to 8 pyoverdines [65]. Vangelooven has made several CFD simulations on the column design and optimized the sidewall region of the pillar bed in order to reduce the local band broadening. The sidewall region differs fundamentally from the pillar bed due to the different volume to surface ratio and hence has a different flow resistance compared to the rest of the pillar bed. By shifting the wall closer and further from the pillars and also incorporating pillars inside the wall, he was able to find, for different porosities and shapes, a “magical distance” for which the flow resistance matched that in the central region of the pillar array [66]. Using CFD simulations, Vangelooven also designed distributors at the in- and outlets of the pillar array column, mimicking the frits of a commercial column format [67].

The pillar array columns do look really promising from a fundamental point of view, however from a practical point of view, there are still several technical limitations that need to be addressed before they can compete with HPLC and its dominance in the field of analytical separation sciences. In order to connect the pillar array to commercial injectors and detectors, a smooth transition is needed between the broad rectangular pillar channels and the narrow pre- and post-column channels leading to the capillaries of the injector and detector respectively. The difficulty in connecting the micro-components of a device with the macro-environment of the world, results from the fact that samples and reagents are typically transferred in quantities of microliters, whereas the micro-devices only consume volumes of

nano or pico-liters (or even less). This is often ignored in research environments such as academic laboratories because skilled researchers are aware of the problem and find creative ways to work (even with manual manipulations) around this hurdle to demonstrate the fundamental qualities of their micro-devices. However, in order to become a commercial success, this hurdle can not be put aside especially for high throughput applications where manual manipulations are not economical and good macro-to-micro and micro-to-macro interfaces needs to be developed [68].

Besides the micro-to-macro interface problem, which is the biggest hurdle for pillar array columns to become commercially viable, it is worth noting that also the HPLC field has made substantial advances since the introduction of HPLC [19]. Good examples are the porous packing materials, more specifically the chemically modified monodisperse silica gel particles with well controlled sizes, surface properties and nanoscale porosity [69–71] like the Halo particles (see §2.5.1).

Another reason for the dominant position of HPLC in the analytical separation sciences is the advancement of technologies in other domains outside chromatography which could be easily transferred to HPLC systems and concern mostly pumps (e.g. for UPLC™), valve systems, detectors and column packing methods [70,72].
Emerging new chromatography technologies were therefore always welcomed with skepticism due to the high "standard" conventional HPLC has set to compete with, even though the theoretical advantages of non-conventional systems over conventional HPLC systems were well demonstrated [60,61].

2.5.5. Agilent HPLC-chip

The Agilent HPLC-chip [54,73,74] is a good example of a chip device in which several already mature techniques are incorporated. The chip is made of several layers of polyimide in which all components are shaped by laser ablation and subsequently are laminated together. The injection to the chip is done by using a 3-way rotary valve in combination with an enrichment channel that is incorporated in the polyimide chip. The dead volumes associated with the connections are minimized by installing the HPLC-Chip within a LC rotary valve (see Figure 2.7). The basic commercially available HPLC-Chip has a packed enrichment channel (volume 40nl) and a rectangular LC channel (depth: 50 µm; width: 75µm, length: 50mm) which is packed with porous silica particles but more recently other HPLC-Chips with

longer channels became also commercially available. At the end of the channel, a fine electro spray ionization tip is found, manufactured using the same laser ablation techniques. This spray tip leads to a mass spectrometer (ESI-MS) for detection. Overall, this design is very compact and connects the injector, column and detector with the smallest possible dead volume.

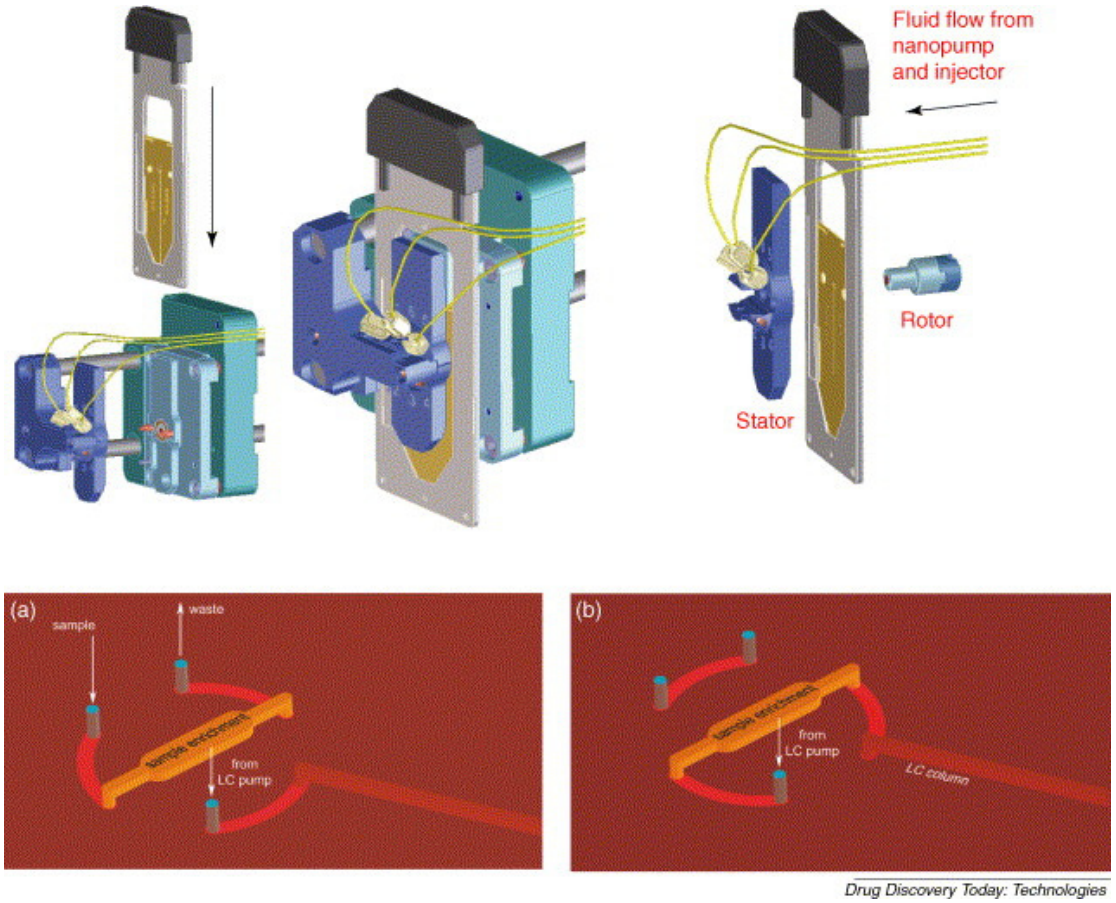

Figure 2.7. Connection of the Agilent HPLC-chip to the sample supply, mobile phase supply and waste. (a) When the rotor is put in injection mode, the sample loop (or enrichment column) is filled with sample while the column is flushed with mobile phase. (b) When the rotor switches, the filled injection loop is injected in the column for separation. (figure taken from [75])

In the first prototypes, the column was semicylindrical due to the laser ablation process and was packed with porous silica particles which can be coated with a stationary phase. The group of Tallarek has done a lot of studies on characterizing the performance of the column in terms of channel geometry and packing [76–79]. Simulations have shown that columns with non-circular geometries compared to columns with circular geometries have a larger hydrodynamical dispersion due to the presence of corners where the local fluid flow velocity is higher. Amongst the three non-cylindrical geometries studied, the square (quadratic) format had the best performance followed by the rectangular format and the semi cylindrical format had the worst performance. For this reason it was concluded that, besides the presence of

corners, symmetry also affects the hydrodynamical dispersion. Reduced symmetry leads to a longer characteristic length of the solute molecules for lateral equilibration between different velocities and hence a larger axial dispersion.

The group of Tallarek also found that the hydrodynamical dispersion in non cylindrical columns was affected more strongly in highly porous packings. At lower porosity (in densely packed non cylindrical columns) the hydrodynamical dispersion comes close to those of packed cylindrical columns. The fabrication of densely packed micro columns with silica particles was done using ultrasound and stainless steel holders so higher packing pressures could be applied without mechanical failure of the chip. These HPLC chips were as densely packed as the cylindrical fused silica capillaries used in nano-HPLC and it was demonstrated that the efficiencies of the HPLC-chip separations were comparable to those achieved in nano-HPLC.

Whilst the packing procedures can be optimized for the existing geometries, a more fundamental solution would be to find alternatives for the densely packed non-cylindrical format. A very promising approach would be to replace the packed polyimide column, with a microfabricated-2D pillar bed. Due to the planar nature of lithography and the subsequent processing steps, the final result of the substrate with the pillar bed is also planar which makes it geometrically very compatible with the planar HPLC-chip format. Another advantage of the 2D-pillar-arrays is that these avoid all the packing of micro channels with particles while the versatility in applicable stationary phase coatings remains the same. It can also be expected that the manufacturing costs with the 2D pillar beds are substantially lower since the different processes can be done in parallel. Many silicon columns can be made in one “batch” while the laser ablation process and also the packing process are fundamentally linear/serial in nature (piece by piece).

The 2-D pillar beds are also non-cylindrical in nature but their porosity, depth, width, etc. can be tuned with the design of the mask and subsequent etching processes. Similar to Tallarek’s observations, these 2D pillar beds also have “corners” but these are called sidewalls. These sidewalls already have been tuned for the “ideal sidewall distance” and the local fluid flow velocity is exactly the same in these regions as in the center of the pillar bed [67]. This implies that the characteristic length of the solute molecules for lateral equilibration is the same for the whole width of the column, including the sidewalls, and there is no additional

hydrodynamical dispersion due to these. Another great advantage of these 2D-pillar beds is the symmetry. As Tallarek found that increasing symmetry in column geometry reduced the characteristic length of the solute molecules for lateral equilibration, these 2D pillar beds are in design perfectly symmetrical. The pillars (which replace the particles) are perfectly symmetrically ordered on the lithographical mask and in fact make the packing symmetrical, which is something that even with the best packing procedures can not be achieved in packed bed columns.

2.6. Microfabrication

The techniques to design and fabricate microfluidic systems like the micro-pillar arrays have been adopted from the field of microelectromechanical systems (MEMS) which in turn is a descendant of the process technology of the integrated semiconductor circuit industry [80,81]. MEMS devices are now widespread and can be found in automobiles, printers, computer games, operation rooms, laboratories, high tech devices send into space and many more.

2.6.1. MEMS and microfluidics

The basic techniques to fabricate most of the modern microfluidic devices all involve (one or more of) the basic techniques from MEMS which are: deposition of layers, patterning by lithography and etching to produce the desired shape. Similar to the evolution of conventional HPLC which benefited from the advancements in pumps and valves made in other fields [19], microfluidics had the great advantage that most of the needed techniques to create these devices were already optimized and fine tuned for the field of MEMS [82]. While MEMS focuses on fabricating and assembling very small components in the range of 1-1000 micrometers and while microfluidic devices are in comparison relatively large (chip-dimensions of several centimeters by several centimeters), both fields require a very high quality in shape control on the microscopic level, and lately, even on the nanoscopic level.

The widespread use of silicon as substrate material is due to the well known techniques to “micro-machine” this material. This is mostly due to the semiconductor characteristics and the development of microprocessors in the last century which meant a huge revolution in the micro-electronics field. For MEMS, the mechanical properties of silicon are excellent since it acts as a nearly perfect Hookean material with virtually no hysteresis and hence almost no energy dissipation due to intergranular slip or movement of dislocations in single-crystal silicon below 500°C [80]. As a consequence, silicon suffers very little fatigue in applications

with highly repeatable motion and can have service lifetimes in the range of billions to trillions cycles.

Silicon oxide in its crystallized form (quartz) as well as it amorphous form (glass and fused silica) is also very interesting as a material in MEMS for its mechanical and piezoelectric properties and is therefore often found in resonator applications [83,84]. The techniques to shape quartz originated from the integrated circuit industry in which thin layers of thermally grown silicon oxide were used as an insulating material in transistors. Since then, these techniques have been improved tremendously for MEMS purposes and are capable of shaping 3D structures, rather than 2D thin layers [85,86]. Of course, fused silica is a very interesting material for on chip chromatography as it is chemically identical to the silica particles used in conventional HPLC.

Polymers gained a lot of interest in the last decade, partly because silicon is a complex and relatively expensive material to produce in large quantities. Polymers can be produced in huge volumes and also have the advantage that a great variety can be found in material characteristics as well as in applicable processing procedures.

Thermosets are usually shaped by molding when the used polymer is cured thermally (e.g. PDMS) or by lithography when the used polymer is cured with light (e.g. SU-8). SU-8 and PDMS (polydimethylsiloxane) are commonly used thermosetting polymers for microfluidic applications. SU-8 can be used to make thick structures with high aspect ratio without requiring expensive techniques but with broadband UV lithography. SU8 is often used to create microfluidic and lab-on-a-chip devices and a whole range of methods have been reported (for an excellent review, the reader is referred to [87]) to produce simple and complex microfluidic channels [88–96] and microfluidic structures such as needle connectors [97] mixers [98], nozzles [99], checks valves and many more [100,101].

PDMS is a silicon-based organic polymer with interesting properties related to its molecular structure. It has a relatively low density and high permeability for gases due to the long Si-O and Si-C bond lengths (compared to C-C bond lengths) [102]. The low glass transition temperature and deformability are mostly related to the polymer chain packing and the high degree of so-called “free volume”. PDMS structures are commonly made by molding (also called “soft lithography”) which can duplicate inverted structures from rigid molds [103],

however recently structures can also be defined with lithography by introducing photoinitiators in the PDMS prepolymer mixture [104]. PDMS is found in many lab-on-a-chip and microfluidic devices [105,106] for many reasons amongst which: biocompatibility, easy molding methods that do not require intensive expertise or expensive equipment, variable thickness, transparent from UV up to infra red, less fragile than silicon or glass, etc. PDMS also can be bonded very easily with silicon, glass or other PDMS structures in a reversible or irreversible manner [107].

Some PDMS alike thermosets (e.g. Ormocer®) can also be shaped using two-photon polymerization [108–110] besides standard lithography [111]. The two-photon polymerization technique is very similar to stereolithography, which is an interesting technique for quickly shaping 3D prototypes with low resolution (within the range of a few micrometers). In stereolithography [112], a UV-laser scans the surface of a photosensitive material and polymerizes the exposed parts of the resin in a 1-photon polymerization process. Therefore, 3D profiles can be generated by a layer-by layer approach. Since the photosensitive materials are highly absorbent in the UV range and are highly transparent in the infra red (IR) range, it is possible to initiate two-photon polymerization within a small volume of the resin using precisely focused IR laser pulses which makes it possible to write the structures in 3D. The two-photon polymerization process is fundamentally non-linear (probability of n^{th} order absorption is proportional to the n^{th} order of the photon flux density [113]) and due to this it displays a threshold behavior because 2-photon polymerization initiation can only occur above a certain threshold intensity. This in effect makes it possible to create structures smaller than the used wavelength and feature sizes of 100nm (and smaller) have been reported [114,115]. This is a very useful and interesting technique for prototyping, but less amendable for high-throughput fabrication of devices because of the high costs of optical components as well as the resin used. However, the technique is still fairly young and improves rapidly and it can be expected that this technique will improve over the next few decades to compete with the other microfabrication techniques.

Thermoplasts are usually shaped by either (injection) molding or embossing. Injection molding is very promising for many MEMS applications, however, due to the cavities (the channel) inside microfluidic devices, it is impossible to create a suitable master for microfluidics. On the other hand, embossing and molding half-open channels can be done very effectively. This is mostly due to the replicative nature of the technique and thus the

inverted 3D profiles of silicon master substrates that are shaped with state of the art technology can be transferred to the polymer substrate without loss in shape resolution. The microfluidic channel is subsequently made by ceiling the half-open channel with another substrate. The other advantage of this technique is that a broad range of thermoplastic polymers can be used [116].

Besides molding, embossing and lithography, thermosetting and thermoplastic polymers can also be shaped by a lot of other techniques like etching, milling, laser ablation, and other techniques [117].

2.6.2. Photolithography

Structuring substrates in the desired shape is usually done by patterning a mask by lithography on the substrate and removing the exposed parts by etching [80,118]. The pattern can be copied by projecting the photomask onto the substrate or by bringing the photomask in close contact with the substrate. In this thesis, lithography was done by bringing the resist in contact with the photomask using a contact aligner.

In the first step of contact lithography, a clean substrate is coated with an adhesion promoter and photoresist by spinning. The viscosity of the resist, spinning speed, spinning acceleration and spinning time determine the final layer thickness and uniformity. During the spinning, the solvents inside the photoresist evaporate and the liquid resist becomes very viscous. Usually a "soft bake" is done after that to evaporate the remaining solvents without curing the resist, to prevent sticking of the photoresist layer during the contact with the photomask. In the next step, the soft baked wafer is aligned with a photomask and illuminated. The required time depends on the power of the illumination source, the layer thickness and the type of the photoresist. Usually UV is used as illumination source to modify the molecules in the illuminated area. For positive photoresist, the illuminated areas become soluble in mild alkali solutions (e.g. tetramethylammonium hydroxide, TMAH) and for negative resist, the illuminated areas become soluble in specific solvents. The change in solubility is a consequence of the changed molecular structure of the resist in the illuminated areas. For positive resist, the molecules in the illuminated areas become polar or are broken up in smaller molecules, for negative resist, the molecules in the illuminated areas become apolar or make bonds (e.g. crosslinks) and become much bigger molecules.

The resolution of features (R) or the minimum resolvable distance (b_{min}) that can be resolved by lithography (eq 1.21) is limited by the wavelength (λ) of the illumination source, the distance of the gap between the mask and resist layer (s) and the photoresist thickness (z) and a parameter (k) depending on the process [80].

$$R = b_{\min} = k \cdot \sqrt{\lambda \cdot \left(s + \frac{z}{2} \right)} \qquad (2.21)$$

Features smaller than b_{min} will not be resolved well due to diffraction of the illumination light through the photomask. In "hard contact" mode, a pressure is applied on the photomask removing the gap between resist layer and mask (s=0) which is needed when small features need to be resolved. Using thinner resist layers and smaller wavelength (e.g. extreme UV [119]) will also result in better resolution. The most commonly used lamps for illumination are broadband mercury lamps of which the i-line (λ = 365nm) has the highest intensity and is mostly used in broadband UV lithography.

Photomasks can be made through several ways of lithography. A nearly optical flat glass plate (or quartz when deep UV is used) is coated with a thin absorber layer, often chromium. The glass (or quartz) plate is transparent to the UV light while the absorber layer (chromium) is opaque. Laser lithography is a commonly used method to fabricate photomasks. In this lithographical technique a laser dot scans a layer of photoresist on a photomask and selectively illuminates the resist duplicating the virtual design in the photoresist. The smallest features that can be made with laser lithography (λ = 422nm) are in the order of 600 nm. However for complex designs, there are more limitations due to the accuracy of the translation stages, the used optical system and the stability of the laser source. For such designs the minimal line width is more important and usually is in the order of 1.5μm (using a laser source with λ=422nm) [120,121]. Smaller features (200nm) and thinner minimal line widths (600nm) can be made by using more advanced laser lithography tools which use deep UV (λ=244nm) and state of the art translation stages and optics [122]. In this thesis, only photomasks made by laser lithography were used to pattern the substrates through broadband UV photolithography.

When smaller features are required on the photomask that can not be resolved by this technique, electron beam lithography can be used. In stead of a light beam, an electron beam is used which can be focused in smaller dots more reliably. The smallest resolution obtainable is however not only defined by spot size, but also by the backscatter of the electrons inside the

resist and substrate resulting in exposing the resist over areas larger than the beam spot size limiting practical resolutions to dimensions greater than 10nm. Compared to laser lithography, the writing speed is a lot slower and the cost of equipment a lot higher. A solution to the speed issue is the use of multiple electron beams in parallel, a concept that is now on its way to commercial application [123].

Ion beam lithography (IBL) is similar to electron beam lithography, but since the removal of material is purely physical due to the bombardment of ions, harder materials can be patterned. Resolution with IBL can be of the order of 5 nm. [124]. IBL should not be confused with focused ion beam (FIB) milling or etching in which the emphasis is on the removal of material.

2.6.3. Etching

After patterning the surface of the substrate with lithography, the substrate can be etched to give it the desired shape [80,125,126]. It is important that the used masking material has enough selectivity with the substrate, i.e. the substrate should have a significantly higher etching rate than the masking material. For some applications, photoresist can be sufficient as masking material, but often the pattern defined in the photoresist has to be transferred to a "hard mask". The selectivity between materials depends on the used etching process and the required thickness of masking material can be estimated from the selectivity and the required etching depth.

As explained previously in §2.6.2, thinner photoresist layers will make it possible to resolve smaller features. However, these thinner layers are less protective in the subsequent etching steps and will be etched through if the required depths are too high. The hard mask has a high selectivity with the bulk material and will not get etched through nor damaged by the etching agent. This hard mask is often deposited on the substrate and the lithography is done on this layer. Frequently used masking materials are siliconoxide (for silicon reactive ion etching), silicon nitride (for anisotropic wet KOH etching in silicon) and polycrystalline silicon (for fused silica RIE). Metals are also often used as hard masks, but preferably avoided since potential metal contamination can be very disastrous in many applications (including chromatography [127]).

The etching can be done in an isotropic or in an anisotropic way. Isotropic etching is usually done by wet etching, immersing the substrate in a solution. Anisotropic etching is usually done by dry etching with a plasma. However silicon, due to its single crystal structure, can be etched anisotropically in a wet environment of e.g. KOH due to the different etching speed of the different crystal planes.

Wet etching is in general used as “bulk micromachining” (to remove large parts of the substrate) for shaping 3D structures, to remove thin films (e.g. masking layers) or to clean the substrates of contaminants. When etching isotropically, the masking material will be undercut by the same distance as the etching depth and this needs to be accounted for in the design.

Nowadays, there is an overwhelming push in the micromachining industry towards dry processing and deep dry etching. In the past, dry etching techniques demonstrated low selectivity and were primarily used for etching structures with very fine dimensions with a low depth (e.g. through a thin film) due to the low etching rate. In the last decades large progress has been made in dry etching technology [128,129], causing the use of dry etching technology to expand from surface microfabrication (thin films) to bulk micromachining (removal of a lot of material) with high aspect ratio (high ratio of trench depth over trench width) [130].

The most frequently used dry etching process is reactive ion etching, shortly RIE. In RIE, a plasma is generated from the feed gas which is done preferably in the inductive coupling plasma configuration (ICP). The plasma can also be generated in capacitive mode (planar plates) but due to the high voltage being present within the chamber, surfaces will be sputtered by ionized species from the plasma. The etching mechanism can be chemically (reaction), physically (impact of ions on surface will sputter) or a combination of both. For anisoptropic etching, the mechanism will always involve physical etching in order to obtain a more directional etch profile. Due to the many parameters involved in the process, tuning a recipe is not a straightforward procedure and changing one parameter often results in adapting many other parameters in order to obtain the desired effect. However, Janssen en De Boer made reports in which they presented algorithms (e.g. their "black silicon method" [131]) in order to tune the recipes based on the etching profiles for several RIE techniques like cryogenic etching [132].

Cryogenic etching is the most advanced form of pure RIE etching and is classified as deep reactive ion etching (DRIE) to emphasize the high aspect ratios that can be achieved. In this process the substrate is cooled to very low temperature (in the order of -100°C). The reactive species inside the plasma etch the substrate and the reaction products from the etching reaction condense quickly in the direct neighbourhood of the impact site and form a passivation layer, a barrier which protects the underlying material from the reactive etching gases. Due to the electrical bias of the substrate, the ions inside the plasma are accelerated towards the substrate and physically etch the passivation layer exposing the underlying material which then can be etched again by the etching gases. Due to the vacuum and the electrical bias, the ions are directed perpendicular to the substrate and mainly bomb the bottom surface of features, which results in an anisotropic etching profile.

Bosch® [133] is a two-step cyclic silicon etching process with an etching step and a passivation step. In the first step (see Figure 2.8a), etching gases (e.g. SF_6) are inside the plasma which will etch the silicon isotropically. In the second step (see Figure2.8b), the plasma will constitute of reactive species of a passivation gas (e.g. C_4F_8) which will form a passivation layer on the walls and bottom of the trench. When the cycle restarts with the etching step (see Figure2.8c), the passivation layer will be physically etched at the bottom of the trench or pit exposing the silicon for the etch gas to react.

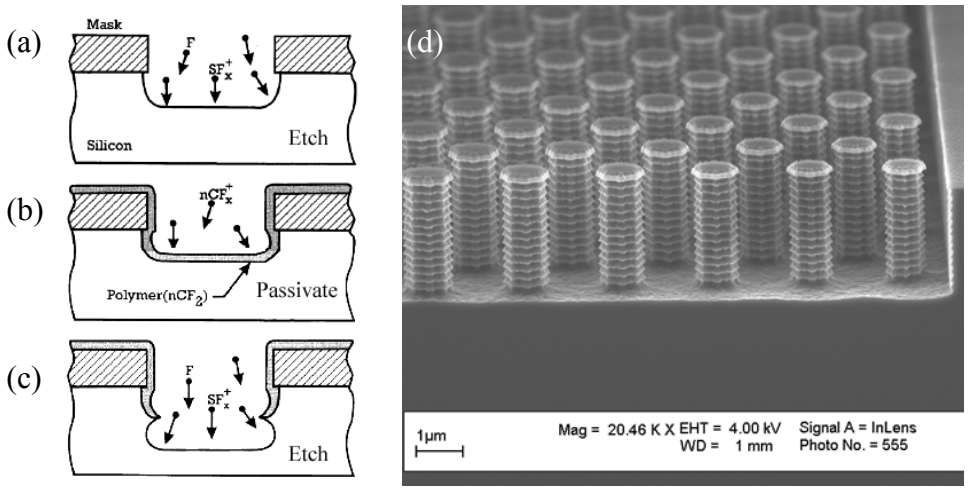

Figure 2.8. (a-c) mechanism of Bosch®- etching (figure taken from [134]), (d) the scallops are an artifact of the cyclic nature of the process. (figure taken from [135])

The scallops are an artifact of the cyclic process. Shorter cycles will result in smaller scallops and smoother walls but will lower the etching speed. The frequency of switching between the

steps is limited by the time needed to empty and refill the reactor volume with the required gases, so in fact by the hardware controlling the process (pumps and valves).

Silicon can also be electrochemically etched in solutions containing fluoride ions. For highly doped p-type silicon, which is the only substrate material that was used for this purpose in the presented thesis, porous silicon is formed at low current densities (lower than i_p in Figure 2.9). Increasing the current density will increase the porosity and will result ultimately in electro-polishing at high current densities (higher than i_p in Figure 2.9) in which the etch rate can be controlled with the current density.

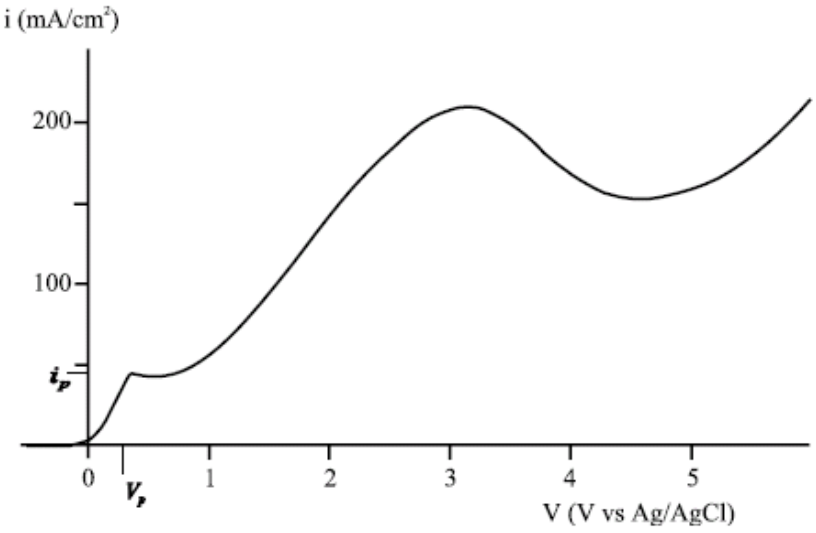

Figure 2.9. i-V curve of a p-type silicon wafer in a 5% HF solution.
Resistivity of the wafer 0.01-0.018 Ω/cm, scan rate 500 mV/s. Figure taken from [136]

With these observations, Tjerkstra et al. were able to create micro-sieves in silicon [136,137]. The exact initiation mechanisms to produce porous silicon are still not clear. The porous layer formation does resemble a lot like pitting corrosion which in general is associated with material defects and leakage from a passive layer and given the single crystal structure of silicon, the formation of the pores is quite intriguing. One plausible explanation for the pitting behavior is the presence of atomic hydrogen which is known to create structural defects in the same direction as the pores along the <100> plane of the silicon crystal [138,139]. These defects however have not been observed yet due to the low lifetime (a defect is etched away instantly) and the very low density of defects. Many models have been proposed to explain chemistry and reactions behind the porous layer formation but are not within the scope of this thesis. For those, the reader is referred to [140].

2.7. References

[1] M. Tswett, *Ber Deutsch Bot Ges* **1906**, *24*, 316–323.

[2] L. S. Ettre, *LC GC North America* **2001**, *19*, 506–512.

[3] G. Guiochon, *Journal of Chromatography A* **2006**, *1126*, 6–49.

[4] C. Horvath, *Chromatography: A Century of Discovery 1900-2000*, Elsevier Science & Technology, Amsterdam, **2003**.

[5] J. F. K. Huber, *Journal of Chromatographic Science* **1969**, *7*, 85–90.

[6] J. J. Kirkland, *Journal of Chromatographic Science* **1969**, *7*, 7–12.

[7] J. C. Giddings, *Dynamics of Chromatography, Part I: Principles and Theory (Chromatographic Science Series, Vol. 1)*, Marcel Dekker, New York, **1965**.

[8] A. J. P. Martin, R. L. M. Synge, *Biochemical Journal* **1941**, *35*, 1358.

[9] J. J. Van Deemter, F. J. Zuiderweg, A. Klinkenberg, *Chemical Engineering Science* **1956**, *5*, 271–289.

[10] J. C. Giddings, *Journal of Chromatography A* **1961**, *5*, 46–60.

[11] J. H. Knox, J. F. Parcher, *Analytical Chemistry* **1969**, *41*, 1599–1606.

[12] U. D. Neue, *HPLC Columns*, Wiley-VCH, New York, **1997**.

[13] K. M. Usher, C. R. Simmons, J. G. Dorsey, *Journal of Chromatography A* **2008**, *1200*, 122–128.

[14] L. Kirkup, M. Foot, M. Mulholland, *Journal of Chromatography A* **2004**, *1030*, 25–31.

[15] R. E. Majors, *American laboratory* **2003**, *35*, 46–54.

[16] D. C. Harris, *Quantitative Chemical Analysis*, WH Freeman, **2006**.

[17] D. A. Skoog, D. M. West, F. J. Holler, *Fundamentals of Analytical Chemistry*, Saunders College Pub, Philadelphia, PA, **1982**.

[18] J. H. Knox, M. Saleem, *Journal of chromatographic science* **1969**, *7*, 614–622.

[19] N. V Lavrik, L. T. Taylor, M. J. Sepaniak, *Analytica chimica acta* **2011**, *694*, 6–20.

[20] A. D. Jerkovich, J. S. Mellors, J. W. Jorgenson, *LC GC NORTH AMERICA* **2003**, *21*, 600–611.

[21] J. W. Jorgenson, K. D. Lukacs, *Journal of Chromatography A* **1981**, *218*, 209–216.

[22] R. E. Majors, P. W. Carr, *LC GC North America* **2008**, *26*, 118–168.

[23] D. Guillarme, J. Ruta, S. Rudaz, J.-L. Veuthey, *Analytical and bioanalytical chemistry* **2010**, *397*, 1069–1082.

[24] S. Heinisch, J.-L. Rocca, *Journal of Chromatography A* **2009**, *1216*, 642–658.

[25] J. Li, Y. Hu, P. W. Carr, *Analytical chemistry* **1997**, *69*, 3884–3888.

[26] D. Guillarme, R. Russo, S. Rudaz, C. Bicchi, J.-L. Veuthey, *Current Pharmaceutical Analysis* **2007**, *3*, 221–229.

[27] G. Guiochon, F. Gritti, *Journal of Chromatography A* **2011**, *1218*, 1915–1938.

[28] F. Svec, C. G. Huber, *Analytical chemistry* **2006**, *78*, 2100–2107.

[29] K. Nakanishi, N. Soga, *Journal of the American Ceramic Society* **1991**, *74*, 2518–2530.

[30] H. Saito, K. Kanamori, K. Nakanishi, K. Hirao, Y. Nishikawa, H. Jinnai, *Colloids and Surfaces A: Physicochemical and Engineering Aspects* **2007**, *300*, 245–252.

[31] M. Wang, J. Xu, X. Zhou, T. Tan, *Journal of Chromatography A* **2007**, *1147*, 24–29.

[32] N. Tanaka, H. Kobayashi, K. Nakanishi, H. Minakuchi, N. Ishizuka, *Analytical chemistry* **2001**, *73*, 420–429.

[33] S. Xie, F. Svec, J. M. J. Frechet, *Journal of Chromatography A* **1997**, *775*, 65–72.

[34] E. G. Vlakh, T. B. Tennikova, *Journal of Chromatography A* **2009**, *1216*, 2637–2650.

[35] I. Nischang, F. Svec, J. M. J. Fréchet, *Journal of Chromatography A* **2009**, *1216*, 2355–2361.

[36] H. Eghbali, Microfabricated Pillar Array Columns for Liquid Chromatography, Vrije Universiteit Brussel, **2009**.

[37] A. Manz, Y. Miyahara, J. Miura, Y. Watanabe, H. Miyagi, K. Sato, *Sensors and actuators B: Chemical* **1990**, *1*, 249–255.

[38] S. Shoji, M. Esashi, T. Matsuo, *Sensors and actuators* **1988**, *14*, 101–107.

[39] R. Zengerle, J. Ulrich, S. Kluge, M. Richter, A. Richter, *Sensors and Actuators A: Physical* **1995**, *50*, 81–86.

[40] S. C. Terry, J. H. Jerman, J. B. Angell, *Electron Devices, IEEE Transactions on* **1979**, *26*, 1880–1886.

[41] D. J. Harrison, A. Manz, Z. Fan, H. Luedi, H. M. Widmer, *Analytical Chemistry* **1992**, *64*, 1926–1932.

[42] S. C. Jacobson, R. Hergenroder, L. B. Koutny, J. M. Ramsey, *Analytical Chemistry* **1994**, *66*, 1114–1118.

[43] W. H. Grover, A. M. Skelley, C. N. Liu, E. T. Lagally, R. A. Mathies, *Sensors and Actuators B: Chemical* **2003**, *89*, 315–323.

[44] M. Koch, N. Harris, R. Maas, A. G. R. Evans, N. M. White, A. Brunnschweiler, *Measurement Science and Technology* **1997**, *8*, 49.

[45] V. Gass, B. H. Van der Schoot, S. Jeanneret, N. F. De Rooij, *Sensors and Actuators A: Physical* **1994**, *43*, 335–338.

[46] H. Eghbali, W. De Malsche, D. Clicq, H. Gardeniers, G. Desmet, *Lc Gc Europe* **2007**, *20*, 208.

[47] H. Salimi-Moosavi, Y. Jiang, L. Lester, G. McKinnon, D. J. Harrison, *Electrophoresis* **2000**, *21*, 1291–1299.

[48] K. M. van Delft, J. C. T. Eijkel, D. Mijatovic, T. S. Druzhinina, H. Rathgen, R. Niels, A. van den Berg, F. Mugele, *Nano Letters* **2007**, *7*, 345–350.

[49] J. A. Abia, J. Putnam, K. Mriziq, G. A. Guiochon, *Journal of Chromatography A* **2010**, *1217*, 1695–1700.

[50] L. Callipo, P. Foglia, R. Gubbiotti, R. Samperi, A. Laganà, *Analytical and bioanalytical chemistry* **2009**, *394*, 811–820.

[51] Y. T. Yang, C. Callegari, X. L. Feng, K. L. Ekinci, M. L. Roukes, *Nano letters* **2006**, *6*, 583–586.

[52] S. Koster, E. Verpoorte, *Lab Chip* **2007**, *7*, 1394–1412.

[53] Y. Yang, C. Li, J. Kameoka, K. H. Lee, H. G. Craighead, *Lab Chip* **2005**, *5*, 869–876.

[54] H. Yin, K. Killeen, *Journal of separation science* **2007**, *30*, 1427–1434.

[55] I. M. Lazar, B. L. Karger, *Analytical chemistry* **2002**, *74*, 6259–6268.

[56] J. Hardouin, M. Duchateau, R. Joubert-Caron, M. Caron, *Rapid communications in mass spectrometry* **2006**, *20*, 3236–3244.

[57] J. Hardouin, R. Joubert-Caron, M. Caron, *Journal of separation science* **2007**, *30*, 1482–1487.

[58] B. He, N. Tait, F. Regnier, *Analytical Chemistry* **1998**, *70*, 3790–3797.

[59] B. He, F. Regnier, *Journal of pharmaceutical and biomedical analysis* **1998**, *17*, 925–932.

[60] J. H. Knox, *Journal of Chromatography A* **2002**, *960*, 7–18.

[61] P. Gzil, N. Vervoort, G. V Baron, G. Desmet, *Analytical chemistry* **2003**, *75*, 6244–6250.

[62] M. De Pra, W. T. Kok, J. G. E. Gardeniers, G. Desmet, S. Eeltink, J. W. Van Nieuwkasteele, P. J. Schoenmakers, *Analytical chemistry* **2006**, *78*, 6519–6525.

[63] W. De Malsche, D. Clicq, V. Verdoold, P. Gzil, G. Desmet, H. Gardeniers, *Lab on a chip* **2007**, *7*, 1705–1711.

[64] W. De Malsche, H. Gardeniers, G. Desmet, *Analytical chemistry* **2008**, *80*, 5391–5400.

[65] H. Eghbali, S. Matthijs, V. Verdoold, H. Gardeniers, P. Cornelis, G. Desmet, *Journal of Chromatography A* **2009**, *1216*, 8603–8611.

[66] J. Vangelooven, G. Desmet, *Journal of Chromatography A* **2010**, *1217*, 8121–8126.

[67] J. Vangelooven, W. De Malsche, J. O. De Beeck, H. Eghbali, H. Gardeniers, G. Desmet, *Lab on a Chip* **2010**, *10*, 349–356.

[68] C. K. Fredrickson, Z. H. Fan, *Lab Chip* **2004**, *4*, 526–533.

[69] J. J. Kirkland, *Journal of chromatographic science* **2000**, *38*, 535–544.

[70] R. E. Majors, in *LC GC North America*, Advanstar Communications, **2005**, pp. 248–265.

[71] M. E. Swartz, *Journal of liquid chromatography & related technologies* **2005**, *28*, 1253–1263.

[72] J. J. Kirkland, J. J. DeStefano, *Journal of Chromatography A* **2006**, *1126*, 50–57.

[73] G. Rozing, T. van de Goor, H. Yin, K. Killeen, B. Glatz, K. Kraiczek, H. H. Lauer, *Journal of separation science* **2004**, *27*, 1391–1401.

[74] H. Yin, K. Killeen, R. Brennen, D. Sobek, M. Werlich, T. van de Goor, *Analytical chemistry* **2005**, *77*, 527–533.

[75] G. L. Gauthier, R. Grimm, *Drug Discovery Today: Technologies* **2006**, *3*, 59–66.

[76] S. Khirevich, A. Höltzel, D. Hlushkou, U. Tallarek, *Analytical chemistry* **2007**, *79*, 9340–9349.

[77] S. Khirevich, A. Höltzel, D. Hlushkou, A. Seidel-Morgenstern, U. Tallarek, *Lab Chip* **2008**, *8*, 1801–1808.

[78] S. Ehlert, K. Kraiczek, J.-A. Mora, M. Dittmann, G. P. Rozing, U. Tallarek, *Analytical chemistry* **2008**, *80*, 5945–5950.

[79] S. Jung, A. Hȯltzel, S. Ehlert, J.-A. Mora, K. Kraiczek, M. Dittmann, G. P. Rozing, U. Tallarek, *Analytical chemistry* **2009**, *81*, 10193–10200.

[80] M. J. Madou, *Fundamentals of Microfabrication: The Science of Miniaturization*, CRC, **2002**.

[81] R. Ghodssi, *MEMS Materials and Processes Handbook*, Springer US, Boston, MA, **2011**.

[82] T. L. Lamers, B. L. Pruitt, *MEMS Materials and Processes Handbook*, Springer US, Boston, MA, **2011**.

[83] P. Kao, S. Tadigadapa, *Sensors and Actuators A: Physical* **2009**, *149*, 189–192.

[84] T. Abe, Y. Itasaka, *Sensors and Actuators A: Physical* **2012**.

[85] L. Li, T. Abe, M. Esashi, *Journal of Vacuum Science & Technology B: Microelectronics and Nanometer Structures* **2003**, *21*, 2545–2549.

[86] A. Goyal, V. Hood, S. Tadigadapa, *Journal of non-crystalline solids* **2006**, *352*, 657–663.

[87] P. Abgrall, A. M. Gue, *Journal of Micromechanics and Microengineering* **2007**, *17*, R15.

[88] S. Tuomikoski, S. Franssila, *Sensors and Actuators A: Physical* **2005**, *120*, 408–415.

[89] Y.-J. Chuang, F.-G. Tseng, J.-H. Cheng, W.-K. Lin, *Sensors and Actuators A: Physical* **2003**, *103*, 64–69.

[90] B. E. J. Alderman, C. M. Mann, D. P. Steenson, J. M. Chamberlain, *Journal of Micromechanics and Microengineering* **2001**, *11*, 703.

[91] H. Yu, O. Balogun, B. Li, T. W. Murray, X. Zhang, *Journal of micromechanics and microengineering* **2004**, *14*, 1576.

[92] J. Zhang, K. L. Tan, G. D. Hong, L. J. Yang, H. Q. Gong, *Journal of Micromechanics and Microengineering* **2000**, *11*, 20.

[93] S. Metz, S. Jiguet, A. Bertsch, P. Renaud, *Lab on a Chip* **2004**, *4*, 114–120.

[94] M. Agirregabiria, F. J. Blanco, J. Berganzo, M. T. Arroyo, A. Fullaondo, K. Mayora, J. M. Ruano-López, *Lab on a Chip* **2005**, *5*, 545–552.

[95] P. Abgrall, C. Lattes, V. Conédéra, X. Dollat, S. Colin, A. M. Gué, *Journal of Micromechanics and Microengineering* **2005**, *16*, 113–121.

[96] P.-Y. Li, J. Shih, R. Lo, S. Saati, R. Agrawal, M. S. Humayun, Y.-C. Tai, E. Meng, *Sensors and Actuators A: Physical* **2008**, *143*, 41–48.

[97] R. Lo, E. Meng, *Sensors and Actuators B: Chemical* **2008**, *132*, 531–539.

[98] R. J. Jackman, T. M. Floyd, R. Ghodssi, M. A. Schmidt, K. F. Jensen, *Journal of Micromechanics and Microengineering* **2001**, *11*, 263.

[99] S. Li, C. B. Freidhoff, R. M. Young, R. Ghodssi, *Journal of micromechanics and microengineering* **2003**, *13*, 732.

[100] V. Seidemann, J. Rabe, M. Feldmann, S. Büttgenbach, *Microsystem technologies* **2002**, *8*, 348–350.

[101] V. Seidemann, S. Bütefisch, S. Büttgenbach, *Sensors and Actuators A: Physical* **2002**, *97*, 457–461.

[102] R. R. LeVier, M. C. Harrison, R. R. Cook, T. H. Lane, *Journal of clinical epidemiology* **1995**, *48*, 513–517.

[103] Y. Xia, J. J. McClelland, R. Gupta, D. Qin, X.-M. Zhao, L. L. Sohn, R. J. Celotta, G. M. Whitesides, *Advanced Materials* **1997**, *9*, 147–149.

[104] K. Tsougeni, A. Tserepi, E. Gogolides, *Microelectronic engineering* **2007**, *84*, 1104–1108.

[105] K. Hosokawa, K. Sato, N. Ichikawa, M. Maeda, *Lab Chip* **2004**, *4*, 181–185.

[106] M. A. Eddings, B. K. Gale, *Journal of Micromechanics and Microengineering* **2006**, *16*, 2396.

[107] S. C. Jakeway, A. J. de Mello, E. L. Russell, *Fresenius' journal of analytical chemistry* **2000**, *366*, 525–539.

[108] H. B. Sun, S. Kawata, *Advances in polymer science* **2004**, *170*, 169–273.

[109] A. Ovsianikov, S. Passinger, R. Houbertz, B. Chichkov, *Laser ablation and its applications* **2007**, 121–157.

[110] A. Ovsianikov, B. N. Chichkov, *Nanoelectronics and Photonics* **2008**, 427–446.

[111] W. Kim, R. Houbertz, T. Lee, B. Bae, *Journal of Polymer Science Part B: Polymer Physics* **2004**, *42*, 1979–1986.

[112] H. Kodama, *Review of scientific instruments* **1981**, *52*, 1770–1773.

[113] M. Göppert-Mayer, *Annalen der Physik* **1931**, *401*, 273–294.

[114] V. F. Paz, M. Emons, K. Obata, A. Ovsianikov, S. Peterhänsel, K. Frenner, C. Reinhardt, B. Chichkov, U. Morgner, W. Osten, *Journal of Laser Applications* **2012**, *24*, 42004.

[115] S. Juodkazis, V. Mizeikis, K. K. Seet, M. Miwa, H. Misawa, *Nanotechnology* **2005**, *16*, 846.

[116] X. Illa, W. De Malsche, J. Bomer, H. Gardeniers, J. Eijkel, J. R. Morante, A. Romano-Rodríguez, G. Desmet, *Lab on a Chip* **2009**, *9*, 1511–1516.

[117] E. Meng, X. Zhang, W. Benard, *MEMS Materials and Processes Handbook*, Springer US, Boston, MA, **2011**.

[118] D. R. Hines, N. P. Siwak, L. A. Mosher, R. Ghodssi, *MEMS Materials and Processes Handbook*, Springer US, Boston, MA, **2011**.

[119] C. Wagner, N. Harned, *Nature Photonics* **2010**, *4*, 24–26.

[120] "http://www.deltamask.nl/frames.html," **n.d.**

[121] "http://www.himt.de/en/technology/laserlithography.php," **n.d.**

[122] "http://www.himt.de/en/products/special-systems.php," **n.d.**

[123] D. Rio, C. Constancias, M. Martin, B. Icard, J. van Nieuwstadt, J. Vijverberg, L. Pain, *Journal of Vacuum Science & Technology B: Microelectronics and Nanometer Structures* **2010**, *28*, C6C14–C6C20.

[124] M. Aziz, J. Golovchenko, D. Branton, C. McMullan, D. Stein, J. Li, *Nature* **2001**, *412*, 166–169.

[125] S. Tadigadapa, F. Lärmer, *MEMS Materials and Processes Handbook*, Springer US, Boston, MA, **2011**.

[126] D. W. Burns, *MEMS Materials and Processes Handbook*, Springer US, Boston, MA, **2011**.

[127] J. C. Giddings, R. A. Keller, *Advances in Chromatography*, M. Dekker, **1966**.

[128] K. T. Sung, S. W. Pang, *Journal of Vacuum Science & Technology A: Vacuum, Surfaces, and Films* **1993**, *11*, 1206–1210.

[129] X. Y. Li, P. J. French, P. M. Sarro, R. F. Wolffenbuttel, in *Micro Electro Mechanical Systems, 1995, MEMS'95, Proceedings. IEEE*, IEEE, **1995**, p. 398.

[130] M. Elwenspoek, H. V Jansen, *Silicon Micromachining*, Cambridge University Press, Cambridge, UK, **2004**.

[131] H. Jansen, M. De Boer, R. Legtenberg, M. Elwenspoek, *Journal of Micromechanics and Microengineering* **1995**, *5*, 115–120.

[132] M. J. De Boer, J. G. E. H. Gardeniers, H. V Jansen, E. Smulders, M. Gilde, G. Roelofs, J. N. Sasserath, M. Elwenspoek, A. Member, **2002**, *11*, 385–401.

[133] F. Laermer, A. Schilp, **1996**.

[134] H. Föll, "http://www.tf.uni-kiel.de/matwis/amat/semitech_en/kap_7/backbone/r7_2_2.html," **n.d.**

[135] W. De Malsche, Solving Advanced Micromachining Problems for Ultra-rapid and Ultra-high Resolution On-chip Liquid Chromatography, University of Twente, **2008**.

[136] R. W. Tjerkstra, Isotropic Etching of Silicon in Fluoride Containing Solutions, University of Twente, **1999**.

[137] R. W. Tjerkstra, G. E. Gardeniers, J. J. Kelly, A. van den Berg, *Microelectromechanical Systems, Journal of* **2000**, *9*, 495–501.

[138] N. M. p Johnson, F. A. Ponce, R. A. Street, R. J. Nemanich, *Physical Review B* **1987**, *35*, 4166.

[139] R. L. Smith, S. D. Collins, *Journal of Applied Physics* **1992**, *71*, R1–R22.

[140] L. Canham, Properties of Porous Silicon, Emisdata Reviews Series, V. 18, INSPEC Publication, London, **1997**.

Chapter 3

Materials and Methods

Abstract

In this chapter an overview is given of the fabrication processes to manufacture the different microfluidic devices that were investigated during the PhD thesis. All micromachining procedures were carried out in the NanoLab of the MESA+ Institute. The reader is referred to the MESA$^+$ NanoLab website [1,2] *for a detailed description of the employed instruments.*

3.1. Standard cleanroom processes

The standard cleaning of the wafers was done by immersing the wafers twice in fumic nitric acid (Selectipur: Merck 100453) for the removal of organic contaminants followed by rinsing the wafers with deionized (DI) water. The metal contaminants are removed by immersing the wafers in hot 69% nitric acid (VLSI: Merck 116445) for 10min followed by rinsing the wafers with DI-water. Photoresist was stripped by immersing the wafer in fumic nitric acid or by using an oxygen plasma etcher (Tepla 300E, PVA TePla AG, Wettenberg, Germany). The oxygen plasma etcher was preferred between etching steps without lithography and when small features had to be micromachined.

Oxidation of the silicon wafers and burning of the residual fluorocarbons was done in an atmospheric wet oxidation tube oven (Amtech Tempress omega junior 4stack, Tempress® Systems B.V., Vaassen, the Netherlands).

The used lithography mask drawings were made in CleWin version 4 (WieWeb Software, Twente, the Netherlands). In the fist step of the lithography, the wafers were dehydrated by heating at 120°C for 1 min (or alternatively put in an oxygen plasma for 10min) and primed with HexaMethylDiSilazane (HMDS, Merck 112186, Germany) either by spinning, or by evaporation in a homemade setup designed by MESA+. Positive resist (Olin series, Arch Chemicals Inc., Zwijndrecht, Belgium) was applied to the wafer by using a spinner (spinner Delta 20, SÜSS MicroTec, Garching, Germany). The resist was subsequently soft baked (90°C for ca. 90sec) to evaporate the solvents without curing the resist. These wafers were aligned to their corresponding masks and illuminated with broadband UV using the mask aligner (EVG 620, EV Group, St.Florian am Inn, Austria). The illuminated resist is developed by immersing the wafers in OPD4262 (FujiFilm, Japan) for 1min (last 30sec in fresh OPD4262). Finally, after all the UV-exposed photoresist is washed away, the wafers are rinsed with deionized water, spun dry and hard baked (>10min at 120°C) on a hot plate.

Bosch®-etching of silicon was carried out in the Adixen AMS100SE (Alcatel Vacuum Technology, Culemborg, The Netherlands) using a SF_6/C_4F_8-plasma. Etching of fused silica and silicon dioxide layers was done in the Adixen AMS100DE (Alcatel Vacuum Technology, Culemborg, The Netherlands) using a C_4F_8/CH_4^-plasma. All the recipes that were used on the Adixens were developed at MESA+ by HV Jansen and MJ De Boer.

During the different process steps, several non-destructive characterization techniques were used. The layer thickness after oxidation or LPCVD was estimated using the ellipsometer (SD 2002, Plasmos GmbH, München, Germany)). Etching depths were measured with the Dektak (Dektak 8, Veeco, USA) if the depth was lower than the width of the trench (aspect ratio < 1). The SEM (Jeol 5610, Japan) was also used to measure profiles on non-insulating materials. To measure high aspect ratio trenches or pillar arrays, the wafer had to be broken for a cross-sectional image. When information was needed that only could be obtained from cross-sectional images, a couple of test wafers were added to the process schedule. The HR SEM (LEO1550, Zeiss, Germany) was used when high resolution images were needed which for example was the case with porous silicon samples.

After all the lithography, etching and cleaning steps, the micromachined wafers often had to undergo a back-end process which was bonding, dicing or both. Bonding of the silicon substrate with a pyrex top plate was done by anodic bonding using the EVG (EV-501, EV Group, St.Florian am Inn, Austria). Prior to the anodic bonding process, the cleaned substrates were stored in DI-water, spun dry, and pre bonded to avoid particle contamination. The dicing of the wafers into chips was done using the disco DAD dicing saw (Disco DAD-321, DISCO Corporation, Japan).

3.2. SDC silicon

Below is an overview of the different fabrication processes developed to produce the different types of shear driven chromatography (SDC) channels in silicon. These devices were tested by Veronica Fekete at the “Vrije Universiteit Brussels” and the results were presented as a poster with the title ‘Anodized porous silicon layer combined with detection groove in nanofluidic shear driven device for chromatographic separations” at the “10th International Symposium on Hyphenated Techniques in Chromatography and Hyphenated Chromatographic Analysers”, in Bruges, Belgium in 2008 (30januari).

3.2.1. First Lithography and etching steps

The nanochannels were fabricated on the surface of a silicon wafer. In the first step, a silicon nitride layer was deposited by low-pressure chemical vapor deposition (LPCVD) on top of the cleaned wafers and the thickness of the layer was verified using an ellipsometer. Using standard broadband UV lithography techniques, the design is patterned in the 1.2 μm thick

(a)

1. Silicon

2. SiRN LPCVD (layer thickness = channel depth)

3. Patterning of channels: Photoresist spinning, illumination and development

4. SiRN anitsotropic etch of channels

5. Oxygen plasma cleaning for removal Photoresist

6. High temperature step (dry@700°C) for removal remaining fluorocarbons + subsequent HF dip + HNO_3 cleaning

7. Creating a porous layer in anodization unit (optional) and subsequent HNO_3 cleaning.

8. Pattern detection grooves: Photoresist spinning, illumination and development

9. Bosch® etch of detection grooves

10. Oxygen plasma cleaning for removal Photoresist and high temperature step (dry@700°C) for removal remaining fluorocarbons + HF dip + HNO_3 cleaning

10. Dicing into chips

Steps 6&7 can be skipped if no porous layer is wanted

Steps 8&9 can be skipped if no detection groove is wanted.

(b)

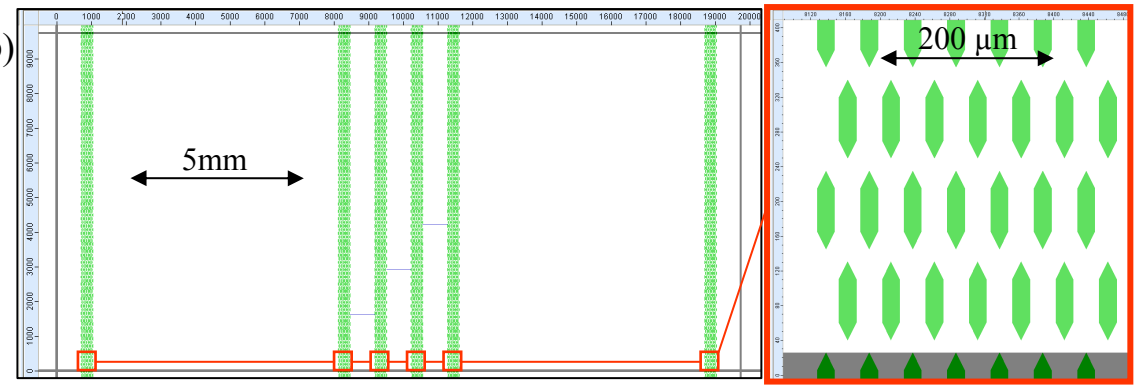

Figure 3.1. **(a)** Process flow of the manufacturing of SDC-chips in silicon. **(b)** Design of the SDC-chips with a close-up of the spacers.

photoresist (Olin 906-12). After development and hard baking of the resist, the silicon nitride was etched using deep reactive ion etching (DRIE) in the Adixen AMS100DE etcher (Alcatel). The silicon nitride layer was nearly completely removed in this etching step, leaving only a pattern of silicon nitride spacer structures which define the borders of the channels. The depth of the resulting channels was verified using the Dektak (see above) after cleaning the etched wafer with an oxygen plasma and HNO_3. The resulting channels were slightly deeper than the thickness of the silicon nitride layer which was due to a slight over-etching which was performed to ensure that the nitride layer is etched through over the complete wafer surface. Although the wafers were cleaned thoroughly with an oxygen plasma and nitric acid, a "burn" step was done (15min at 800°C at atmospheric pressure and in the presence of air) to remove the fluorocarbons that are still present on the surface. Inevitably, a thin layer of silicon oxide (typically a few nm) was formed in this way, which was removed by immersing the wafers for ca. 1min in HF (HF 1% VLSI grade, Merck 112629.500) until the silicon surface was hydrophobic.

3.2.2. Porous Layer production

If a porous layer was wanted, highly doped wafers (1mm thick, p/Boron-type, 0.01-0.02 Ω/cm, Virginia Semiconductor Inc.) were used. The porous silicon was made by anodization of the silicon substrate in 5% HF. To carry out the anodization, the silicon wafer with the channels was screwed tightly in a homemade Teflon anodization vessel. After checking with water whether the set-up was leak-free, the vessel was filled with 5% HF and a counter electrode of Pt was put into the solution.

From previous studies [3] it appeared that the small H_2-bubbles give small defects in the porous layer during anodization, decreasing the homogeneity of the porous layer, which is detrimental for the chromatographic characteristics. The homogeneity of the porous layer was enhanced by using an impeller which was put in the solution to improve mass transport and to facilitate the release of the H_2-bubbles from the surface. The convection was done by using a homemade round Teflon cylinder attached at the lower end of the impeller which transmitted the motion of the impeller to the solution without any spatters. This impeller was controlled by a commercial motor controller (ADI1012, Applikon, Schiedam-Holland).

The anodization process was done in constant current mode and the electrical current between the silicon substrate (which is the anode) and Pt-counter electrode (which is the cathode) was supplied by a simple commercial power supply (Delta Elektronika, E030-1). The current was adjusted manually based on the readout of a multimeter (Keithley, 2700 Multimeter, Integra series). Prior to the anodization of the micromachined wafers, blank wafers were anodized in constant current mode and the different voltages were registered relative to the reference electrode. It was verified that the voltage between the two electrodes was never higher than 0.1V, and that with these conditions, electro-polishing was never observed [4].

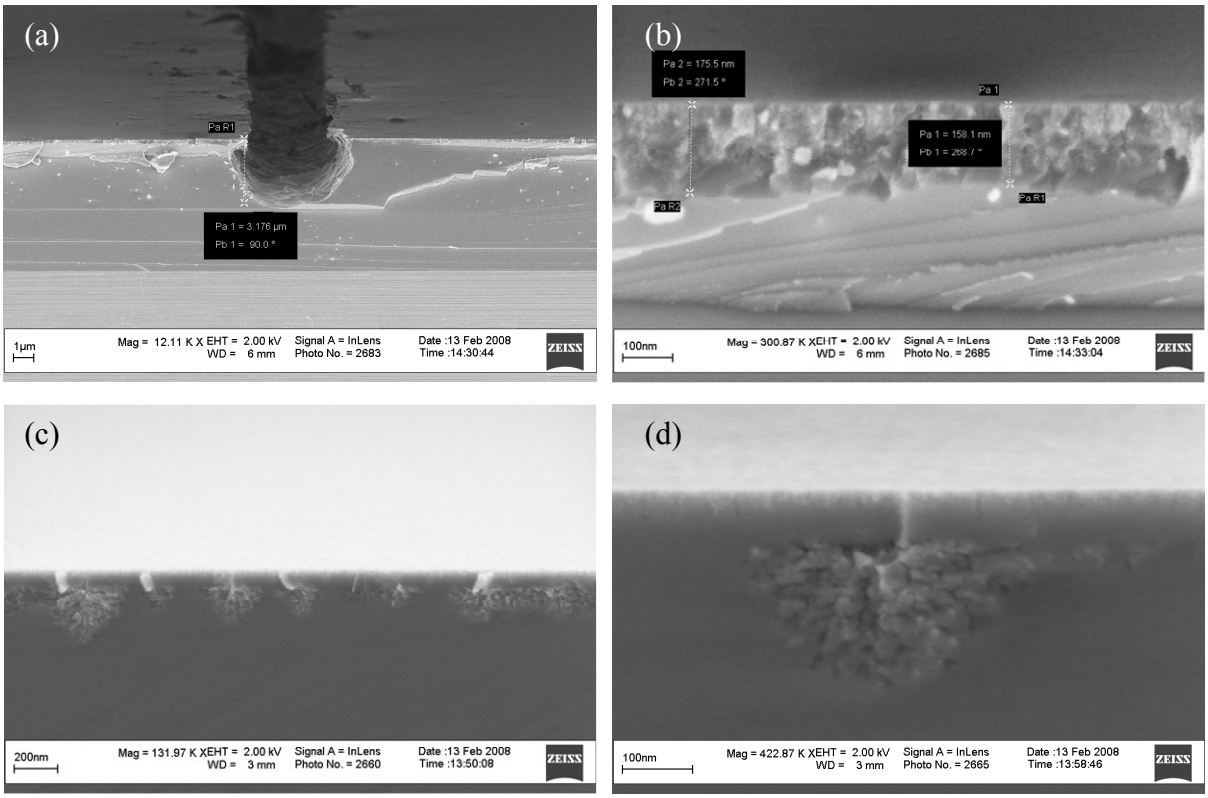

Figure 3.2. SEM pictures of the manufactured SDC chips with **(a)** detection groove and **(b)** porous layer. The detection groove (depth = 3.75µm) was etched through the porous silicon layer (thickness = 175nm). The layer was made with a constant current of 50mA for 1min. **(c-d)** SEM images of a porous layer made with a constant current of 15mA for 5min yielding a non-uniform layer.

3.2.3. Second Lithography and Etching step

After manufacturing the porous layer, a detection groove perpendicular to the channel axis was made. Due to the polluting nature of the porous layer manufacturing process, the wafers had to be very thoroughly cleaned before further processing to remove potential metal contamination from the copper electrode used in the Teflon vessel. This was done by immersing the wafers 3 times 10min in fresh 69% hot nitric acid and rinsing thoroughly with deionized water in between. Subsequently, a fuming nitric acid cleaning step was done.

Lithography of the detection grooves was done on the cleaned wafers using standard broadband UV techniques. After development and baking the photoresist, the detection grooves were etched (Adixen SE) using a Bosch®-etching recipe (see Figure 3.2a). The photoresist was stripped off using an oxygen plasma etcher and the wafers were subsequently cleaned using HNO_3. The cleaned wafers were put in an oxidation tube oven at 800°C for 15min to remove the fluorocarbons remaining in the detection groove after the Bosch® process. Finally, the wafers were cut into chips (disco DAD dicing saw).

3.3. SDC fused silica

Below an overview is given of the different fabrication processes developed to produce the shear driven chromatography (SDC) channels in fused silica tested in the frame of the present thesis (see also Chapter 6). These devices were also tested by Frederik Detobel et al. who reported the "Estimation of surface desorption times in hydrophobically coated nanochannels and their effect on shear-driven and pressure-driven chromatography" in Analytical and Bioanalytical Chemistry [5].

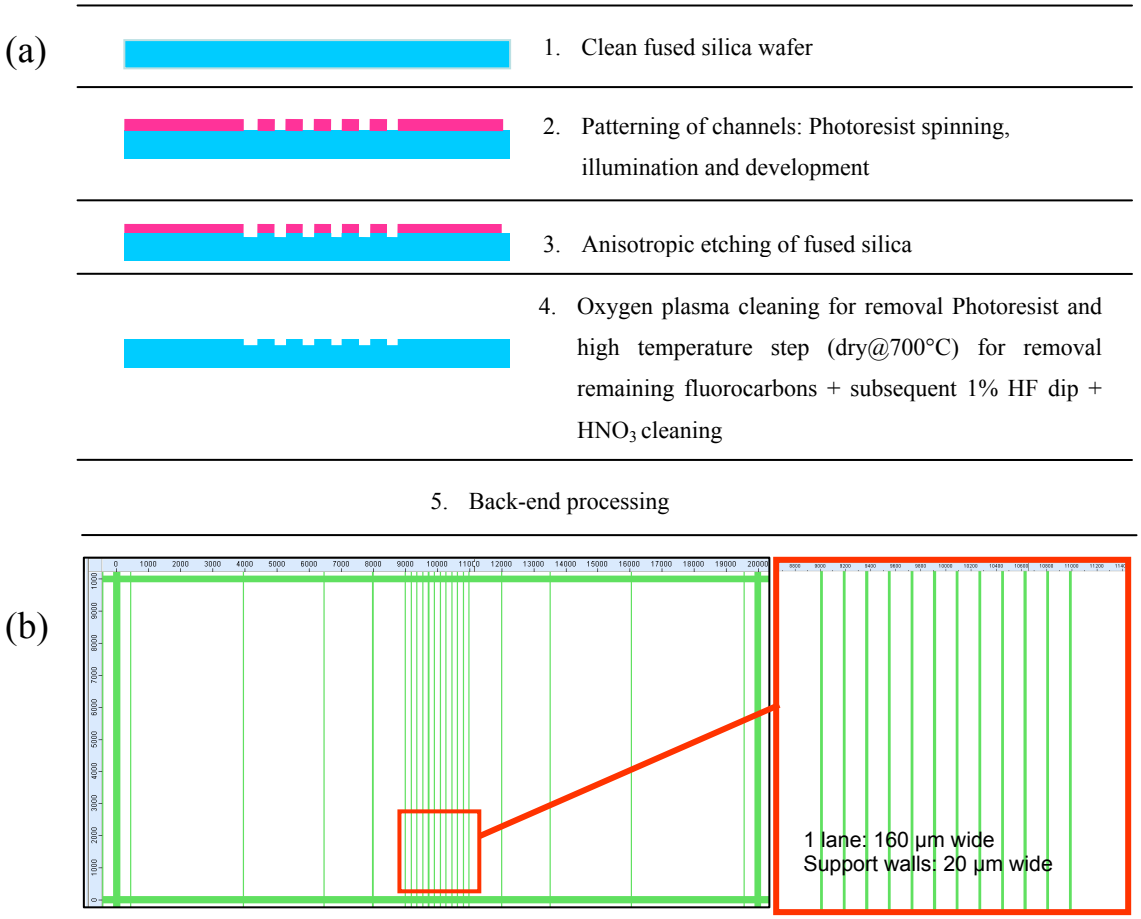

Figure 3.3. **(a)** Process flow of the manufacturing of SDC-chips in silicon. **(b)** Design of the SDC-chips with a close-up of the spacers.

3.4. Fused silica chip for radial dispersion study

Below an overview is given of the different fabrication processes developed to produce the fused silica chip which was used for radial dispersion experiments in the framework of the present thesis (see Chapter 4&5). The pillar channels were obtained by bonding a processed wafer, containing half-open pillar channels with in- and outlets, with an unprocessed wafer and sealing the half-open pillar channels.

An important issue when etching defined structures in substrates is to have an adequate selectivity between masking material and substrate. Conventional photoresist cannot be used in this case because the photoresist layer (Olin 906-12) has to be very thin (1.2 μm) to define the smallest structures (2.5 μm) with the available broadband UV-lithography. Such a layer would already be etched away before reaching the required depth of 10 μm. To circumvent this, a hard mask of polysilicon is used because it can be etched through with a high selectivity using photoresist as a masking material, and it also has a good selectivity as masking material in the etching of fused silica. Therefore a poly-silicon layer of 1200nm was deposited on a 100 mm diameter fused silica substrate (Schott Lithotec) in a LPCVD-furnace (Amtech Tempress omega junior). After this, broadband UV-lithography (EVG 620) was used to define the pillar array design (photoresist: Olin 906-12; developer: OPD4262; Fujifilm Electronic Materials) in the polysilicon layer. After the lithography, the polysilicon was anisotropically etched through on the Adixen AMS100SE (Alcatel) exposing the underlying fused silica. Subsequently, the underlying fused silica was etched 10 μm deep (Adixen AMS100DE, Alcatel).

After completing all the etching steps, the remaining photoresist near the edges of the wafer was stripped off using an oxygen plasma etcher. The in- and outlets (wafer through-holes) of the channels were subsequently defined in another lithography step on a dry resist foil (Ordyl BF410) and powder blasted using 30μm Al_2O_3-particles. After stripping the resist and cleaning the substrate (ultrasonic and HNO_3), the remaining polysilicon was removed by immersing the wafer in a KOH-bath (25w%@70°C) for several minutes until it was completely dissolved. After rinsing the substrate thoroughly with deionized water, it was pre-bonded with an unprocessed wafer, ceiling the channels. When the pre-bond was successful, the wafer stack was thermally bonded by putting it into an oven @1050degrees (6h rise from room temperature to 1050°C, 6h 1050°C, 12h cool down to room temperature).

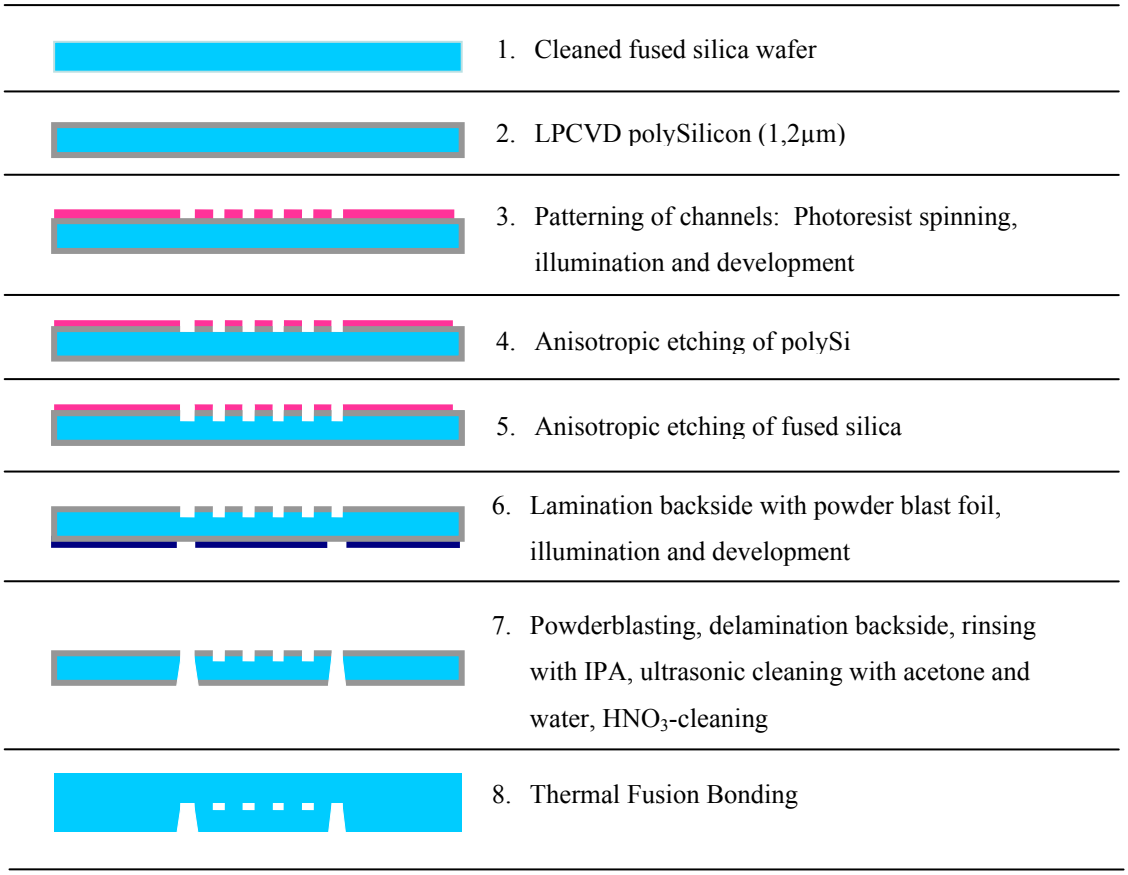

Figure 3.4. Process flow of the manufacturing of the fused silica chip for radial dispersion study. The mask layout and different designs are shown in chapter 4 (See Figures 4.4 and 4.5).

3.5. Micro-Pillar Array Columns (µPAC's)

3.5.1. µPAC's with through-holes

Below is an overview of the different process steps involved in the manufacturing of the µPAC's used by Detobel et al. who studied the formation of silica monoliths in a µPAC [6] (see §3.5.1.1) and also reported on the fabrication and performance of a porous shell µPAC [7] (see §3.5.1.2).

3.5.1.1. µPAC for silica monolith formation study

Figure 3.5 illustrates the procedure for the fabrication of microfluidic channels with an ordered array of micro-pillars. The pillar channels were defined in a silicon–glass sandwich. First, a silicon wafer was thermally (dry) oxidized at 1100 °C until 700 nm silicon oxide was formed (Amtech Tempress Omega Junior, Tempress Systems B.V., Vaassen, The Netherlands). Then broadband UV photolithography (photoresist: Olin 907-12) was used to

(a)

1. Silicon

2. Oxide growth by dry oxidation (200 nm)

3. Patterning of channels: Photoresist spinning, illumination and development

4. SiO_2 anisotropic etch of pillar and supply channels

5. Bosch®etch in silicon of pillar channels (depth = 15µm) and also capillary channels (up to a depth of ca.130µm)

6. Oxygen plasma cleaning for removal Photoresist and high temperature step (dry@700°C) for removal remaining fluorocarbons + subsequent HF dip + HNO_3-cleaning

7. Lamination backside with powder blast foil, illumination and development

8. Powderblasting, delamination backside, rinsing with IPA, ultrasonic cleaning with acetone and DI-water, HNO_3-cleaning

9. Anodic bonding to seal the channels

10. Dicing into chips

(b)

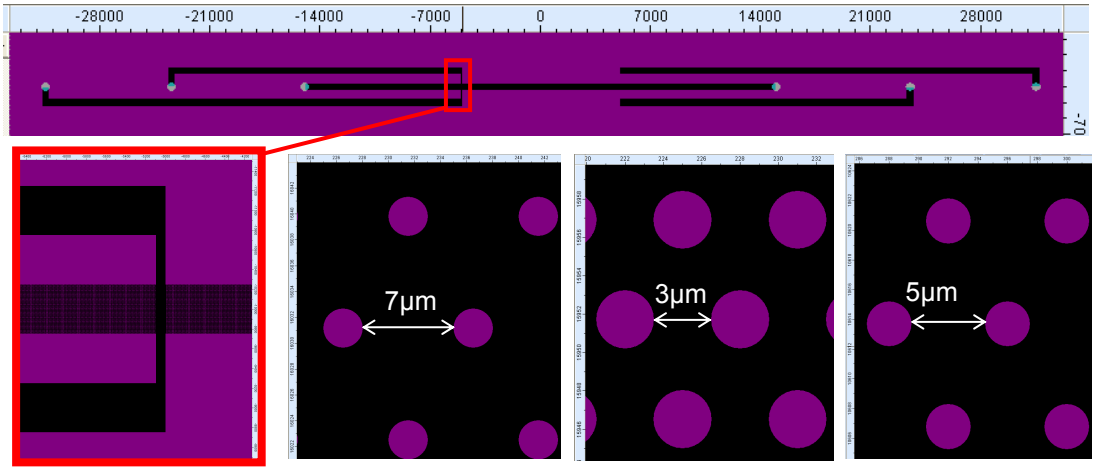

Figure 3.5. **(a)** Process flow and **(b)** Mask layout of the manufacturing of the µPAC-chip used by Detobel et al. in [6].

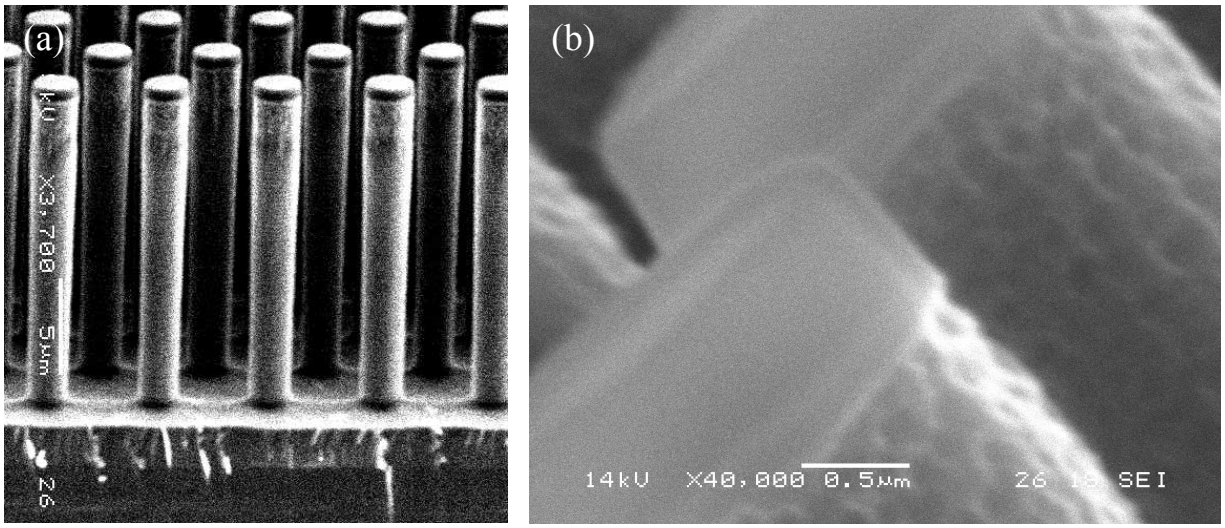

Figure 3.6. **(a)** Cross-sectional SEM image of the bed. **(b)** Close-up of the silicon hard mask on top of the pillars and the underetch of the Bosch® process.

define the pillar array column. Subsequently, the exposed silicon oxide was dry etched (Adixen AMS100DE, Alcatel Vacuum Technology, Culemborg, The Netherlands), leaving a patterned silicon oxide layer, which serves as a mask for a second etching step. In this step, the exposed silicon was etched with a Bosch-type deep reactive ion etch (Adixen AMS100SE, Alcatel Vacuum Technology, Culemborg, The Netherlands), leaving pillars of 20–25 µm height. Then, the remaining resist was removed by an oxygen plasma and nitric acid. Through-holes, necessary for liquid handling in the micro-channel were defined by photolithography on a dry resist foil (Ordyl BF410, Tokyo Oga Kogyo, Kanagawa, Japan). The exposed glass was subsequently powder blasted using 30 µm alumina particles. To remove the fluorocarbons, the wafers were set in a (wet) oxide furnace (Amtech Tempress Omega Junior) at 700 °C for 15 min, after which the wafers were cleaned in nitric acid and dipped in hydrofluoric acid (1% in H_2O). Subsequently, the wafers were wet oxidized again for 15min in order to provide a maximum amount of silanol groups to ensure a good chemical bonding of the siloxane-based gels (see below). The top of the channels was formed by a 100 mm diameter Pyrex wafer (thickness 0.5 mm), anodically bonded to the siliconwafer (EV-501wafer bonder, EVG). The rectangular microfluidic channels used in this work were 30 mm in length, 500 µm wide and about 20–25 µm in depth. The micro-pillar array consists of cylindrical micro-pillars with a diameter of 2.4 µm, arranged according to a perfectly ordered equilateral triangular grid as visualized in Figure 3.5. Three types of grids were considered, each type having a different inter-pillar distance respectively corresponding to 7.6, 5.6 and 3.6 µm after etching.

3.5.1.2. µPAC for porous shell fabrication and characterization

The manufacturing of these devices is nearly identical to the ones described in §3.5.1.1 and Figure 3.5 except that the through-holes were etched using a high speed Bosch® etching recipe in stead of powderblasted. This was done because the through-holes had to be made in the middle of the pillar bed (see Figure 3.7) for which the powderblast process is not suitable since the particles would damage the high aspect ratio pillars in the near vicinity of the through-hole. The Bosch® etching of the through-holes through the pillar bed also required an extra cleaning step since some pillars (at the through-hole) detached from the wafer after etching (Figure 3.7c). An additional ultrasonic cleaning step had to be carried out to remove these loose cylinders since these would either (further) damage the pillar bed or pose problems during anodic bonding (and contaminate cleanroom equipment with particles). The high temperature step to remove the fluorocarbons was done after the ultrasonic cleaning step.

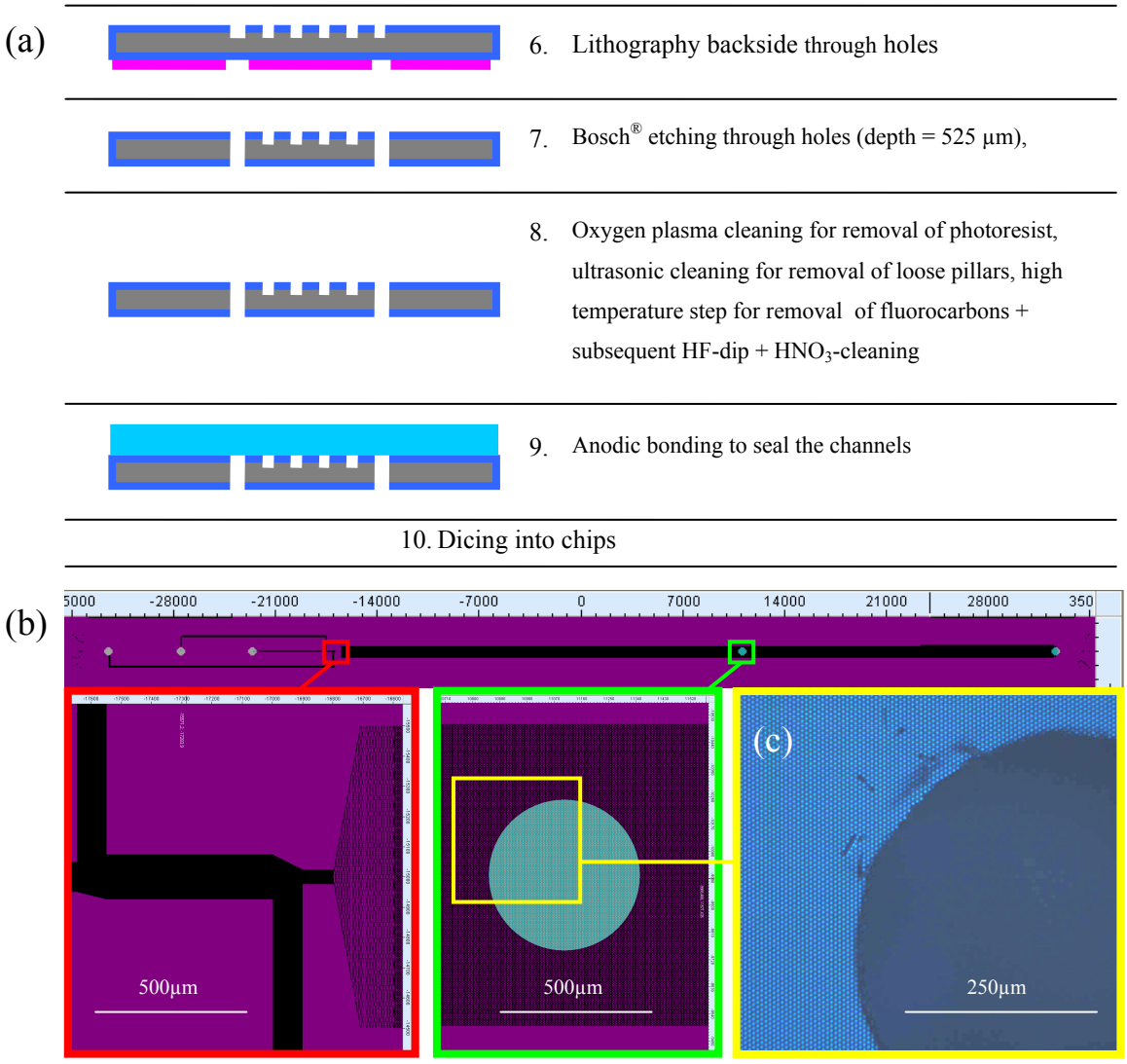

Figure 3.7. (a) Process flow and **(b)** Mask layout of the manufacturing of the µPAC-chip used by Detobel et al. in [7]. **(c)** Microscope image of the loose pillars after Bosch® etching through-holes.

3.5.2. µPAC's with in-plane capillary grooves

Figure 3.9 is an overview of the fabrication processes developed to produce the very long pillar array column yielding 1.10^6 theoretical plates and the porous shell pillar array column (see also Chapter 7 & 8).

3.5.2.1. Very long pillar array column

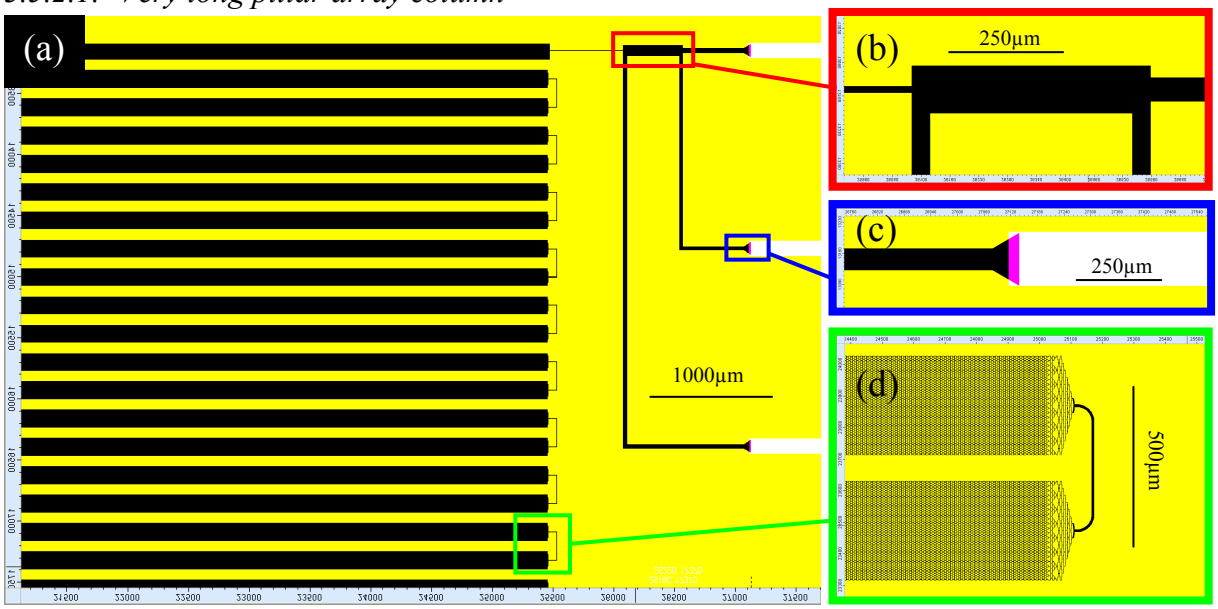

Figure 3.8. (a) Partly overview of the mask layout depicting all the crucial components of the used µPAC (length 3m) with **(b)** the on-chip injector and **(c)** a connection of the capillary groove to the on-chip injector. **(d)** The different lanes are delimited with distributors and are connected by turns.

The pillar-array columns (5 µm diameter pillars, inter-pillar distance 2.5 µm) were patterned using broadband UV photolithography (photoresist, Olin 907-12), followed by a dry etching step (Adixen AMS100DE) to etch the 200 nm thick SiO_2 hard mask underneath. Next, the supply channels were defined by broadband UV lithography and Bosch® etched in the silicon (Adixen AMS100SE) reaching a depth of 130 µm. After this, the resist was removed by oxygen plasma and nitric acid. The pillars defined in the SiO_2 mask (and also the already defined and partly etched capillary groove) were subsequently Bosch® etched to a depth of 7.2 µm deep (and the capillary channel obtained a total depth of about 140 µm).

The microfluidic channels were subsequently sealed with a Pyrex wafer (thickness 0.5 mm), by anodic bonding (EV-501). Next, the chip was partly diced 100 µm deep at both sides (Disco DAD-321) of the wafer and subsequently cleaved, exposing the grooves wherein the interfacing capillaries fit (108 µm OD and 40 µm ID). Subsequently, the capillaries were inserted in the grooves and sealed by epoxy glue.

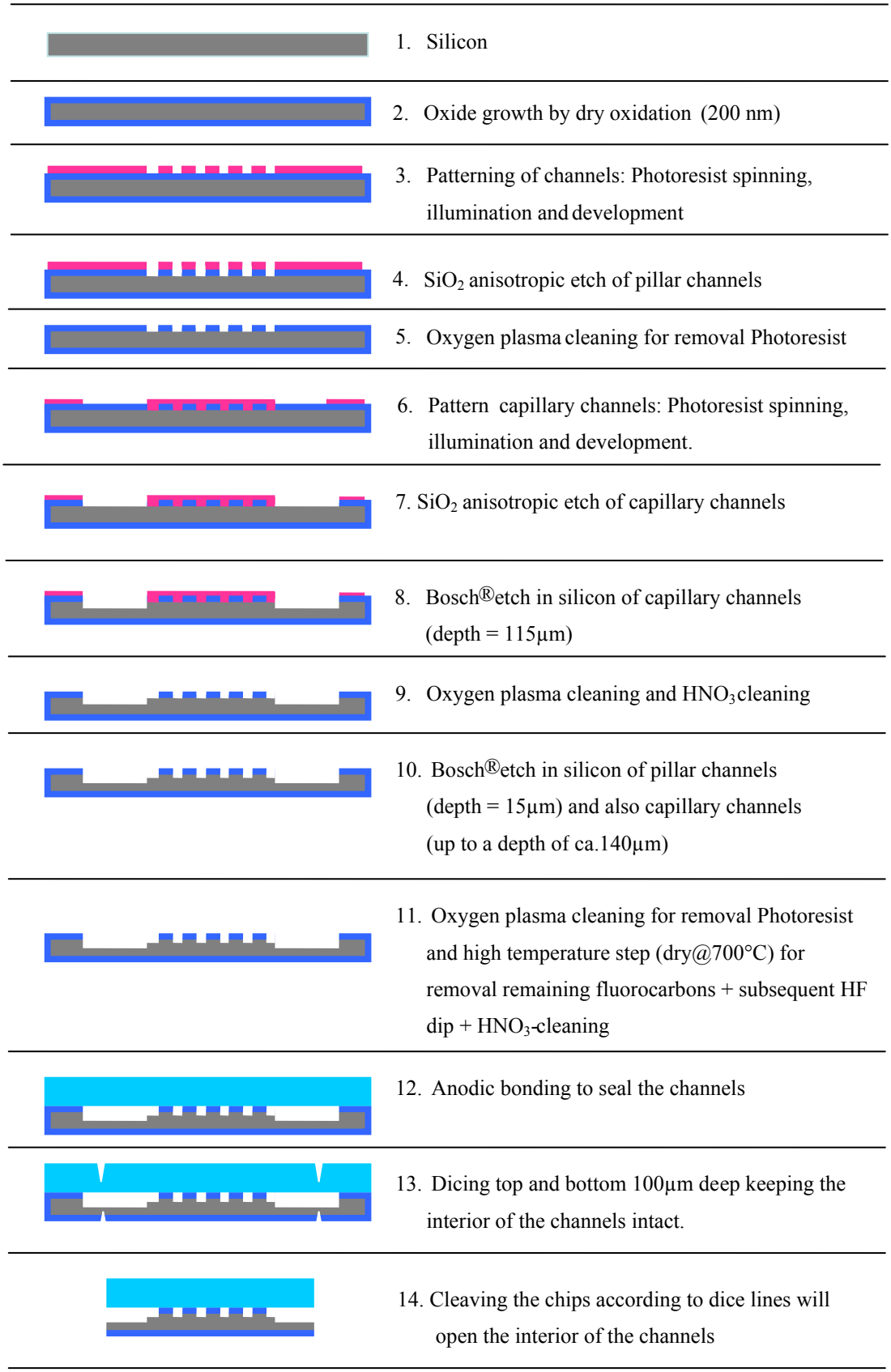

Figure 3.9. Process flow of the manufacturing of the µPAC-chip used in Chapter 7&8.

3.5.2.2. Porous shell pillar array column

The process flow for these devices is identical to the one used for the very long pillar array described in the previous paragraph (§3.5.2.1) and the design (see Figure 3.10) was put on the same mask.

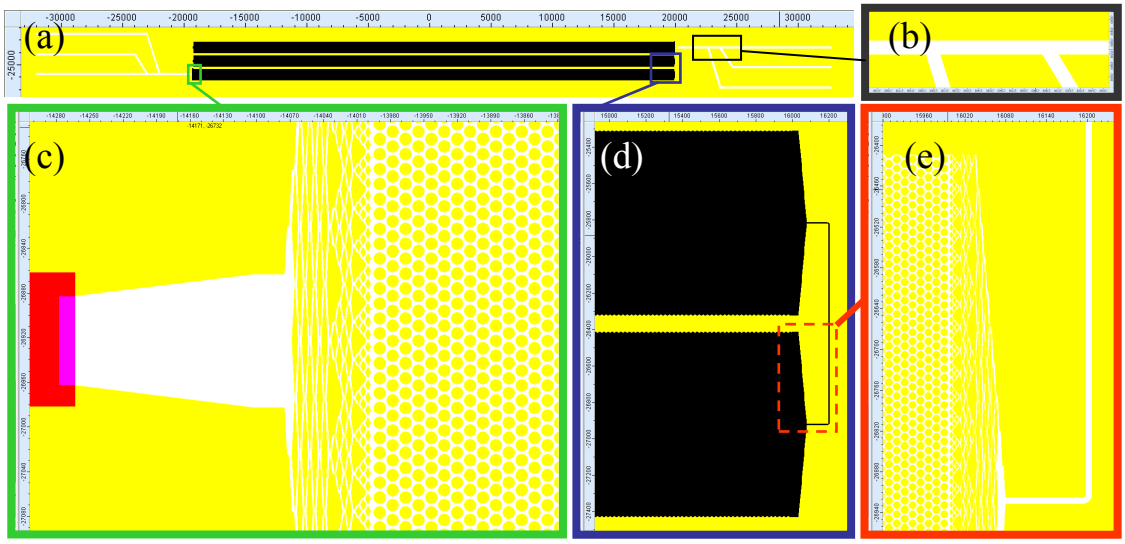

Figure 3.10. (a) Mask layout of the µPAC used in Chapter 8 (length 12 cm). **(b)** The on-chip injector was made in the capillary groove allowing a capillary to be inserted up to **(c)** the distributor. **(d)** the different lanes are delimited by **(e)** distributors and connected by turns

3.5.3. Hybrid Agilent HPLC-chip [unpublished results]

The aim of the Agilent HPLC-chip project was to develop a "hybrid-chip" which combines the separation potential of the pillar array chip (see chapters 7&8) with the low volume injection and detection control of the HPLC-chip system commercialized by Agilent. This project occurred in cooperation with Dr. Hamed Eghbali (VUB, CHIS-department) and Agilent Technologies (Waldbronn).

A design was made in which the VUB was responsible for the channel fabrication and Agilent was responsible for all the connections concerning injection and detection inside the device. With this approach, both partners combined the know-how of their research or products in an optimal way. More specifically, Agilent has state-of-the-art know-how and capabilities in processing polyimide for creating injection loops and electro spray nozzles, while the VUB has substantial know-how in creating micro pillar arrays in silicon. It was chosen to create a "safe" design in which dead volumes are not optimally minimized, but this "safe" design also has the most chance on success since both partners only had to fabricate parts for which they already had the technology in house.

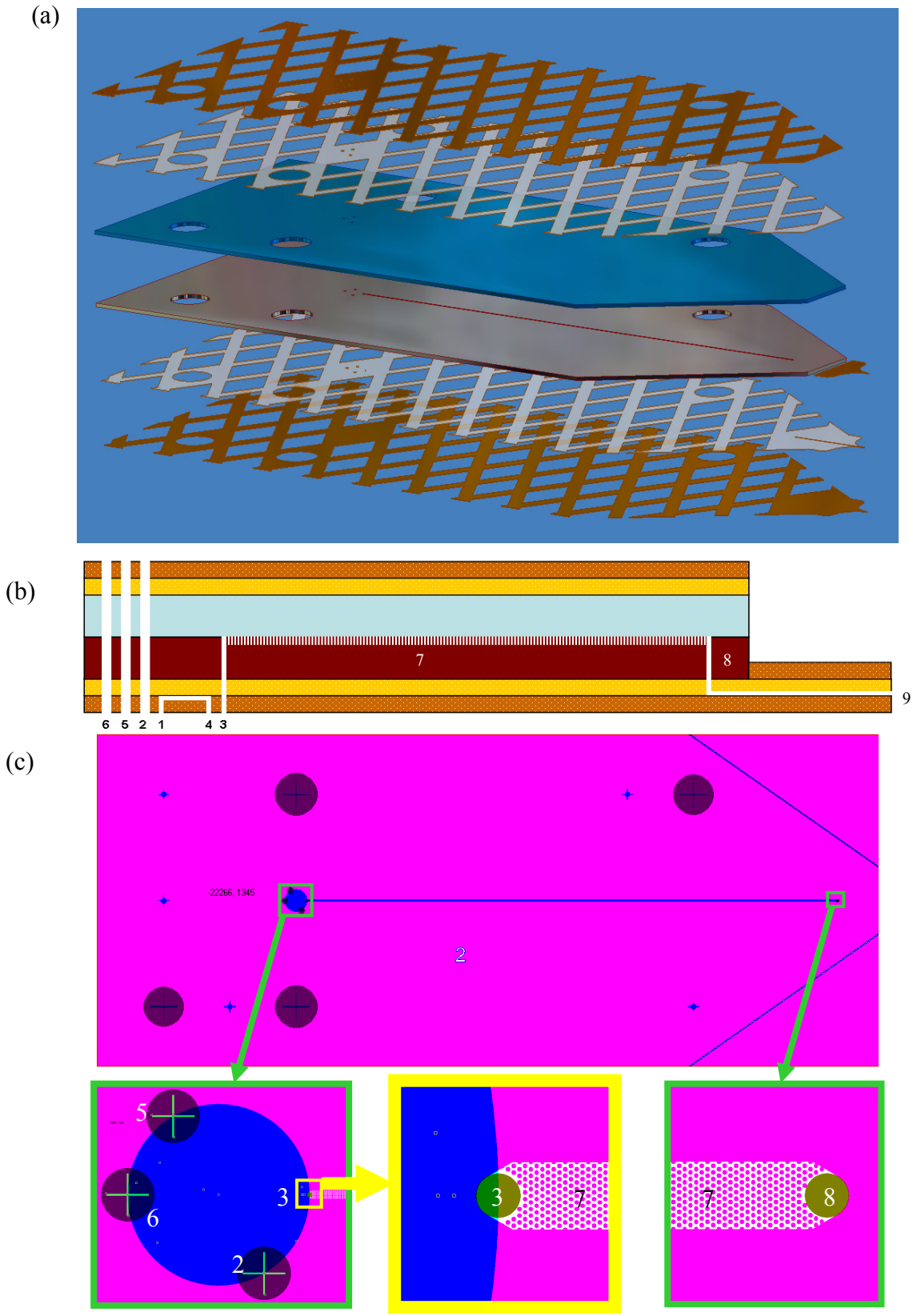

Figure 3.11. (a) Schematical drawing in perspective showing all the layers in the hybrid Agilent Chip design. **(b)** View from the side showing the different drilled through-holes (2, 5 and 6) and injection loop (between 1 and 4) in the polyimide and the micromachined through-hole (3) in the silicon. At the right side of the µPAC channel (7), another through-hole (8) through the silicon is found going to a polyimide channel leading to an electro spray nozzle (9). **(c)** Mask design of the micromachined chip (top view)

The biggest challenge in the design was to create the through-holes (holes 2,5 and 6 in Figure 3.11) since Pyrex can not be anisotropically etched and thus these through-holes had to be made in a different way. The most straightforward way would be to drill these holes. However, both VUB and Agilent did not have any experience with such processes and therefore a specialized company (Hellma GmbH, Germany) was contacted to perform drilling test on blank silicon-pyrex chips (see Figure 3.12).

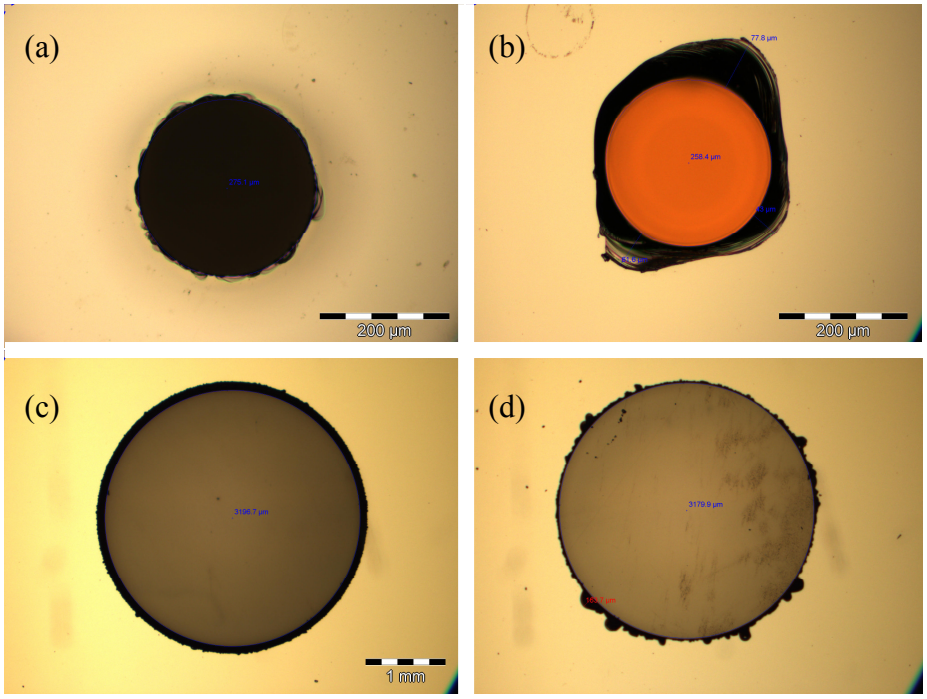

Figure 3.12. Microscope images of the holes drilled by Hellma GmbH. **(a-b)** are the holes 2, 5 and 6 on Figure 3.11. **(a)** view from the Pyrex side (diameter = 275µm), **(b)** drilled hole viewed from the silicon side (diameter = 260µm) with chipping, **(c-d)** Alignment holes (diameter = 3170µm), **(c)** view from Pyrex side, **(d)** view from silicon side.

The results of these tests were very promising since there was no failure (chip breaking). Due to the difference in hardness of Pyrex and silicon, a glass drill was chosen. It was expected that "chipping" would occur at the silicon side since the glass debris (which is harder than silicon) produced during the drilling would "carve" into the silicon. This effect can be minimized by optimization of the drilling process, but it was decided to leave this for a later stage of the project. The extra dead volume due to this effect was acceptably low (less than 5% of the total volume of the injection loop) and it was agreed that this effect will not have implications on the rest of the development.

A mask and process flow were (see Figure 3.11c and 3.14 respectively) developed for the manufacturing of the silicon-pyrex channel. First, a silicon wafer was thermally (dry) oxidized at 1100 °C until 700 nm silicon oxide was formed (Amtech Tempress Omega Junior,

Tempress Systems B.V., Vaassen, The Netherlands). Then broadband UV photolithography (photoresist: Olin 907-12) was used to define the pillar array column. Subsequently, the exposed silicon oxide was dry etched (Adixen AMS100DE), leaving a patterned silicon oxide layer, which serves as a mask for a second etching step. The silicon (and Pyrex) had to be very thin to reduce the dead volumes associated with the through-holes and extra precautions had to be taken for the etching of the thin silicon wafers. Inside both dry etching machines (Adixens DE and SE), the resist of the wafers burned because the thin wafers did not seal the cooling chamber on the backside well enough and helium (which cools the backside) leaked. It was tried to stick a carrier with Fomblin® oil underneath the thin wafer, which worked well in the adixen SE, but not in the Adixen DE and the resist still burned during the etching. To avoid the burning of the photoresist, silicon rings of 525 µm thick were cut using a laser and were put on top of the thin wafer before entering the Adixen DE. Using this method, most wafers (80%) were etched properly (when the leak was very low), but some still suffered from burning which was probably due to the bending of the wafer which resulted in a larger gap between the middle region and the cooling element (the gap should be 50 µm).

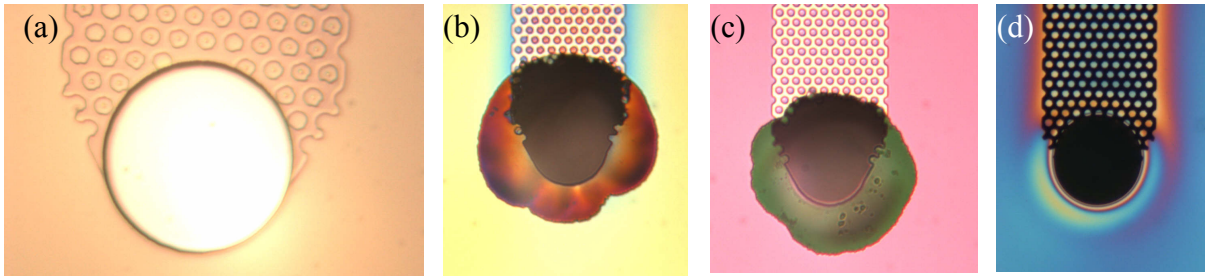

Figure 3.13. Problems associated with etching the through-hole (diameter = 50µm) from the pillar bed side. **(a)** Lithography of the through-hole, **(b)** High speed etch of the through-hole with the underetch in the vicinity of the through-hole, **(c)** High speed etch of the through-hole after stripping the resist showing the pillar bed still intact (not etched), **(d)** Etching of the through-hole with high aspect ratio recipe avoids the underetch, however the resist on top of the pillar bed was consumed and the pillar bed was already partially etched.

After patterning the pillar design and removing the resist with an oxygen plasma, the through-holes were defined using broadband UV lithography (photoresist: Olin 908-35 spun at 1000rpm). It was tried to etch the through-holes from the same side as the pillar channel, however the photoresist layer was already consumed at some regions before the through-hole was made and the pillar channel was already partially etched. It was also tried to use a high speed etching recipe, but this resulted in extensive under-etching. These problems (see Figure 3.13) were completely avoided by etching from the backside. After defining the through-holes on the backside, the silicon oxide was dry etched (Adixen DE) with a ring to avoid burning of

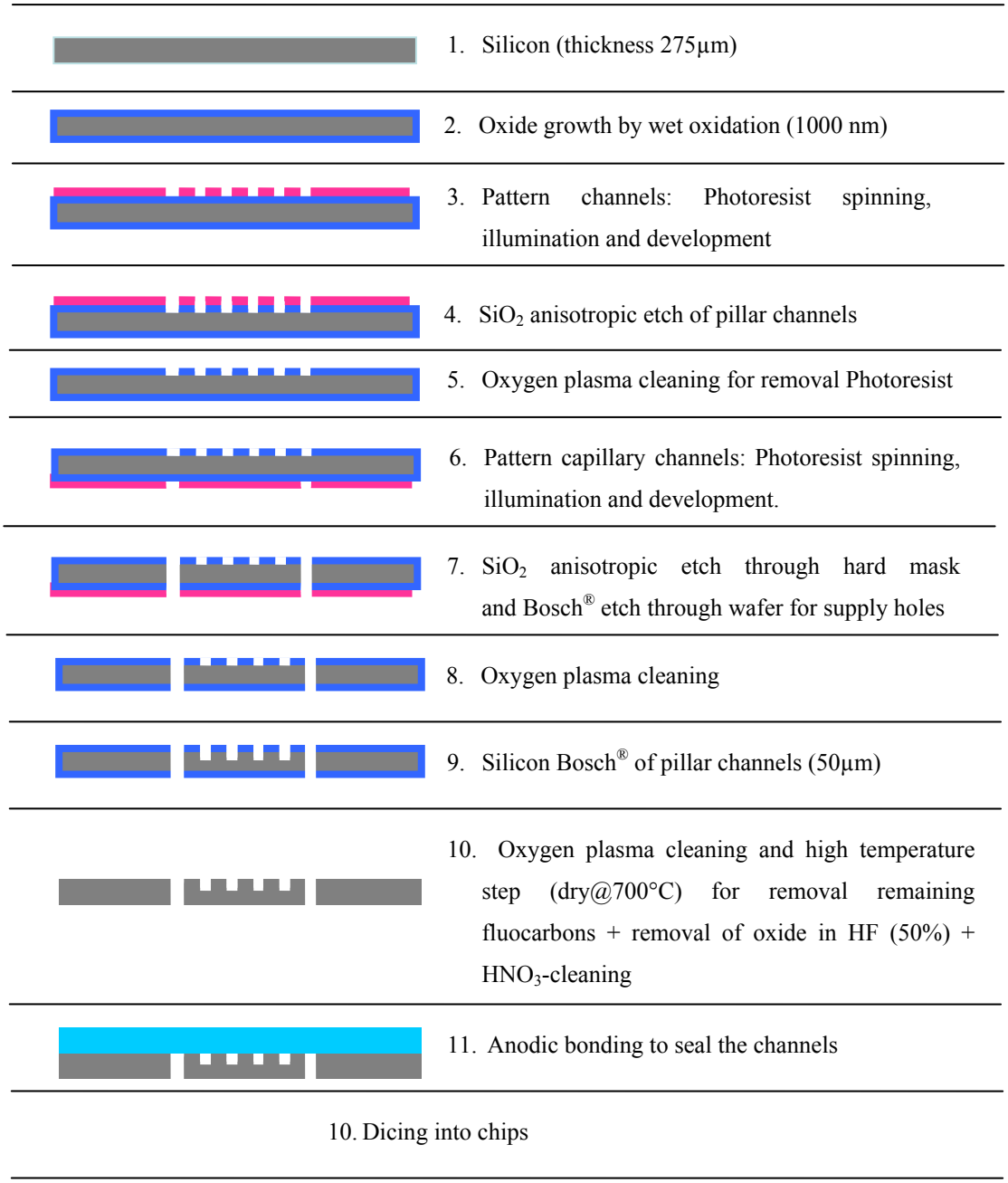

Figure 3.14. Process flow of the manufacturing of the µPAC used in the hybrid Agilent HPLC-chip. The etching in step 4 and 7 was carried out with a ring on top of the wafer to reassure good cooling. Step 9 was done with a carrier wafer underneath.

the photoresist and subsequently the through-hole was Bosch® etched using a high aspect ratio recipe (Adixen SE). After the through-holes were made and the resist was removed with an oxygen plasma, the pillars were etched with a high aspect ratio Bosch® etching recipe (Adixen AMS100SE), yielding pillars with a height of 50 µm (see Figure 3.15). After the final etching step, the resist was removed with an oxygen plasma and the fluorocarbons were burned off with a high temperature step (700°C for 15min). In the next step, the channels were anodically bonded with a Pyrex wafer (EV-501) and diced into chips (Disco DAD-321).

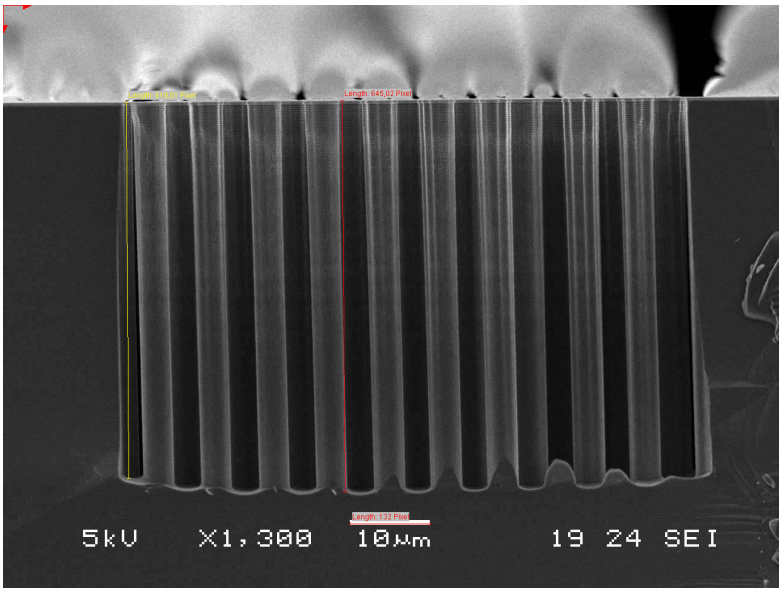

Figure 3.15. Cross sectional SEM image of the pillar bed etched with a high aspect ratio recipe yielding pillars with a height of 50µm.

The manufactured chips were tested at the Agilent site in Waldbronn by Hamed Eghbali. Unfortunately the chips clogged very fast (presumably due to debris of the drilling process) and a very steep pressure drop increase was observed. An ultrasonic cleaning with isopropylalcohol was developed which could remove the debris in front of the distributor (in the through-hole) which was very successful, however, the chips clogged again very fast after each cleaning step. Although both Agilent and the Vrije Universiteit Brussel recognized the potential of the hybrid chip, the project was stopped at that point.

3.6. Zero Dead Volume connection

3.6.1. Introduction

In the last decade, several theoretical and practical studies of chromatography-on-a-chip have demonstrated that when the dimensions of the separation column are downsized, the quality and efficiency of the separation can be drastically increased. However, one major disadvantage encountered when down scaling these devices, is the influence of the connection volumes since these are generally not downsized in relation to the devices, and will make up a relatively bigger part of the total column volume and therefore wipe out the increased efficiency and quality obtained with the micro pillar channel. This disadvantage can be avoided by performing all the actions, like injection and detection, on chip, which has been done in the past to study the potential of these micro pillar channels. However, when using on chip injection and detection, the amount of analytes that can be tested is rather small in

comparison to the commercially available HPLC-column technology, since the technology of on chip detectors is not that advanced compared to the commercially available ones. Another disadvantage of using on-chip detectors, is that these are not interchangeable and one column equipped with only one detector can limit the analytes that can be tested with one device. To completely avoid these problems, an approach is made in which the injection and detection are performed with commercially available equipment, and these are connected to the micro-channel. To avoid the influence of dead volumes between injector and chip, and between chip and detector, a connection method has been made in order to minimize these volumes.

3.6.2. State-of-the-art connections between macro and micro

Several solutions trying to minimize the dead volume between chip and off chip equipment already exist. Well connectors are by far the most primitive, but are excellent for EOF applications since the pumping is done on chip and these wells act like “reservoirs”. A more advanced type of well connectors are Nanoports™. These are widely used and these are one of the most popular connection methods in order to avoid dead-volumes. When using these, the nanoport is screwed tightly onto the chip connecting the capillary with the interior of the chip and the transition is sealed by using a polymeric ferrule. In the ideal case, the transition between capillary and chip is seamless without any variation in internal diameter.

This approach starts however from the assumptions that the cleavage of the capillary is perfect and that the positioning nanoport on the chip is also perfect. In reality, the cleavage is never perfect and there is a relatively large volume inside the ferrule at the interface of the chip as can be seen in Figures 3.16 and 3.17.

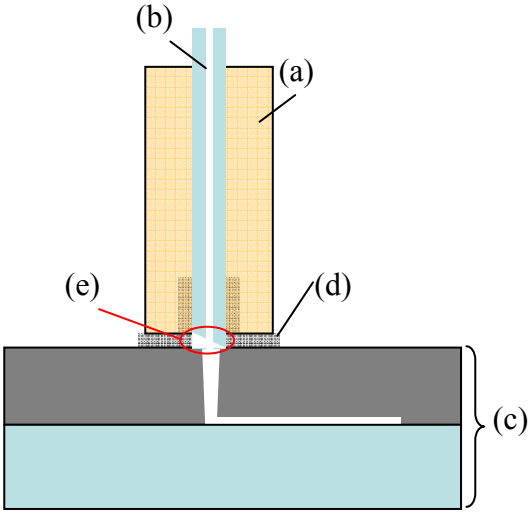

Figure 3.16. Schematical illustration of the Nanoport™ connection showing **(a)** the hollow polymeric screw that mechanically seals the connection between **(b)** the capillary and **(c)** the chip using a ferrule **(d)**. Due to the cleavage of the capillary, there is **(e)** a dead volume inside the ferrule.

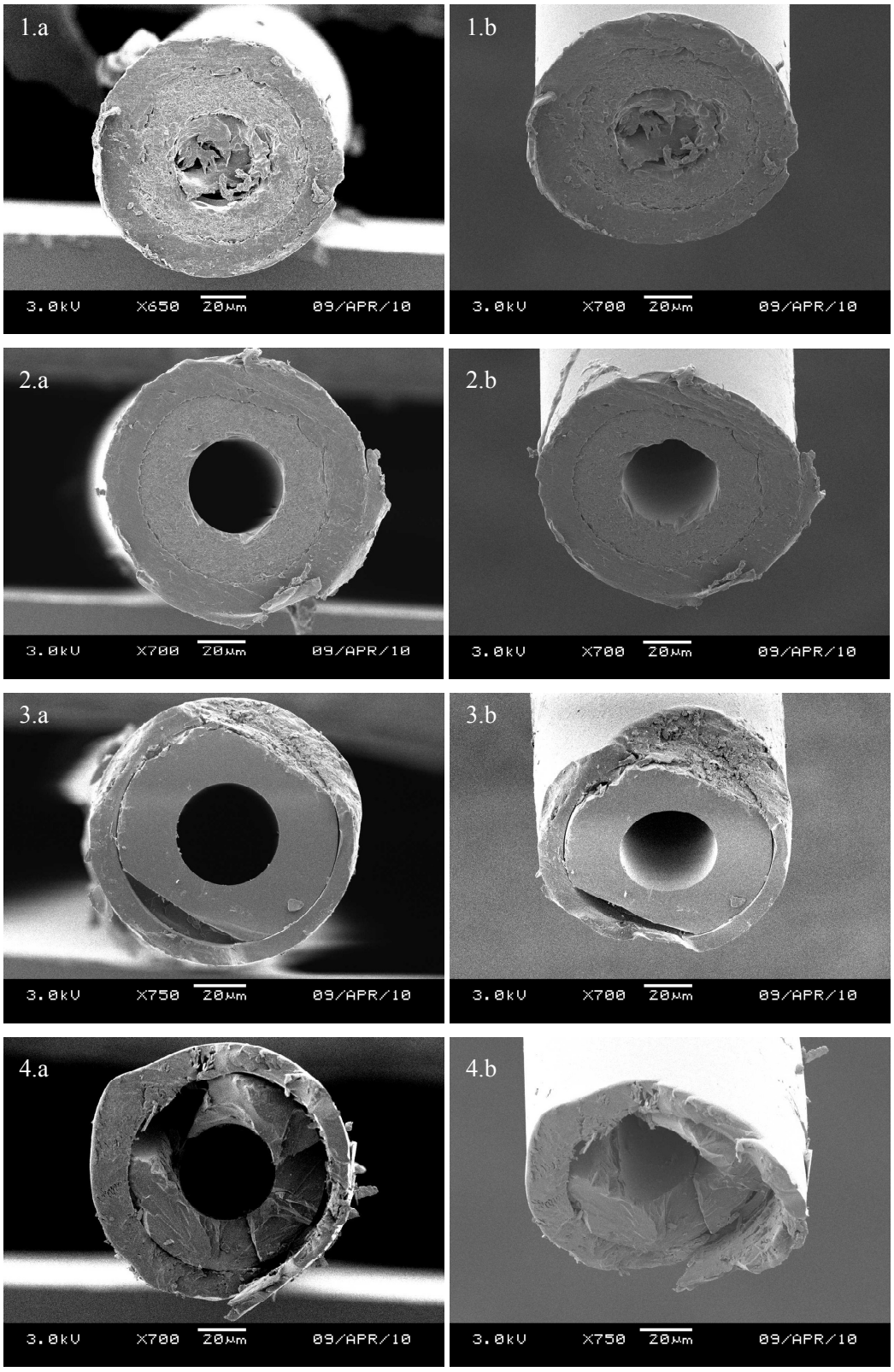

Figure 3.17. SEM-images of capillaries cleaved with different methods with **(a)** an axial view and **(b)** a view from perspective of the cross section. **(1)** & **(2)** are both ends of a sawed capillary. **(1)** contains a lot of debris originating of the sawing process while **(2)** is clear from debris, although the polyimide coating is heavily damaged at the interface. **(3)** has been cut with a ceramic knife, a small scratch has been made through the polyimide coating in the fused silica capillary and a nearly perfect cut is obtained, however, the polyimide coating is heavily damaged. **(4)** was the cleavage of ordered pre-cleaved capillaries. These had already a really poor quality, as can be noted on the image.

Since the capillaries connecting the chip with the external equipment are also considered as "dead" volume, these should also have a short length and narrow internal diameter. Decreasing the internal diameters of the through-hole and the connection capillary will increase the probability of leakages at the interface, due to an increasing pressure drop.

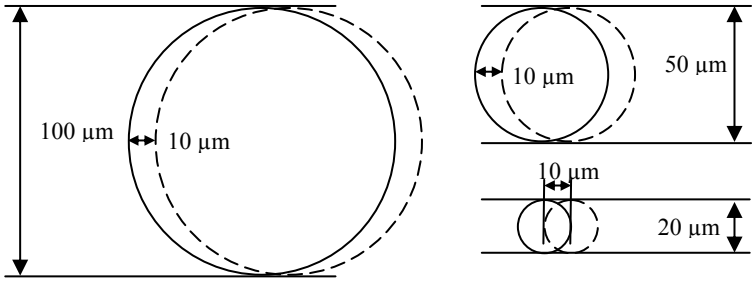

Figure 3.18. Misalignment of through-hole and capillary. For the illustrated examples the ratio of interfacial surface to the flow through surface are **(a)** 87%, **(b)** 75% and **(c)** 39**%.** If the misalignment is kept constant and the internal diameter is decreased, the interfacial surface will become a flow resistance increasing the pressure drop.

Another disadvantage of the Nanoport^{TM} method, is the fabrication of the wafer through-hole. When down-scaling the internal diameter of the capillary and the wafer through-hole, the fabrication of the wafer through-hole will become a lot harder to achieve due to the increasing aspect ratio. One way to circumvent this would be to use thinner wafers, but these are a lot more fragile and more difficult in handling resulting in lower yields of the fabrication process. They will also be vulnerable to mechanical failure when performing experiments at high pressures.

Another type of macro-to-micro interface are "integrated interconnects". These connectors are part of the chip and not attached to the chip like the well connectors. Harrison et al. [8] devised a coplanar connector at the sawn edge of a chip. The connector is made by drilling a hole from the edge of the chip to the channel. By finishing the hole with a square tipped drill bit, the tapered section of the pointed tip drilling has been corrected allowing the capillary to butt up against the channel and reducing the dead volume. The capillaries were anchored to the chip with the use of adhesives and channel contamination with adhesives was prevented with the use of a specialized technique.

Kovacs et al. [9] used deep reactive ion etching to define wells to accept capillaries which were secured in a reversible manner by molded polyoxymethylene fittings. A similar design has been done by Meiners et al. [10] who reinforced the device with epoxy and made it more

user friendly for the insertion of capillaries. These connectors could withstand a pressure of 1.4 bar which is similar to the other non-permanent integrated connectors.

Puntambekar and Ahn [11] devised flanged interconnects which could be created in a serial or parallel manner. The flanges were made by using thermoplastic tubes fitting around the capillaries that were melted and pushed inside a confined space. Pressures up to 2 bars could be applied and mechanical failure always occurred at the glass bond and never at the interconnection in their tests. An important note is that their bonding procedure and design were not optimal for higher pressures since pressures up to 700 bars have been reported inside glass chips without having mechanical failure at the bonding interface.

Pattekar and Kothare [12] expanded the technique by using the flange as a temporary seal to prevent blocking of the channel and interconnection by epoxy glue. They noted that failure occurred often at the capillary/epoxy interface and they strengthened the capillary by gluing a PTFE tube around it to elevate the stress. This interconnect was more robust and could withstand 20 bars at elevated temperatures of 275°C.

Tiggelaar et al. [13] created an interconnection similar to the one devised by Harrison, but the coplanar hole is etched in stead of drilled. “Breaking lines” made by dicing the chips partially on both sides allowed the holes to be readily accessed after breaking the wafer stack into chips. This method reassured that no dicing debris entered the etched trenches so the capillaries could be glued in after without risking particle contamination. Several designs were tested and several important conclusions were made in terms of pressure resistance. First of all, the smoother the edges and the less sharp corners the design had, the higher the pressure could be applied without failure. A second important conclusion was that the interconnections in an anodic bonded silicon-pyrex chip could withstand higher pressures compared to a thermal bonded pyrex-pyrex chip with similar design. A third important conclusion was that the design using thinner capillaries and thus using thinner capillary holes were more pressure resistant.

Another type of interconnects are the modular ones in which a lot of tools can be installed/replaced and module connects them to the chip. An example of this approach is the Agilent HPLC-chip [14]. These types of connectors are by far the most user friendly, but they require a standardized design of chips and due to the complex design and manufacturing costs, these are only made as the last step in the development of a commercial product.

The choice of which interconnect is most suited for the intended application, is determined by the order of importance of several characteristics like the materials used, the operation conditions, the ease of handling,… and are often a trade off since every different interconnection excels at one of the characteristics.

3.6.3. First new design

Since the largest disadvantage of the Nanoport™ method is the dead volume associated with the transition from capillary to chip, and since the largest fabrication problems occur when high-aspect-ratio through-holes need to be made, the well connector type was not taken into consideration into the further development of the "zero dead volume" interconnector. Since the intended interconnection has to be used at high pressures and needs to be leak free, integrated interconnects like the ones developed by Tiggelaar et al. [13] seem to be the best choice. However, the dead volume at the interconnection interface was quite large due to the gluing method with epoxies and could not be minimized without risking the channel to be blocked. A UV-curable glue might however solve this issue. The advantage of this coplanar approach is that the alignment of the capillary would be a lot easier since the trench will be etched and will have known dimensions. Once the capillary fits this trench, it is guided automatically to the channel inlet by sliding the capillary deeper into the chip. Another advantage in this approach is the large contact surface between chip and capillary, which should avoid breakage due to stress. In addition, the final result can be easily visually monitored through the top glass substrate of the silicon-pyrex chip.

Several process flows were made, resulting in different new designs which are shown in Figure 3.19. In the first design, it was chosen to keep the center of the capillary in the same plane as the pillar bed which would require isotropic etching of the pyrex top substrate. In the second design, it was chosen to avoid this wet etching step making the process flow less complex.

As shown in Figure 3.19 (1b), the disadvantage of the design in which the glass substrate is etched, is the rounded etching profile in the pyrex substrate. This would create a large dead volume at the exit of the capillary which can be seen from the top view but also from the side view. Another disadvantage of this approach is that another alignment step is needed before the anodic bonding. In the other design in which the trench would be anisotropically etched in the silicon, the center of the capillary would not be in the same plane as the pillar column. In this design, there will also be a dead-zone at the end of the capillary volume since the

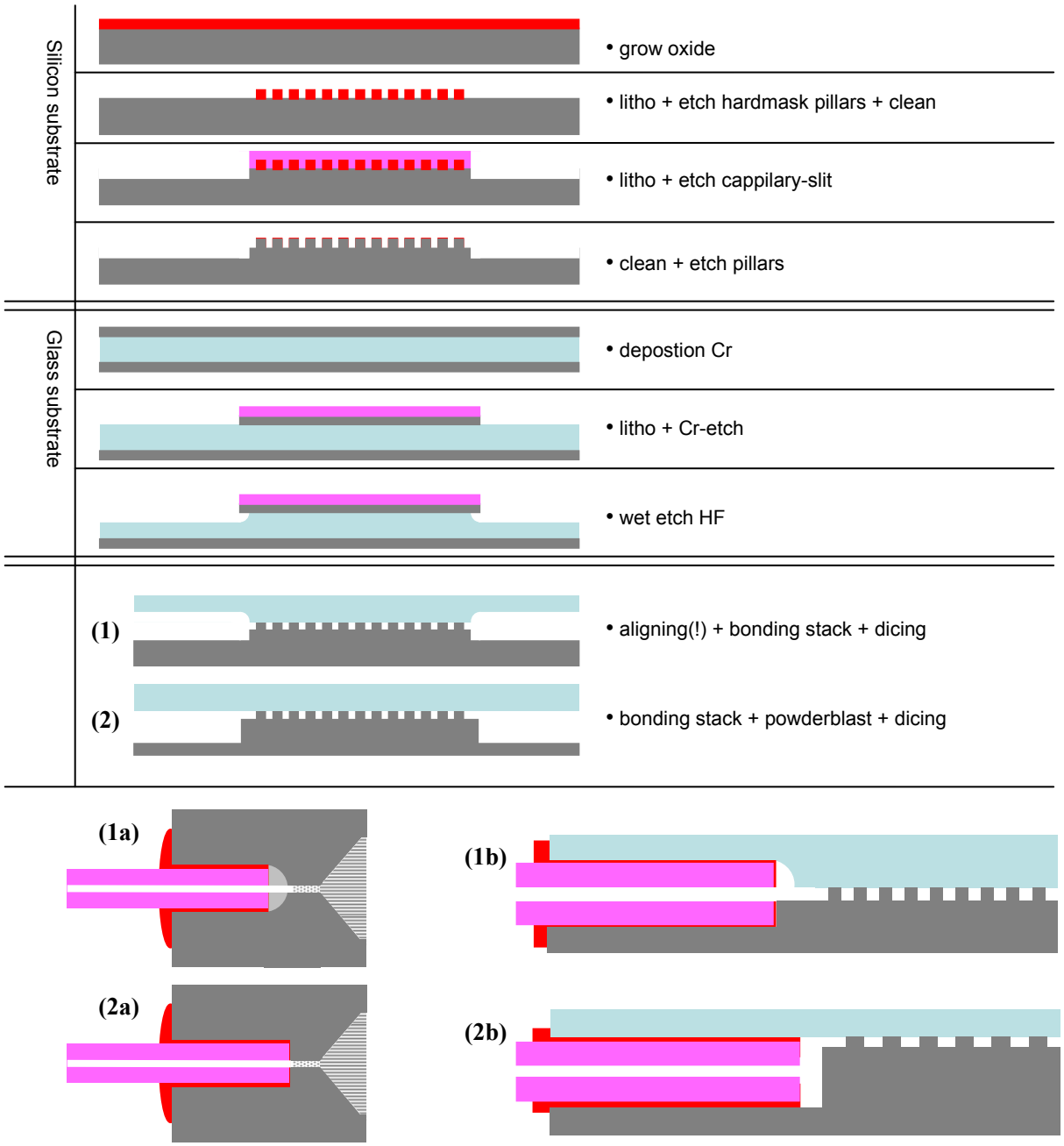

Figure 3.19. Proces flow and the different final designs. In the first design, both silicon as pyrex are etched resulting in (1), In the second design, the capillary slit is etched deeper and the pyrex substrate remains unetched resulting in (2). The images below represent the persued result after the capillary has been glued in with (1a) and (1b) representing the top and side view of the first design with the glass substrate etched. (2a) and (2b) represent the top and side view of the second approach without etching the glass substrate.

anisotropical etching profile of the trench matches the rectangular shape of the capillary perfectly. A compromise had to be made, since a “seemless” transition from capillary to chip can either not be made due to the isotropical etching behavior of the glass substrate (design 1), or because the center of the capillary is out of plane when solely etching in the silicon (design 2). When looking from the processing point of view, the design with the isotropically etched

pyrex substrate would involve a more complicated aligned bonding step which works really well in theory, but in practice is one of the hardest steps to perform since there is a large probability of particle contamination during alignment, which would lower the fabrication yield in a quite drastic way, which in turn would increase the manufacturing cost a lot.

3.6.4. Chip design and methods for applying glue

A mask drawing was made in which several designs were included that had various channels for applying glue to the connection. In the simplest design, there is only one groove for the capillary and none for applying the glue. In the most advanced design, six grooves were included for applying the glue in a controlled manner. The other designs that were put on the mask drawing are hybrid designs of the former two.

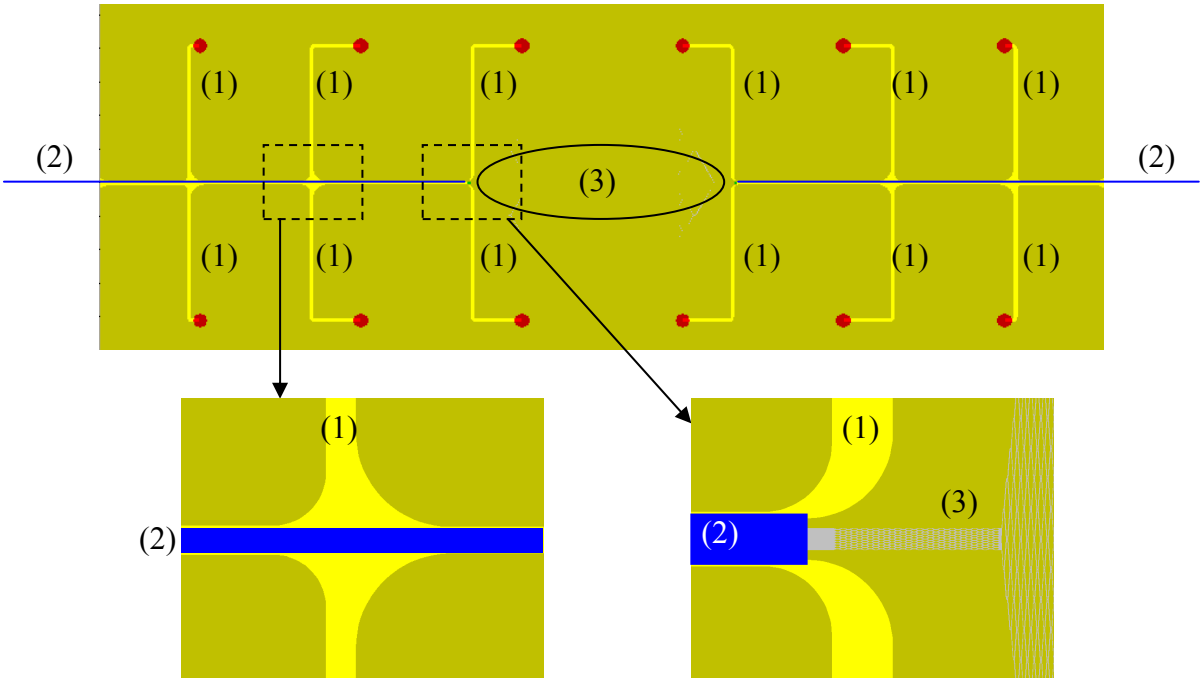

Figure 3.20. Most advanced design (top view) for applying glue to the chip. The "glue-channels" **(1)** connect a through-hole with the capillary **(2)** which leads to the pillar channel **(3)**.

The glue chosen to perform these experiments, was an Ormocer® (Ormocore, Micro Resist Technology GmbH, Germany), which is an organically modified ceramic. This glue has a very good chemical resistance against many solvents commonly used in HPLC and shows good adhesion with glass and silicon surfaces. But the most important characteristic of all is that this glue is UV-curable. This makes it possible to locally cure the glue without time constraints which would not be possible with thermal curable glues or solvent based glues.

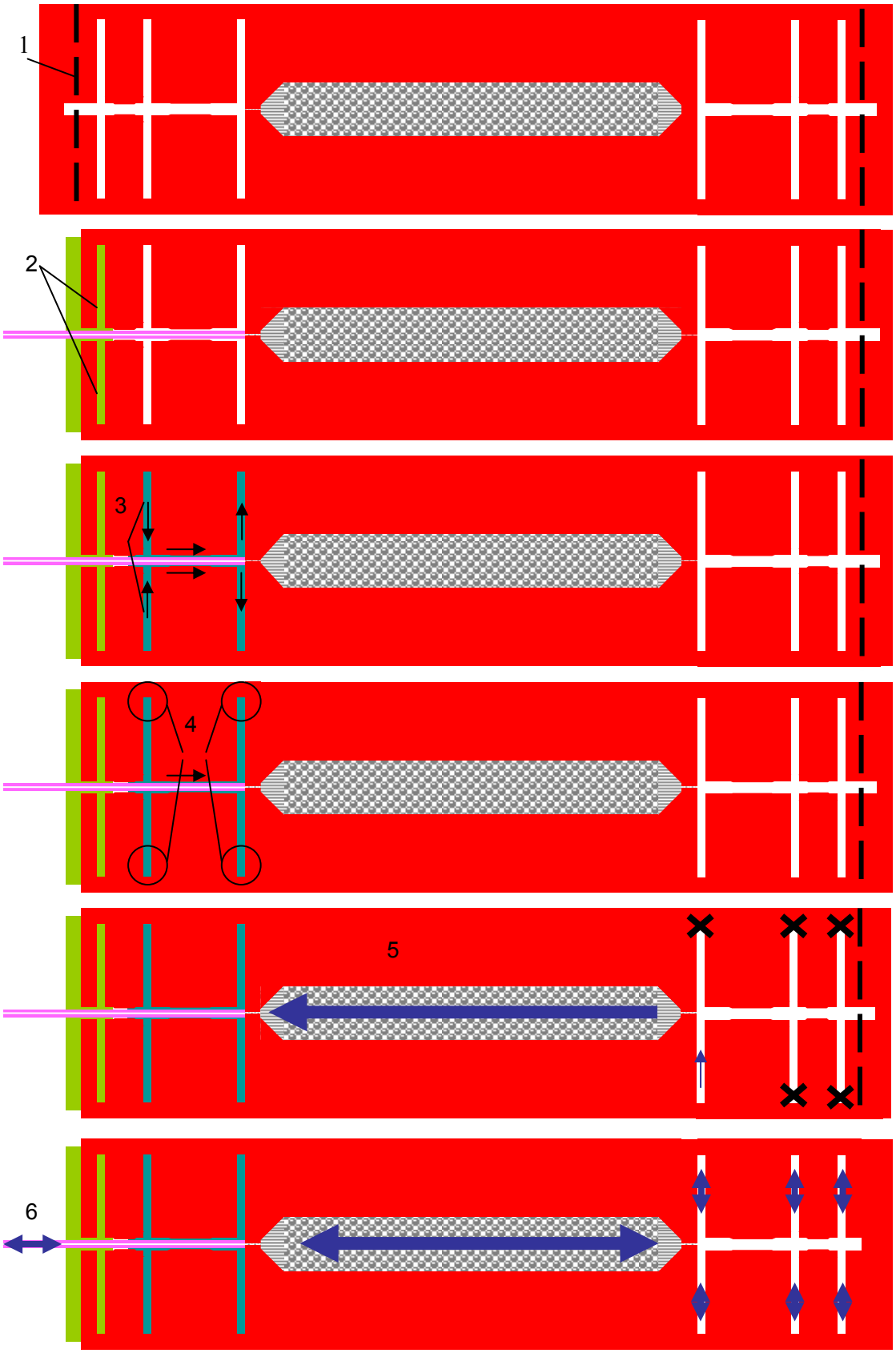

Figure 3.21. (1) Opening of the capillary groove, **(2)** "anchoring" of the capillary inside groove with glue, **(3)** filling of the volume in between the capillary and its groove, **(4)** curing of the glue near through-holes, **(5)** flushing of the channel and capillary with solvent, **(6)** Drying of the channel with dry nitrogen gas.

The working method developed for gluing the capillary in the chip in the most advanced design involved many steps as illustrated in Figure 3.21. In the first step, the capillary groove is opened by breaking the chip. The "breaking" can be done in a controllable manner by dicing the top and bottom side of the chip for 1/3 of its thickness resulting in a predefined fracture line. Dicing through the capillary groove should be avoided since this would lead to debris and particle contamination inside the channel. When the channel is opened, a cleaved capillary is introduced inside the capillary groove and pushed to the channel entrance. When the capillary is in place, the position is fixed by anchoring it with glue near the edge of the chip. Subsequently, the volume between the capillary and its groove is filled up with Ormocer® using the side channels leading to the capillary groove. The channels leading away from the capillary end (or pillar channel entrance) were included in the design to give the excessive amount of glue another way to escape than via the channel itself. This avoids unnecessary and excessive contamination inside the capillary and the pillar bed. Once these volumes were filled with glue, the glue near the through-holes was cured. In the next step the channel and capillary were flushed with solvent to remove potential residues of the glue inside the pillar bed and capillary. Once a stable flow was established, which can be verified at the capillary entrance, all the remaining glue was cured without switching of the flow of flushing solvent. In the next step, the channel and capillary ware dried with dry nitrogen. At this point, a zero-dead volume capillary-chip connection has been established on one side of the chip, and the whole process can restart to accomplish the same on the other side of the chip.

In the simplest design, there were no side channels leading to the capillary groove, and the filling of the volume between capillary and groove with glue was done by capillary forces. In the "hybrid" designs, there were fewer side channels and these were made to test if the same could be accomplished as in the most advanced design. In one of these hybrid designs, for example, only one side channel was used, but the same method could be applied as in the most advanced by combining step 2 and 3. With this design, the capillary could be anchored by locally illuminating the glue near the edge of the chip once it was reached. In some of these hybrid designs, the two channels near the end of the capillary were also left out of the design. This gives the excessive glue no way to escape but via the channel, which thus needs to be thoroughly flushed out in the next step.

3.6.5. Discussion of the first new design and detailed study of the capillary flow inside the capillary groove.

The method has been tested extensively and has never led to the desired result. Step 1 to 4 could be done in a reproducible manner and it was found that the side channels for applying the glue were not necessary since the same could be obtained using capillary forces only. The major problem with this method was the flushing and curing step (step 5 in Figure 3.21). It was possible to establish a flow of solvent, thus flushing the channel. However, when curing the glue, the flow of solvent always stopped which means that there was still some glue inside the capillary (or capillary-pillar bed transition) that was cured and that was subsequently blocking the flow. Many different solvents were tested without any demonstration of improvement. Also the time interval used for flushing with solvent has been extended for longer periods, but the flow of solvent always stopped when curing the glue. The real reason for this blocking behavior has not been found, but is most likely due to the heating accompanying the curing of the glue. When heating up, the chip, glue and capillary all expand differently. This implies that the volume between the capillary and its groove will also change. Furthermore, since the glue is of a polymeric nature and thus has an expansion coefficient (100-130 ppm/°C) that is an order of magnitude higher than the chip (3 ppm/°C), it is very likely that during curing the glue expands and blocks the transition between capillary and chip before it is fully cured. The logical solution to avoid the flushing step and its related problems was avoiding glue contamination in the insides of the pillar bed and the capillary. For this reason, another series of experiments was started with the focus on the capillary flow inside the volume between the capillary and its groove in an attempt to control it and to avoid the glue blocking the "passage" during curing.

3.6.5.1. Study of the capillary flow inside the capillary groove

In the first experiment, the capillary flow was tested in an open square channel without the presence of a capillary inside which can be seen in Figure 3.22. The open square channel has a width and depth of approximately 120 μm by 120 μm. The horizontal white line that can be seen in the picture is an artifact of the Bosch etching process. In the used recipe, the obtained bottom of the groove is not perfectly flat, but has the shape of an accolade and thus the illumination light of the camera is reflected differently in the middle of the groove.

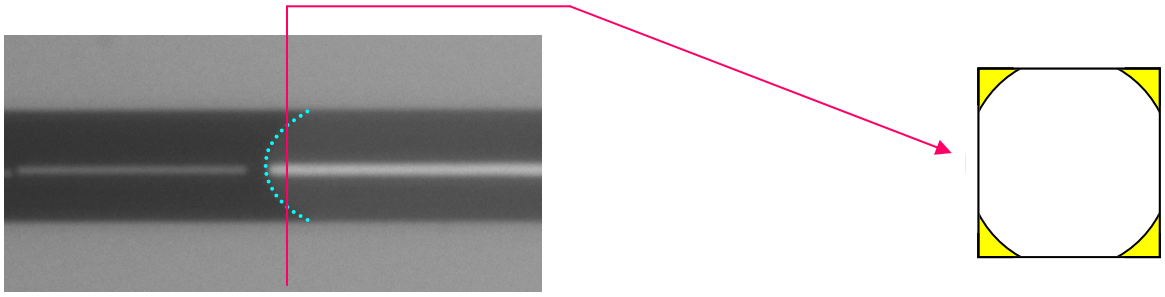

Figure 3.22. Capillary flow in an open square channel. The dotted line represents the front of the capillary flow. On the right hand side, an attempt was made to illustrate the cross section of the front.

The concave shape of the front reveals that the adhesive forces between the sidewall and glue are stronger than the intermolecular forces inside the glue. As a consequence the glue will migrate faster near the sidewalls and in the corners.

In the next experiment, the capillary flow was tested in an open square channel with the identical same dimensions as in the previous experiment, but now with the presence of a circular capillary inside which can be seen in Figure 3.23.

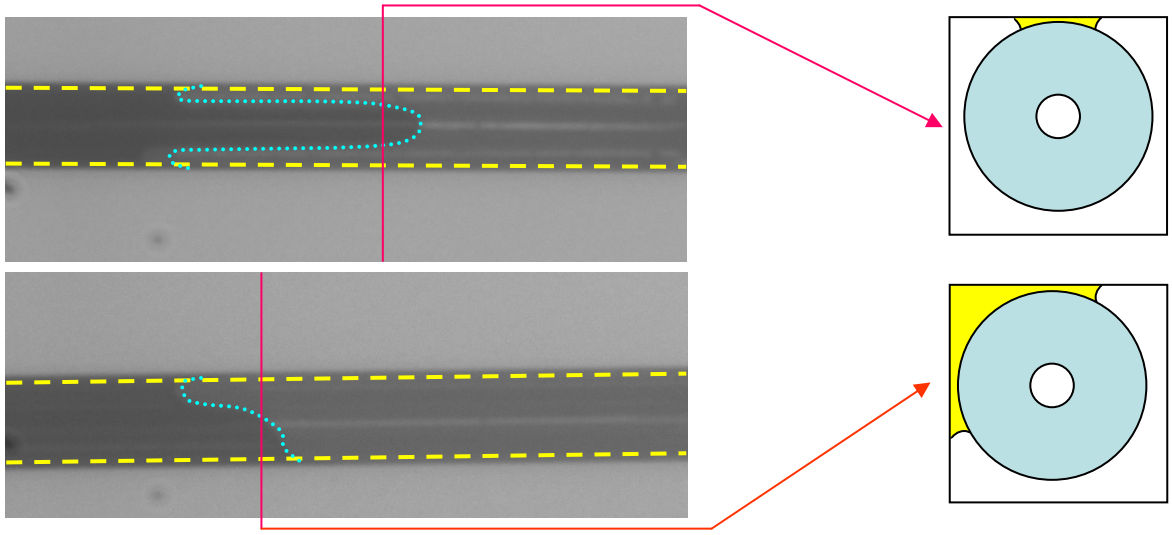

Figure 3.23. Capillary flow in an open square channel with a capillary inside. The dashed lines highlight the capillary and the dotted line represents the front of the capillary flow of the glue. On the right side, an attempt was made to illustrate the cross section of the menisci.

By introducing a capillary in the middle of the channel, an additional type of surface is introduced inside the channel. The coating of the capillary is made of polyimide which has also a lot of stabilizing interactions with the glue. As can be noted on Figure 3.23, the front of the capillary flow was not concave anymore but altered in a quite fundamental way. The glue migrated the fastest in the most confined regions which are where the capillary is closest to the sidewall. Since it is not always possible to center the capillary perfectly inside the channel, the shape of the front is not symmetrical. Since the capillary flow tends to prefer the confined

spaces inside the channel to migrate faster and the shape of the front is altered in a quite fundamental way with the presence of the capillary, it can be expected that there is a transition in the shape of the front of the capillary flow when switching between the two previously described regimes (Figures 3.22 and 3.23).

Therefore another experiment was done in which the capillary flow was tested in a channel with a capillary inside, but now with focusing on the end of the capillary inside the channel, which is illustrated in Figure 3.24. It can be seen that the volumes around the capillary are filled in a "self-controlling" way, meaning that the dead volumes around the capillary will be filled before switching to the other regime in which it will block the outlet of the capillary. However, there is a need to "freeze" this transition state to prevent the next regime to initiate.

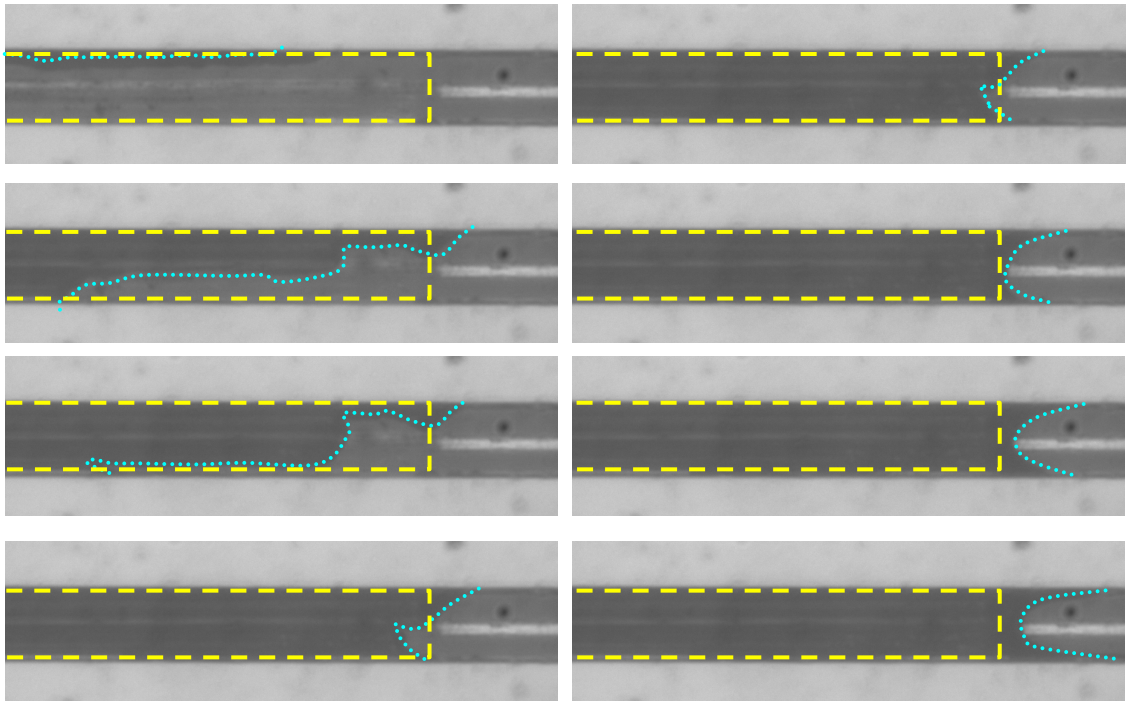

Figure 3.24. Capillary flow in an open square channel with a capillary inside at the end of the capillary. The dashed lines highlight the capillary and the dotted line represents the front of the capillary flow of the glue.

3.6.6. Controlling the capillary flow and curing of the glue

Due to the need to "freeze" the front of the capillary flow of the glue before it blocks the outlet of the capillary, an illumination method had to be devised (see Figure 3.25). In a first approach this might be done by observing the capillary flow of glue and illuminate at the right time. But this will require someone who carefully looks through a microscope and presses the button at the right time to cure the glue (see design A in Figure 3.25).

Another approach would be to have a bundle of light focused at the end of the capillary so that when the glue reaches this point, it does not have the chance to switch to block the outlet of the capillary. The downside of this approach is that one needs to do a lot of aligning, but also the focusing of the light beam on the end of the capillary in a tiny spot with enough intensity to cure the glue. It is also worth noting, that there is a 3^{thd} dimension, and a focused light beam can hence not be in focus over the whole depth of the square channel unless a laser beam with a rectangular shape is used. This approach seems to be quite cumbersome due to the aligning which would require a setup with many micro adjustors and a lot of manual input (see design B in Figure 3.25).

With the use of a wave-guide and a collimator lens in a robust setup, the previous approach can be simplified, minimizing the need for many micro-adjustors to align the curing light at the capillary outlet in the rectangular groove (see design C in Figure 3.25).

In order to simplify the method more extensively and to avoid any need for micro-adjustors to align and focus the curing light onto the outlet of the capillary, a method was conceived wherein the capillary would act as the waveguide leading the curing light to its outlet (see design D in Figure 3.25). This approach seems quite complicated at first sight, but has more advantages and the biggest challenge in this approach is coupling the curing light into the capillary. Optical misalignments cannot be made unless the capillary's outlet is positioned badly which would also present a problem in the previously described approaches. The capillary is made of fused silica, which is an excellent waveguide material for the UV curing light. The only problem that could arise is that the curing light exits the capillary before the outlet and cures the glue early, to be more specific, before the capillary flow of the glue reaches the exit of the capillary. Due to the small differences in refractive indices of fused silica (n_d = 1.46 at 587.6nm) of the capillary, the polyimide coating (n_d = 1.67 in IR) and the UV-curing glue (n_d = 1.51 at 635nm), the waveguide effect would be lost during the capillary flow of the glue around the capillary inside the rectangular channel. However, the polyimide coating of the capillary absorbs UV light very strongly but also has a higher refractive index than that of the fused silica capillary and the glue. This means that a lot of the intensity of the light coupled into capillary will be lost early. Another issue is that the capillary has a hollow core, a geometry which is far from the ideal waveguide.

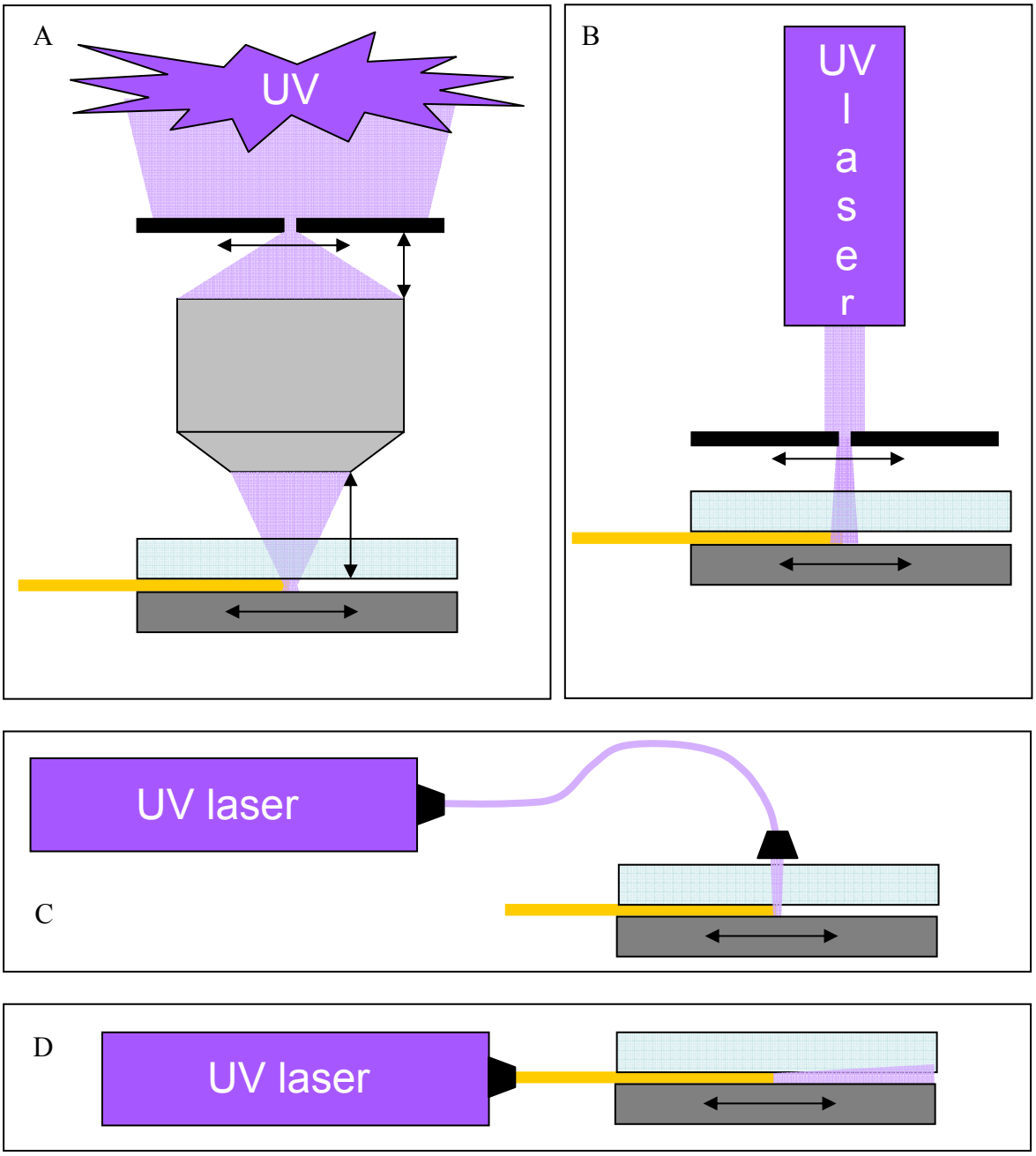

Figure 3.25. Overview of the proposed methods to cure the glue at the outlet of the capillary. **(A)** Using a microscope, **(B)** using a laser and a pinhole, **(C)** using a laser coupler, a waveguide and a collimator lens, **(D)** using a laser coupler and the capillary as a waveguide.

3.6.7. Laser Assisted gluing of the capillary

In a first test, the coupling efficiency of the UV light was measured after the capillary (ID = 40µm, OD = 105µm, polyimide thickness = 12µm) with a length of 30 cm. Unfortunately, the intensity was too low and was not noticeable through the noise and thus the efficiency was less than 0.3% since the laser emitted a beam with a power of 300 mW. However, it could be seen visually that the capillary emitted yellow-orange light probably due to fluorescence effects of the polyimide. This effect was the strongest close to the collimator lens, which was

expected given the non-ideal waveguide characteristics of the capillary. The effect was stronger when bending the fiber and the light lost a lot of its intensity in the polyimide coating due to its similar refractive index with fused silica. It was also possible to see the UV-light exiting the cleaved end using a camera, as shown in Figure 3.26.

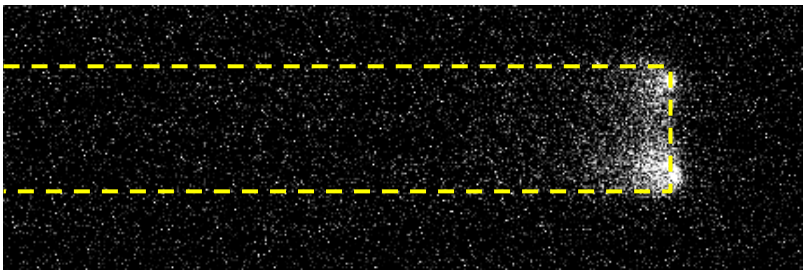

Figure 3.26. Laser light coupled into the capillary (indicated by yellow dashed line). After adding intensity and contrast to the image, the curing light exiting the capillary inside the chip can be seen due to scattering at the cleaved end of the capillary.

Figure 3.27 depicts the laser assisted method using the setup proposed in Figure 3.25D. It can be clearly seen that the front of the capillary flow stops when reaching the cleaved end due to the presence of the UV-light at the cleaved end where the glue is cured and the capillary flow stops. After 5min the shape of the front did not change anymore and the laser was turned off. Another 30min passed by without curing the rest of the glue in order to check if this front was actually cured, and as there could not be found any difference in the shape of the front, it was concluded that it was frozen at the end of the capillary. After this the rest of the glue surrounding the capillary was cured using a handheld UV-curing lamp and was put under another UV-lamp for 1h. A flow test was performed to check if the channel was blocked which was not the case.

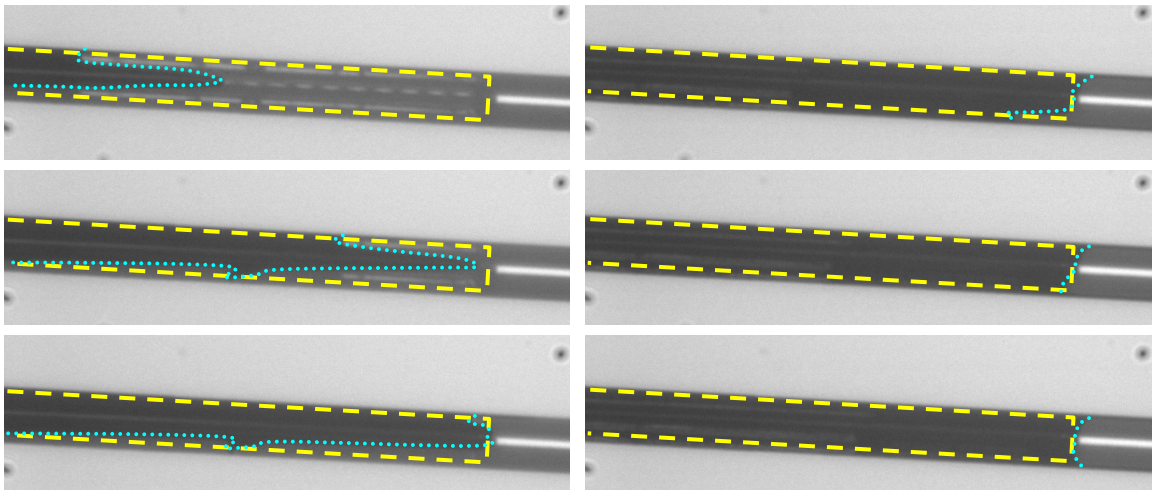

Figure 3.27. Laser assisted gluing of the capillary. The dashed lines highlight the capillary and the dotted line represents the front of the capillary flow of the glue. The UV-light exiting the capillary cures the glue and prevents the capillary flow to continue.

References

[1] "http://www.utwente.nl/mesaplus/nanolab/equipment/," **n.d.**

[2] "http://mesaplusnanolab.ewi.utwente.nl/MICMEC/tts/viewdatabase/findequipment," **n.d.**

[3] D. Clicq, R. W. Tjerkstra, J. G. E. Gardeniers, A. Van den Berg, G. V Baron, G. Desmet, *Journal of chromatography A* **2004**, *1032*, 185–191.

[4] L. Canham, *Properties of Porous Silicon, Emisdata Reviews Series, V. 18*, INSPEC Publication, London, **1997**.

[5] F. Detobel, V. Fekete, W. De Malsche, S. De Bruyne, H. Gardeniers, G. Desmet, *Analytical and Bioanalytical Chemistry* **2009**, *394*, 399–411.

[6] F. Detobel, H. Eghbali, S. De Bruyne, H. Terryn, H. Gardeniers, G. Desmet, *Journal of chromatography. A* **2009**, *1216*, 7360–7367.

[7] F. Detobel, S. De Bruyne, J. Vangelooven, W. De Malsche, T. Aerts, H. Terryn, H. Gardeniers, S. Eeltink, G. Desmet, *Analytical Chemistry* **2010**, *82*, 7208–7217.

[8] N. H. Bings, C. Wang, C. D. Skinner, C. L. Colyer, P. Thibault, D. J. Harrison, *Analytical chemistry* **1999**, *71*, 3292–3296.

[9] B. L. Gray, D. Jaeggi, N. J. Mourlas, B. P. Van Drieenhuizen, K. R. Williams, N. I. Maluf, G. T. A. Kovacs, *Sensors and Actuators A: Physical* **1999**, *77*, 57–65.

[10] H. Chen, D. Acharya, A. Gajraj, J.-C. Meiners, *Analytical Chemistry* **2003**, *75*, 5287–5291.

[11] A. Puntambekar, C. H. Ahn, *Journal of Micromechanics and Microengineering* **2001**, *12*, 35.

[12] A. V Pattekar, M. V Kothare, *Journal of Micromechanics and Microengineering* **2003**, *13*, 337.

[13] R. M. Tiggelaar, F. Benito-López, D. C. Hermes, H. Rathgen, R. J. M. Egberink, F. G. Mugele, D. N. Reinhoudt, A. van den Berg, W. Verboom, H. J. G. E. Gardeniers, *Chemical Engineering Journal* **2007**, *131*, 163–170.

[14] H. Yin, K. Killeen, *Journal of separation science* **2007**, *30*, 1427–1434.

Chapter 4

Optical assisted methods to study radial dispersion effects in 2D-micro pillar arrays

Abstract

With its ability to wipe out local radial velocity differences, radial dispersion is a key parameter controlling the band broadening in liquid chromatography. In principle, if radial dispersion would be infinitely strong, the A- and C-term contributions in the so called Van Deemter band broadening equation, would be completely absent. Unfortunately, the radial dispersion in packed columns is rather weak, hence the band broadening phenomena that occur in liquid chromatography. In order to investigate these fundamental effects, a novel experimental approach has been conceived using an uncaging fluorescent dye to inject very locally tracers, and monitor subsequent dispersion. These injections can be performed continuously or discretely in time, allowing monitoring of radial and axial dispersion for any Peclet-number.

4.1. Introduction

The earliest experiments, in which dispersion was recognized, were carried out in 1905 by Slichter in the field of hydrology. He created a technique of salting an upstream well and record its appearance downstream and concluded that dispersion rather than diffusion was responsible for the distribution of the solute [1]. Although he did not use the term "dispersion" the phenomenon was recognized by him. In 1953, Taylor [2,3] analyzed and modeled solute transport and its dispersion in capillary tubes. Due to the shear flow, the concentration distribution of solute tends to smear out in the direction of the flow increasing the effective diffusivity and called this mechanism "Taylor dispersion". Since then, a great deal of work has been done on the transport mechanisms of solute in porous media [4,5] in which axial and transverse (or radial) diffusion are being recognized [6–11]. Experimentally, the focus has been mostly on longitudinal rather than on transverse dispersion due to the difficulty of obtaining information about the transverse dispersion mechanisms [12]. This is mainly due to the difficulty of obtaining experimental dispersion information "inside" packed beds, which is hindered by several factors. First of all most columns have a non-transparent stainless steel shell to contain the particles. Secondly, even if the column shell is made from glass, the silica particles inside the column will render it opaque due to the many silica/mobile phase interfaces with non-matching refractive indices scattering the light. As a consequence, early experiments attempting to characterize dispersion phenomena have been carried out post column. Therefore, obtaining accurate information about the transverse (and even axial) dispersion effects is limited because the extra-column effects are influenced by sample injection and detection procedures but also by the geometries of inlet and outlet frits [13–17].

Knox et al. [18] circumvented this partially by using polarographic detectors right after the column exit frit which allows monitoring the radial diffusion of a centrally injected compound by detecting locally at different radial positions at the column exit. Baur et al. [16,19] refined this method by using carbon nanofiber micro electrodes as electrochemical detectors which are incorporated inside the column exit. Later on this method was adapted by Farkas et al. [20] who also used gold electrodes instead of carbon nanofibers. They also expanded this technique by using optical fibers and fluorophores as analytes so that more detectors could be incorporated in the frit and therefore more information about the radial dispersion could be obtained simultaneously [21]. As a result, this reduced the effect of the variation in retention

and peak shape which always differs in different runs, even when special care has been taken to keep them as constant as possible.

A less "invasive" method was developed in the same group by Tallarek et al. [22,23] who used NMR to visualize the dispersion effects inside the column. As tracer, the gadolinium ion (Gd^{3+}) was used which can form different chelate complexes that can be separated by chromatography. Another advantage was that Gd^{3+} reduces the relaxation time of nearby protons considerably and thus the Gd^{3+} complexes could be visualized indirectly by the relaxation time differences of nearby mobile phase protons so that the ^{1}H NMR signal could be used. Also their response factors are the same in the different complexes, allowing direct use of relative response as a measure for concentration.

A method to look inside the column without the need for NMR equipment was devised by Shalliker et al. [14,15,24] who rendered the opaque column transparent by choosing chloroform as mobile phase which has an identical refractive index as the silica particles. By placing the column in a glass rectangular vessel filled with chloroform, the cylindrical lens effect of the column was avoided and the three dimensional profile of the tracer was registered by two reflex cameras placed perpendicular with each other and with the faces of the glass vessel. Iodine was used as a tracer and was clearly observed by the reflex cameras equipped with optical filters when UV light was used as illumination source. The photographic image was subsequently digitally scanned and analyzed.

A different method for obtaining transverse dispersion information inside packed columns was devised by Coelho and Guedes de Carvahlo [25]. After solving the mass balance equation for the mass transfer from a buried flat wall aligned with the flow, it was concluded that the rate of dissolution of the solid slab may be used to determine the coefficient of transverse dispersion and an experimental setup, in which a dissolving cylinder of benzoic acid was buried in a packed bed, was used to obtain transverse dispersion coefficients. Delgado [26] refined the technique by using 2-naphtol as the dissolving cylinder to increase the temperature range over which experiments could be done. Due to this, the Schmidt number could be varied over a broader range and its influence on the transverse dispersion could be investigated.

4.2. Discussion and novel setup

The methods depicted in §4.1 -excluding the NMR method of Tallarek [22,23] and the one devised by Coelho and Guedes de Carvahlo [25,26]- all had the big drawback that it was required to inject a tracer inside the bed. This not only altered the flow lines near the injection point, but also, and more importantly, the mass balances inside the packed bed before and after the injection point. This approach has proven its success in obtaining qualitative data in terms of the radial dispersion behavior due to non-uniformities (wall regions, blocked frits, etc.) The acquisition of data for very local measurements near the injection point was however impossible due to the disturbed flow regime near the injection point. Coelho and Guedes de Carvahlo's set-ups [25] circumvented these problems, but the used setup was not able to visualize dispersion of the bands inside the column, despite having a great potential to acquire quantitative data about the transverse dispersion process.

In an approach to fundamentally circumvent these problems, a design has been made that replaces the tracer injection by an optically assisted injection using a caged fluorophore or uncaging dye. The unique characteristic of an uncaging dye is that it becomes fluorescent after activation. This is achieved by illuminating the dye with light of the proper wavelength. Due to this ability and the usage of optics, it is possible to create small illumination spots at any location inside a flat-rectangular 2D micro-pillar array, hereby "injecting" tracer by activating the uncaging dye which becomes fluorescent. In this approach, the mass balances are not altered over the channel and there also is no need to make a connection between the sample reservoir and the injection point.

In the past, two designs have already been proposed in our group based on the uncaging dye principle, but all of these lack the possibility to change the shape or size of the injection band. They also lack the ability to look further down the channel without moving the injection zone while doing a continuous injection [27,28] which is absolutely necessary in the present application. In a first design [27], this was due to the fact that the activation and excitation light go through the same objective and the injection zone will always stay at the same place relative to the image window, which implies that it is impossible to look further downstream without moving the injection zone when performing a continuous injection. In a second design [28] the activation light went through an on-chip optical slit, which means that the spot size and shape is defined by this irreplaceable slit.

To circumvent these restrictions, a new setup was built in which two separate objectives were used for activating and exciting the tracer (see Figure 4.1). These objectives have to be at opposite sides of the channels because else the activated tracer cannot be excited and visualized near the injection (or activation) zone. On the one hand, this is an advantage because it allows manipulation of the injection and detection window independently from each other (e.g. allowing changing the spot size for activation, but also the magnification for excitation and visualization of the uncaged fluorescent tracer). It also permits the usage of a commercially available microscope which is always superior to a home-built microscope in terms of homogeneity and intensity of the excitation field, and its transfer to the camera. On the other hand, it also implies that channels with transparent top and bottom walls are needed.

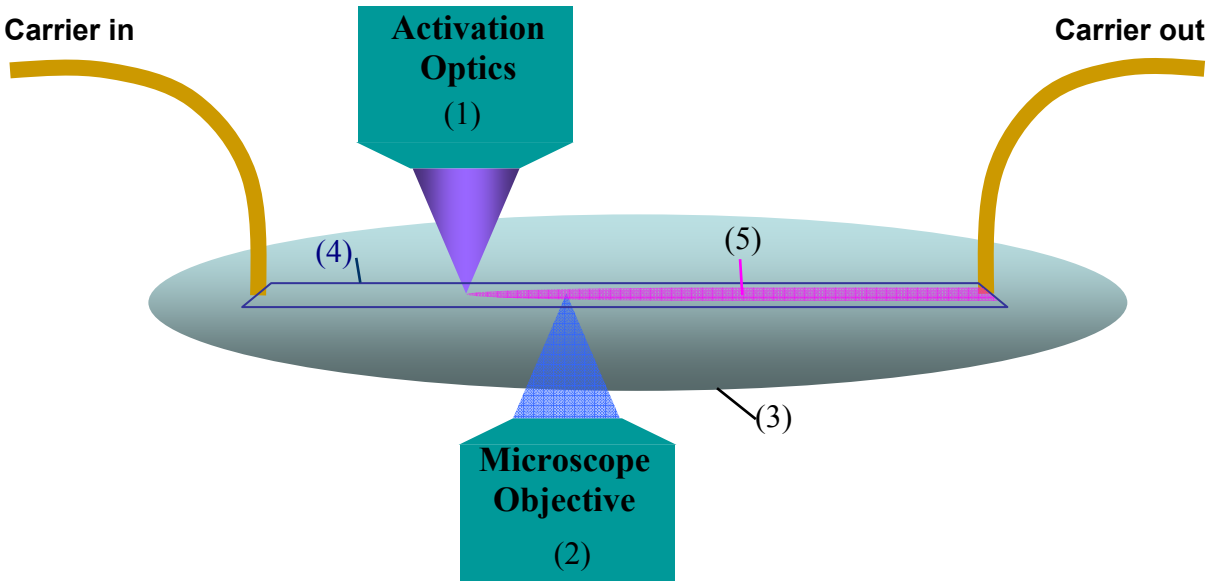

Figure 4.1. Conceptual design of the new optical setup, showing the activation **(1)** and visualization **(2)** optics, the microfluidic chip **(3)** containing the channel **(4)** and the established dye pattern **(5)**. The transparent channels allow activation of the uncaging dye from the top and visualization through the bottom.

As a consequence, fused silica was chosen as substrate material to manufacture the pillar channels because these well known transparent materials can be etched anisotropically easily with the equipment available at the MESA$^+$ NanoLab. This implies, for example, that the silicon pillar columns described by De Malsche et al. [29] cannot be tested on this setup.

4.3. Materials & Methods

4.3.1. Uncaging Dye

The uncaging dye used in the present study was *Fluorescein bis-(5-**c**arboxy**m**ethoxy-2-**n**itro**b**enzyl)-ether* or shortly CMNB-caged fluorescein. The fluorescence of the fluorescein is normally prohibited by the two aromatic side groups. The fluorescein can be released by illuminating this molecule with UV-light ($\lambda \approx 350$ nm), the so called "photo-activation". After the release of the fluorescein, it can be excited by using blue light ($\lambda \approx 470$ nm) and will emit green light ($\lambda \approx 525$ nm).

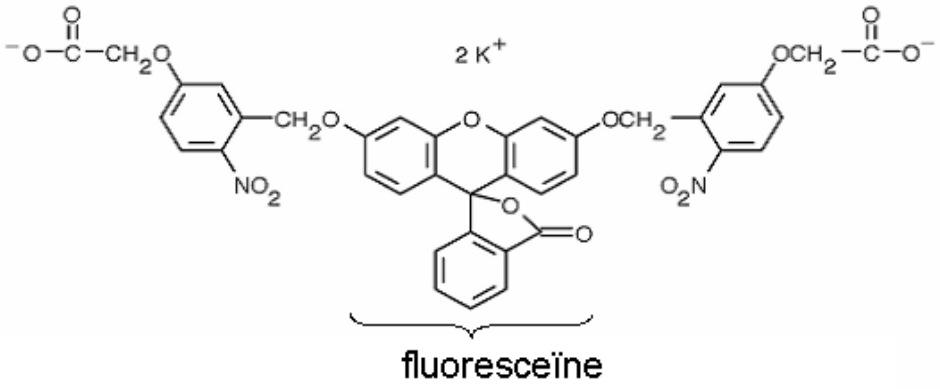

Figure 4.2. CMNB-caged fluorescein

The uncaging dye solutions were always made starting from small volumes (ca. 10ml) with a concentration of 1mM by dissolving CMNB-caged fluorescein (Invitrogen™, CA, USA) in water. These concentrated solutions were filtered (Chromafil® Xtra, PTFE-20/25, 0.20µm, Machery-Nagel, Germany) and used as a "stock solution" which were subsequently mixed with different solvents like glycerol when a different viscosity was required. Subsequently, these solutions were filtered a second time to remove particles originating from the other solvents. The reason the solutions were made starting from an aqueous standard and subsequently mixed was that the CMNB-caged fluorescein dissolved a lot slower in viscous solvents such as glycerol and these also could not be filtered using the standard laboratory equipment due to the high flow resistance of the viscous solvents through the micro-pores of the filter.

After preparation and during the experiments, the solutions were always kept away from light sources to avoid dissociation of the CMNB caged fluorescein and release of the fluorescein. When the solutions were not used over longer periods of time, these were kept in the freezer at -18°C to reduce the dissociation.

4.3.2. Optical Set-up

A state-of-the-art epi-fluorescence microscope (Olympus IX71) equipped with a mercury vapour lamp and a camera, was used for visualization of the fluorescence signal. The employed filter setup consists of the typical combination of an excitation (D460/50x, AF Analysentechnik, Germany) and emission (HQ 525/50m, AF Analysentechnik, Germany) filter in conjunction with a dichroic mirror (500dxcru, AF Analysentechnik, Germany) and is placed in a filter cube inside the microscope. The visualization and detection of the fluorescence signal of the released fluorescein was done by using a CCD-camera (Hamamatsu digital CCD-camera C4742-95).

For the activation of the dye, an argon laser (Coherent Innova 90-6 Argon Ion Laser) was used. In its standard use, this laser has 10 different wavelengths in the spectrum between 454.4 nm and 528.7 nm. By replacing the prism in the laser cavity, wavelengths from the UV-spectrum (334 nm; 351.1 nm; 351.4 nm en 363.8 nm) can also be reached. The line of λ = 351.4 nm possesses the highest intensity and was used for the experiments.

The light exciting the laser was coupled into a multi mode optical fibre (QMJ-33-UVVIS-400/440-3-2, OZ Optics) using a laser coupler (HPUC-23-330-M-10BQ-1, OZ Optics) and was led to the collimation lens (HPUC-23-330-M-10BQ, OZ Optics) of a home built optical setup on top of the microscope table. Inside this home-built setup, the collimated light was directed to a holder for a pinhole or slit and a diaphragm and the light was focused in the channel using a lens (f=75mm, LA4725, Thorlabs, Applied Laser Technology, The Netherlands) and an objective. The final shape of the activation zone inside the channel could be altered by changing the shape of the pinhole or slit and its size can be manipulated by using a different objective or changing the size of the pinhole or slit. The used pinholes and slits were both from the Thorlabs series and the OZ optics series. The used objectives for 5x, 10x and 20x magnification were respectively LMU-5x-266, LMU-10x-266 and LMU-20x-266 from OFR (Applied Laser Technology, The Netherlands) and for 40x magnification, Achrostigmat 40x/0,55 from Zeiss (Carl Zeiss NV-SA, Belgium) was used. It is important to note that the 5X and 20X objectives were in duplicate so these identical objectives could be used for activation and visualization. A schematical overview of the employed set-up is shown in Figure 4.3.

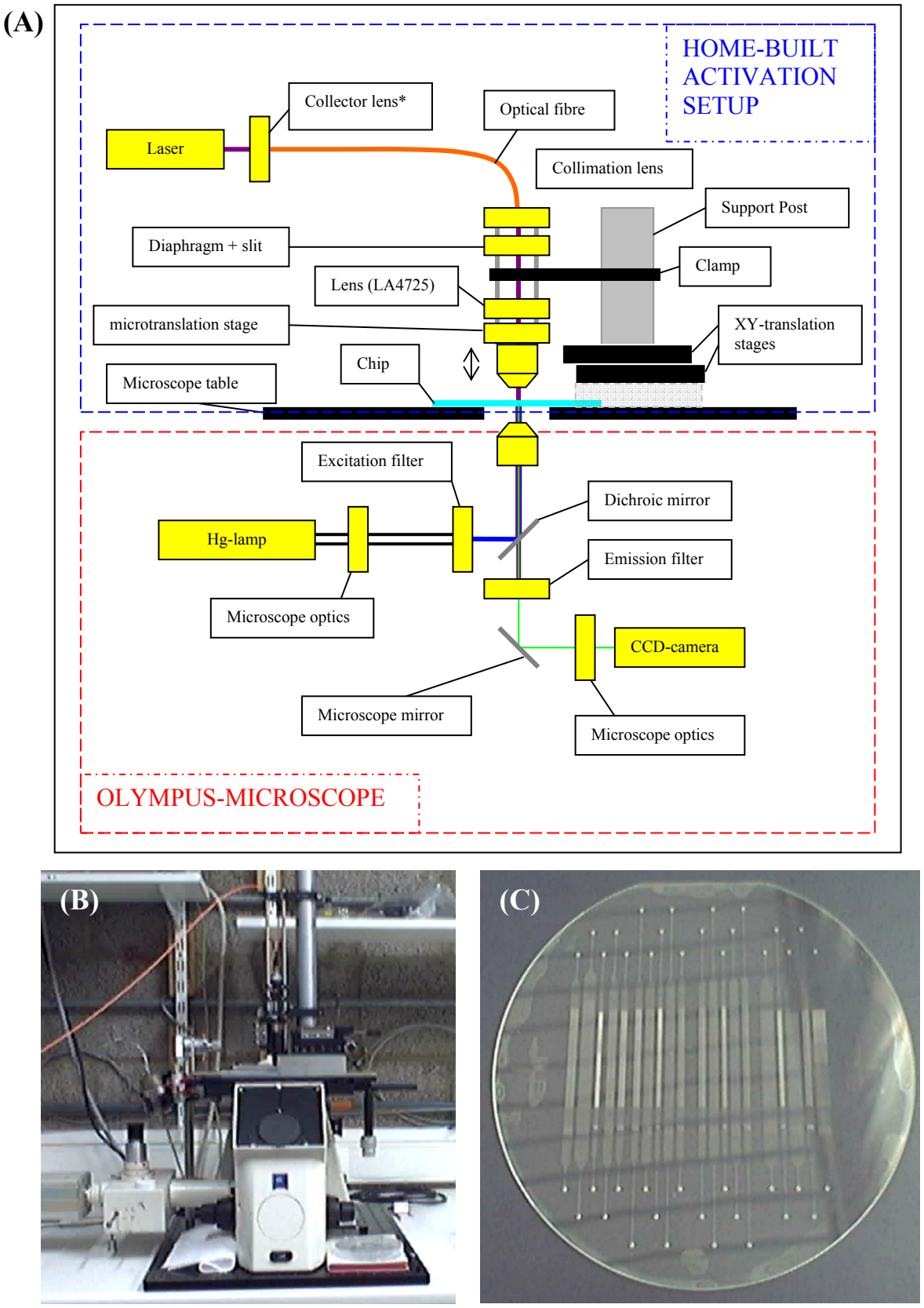

Figure 4.3. (A) Schematical overview of the setup used for radial dispersion measurements. The upper part (home-built activation setup) is used for activation. Detection and visualization is done with a commercially available microscope in combination with a CCD-camera. **(B)** Photograph of the set-up in the lab. **(C)** Photograph of the used fused silica-chip containing the 2D-structured micro-pillar channels.

4.3.3. Activation and Detection Settings

In subsequent paragraphs, the settings of the activation laser and the CCD-camera during the experiments are being described. When fine-tuning the setup according to the various experiments, some general principles should be kept in mind.

1. The activation of the caged fluorescein can be treated as a reaction of 0^{th} order since the amount of released fluorescein is proportional with the duration of photolysis [30].
2. The reaction rate constant only depends on the intensity of activation light.
3. The maximum intensity that can be obtained is limited by the concentration of the uncaging dye in the solution.
4. Increasing the activation intensity will result in a decrease of the activation time needed to release the available uncaging dye in the solution.
5. Broader slits will result in broader peaks with more peak volume

Due to above mentioned reasons, it was chosen to start with a concentrated CMNB-FITC solution in combination with the activation light put at maximum since these will increase the likelihood to obtain a sharp signal with a good signal-noise ratio with very short activation time intervals. It is important to keep the required activation time at a minimum since this will also minimize the dispersion during activation which results in sharper peaks. If more peak volume is required for the experiment, a broader slit or pinhole can be used at the expense of less narrow peaks.

When adjusting the camera accordingly, some important notes should be made which will affect the analysis of the experiments.

1. The observed intensity on the CCD-camera of the released dye is linear with the concentration if there is no intensity or contrast added by the camera software and the camera should be used this way when peak shape data is wanted.
2. Fluorescein is susceptible to photo bleaching and will loose intensity when excited over longer periods of time.
3. For non-steady-state experiments, the maximal frame rate of the camera should be used since more data can be acquired in the same time frame.

4.3.4. Velocity experiments

To make accurate measurements of the fluid velocities, a very narrow band with a high peak intensity needs to be injected and should be measured over a large distance while traversing the pillar bed. In order to achieve this, a lower magnification objective (5X) was used for detection to have the widest distance available (ca.1800µm) and the frame rate of the camera was maximized (52fps with a capture time of 18.7 ms) to obtain a larger number of data points of the peak traversing the pillar bed. For the activation, the shutter times were kept as short as possible (50-60ms) to minimize band broadening while injecting. Brightness and contrast settings of the camera were adjusted to make the peaks clearly visible. This approach is justified since the aim of the velocity experiment is not to obtain peak shape data (2^{nd} order), but peak position data (1^{st} order). When the peaks could not be clearly visualized on the camera due to bad signal/noise-ratio, a larger peak volume was added by using a broader slit and the brightness and contrast settings were adjusted again. In the extreme case of a high velocity and a high Peclet number, a slit of 200 µm in combination with a 20x objective was used. In the other extreme of having a very low velocity and a low Peclet number, a slit of 20 µm wide was used in combination with a 20x objective resulting in a 1 µm wide activation area. A disadvantage of using the 20x objective is that the peaks are injected locally and not over the whole width of the channel compared to the 5x objective. It was however not possible to meet previous requirements when using the 5x objective since the intensity of activation light was not sufficient to obtain sharp peaks with enough peak volume especially for higher velocities. For low velocities, peaks as wide as the channel could be achieved by rapidly moving the activation optics over the channel while keeping the shutter open.

4.3.4.1. Molecular Diffusion Experiments

To make accurate measurements of the molecular diffusion coefficient, a very narrow peak needs to be injected and should be measured over a long period of time over a large area while it broadens due to diffusion. The camera and activation settings for measuring fluids with a high viscosity were similar to those applied when measuring fluids with a low viscosity. For activation, usually a 50 µm slit was used in combination with a 20x objective and the activation optics were moved rapidly over the channel.

The capture time of the CCD camera was increased so that the peak maximum did not exceed the saturation levels. There was no need to measure at the highest frame rate and the capture times could be increased since the dispersion effects were rather slow (especially for the more

viscous solutions) and the capture times were still negligible compared to the length of the experiment. The use of smaller slits resulted in narrower peaks without sufficient peak volume making them disappear quite fast in the background so that the peak area dropped rapidly over time.

A 5x objective was used for detection so that the band broadening could be measured over a longer distance and time period. Higher magnifications could have been used for detection, but would have made it necessary to measure the diffusion in a shorter time interval since the peak width would have exceeded the detection window much faster. The acquisition of data points was done in a discrete manner to minimize the effects of photobleaching. This was done by blocking the excitation light of the microscope and opening it shortly at precise time intervals. It is also important to note that the peak volume will always decrease towards the end of a diffusion experiment. This is mainly due to photobleaching, which can be minimized, but is anyhow always present. In addition, the signal/noise ratio also inevitably decreases towards the end of an experiment, hence loosing some extra peak area in the noise.

4.3.4.2. Radial Diffusion Experiments

To make accurate measurements of radial diffusion coefficients, a very small continuous point injection needs to be made and the broadening of the plume should be measured over a large distance. A major difference between the experiments needed to determine the radial diffusion coefficient compared to the previously described ones, is that these happened in a steady state regime which removed the necessity to measure in function of time. This means that photobleaching was avoided by keeping the excitation light blocked during the experiment and the dispersion plume was only measured shortly after opening the shutter.

The measurements of radial diffusion coefficients in the range of low Peclet numbers area have been done using a 50µm pinhole in combination with a 20x objective for activation. In this range, the increase in plume width could also be measured in the same image as the injection point since the plume disperses quite rapidly while traversing the channel. Because of the latter, the peak width near injection point is negligible compared to the peak width of the plume exiting the image using a 5x objective.

In the higher Peclet number range, it is required to take more images over a longer distance since the plume disperses very slowly while traversing the channel and the differences in peak width would be too low to be valuable for analysis when measuring the plume width in only

one image. In the very high Peclet range, the detection was therefore also done using a 10x objective to obtain more peak data since the peaks remained very narrow after leaving the pillar bed.

4.3.4.3. Discrete point injection

When using small pinholes in combination with a high magnification objective for activation, it was possible to create spot sizes smaller than the inter pillar distance inside the pillar bed, and thus it was possible to inject locally between the pillars. When using a higher magnification objective for detection, it was possible to monitor the subsequent flow behavior of these injections. Since the interest of these experiments is rather visualization and due to the high magnifications and the non-steady-state regime, the camera settings had to be adjusted to the maximum frame rate in order to acquire enough images before the peak leaves the image window of the CCD-camera. The advantage of the higher magnification objective for detection, is that it also increases the intensity of excitation light on the region of interest and thus the injected peaks could be monitored with lower capture times resulting in a higher frame rate without added intensity. However, this effect was not pronounced enough and intensity still had to be added when switching to maximum frame rate. Combining this with the increased effect of photobleaching due to the increased intensity of the excitation light on the area of interest, the data acquired in this way is not optimal for quantitative analysis.

4.3.5. Mask Layout and Fabrication

A mask design containing a large number of different channels with varying pillar shapes and dimensions was made using Clewin (WieWeb software, The Netherlands).

Having the freedom of drawing the packed bed also implies having the freedom of putting the pillars in an ordered or in a disordered array and thus respectively eliminating or introducing eddy-dispersions in the packed bed at free will. A disordered array was made in which the pillars were made smaller or bigger and their center points were moved away from the original closed packed bed configuration without changing the porosity. The unit cell with random diameter and particle displacement distances for each individual particle was generated by using the evenly distributed random number generator of MS Excel®. The maximal variation of the particle size and displacement was taken as 10% of the mean particle size. After taking into account the modified particle size, the maximal shift of the particle centres was equal to 90% of the pore size. Since each particle displacement occurs

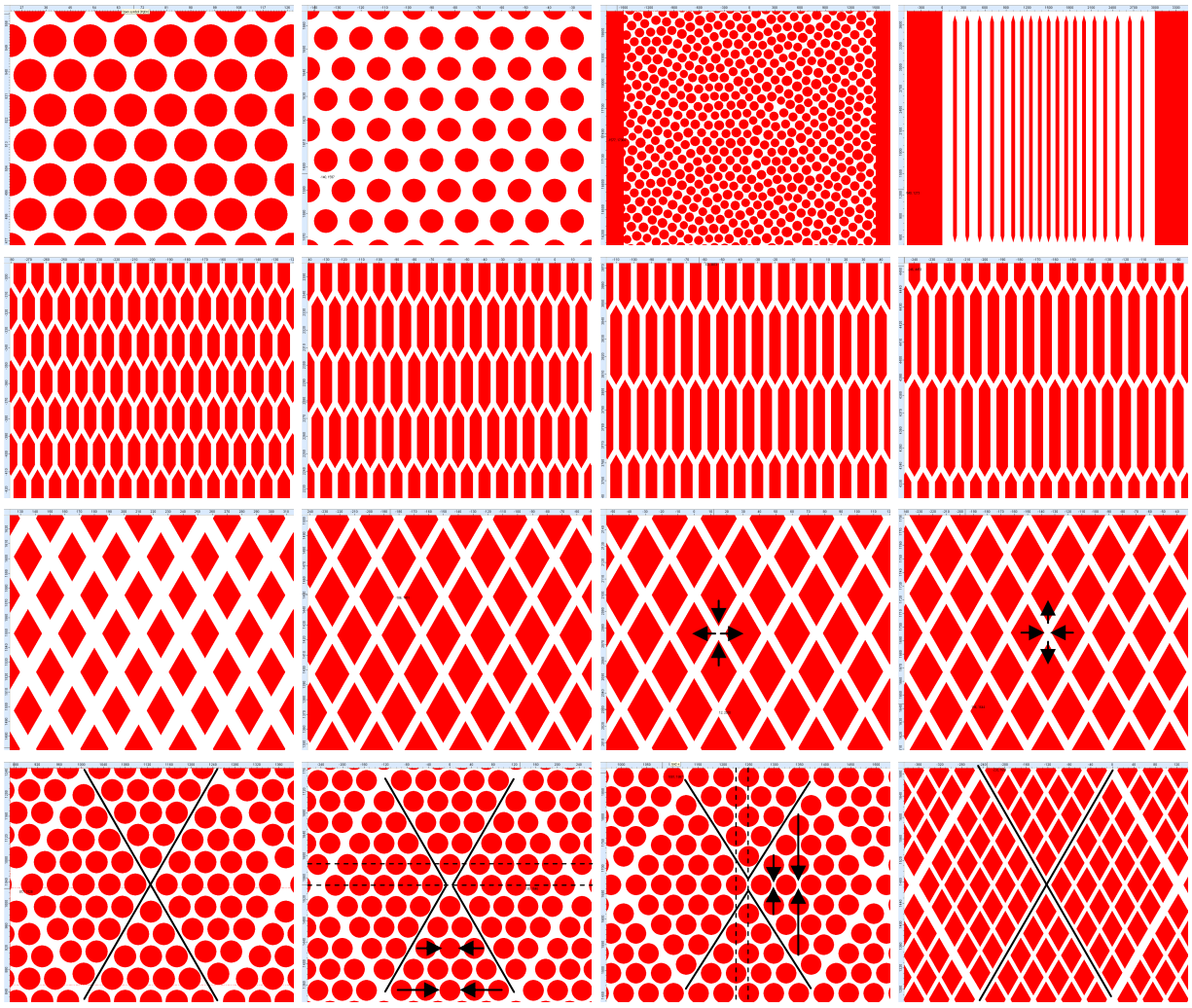

Figure 4.4. Various pillar designs and shapes found in the mask design.

independently of its neighboring particles, this results in a heterogeneous packing with only a short-scale randomness [31], as defined by Giddings [6]. The unit cell was developed by J. Billen and was used by me to draw the mask. This was done by converting the values of the unit cell in the MS Excel® worksheet to a C-format which was imported into Clewin. One channel on the mask was dedicated to a single disordered design. This channel had one disordered array conformation with different characteristic lengths replicated over the channel. This was done by putting the arrays with the same characteristic lengths in parallel channels, and these channels were put in series with the arrays with a different characteristic length (see Figure 4.5).

The pillar channels were obtained by bonding a processed wafer (see §3.4 for a detailed description of the manufacturing of these channels), containing half-open pillar channels with in- and outlets, with an unprocessed wafer and sealing the half-open pillar channels. The reason for using fused silica as substrate material was already explained in §4.2.

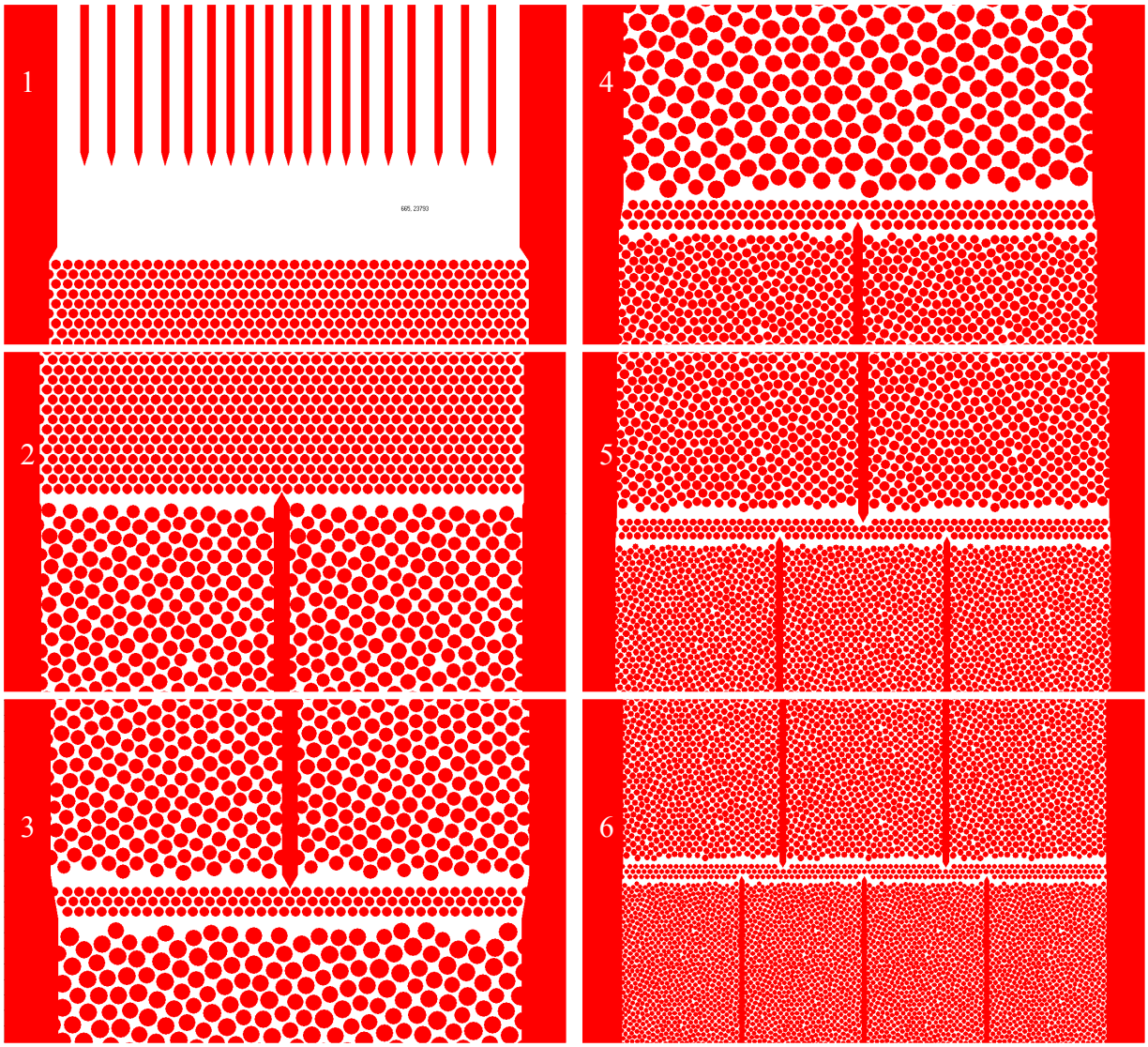

Figure 4.5. Mask drawing of the disordered channel. (1) parallel plates, (2)-(6) channels with the same characteristic length are in parallel and in series with channels with a different characteristic length.

4.3.6. Flow Control

The flow of fluid through the channels was controlled using low hysteresis pressure regulators (LRP-1/4-25 up to 2.5bar and LRP-1/4-10 up to 10bar, Festo NV, Belgium) and a home-built high-pressure vessel was used to transfer the pressure of the dry nitrogen to the liquid. Two valves in the gas line are used to depressurize the system without changing the value of the pressure regulator. No valves were used in the liquid line since the presence of extra connections increases the probability to form air bubbles and create leakages, which all increase the ramp up time to a stable flow inside the channels. In the first attempts to measure the fluid velocity, rotor-stator switching valves were used and peaks were injected locally at zero velocity. After switching the valves, it was immediately observed that the velocity was

not constant right after the switch and by the time the flow stabilized the peak was already broader than the image that could be acquired with the CCD-camera at lowest magnification. These disadvantages can be completely avoided by doing experiments in a constant flow. Since there was no real necessity to block the fluid stream, the valves were eliminated from the setup thus reducing the number of connections and potential cavities for bubbles to settle (see Figure 4.6).

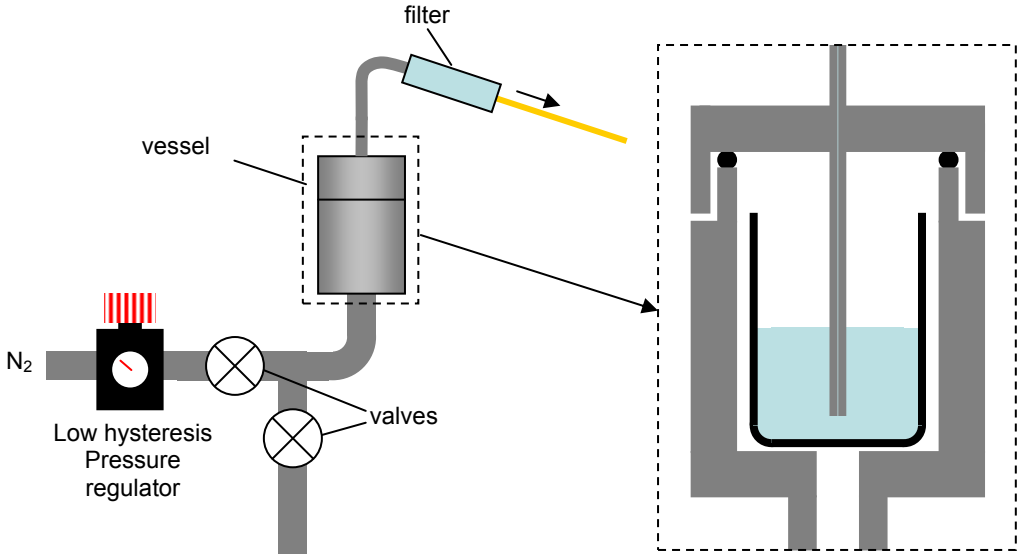

Figure 4.6. Home-built setup used for flow control. Inside the high pressure vessel, the pressure of the dry nitrogen is transferred to the fluid. The vessel can be vented without changing the pressure regulator with the use of the two valves in the gas line. The vessel is connected with the capillary with a filter in between to prevent particle contamination to the micro-channels.

Before starting a series of experiments in a new channel, a small beaker with demineralized filtered water was placed inside the vessel and the whole fluid line was flushed. When the channel was bubble free, the beaker inside the vessel was replaced with the CMNB-FITC-solution and put under pressure. It could be easily observed when the solution reached the channel by exposing the channel with the activation light.

4.4. Measurement of Fluid Velocities

Figure 4.7 shows a series of subsequent pictures recorded during a typical experiment used to measure the fluid velocities. Using the simple PCI software accompanying the CCD-camera, a rectangular region was selected and cut out. The values of the signals in this region were being averaged in the vertical direction yielding one row with averaged values for each time step.

A picture compilation was subsequently made wherein each row represents the averaged values of the selected region. The data from this compilation was then put into a numerical form and imported into Excel with the corresponding time steps. The conversion from pixels to distance was done after a calibration done by making images of structures with know distances. For example, the amount of pixels between two structures can be easily obtained after examining the image, whereas the actual metric distance can be readily found on the mask drawing.

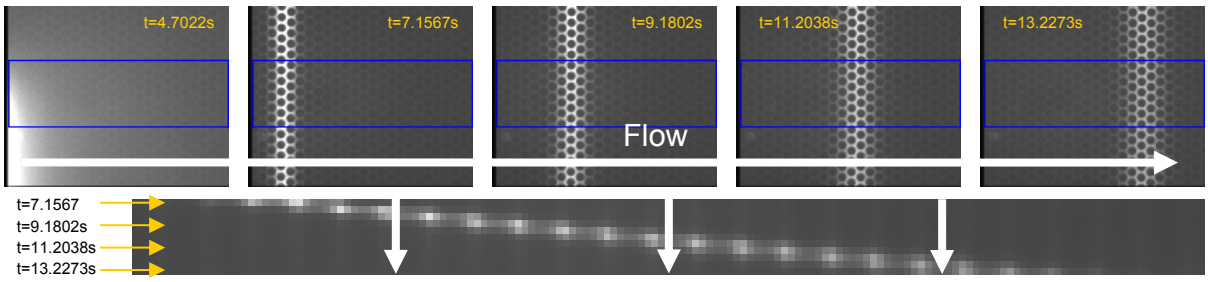

Figure 4.7. Image manipulation in Simple-PCI. The relevant images were selected and the intensity values in the blue omitted area were averaged in the vertical direction.

After collecting the data in Excel, this file was imported into OriginPro. The advantage of this package is that it has a function to fit a Gaussian curve with baseline off set through the collected data points of the peaks. Another advantage of this package is that it is also capable of performing several peak analyses in parallel which greatly reduce the analysis time for one velocity experiment. The acquired peak signals can be put in a graph with their corresponding fitted Gaussian peak and it can instantly be noted that the peak shapes are strongly disturbed by the presence of the pillars. However, the fitted peaks still give very good approximations of the average peak distances and their quality was sufficient to determine the velocity of the fluid inside the pillar bed (see Figures 4.8 and 4.9).

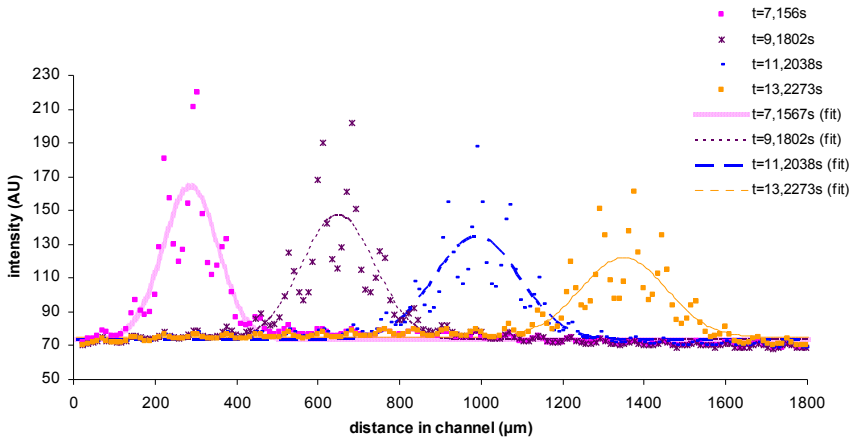

Figure 4.8. The peak signals of a velocity experiment in a packed bed with their corresponding fitted Gaussian curve. The peak is strongly influenced by the presence of pillars, but the peak fitting software could still fit a Gaussian curve and yield the mean values of the peak distances (± 6µm) .

After OriginPro returned the fitted values of the mean peak distances, these values were graphically represented as a function of their corresponding time. A straight line was subsequently fitted through the data points. The slope of this straight line equals the velocity.

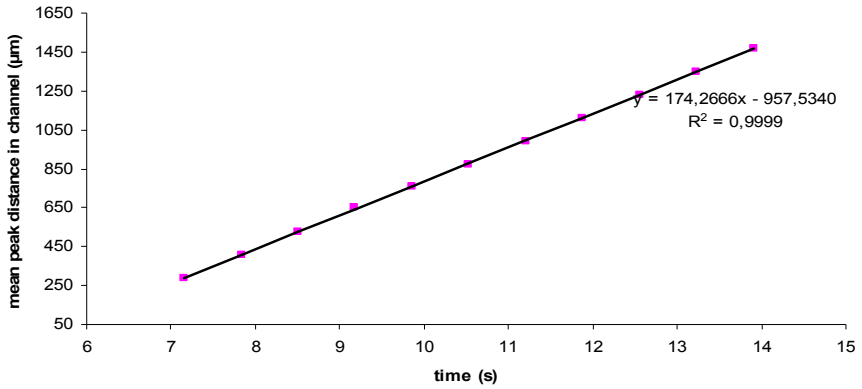

Figure 4.9. Plot of mean peak distance as a function of time. The slope represents the velocity.

At very high Peclet numbers (>1000), the dye could only be injected over a small region of the channel because the increased axial dispersion made it impossible to inject over the whole width of the channel by moving the activation optics. Injecting a small band in the middle (see Figure 4.10) has proven to be sufficient to have a good measurement of the velocity.

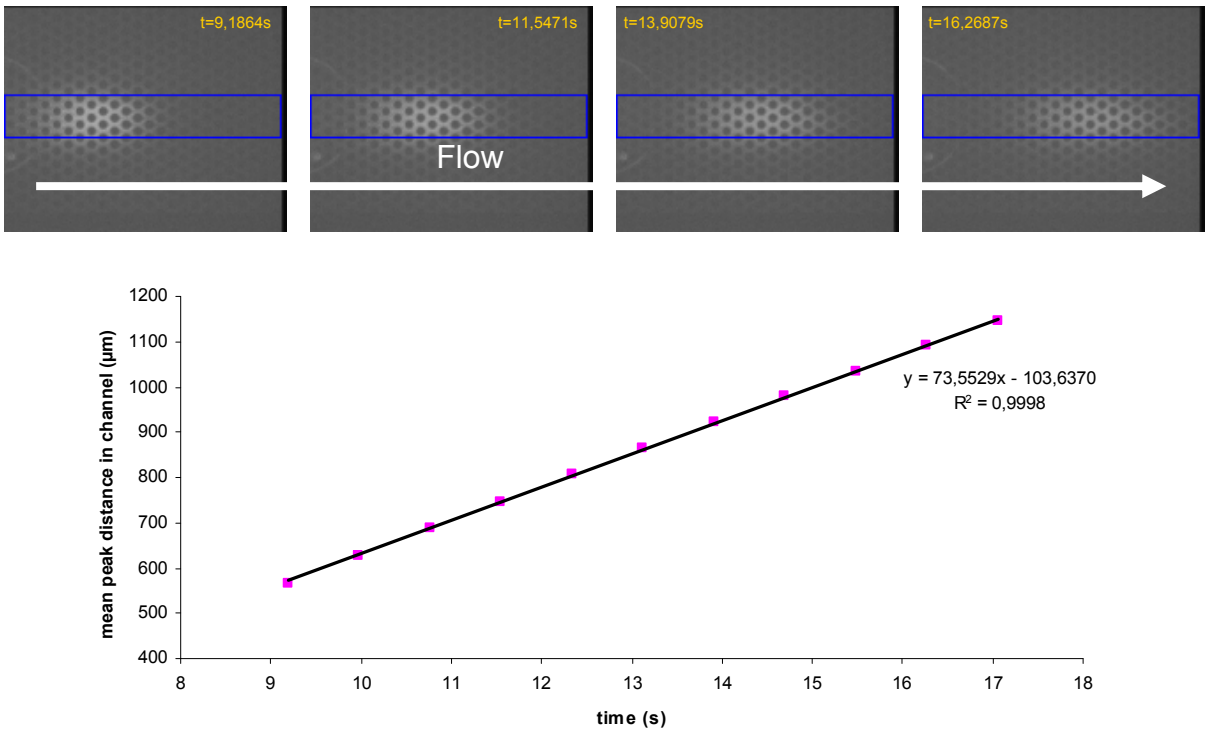

Figure 4.10. Example of a velocity experiment at very high Peclet. An injection could only be made locally in the middle of the channel

4.4.1. Measurement of Molecular Diffusion Coefficients

During previous experiments made in our group [32], it has always been noted that, the wider the channels are, the more difficult it is to inject peaks with a homogeneous width and intensity. To counter these problems, parallel plates were added at the end of the channels in the design to artificially reduce the channel width so that homogeneous bands can be made more easily. The walls of the parallel plates also have a mechanical function as a support connecting the upper and lower substrate of the chip, and preventing channel breakage when working at higher pressures.

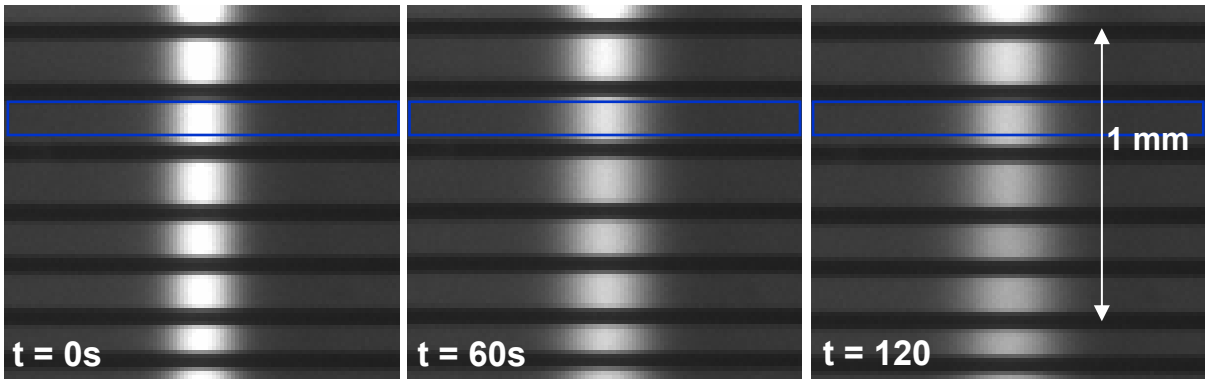

Figure 4.11. Diffusion measurement of uncaged fluorescein in 90vol% glycerol in water in 8 parallel lanes (D_{mol} = 1,72 ± 0,02) • 10-11 m²/s)

Similar to the velocity experiments, a region was selected and cut out (see Figure 4.11). The pixel intensity values in these regions were subsequently averaged in the vertical direction and a compilation was made of the collected data (see Figure 4.12). In this compilation, each row represents the averaged value for one time step. The numerical values with the appropriate time steps were subsequently imported into Excel and the diffusion profiles obtained after opening the excitation light were selected and imported into OriginPro for peak analysis.

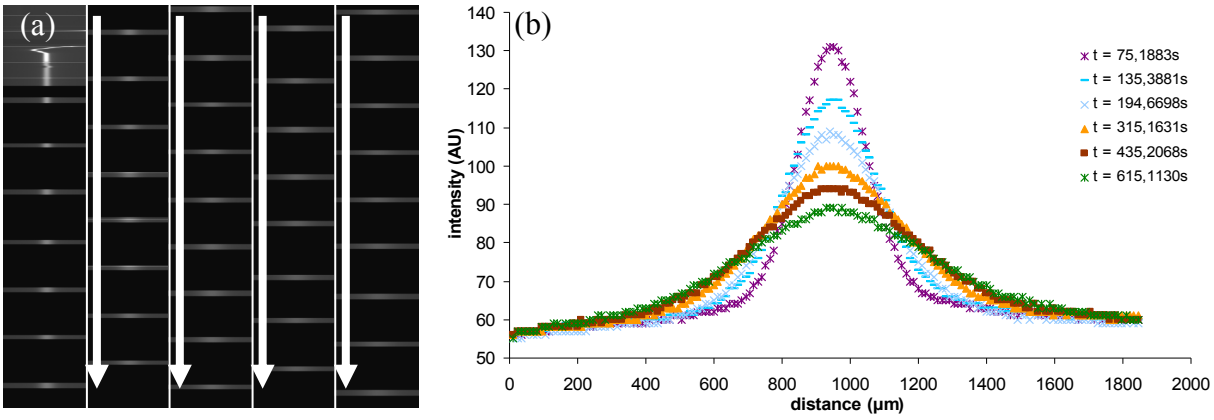

Figure 4.12. **(a)** Image compilation diffusion experiment. Data was only acquired at very short moments to avoid photobleaching and the excitation light was mostly blocked during the experiment. **(b)** Intensity profiles obtained during the diffusion experiment

After OriginPro returned the fitted parameter values for the peak widths, the peak variances were plotted as a function of their corresponding time in Excel. A straight line relationship was fitted through the data points and the slope of the line is equal to two times the value of the molecular diffusion coefficient [32].

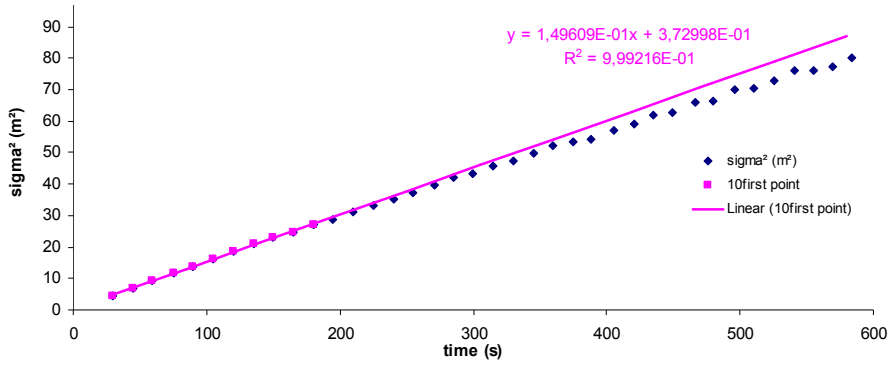

Figure 4.13. Peak broadening during a diffusion experiment. The relationship between variance and time is linear in the first points during the experiment, whereas the last points bend off due to the "disappearance" of peak volume by photobleaching and a decreasing signal-noise ratio.

As can be noted on the graph, the points bend off near the end of the experiment. This is due to the decreasing peak area, which can be seen after fitting in OriginPro as it also fits the peak area besides the other parameters. This behavior was unavoidable and is a consequence of photobleaching and the decreasing signal/noise ratio towards the end of the experiment. However, it can also be noted that the behavior is linear in the first part of the experiment and these data points were used for the quantification of the molecular diffusion coefficients.

In order to validate the set-up, the diffusion coefficient of uncaged fluorescein in water was measured, $D_{mol}=(3{,}90 \pm 0{,}05) \cdot 10^{-10}$ m²/s (@20°C). This value is in good agreement with the value ($D_{mol}=(4{,}15 \pm 0{,}05) \cdot 10^{-10}$ m²/s (@25°C)) found in the literature. It is also trivial to point out that obstructed diffusion coefficients can be gathered as well using this method in a packed bed.

4.4.2. Measurement of radial diffusion coefficients

For low Peclet numbers (<500), the intensity of the dispersing plume was measured immediately after leaving the pillar bed by using a monitor line so that the pillars did not interfere with the obtained profile. The capture time of the camera was increased until the intensity of the peak maximum was 80-90% of the saturation intensity of the camera. If the dispersing plume was too broad and exceeded the image boundaries, the laser spot was positioned closer to the monitor line, hence decreasing the time for the plume to disperse.

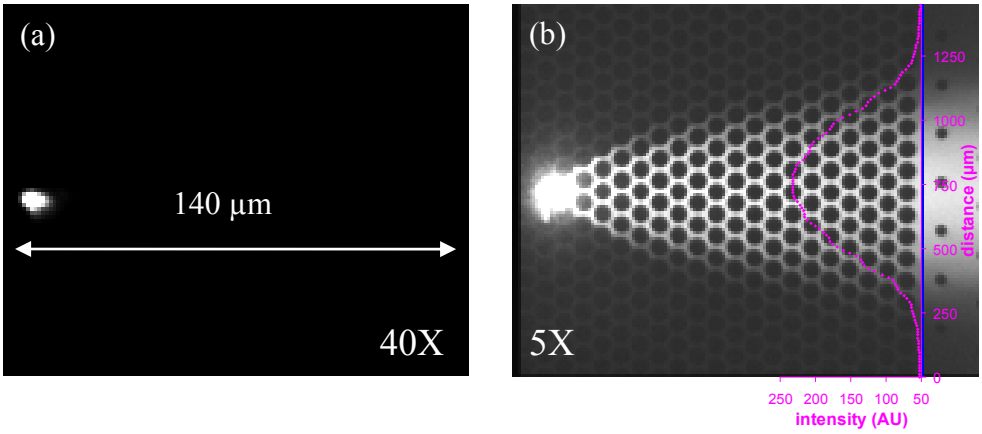

Figure 4.14. CCD-camera images of **(a)** the uncaging dye activation laser spot (excitation source switched off; 40X magnification) and **(b)** the resulting radially dispersed uncaging dye concentration profile (excitation light switched on; 5X magnification).

The laser spot gives saturated values at the injection point and appears wider due to reflections within the system and since the camera settings are adjusted to have a good signal/noise ratio at the monitor line. When using a higher magnification (40X) and lower capture times, the activation spot can be clearly seen and appears to be 5-6µm wide. At these very low values of Peclet, the initial width of the injection point is negligible compared to the peak width at the monitor line. For example, in Figure 4.14, the initial peak variance ($\sigma^2 = w^2/12$) is 0.05% of the peak variance measured at the monitor line when using the inter pillar distance (= 17µm) as the peak width of rectangular peak [33] which is an overestimation of the reality. Since these experiments occurred in steady state regime, the excitation light could be blocked before the actual measurement of the plume in order to minimize the effects of photobleaching. After exposing the plume to the excitation light, the first image acquired by the camera was taken for analysis. The numerical values at the monitor line were imported in Excel and subsequently in OriginPro as well for peak analysis.

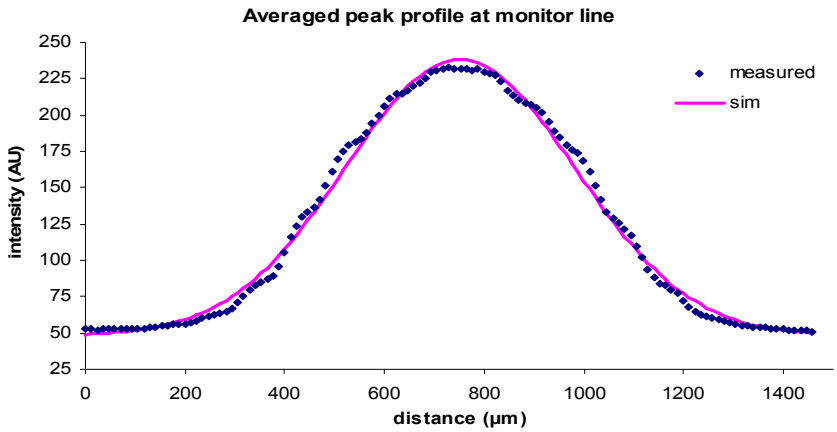

Figure 4.15. Intensity profile and the fitting by OriginPro at the monitor line in Figure 4.14.

The radial diffusion coefficient was derived from the variance of the plume at the monitor line and the dispersion time which was obtained by dividing the distance between the activation spot and monitor line by the velocity of the fluid. When performing these measurements, it is important to verify that the velocity stays constant since the dispersion of the plume and the related radial dispersion coefficients are dependent on the fluid velocity inside the pillar bed. This was verified by measuring the fluid velocity before and after one radial diffusion experiment so that "bad" measurements could be detected during analysis.

At high Peclet numbers (>500), the dispersion of the plume is much smaller in function of the length of the pillar bed, and thus the plume had to be characterized over a longer pillar bed. This was done by measuring the intensity of the plume before and after the pillar bed with known length. The monitor lines were put at regions where the pillars did not interfere with the obtained signals of the plume that was injected in the precedent pillar bed. A 10X objective had to be used for detection in order to acquire more data points per peak, since the plumes remained relatively narrow when traversing the pillar bed. The capture time of the camera was increased until the maximum intensity of the peak entering the pillar bed was at 80-90% of the saturation intensity of the camera (see Figure 4.16). This was possible with all the geometries that were tested except the 40% ordered one. This was due to a positional compatibility problem of the chip in the holder and the microscope objectives and it was impossible to position the objectives after the bed.

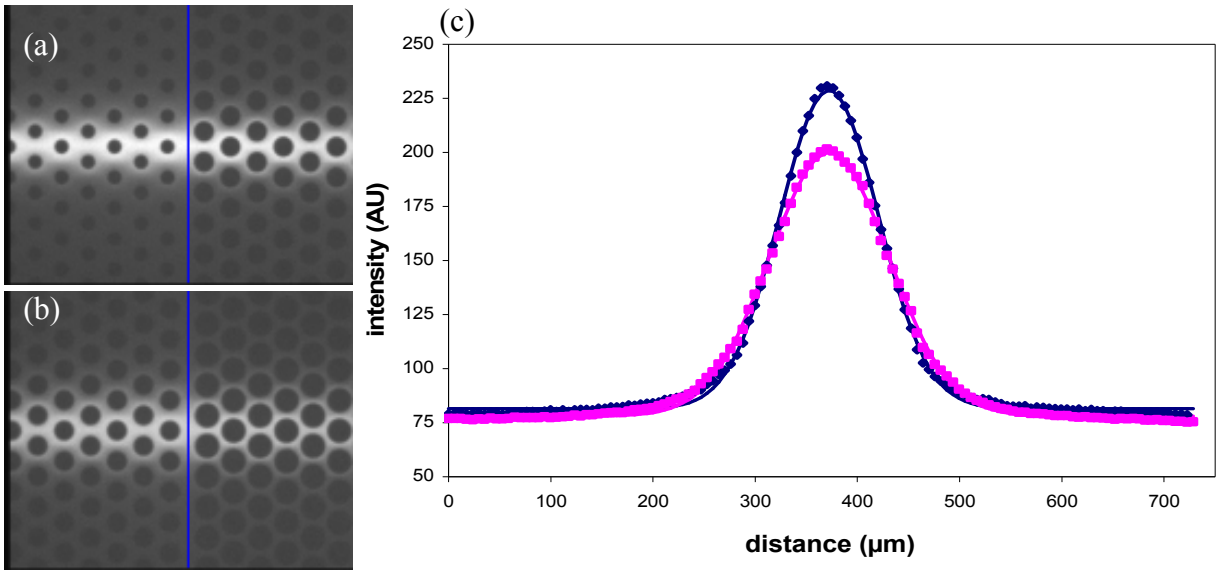

Figure 4.16. **(a)** Image of the plume entering the pillar bed with the monitor line. **(b)** Image of the plume exiting the pillar bed with monitor line. **(c)** The acquired intensity profiles at the monitor lines (◆ entrance (a), ■ exit (b)), the fitting was done with OriginPro (full lines).

4.5. Conclusions

A new and original set-up was built to make detailed measurements of the radial dispersion in 2D packed bed columns using an inverted microscope and a home-built optical injection system positioned on top of the microscope. The set-up enables optical "injections" (=local activation or uncaging of caged fluorophores) with a spatial resolution down to 5 μm. The set-up allows to measure fluid velocities with an accuracy of about 99% from low Pe to high Pe numbers. The actual radial dispersion coefficient values can be determined from the radial variance of the steady-state dispersion plume formed upon a continuous local "injection" of the fluorophore. The radial intensity cross-section of this fluorescent plume could be fitted with a Gauss distribution function with a $r^2 > 99\%$. Overall, the measurement accuracy of the D_{rad}-values was about 96% for the beds with 60% or 80% porosity.

References

[1] C. S. Slichter, *United States Geological Survey Water-Supply and Irrigation Paper* **1905**, *140*.

[2] G. Taylor, *Proceedings of the Royal Society of London. Series A. Mathematical and Physical Sciences* **1953**, *219*, 186–203.

[3] G. Taylor, *Proceedings of the Royal Society of London. Series A. Mathematical and Physical Sciences* **1954**, *223*, 446–468.

[4] J. Bear, *Dynamics of Fluids in Porous Media*, Dover Publications, **1988**.

[5] F. A. L. Dullien, *Porous Media: Fluid Transport and Pore Structure*, Academic Press San Diego, **1992**.

[6] J. C. Giddings, *Dynamics of Chromatography, Part I: Principles and Theory (Chromatographic Science Series, Vol. 1)*, Marcel Dekker, New York, **1965**.

[7] S. T. Sie, G. W. A. Rijnders, *Analytica Chimica Acta* **1967**, *38*, 3–16.

[8] D. J. Gunn, *Trans. Inst. Chem. Engrs* **1969**, *47*, 351–359.

[9] P. G. Saffman, *Journal of Fluid Mechanics* **1959**, *6*, 321–349.

[10] A. Eidsath, R. G. Carbonell, S. Whitaker, L. R. Herrmann, *Chemical Engineering Science* **1983**, *38*, 1803–1816.

[11] T. K. Sherwood, R. L. Pigford, C. R. Wilke, *Mass Transfer*, McGraw-Hill New York, **1975**.

[12] A. Scheidegger, *The Physics of Flow Through Porous Media*, University Of Toronto Press, Toronto, Buffalo [N.Y.], **1974**.

[13] T. Farkas, M. J. Sepaniak, G. Guiochon, *AIChE Journal* **1997**, *43*, 1964–1974.

[14] R. A. Shalliker, B. Scott Broyles, G. Guiochon, *Journal of Chromatography A* **2003**, *994*, 1–12.

[15] R. A. Shalliker, B. S. Broyles, G. Guiochon, *Journal of Chromatography A* **1998**, *826*, 1–13.

[16] J. E. Baur, E. W. Kristensen, R. M. Wightman, *Analytical Chemistry* **1988**, *60*, 2334–2338.

[17] J. A. Abia, J. Putnam, K. Mriziq, G. A. Guiochon, *Journal of Chromatography A* **2010**, *1217*, 1695–1700.

[18] J. H. Knox, G. R. Laird, P. A. Raven, *Journal of Chromatography A* **1976**, *122*, 129–145.

[19] J. E. Baur, R. M. Wightman, *Journal of Chromatography A* **1989**, *482*, 65–73.

[20] T. Farkas, J. Q. Chambers, G. Guiochon, *Journal of Chromatography A* **1994**, *679*, 231–245.

[21] T. Farkas, M. J. Sepaniak, G. Guiochon, *Journal of Chromatography A* **1996**, *740*, 169–181.

[22] U. Tallarek, E. Baumeister, K. Albert, E. Bayer, G. Guiochon, *Journal of Chromatography A* **1995**, *696*, 1–18.

[23] U. Tallarek, D. van Dusschoten, H. Van As, E. Bayer, G. Guiochon, *The Journal of Physical Chemistry B* **1998**, *102*, 3486–3497.

[24] R. A. Shalliker, B. S. Broyles, G. Guiochon, *Journal of Chromatography A* **2000**, *888*, 1–12.

[25] M. A. N. Coelho, J. R. F. Guedes de Carvalho, *Chemical engineering research & design* **1988**, *66*, 165–177.

[26] J. Delgado, J. R. F. Guedes de Carvalho, *Transport in porous media* **2001**, *44*, 165–180.

[27] W. Meulebroeck, H. Ottevaere, K. Scheir, D. Clicq, G. Desmet, H. Thienpont, in *Photonics Europe* (Eds.: C. Gorecki, A.K. Asundi, W. Osten), **2006**, p. 61881I–61881I–12.

[28] W. De Malsche, H. Eghbali, J. De Smet, H. Gardeniers, G. Desmet, in *Proceedings of μTAS 2006*, Tokyo, Japan, **2006**, pp. 564–566.

[29] W. De Malsche, H. Eghbali, D. Clicq, J. Vangelooven, H. Gardeniers, G. Desmet, *Analytical chemistry* **2007**, *79*, 5915–5926.

[30] Y. Bernardinelli, C. Haeberli, J.-Y. Chatton, *Cell Calcium-Sidcup* **2005**, *37*, 565–572.

[31] J. Billen, P. Gzil, J. De Smet, N. Vervoort, G. Desmet, *Analytica Chimica Acta* **2006**, *557*, 11–18.

[32] K. Pappaert, J. Biesemans, D. Clicq, S. Vankrunkelsven, G. Desmet, *Lab on a Chip* **2005**, *5*, 1104–1110.

[33] G. Desmet, N. Vervoort, D. Clicq, A. Huau, P. Gzil, G. V Baron, *Journal of Chromatography A* **2002**, *948*, 19–34.

Chapter 5

In-Situ Measurement of the Radial Dispersion in ordered and disordered 2D-pillar array structures

Abstract

Using a dedicated optical injection set-up and specifically selected experimental conditions (fully transparent micro-pillar array chips with a wide range of pillar diameters and tested with mobile phases with a wide range of viscosities), highly detailed measurements of the radial dispersion process in 2-D chromatographic beds could be made. The obtained data cover a broad range of reduced velocities ($0<v<3000$) and show a clear leveling-off of the radial dispersion coefficient at large reduced velocities. Depending on the packing density, this leveling off occurs at a value of about $D_{rad}/D_{mol}=10$ ($\varepsilon=0.4$), $D_{rad}/D_{mol}=4$ ($\varepsilon=0.6$) and $D_{rad}/D_{mol}=2,5$ ($\varepsilon=0.8$). Another interesting observation that could be made is that the effect of the bed order on the observed radial dispersion process is relatively small. The observed relation between the measured D_{rad}-values and the reduced liquid velocity furthermore clearly invalidates the classical Galton-board model and corroborates the series-connection transport model recently proposed by Deridder [1] based on a series of computational fluid dynamics simulations.

This chapter has been submitted to *Analytical Chemistry* and is currently being reviewed.

In-Situ Measurement of the Transversal Dispersion in
Ordered and Disordered 2D-pillar beds for Liquid Chromatography

De Bruyne S., De Malsche W., Deridder S., Gardeniers H., Desmet G.

5.1. Introduction

Since band broadening in chromatographic systems is determined by the occurrence of radial velocity differences, in part countered by radial diffusion and dispersion processes, it is evident that a detailed insight of the radial dispersion process is of primary importance in the understanding of the different band broadening processes in chromatographic systems [2].

Traditionally, the radial dispersion in packed columns is represented by the so-called Galton-board model [3]:

$$D_{rad} = D_{mol} \cdot (\gamma_{eff} + \beta \cdot \nu) \qquad (5.1)$$

In Eq. (5.1), γ_{eff} represents the geometrical obstruction to diffusion of the porous medium, and can be calculated from the effective medium theory [4–9]. Further, β is another geometrical constant, for which different values have been proposed in literature (ranging from 0.1 [10], over 1/12 [11,12] and 3/16 [13], up to 7/16 [14]) and ν is the reduced velocity. This is a dimensionless parameter representing the ratio of the time needed to cover a certain distance by diffusion velocity to the time needed to cover the same distance by advection. The form of Eq. (5.1), consisting of the addition of a diffusion- and an advection-driven term, is such that it assumes that the diffusive and the advective contributions to the radial transport occur purely in parallel, an assumption made in many classical studies [12,15], and certainly a valid assumption under turbulent flow conditions. In 2011, a series of detailed numerical flow simulations conducted in our group however showed the inaccuracy and physical inconsistency of this model for the type of laminar flows encountered in liquid chromatography [1]. The inaccuracy of the model manifested itself by the fact that Eq. (5.1) predicts a linearly proportional increase with ν at sufficiently large ν, whereas the simulations showed a nearly complete flattening of the D_{rad} versus ν curve at high ν. The same flattening trend was observed by Daneyko et al. using Lattice-Boltzman simulations [16]. Doubts on the validity of Eq. (5.1) were also already cast in the classical simulation study of Eisdath et al. [17]. The physical inconsistency of the Galton-board model follows from the fact that this model assumes that a molecule moving along a streamline can move to another streamline after each particle. In turbulent flow conditions, this is indeed a good representation of the reality. In laminar flows however, molecules can only move from one streamline to another by diffusion, which is known to be a slow process. To account for this slow intermediate step, it makes sense to assume that the radial dispersion occurs according to a series connection process wherein the normal convective radial dispersion is interrupted at regular intervals by a

purely diffusion-based transport step. Considering that the overall resistance to mass transfer of a series connection of different resistance is equal to the sum of the individual resistances, and considering that the resistance is inversely proportional to the dispersion coefficient, the above can be represented mathematically in the following way [1]:

$$\frac{1}{D_{rad}} = \frac{1}{a.D_{mol} + b.\nu.D_{mol}} + \frac{1}{c.D_{mol}} \tag{5.2}$$

Eventually, after recombination of the a, b, c-constants into the new constants γ_{eff}, β and δ, this expression can be rewritten into the following form:

$$D_{rad} = D_{mol} \cdot \left(\frac{\gamma_{eff} + \beta \cdot \nu}{1 + \delta \cdot \nu} \right) \tag{5.3}$$

Whereas the Eq. (5.1) predicts a purely linear increase of D_{rad} with the fluid velocity at high ν, Eq. (5.3) predicts that D_{rad} will tend to a constant value in the $\nu \rightarrow \infty$–limit.

In the present Chapter, we report on a series of dedicated experiments conducted to investigate the accuracy of Eq. (5.3). This was done using the optical injection method with uncaging dyes described in Chapter 4. Since equations (5.1) and (5.3) essentially differ in the large ν-range, special efforts were made to cover the broadest possible range of reduced velocities, using a broad range of micro-pillar diameters (up to 100 μm) and by increasing the viscosity of the mobile phase by mixing in up to 90 vol % of glycerol. Using an argon ion laser (λ = 351,4 nm), the uncaging dye was activated and the resulting dispersion profiles were observed using an inverted microscope equipped with a mercury vapor lamp and a high speed CCD-camera.

5.2. Experimental

The experimental set-up and procedures are elaborately described in Chapter 4, in which also the accuracy of the procedure for the measurement of the flow velocity, u, and radial dispersion coefficient, D_{rad}, is discussed.

5.3. Results and Discussion

5.3.1. Qualitative Measurements

The dedicated experimental approach (unusually wide pillars, very high viscosity mobile phase, highly localized optical injection) allowed to make very detailed studies of the radial and axial dispersion process in (planar) packed bed systems at high reduced velocities. Both

pulsed (Section 5.4.1.1) and continuous (Section 5.4.1.2) point injections were applied to study the transient as well as the steady-state behavior of the dispersion process. As described in Chapter 4, it was possible to shape the activation spot in various shapes and sizes by using different combinations of magnification objectives and optical pinholes or slits. When using a 5X objective for detection, the activation spot was made using a 20X objective in combination with a 50μm pinhole. When higher magnification objectives were used for detection (10-20-40X), smaller pinholes were used. The employed spot widths were selected as they are small enough to excite the uncaging dye in a region that is smaller than a single individual flow-through pore, while they are at the same time also wide enough to excite a sufficient volume of the uncaging dye tracer in the short time frames needed in the pulsed point injection experiments.

5.3.1.1. Pulsed point injection experiments.

Fig. 5.1 shows the time-lapse recording of the response to a pulsed point injection in an ordered pillar array at large reduced velocity (ν=2500). Because the contribution of the molecular diffusion is in this case very low, the radial dispersion events are slowed down to such an extent that they can be followed in a highly detailed manner using a high-speed CCD-

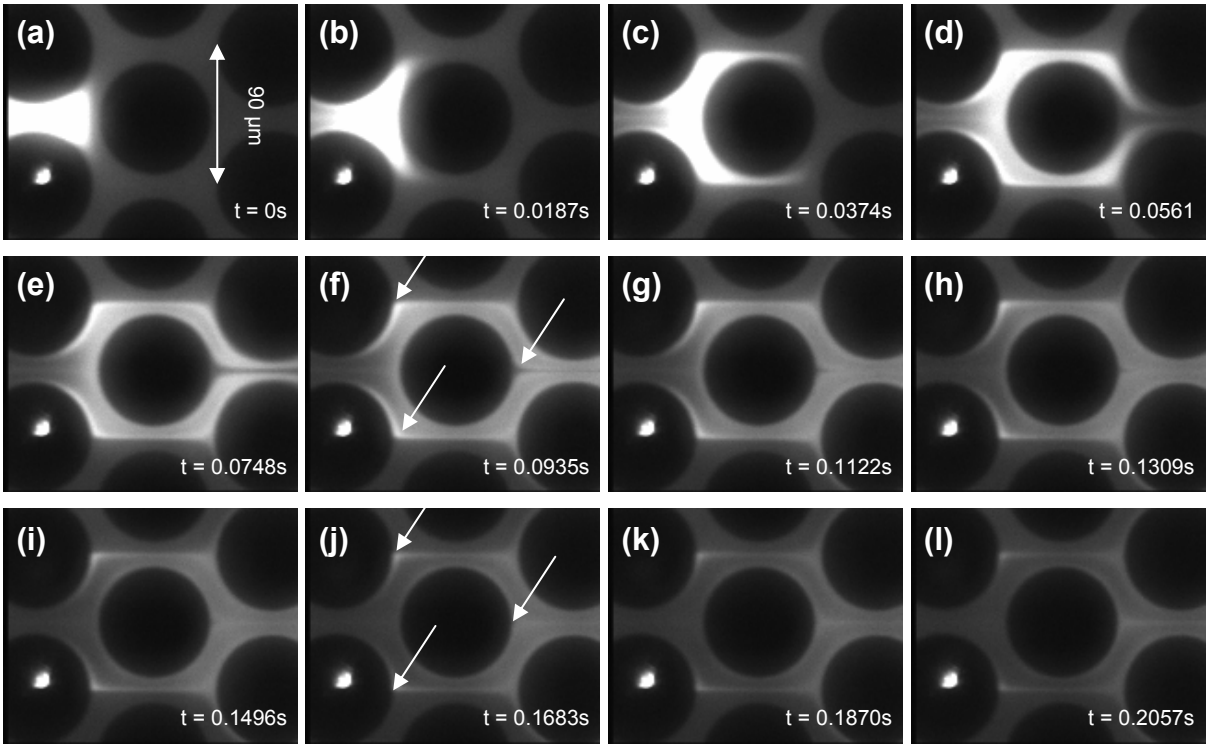

Figure 5.1. Series of CCD camera images visualizing the temporal radial dispersion process at a high reduced velocity (ν=2500) after a localized injection band in between two pillars of an ordered bed (ε=0,4). The band was injected by moving the laser spot in between two pillars when the flow was stopped. The bright dot in the left under corner inside a pillar is the activation light spot.

camera. At ν=2500, the flow of the injected tracer dye species clearly remains restricted to the flow-through-pores they were initially injected in. Because of the high ratio of advective to diffusive transport, the residence time of the species at the interface with the adjacent flow-through-pore is on the order of only 0.025s, leaving insufficient time for an appreciable amount of species to diffuse across the interface with the adjacent flow-through pore. Also clearly visible are the areas of low (radial) velocity, indicated by the white arrows in panels (f) and (j). These are respectively filled earlier and emptied later than the other regions, because of the slow diffusive equilibration between the regions of high and low velocity.

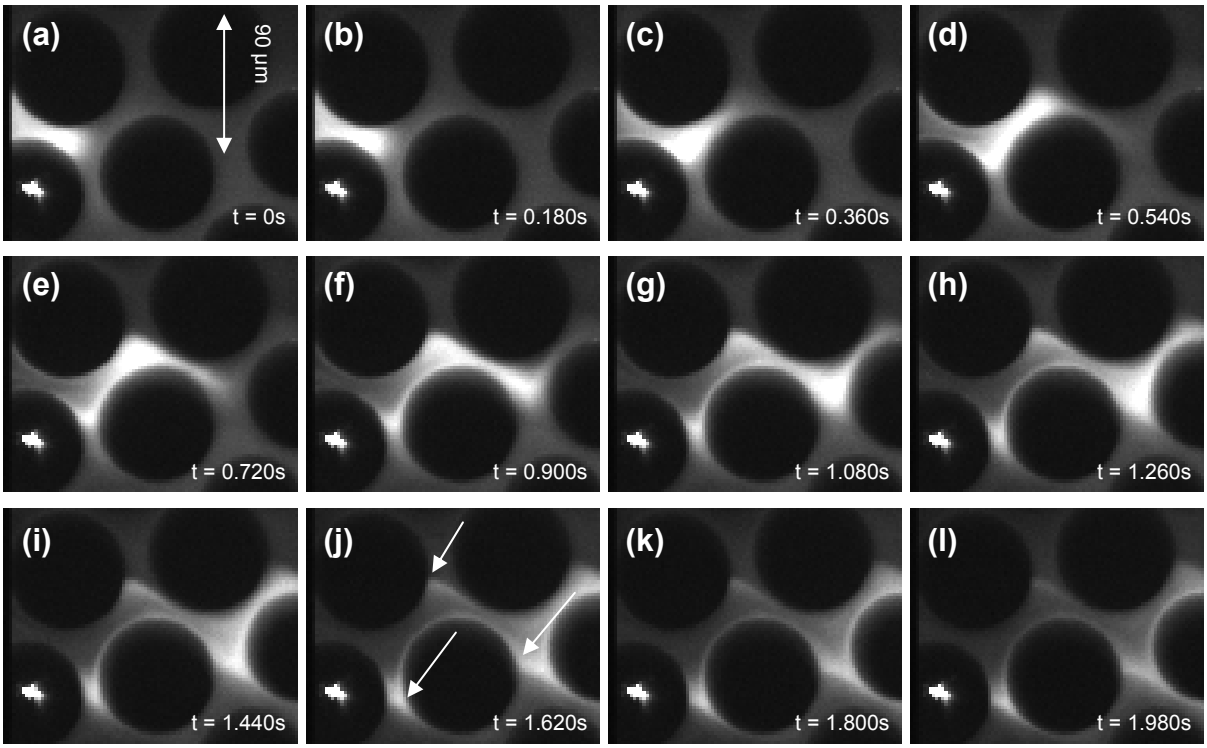

Figure 5.2. Series of CCD camera images visualizing the temporal radial dispersion process at a high reduced velocity (ν=1400) after a localized injection in the through-pore between two pillars in a disordered bed (ε=0.4). The band was injected by moving the laser spot in between two pillars when the flow was stopped. The bright dot in the left under corner inside a pillar is the activation light spot.

As can be noted from Fig. 5.2, this behavior does not significantly change when shifting from an ordered to a disordered array of pillars, as there remain clear interfaces between the adjacent flow-through pores. The only difference with the perfectly ordered case is that these interfaces now run skew instead of parallel with the top and bottom boundary of the picture. Similar to the ordered pillar array case, the injected species do not split randomly after each pillar but remain inside the flow-through pore they were injected in. The areas of low (radial) velocity are again also clearly visible (cf. the white arrows added to Fig. 5.2j).

5.3.1.2. Continuous point injection experiments.

As described in many classical studies [18–20] ,the most accurate and simple measurement of the radial dispersion coefficient can be obtained from the steady-state dispersion plume formed in the long time limit response to a continuous point injection. Fig. 5.3 shows a number of such plumes in an ordered pillar array for cases with a different reduced velocity ν.

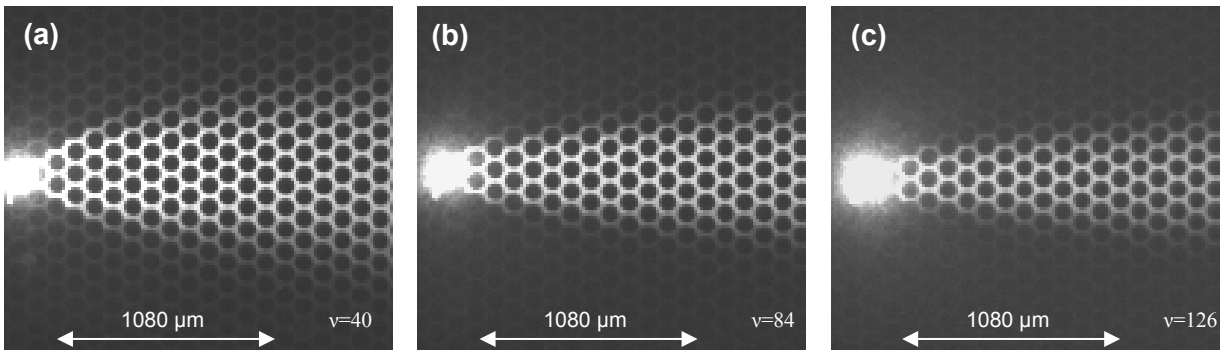

Figure 5.3. 5X images of dispersing plumes at low reduced velocities in an ordered pillar bed with **ε**=0.4 for different values of the reduced velocity: **(a)** ν = 40, **(b)** ν = 84, **(a)** ν = 126

As can be noted from Fig. 5.3a, the tracer rapidly spreads over a more or less triangular ratio with an opening angle in the order of 45° when ν is small. This is due to the fact that, because of the low reduced velocity, there is ample time for a significant fraction of the species to diffuse into the neighboring flow-through pore after each particle. Comparing Figs. 5.3a-c subsequently shows that the dispersion plumes generated during the D_{rad}-measurement

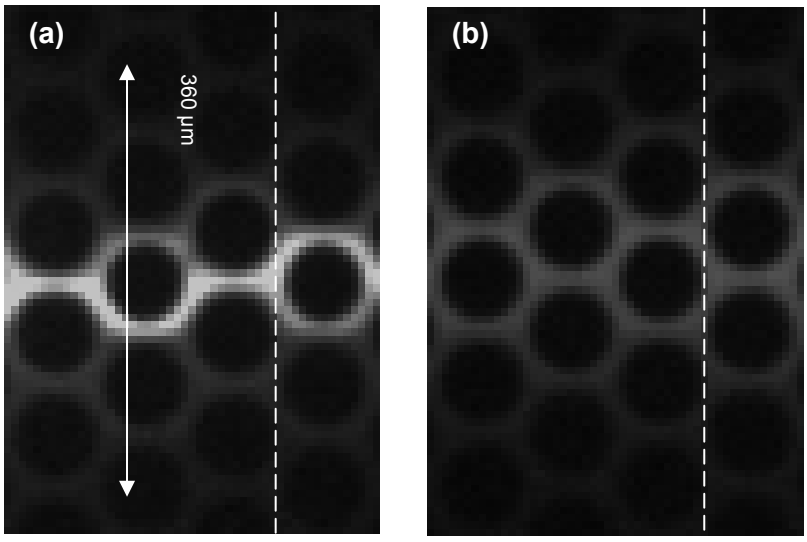

Figure 5.4. 10X images of a dispersing plume at high reduced velocities (ν=2500) in an ordered pillar bed with ε=0.4. **(a)** image at the start of the bed, 500µm after the activation spot, **(b)** image at the end of the bed, 7.5mm downstream of the position of the activation spot.

experiments tends to become narrower and narrower with increasing ν. This also had its implications on the experimental approach. Whereas at low ν a sufficient number of data points could be collected over an axial distance covering about 10 to 20 particles, the monitor lines in the high ν-range (Fig. 5.4) needed to be spread over much larger distances, on the order of 40 (for the ε=0.6 and 0.8-cases) to 100 (ε=0.4-cases) particles, in order to establish an appreciable difference in radial spread between the first and the last monitor line.

At even higher ν, the relative diffusion rate is even so slow that the injected species remain on their initial streamlines within the flow-through pore for a very long time (Fig. 5.5).

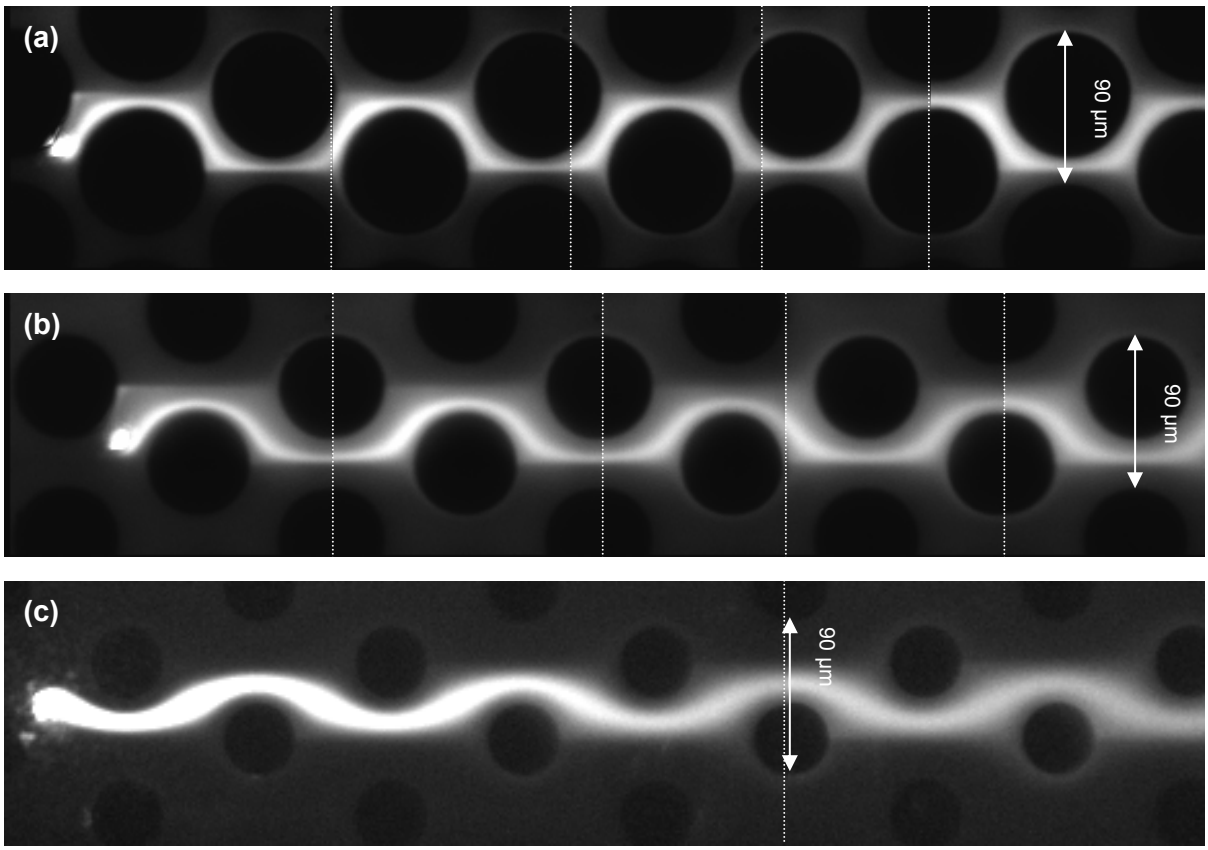

Figure 5.5. Stitched 40X images recorded at high reduced velocity in ordered beds with a porosity of **(a) ε**=0.4 (ν = 2500), **(b) ε**=0.6 (ν = 1650) and **(c) ε**=0.8 (ν = 1250).

Comparing the species plume in the ε=0.4, 0.6 and 0.8-case represented in Fig. 5.5, it can be noted that the path of the streamlines is much more tortuous when ε is small than when ε is large. This is in agreement with the larger space between particles, causing less obstruction to the flow and hence leading to a less strong radial velocity component.

Figs. 5.6 to 5.8 show the results of a series of experiments, similar to those shown in Figs. 5.3 to 5.5, but now in a disordered instead of in an ordered pillar array.

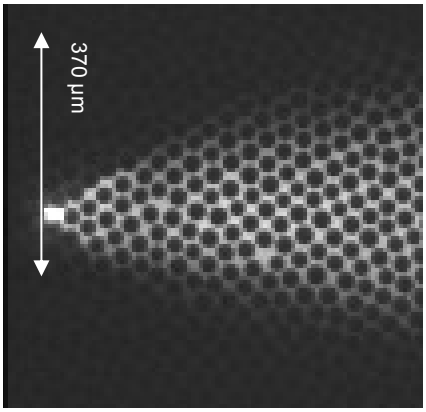

Figure 5.6. 20X image of a dispersing plume at low reduced velocities (ν =1) in a disordered pillar bed with ε=0.4.

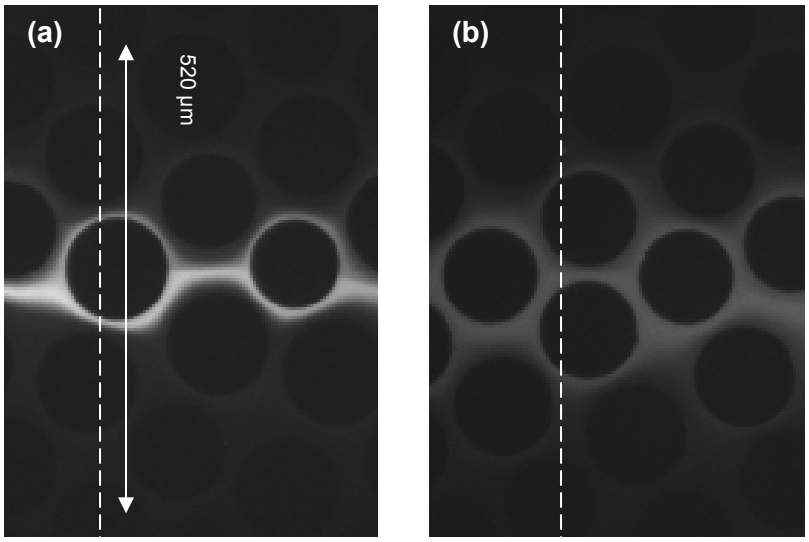

Figure 5.7. 10X images of a dispersing plume at high reduced velocities (ν = 1400) in a disordered pillar bed of ε=0.4. **(a)** image at the start of the bed, 200µm after the activation spot, **(b)** image at the end of the bed, 5.3mm downstream of the activation spot.

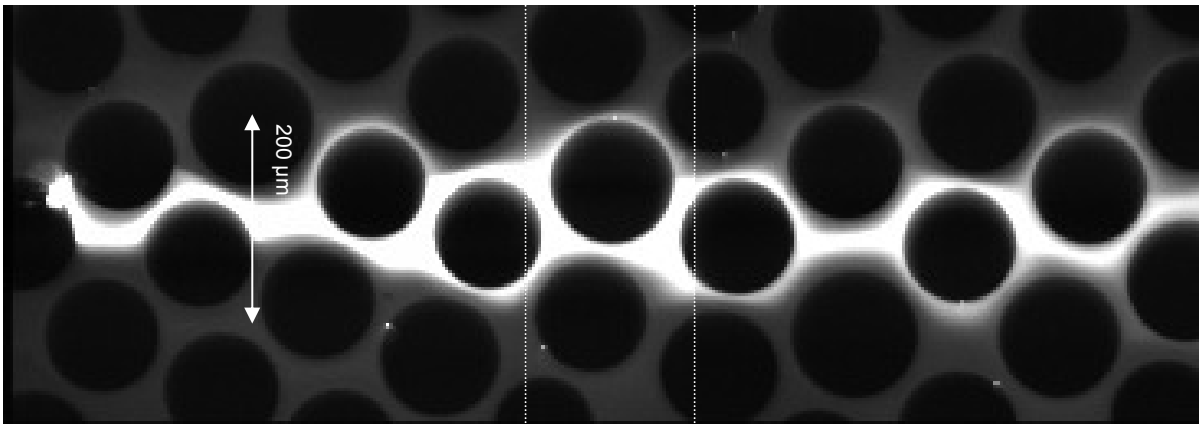

Figure 5.8. 20X images stitched to each other at high reduced velocity (ν = 1400) in a disordered bed with a porosity of ε=0.4.

As can be noted, the spreading angle of the dispersion plume is very similar to that observed in the perfectly ordered array for a similar value of ν. At low ν, the spreading angle is again around 45° (Fig. 5.6), and the spreading angle again decreases with increasing ν, until eventually, at very high ν, the dispersion plume again remains restricted to a region very close to the set of streamlines the tracer species were initially released in (Fig. 5.8).

The small difference observed between the ordered and the disordered case is in agreement with the theory of hydrodynamics, according to which the streamlines in a laminar 2D-flow can never cross, irrespectively of whether the fluid flows through an ordered or a disordered system. The radial transport in both cases hence eventually always becomes rate limited by the exchange process between adjacent streamlines, which, in a laminar flow, is always purely diffusion-driven.

5.3.2. Measured D_{rad}-values

As shown in literature, the radial dispersion coefficient D_{rad} can be calculated from the observed difference in radial variance ($\Delta\sigma^2_{rad}$) between two subsequent monitor lines:

$$D_{rad} = \frac{\Delta\sigma^2_{rad}}{2 \cdot \Delta t} \qquad (5.4)$$

In this expression, the time interval Δt is the time needed for the analytes to flow from one monitor line to the other. Fig. 5.9 shows the evolution of the thus calculated radial dispersion coefficient with changing ν and for different values of the external porosity. As can be noted, the data can be fitted very well with the series transport model proposed in [1] and represented by Eq. (5.2). The fact that all these data sets can be fitted by a single expression is not obvious at all, considering that the data points for each different case (ε=0.4, 0.6, 0.8) are obtained from two or three different channels (containing pillars with different diameter) and using two or three different mobile phase compositions to cover the different ν-ranges.

Also interesting to note is the clear effect of the packing density: the smaller ε, the higher D_{rad}. This observation is in full agreement with the larger tortuosity and the concomitant higher radial velocity components belonging to the low ε-cases, as already observed in Fig. 5.5. At high ν, the observed D_{rad}-values tend to decrease from a value of about D_{rad}/D_{mol}=10 (ε=0.4) over D_{rad}/D_{mol}=4 (ε=0.6) to D_{rad}/D_{mol}=2,5 (ε=0.8).

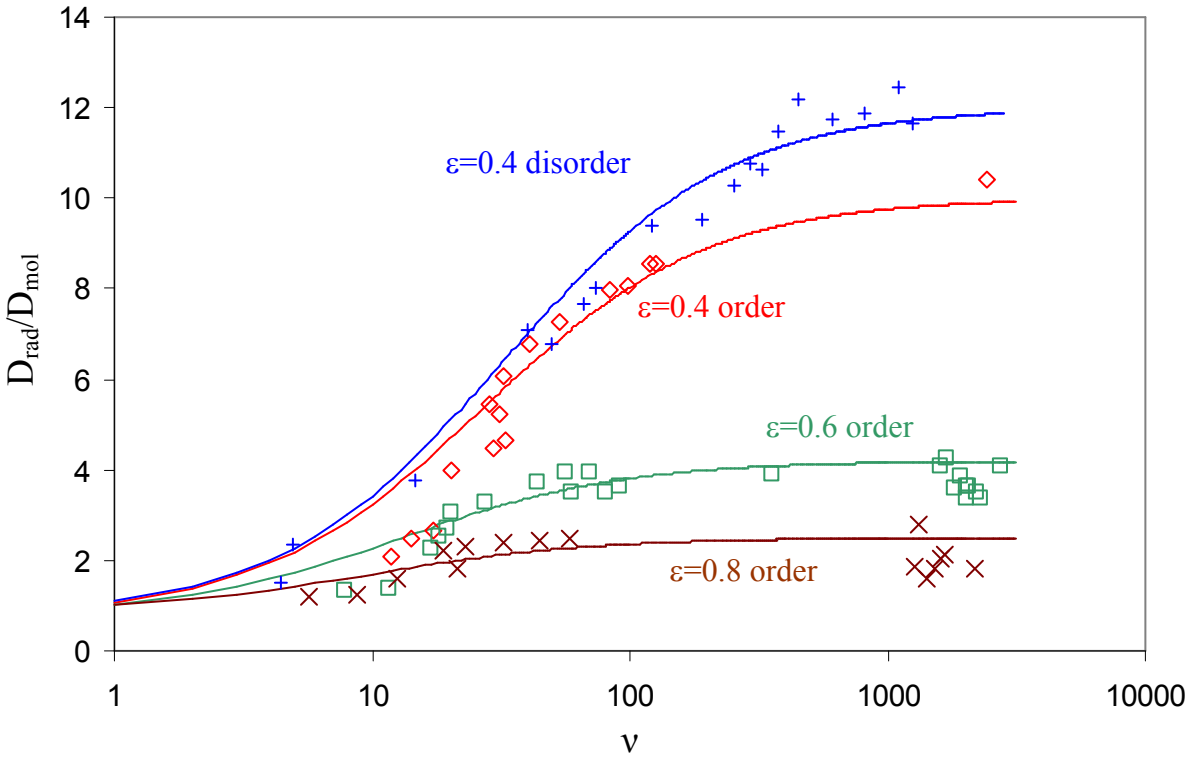

Figure 5.9. Graphical representation of the acquired data and the model (full lines). (+) ε=0.4 and disordered, (◇) ε=0.4 and ordered, (□) ε=0.6 and ordered, (×) ε=0.8 and ordered. See Table 5.1. for the parameters of each fitting.

Interestingly, the difference in D_{rad} between the ordered and disordered bed case is relatively small, as both cases level-off to a value that only differs by some 10 to 20%. This (maybe surprisingly) small difference between the ordered and the disordered case is in full agreement with the small differences in dispersion behavior observed in paragraph 5.4.1 (cf. the high similarity between Figs. 5.3a and 5.6 and between Fig. 5.5 and Fig. 5.8).

Despite the relatively low number of data points in the low ν-range (caused by the poor flow rate stability of the employed set-up), the fitted γ_{eff}-coefficients (see Table 5.1), which correspond to the obstruction factors for the pure diffusive transport (ν=0), agree very well with the values predicted by the effective medium theory [4]. As was shown by Deridder et al. [7,8] the theoretical γ_{eff}-values that can be expected in an ordered array with ε=0.4, 0.6 and 0.8 are respectively given by $\gamma_{eff} = 0.74$, $\gamma_{eff} = 0.77$ and $\gamma_{eff} = 0.85$. These values agree very well with the values of $\gamma_{eff} = 0.62$, $\gamma_{eff} = 0.71$ and $\gamma_{eff} = 0.83$ predicted by Deridder et al for the corresponding ε-value. As a side-note, it can also be remarked that these γ_{eff}-values are also directly proportional to the B-term coefficient appearing in the reduced van Deemter equation (with $B = 2.\gamma_{eff}.D_{mol}$).

Table 5.1. Table of the fitted values for the parameters appearing in Eq. (5.3) based on the data sets shown in Fig. 5.9.

ε	γ_{eff}	β	δ
disorder 0.4	0.75	0.38	0.037
order 0.4	0.74	0.37	0.037
order 0.6	0.77	0.33	0.078
order 0.8	0.86	0.26	0.105

Reminding the main goal of the present study, i.e., differentiating between the parallel connection (Eq. 5.1) and the series connection model (Eq. 5.3) for the radial dispersion process, it is especially the high ν-end of Fig. 5.9 that is of interest. Despite the relatively large scatter, essentially caused by the very small differences in radial variances from which the D_{rad}-value needs to be determined, it is clear that D_{rad} does not increase linearly with ν at high ν as predicted by Eq. (5.1), but instead clearly levels off to a constant or near-constant value, as predicted by Eq. (5.3). The β-values in Table 5.1 are of the same order as those predicted by Saffman [13] and Prausnitz [14] (cf. paragraph 5.1). The values of the δ-parameter listed in Table 5.1 are such that they allow to represent that the leveling off of the D_{rad}-data starts around ν=100.

The observed leveling-off at high ν can be explained by the fact that the slow diffusion step becomes rate limiting again at these high ν, as the time available for the diffusive mass transfer that needs to be made between adjacent streamlines decreases inversely proportional with ν. Despite the fact that the diffusion process again becomes the rate limiting factor in this high ν-limit, the D_{rad}-values are substantially larger than in the low ν-limit. This is due to the fact that the distances that need to be covered by diffusion are much smaller in the high ν-limit than in the low ν-limit.

5.4. Conclusions

Using a dedicated optical set-up to locally and temporarily uncage an uncaging laser dye, using a series of glass micro-channels containing pillar beds with different diameter and packing density, and using different water/glycerol mixtures, detailed measurements of the radial dispersion process in 2D- chromatographic systems could be made. The measurements show that the advective component helps the species to rapidly disperse over the radial region covered by the group of streamlines the species are initially injected in. Moving over to an adjacent set of streamlines however requires an additional diffusion step which, at high ν, becomes rate limiting. As a consequence, the relation between D_{rad} and ν tends to level off to a constant value at high ν. Depending on the packing density, this leveling off occurs at a value of about $D_{rad}/D_{mol}=10$ ($\varepsilon=0.4$), $D_{rad}/D_{mol}=4$ ($\varepsilon=0.6$) and $D_{rad}/D_{mol}=2.5$ ($\varepsilon=0.8$). Interestingly, the effect of the bed order on the observed radial dispersion process (both qualitatively in Section 5.4.1 and quantitatively in Section 5.4.2) is relatively small. All these observations can be represented very well using the series-connection model proposed by Deridder [1]. As also shown by Deridder, even more sophisticated D_{rad}-models can be conceived, based on similar but more complex considerations. Their use however falls outside the scope of the present study, as more accurate measurements would be needed to discriminate them from the presently considered simple series-connection model.

References

[1] S. Deridder, A Computational Fluid Dynamics Study of the Factors Influencing the Kinetic Properties of Chromatographic Columns, Vrije Universiteit Brussel, **2011**.

[2] J. C. Giddings, *Dynamics of Chromatography, Part I: Principles and Theory (Chromatographic Science Series, Vol. 1)*, Marcel Dekker, New York, **1965**.

[3] S. T. Sie, G. W. A. Rijnders, *Analytica Chimica Acta* **1967**, *38*, 3–16.

[4] S. Torquato, *Random Heterogeneous Materials, Interdisciplinary Applied Mathematics 16*, Springer, New York, **2002**.

[5] G. Desmet, K. Broeckhoven, J. De Smet, S. Deridder, G. V Baron, P. Gzil, *Journal of Chromatography A* **2008**, *1188*, 171–188.

[6] K. Broeckhoven, D. Cabooter, F. Lynen, P. Sandra, G. Desmet, *Journal of Chromatography A* **2008**, *1188*, 189–198.

[7] S. Deridder, G. Desmet, *Journal of Chromatography A* **2011**, *1218*, 46–56.

[8] G. Desmet, S. Deridder, *Journal of Chromatography A* **2011**, *1218*, 32–45.

[9] F. Gritti, G. Guiochon, *AIChE Journal* **2010**, *57*, 346–358.

[10] T. Baron, *Chem. Eng. Prog* **1952**, *48*, 118–125.

[11] J. Delgado, *Chemical Engineering Research and Design* **2007**, *85*, 1245–1252.

[12] D. J. Gunn, *Trans. Inst. Chem. Engrs* **1969**, *47*, 351–359.

[13] P. G. Saffman, *Journal of Fluid Mechanics* **1959**, *6*, 321–349.

[14] J. M. Prausnitz, *AIChE Journal* **1958**, *4*, 14–28.

[15] R. H. Wilhelm, *Pure Appl. Chem* **1962**, *5*, 403–421.

[16] A. Daneyko, D. Hlushkou, S. Khirevich, U. Tallarek, *Journal of Chromatography A* **2012**.

[17] A. Eidsath, R. G. Carbonell, S. Whitaker, L. R. Herrmann, *Chemical Engineering Science* **1983**, *38*, 1803–1816.

[18] T. K. Sherwood, R. L. Pigford, C. R. Wilke, *Mass Transfer*, McGraw-Hill New York, **1975**.

[19] T. J. Hanratty, G. Latinen, R. H. Wilhelm, *AIChE Journal* **1956**, *2*, 372–380.

[20] R. C. Acharya, A. J. Valocchi, C. J. Werth, T. W. Willingham, *Water Resources Research* **2007**, *43*, W10435.

Chapter 6

Exploring The Speed Limits of Liquid Chromatography Using Shear-driven Flows Through 45 and 85 nm Deep Nano-Channels

Abstract

We explored the possibility to perform high speed and high efficiency liquid chromatographic separations in channels with a sub-100 nm depth. The mobile phase flow through these nano-channels was generated using the shear-driven flow principle to generate high speed flows which were the equivalent of a 12,000 bar pressure-driven flow. It was found that the ultra-fast mass transfer kinetics prevailing in this range of small channel depths allow to completely eliminate the C-term contribution to band broadening, at least up to the upper speed limit of our current set-up (7mm/s mobile phase velocity), leaving the inescapable molecular diffusion (i.e., B-term band broadening) as the sole source of band broadening. In the absence of any mass transfer limitations, 50,000 to 100,000 theoretical plates could be generated in the span of 1 to 1.5 seconds. This is nearly two orders of magnitude faster than the best performing commercial pressure-driven UHPLC-systems. With the employed channel depths, we appear to have struck a practical lower limit for the channel miniaturization of shear-driven flows. Despite the use of channel substrates with the highest grades of optical flatness, the overall substrate waviness (order of some 5 to 10 nm) can no longer be neglected compared to the etched channel depth, which in turn significantly influenced the local retention factor and band broadening.

This chapter has been published as:

Exploring The Speed Limits of Liquid Chromatography

Using Shear-driven Flows Through 45 and 85 nm Deep Nano-Channels

De Bruyne S., De Malsche W., Fekete V., Thienpont H., Ottevaere H., Gardeniers H., Desmet G.

Analyst, **2013**, *138*, 6127-6133

DOI: 10.1039/C3AN01325A

6.1. Introduction

The separation resolution in liquid chromatography (LC) has basically two enemies: longitudinal molecular diffusion and mass transfer resistance [1]. Whereas the first one is inescapable and is a consequence of the intrinsic molecular diffusion of the analytes, the second one can in principle be completely eliminated by shrinking the distance that needs to be covered by the analytes when exchanging between the mobile and the stationary zone. In an open-tubular LC, this distance is determined by the capillary or micro-channel diameter. Mathematically, the beneficial effect of a reduction of the channel size for an open-tubular system directly follows from the following general plate height expression for open-tubular LC [1–4]:

$$H = 2\frac{D_m}{u_m} + f_1(k')u_m\frac{d_{channel}^2}{D_m} + f_2(k')u_m\frac{{d_S}^2}{D_S} \qquad (6.1)$$

wherein the first term represents the longitudinal molecular diffusion, and the second and third term respectively represent the mass transfer resistance in the mobile and the stationary zone. Eq. (6.1) indeed shows that a thorough miniaturization of the channel diameter $d_{channel}$ and the stationary phase layer thickness d_s can eventually make the second and the third term vanishingly small compared to the first term. To eliminate the mass transfer limitations in liquid chromatography, where the molecular diffusion rates are five orders of magnitude smaller than in gas chromatography, channels with characteristic dimensions in the nanometer range are needed [5–9]. Recent explorations of the nano or extended nano-space have, amongst others, been made by Kitamori et al. [10–12] and Wirth et al.[13–15]. Without any doubt, the most extreme form of miniaturization has very recently been realized by Singhal et al. [16]. They demonstrated that even a single template-grown carbon nano-tube can be used as a separation column to separate attoliter mixtures of fluorescent dyes. The employed columns were 40 μm long, and were only 70 to 200 nm in outer diameter and 60 to 190 nm in inner diameter.

Whereas these groups used pressure forces to propagate the mobile phase, the separations conducted in the present study make use of the shear-driven flow (SDF) principle [17–29] (see Fig. 6.1). To apply this principle, a flow channel is needed that consists of two independently movable parts, further referred to as the top and the bottom plate. Pressing both parts against each other while moving the top plate past the bottom plate, or vice versa, the drag forces originating from the moving plate literally drag the liquid through the channel, as

they generate a fluid flow (having a linear velocity profile) that is mechanically sustained all along the channel length.

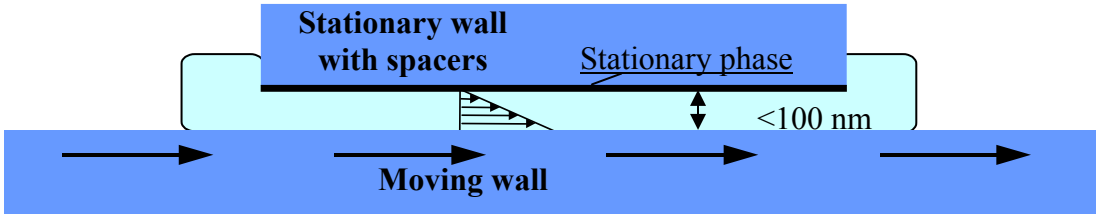

Figure 6.1. Working principle and resulting flow profile of a shear-driven flow (SDF).
The retentive layer needed for the chromatographic separation is attached to the stationary wall.

Since the driving force for the flow is imposed all along the channel length and not only at the channel entrance, as is the case in pressure-driven flow systems, the liquid does not experience any pressure drop at all. Whereas the average fluid velocity in a pressure-driven flow inevitably decreases with increasing channel length and decreasing channel depth (cf. Poiseulle's law [30]), the average fluid velocity in a shear-driven flow through a channel with a flat-rectangular cross-section (with width>>depth) is always equal to one half of the moving wall velocity, completely independent of the channel depth or length [17,18,23]. As a consequence, high speed flows (order of cm/s and more) can easily be imposed in channels with a nanometric depth. The only limitation is the speed of the motorized translation or rotation stage used to drive the moving wall. The channel depth, which is determined by the thickness of the gap formed between stationary and the moving wall is maintained by firmly pressing both channel parts against each other and using a set of spacers structures which are micro-machined on either the stationary or the moving wall to form a fixed gap size (=effective channel height, see Fig. 6.2a). To induce the actual separation, the stationary wall should be coated with a suitable retentive layer (e.g., a layer of C18-alkyl chains) [17].

Up till now, the shallowest channels wherein the SDF principle has been successfully applied were 120 nm deep [25]. In these channels, plate heights as low as 0.25 µm have been reported, with plate generation velocities on the order of 39,000-52,000 plates per second.

In the present study, we report for the very first time on the use of sub-100nm channels (45 and 85 nm). For the specific case of SDF's, the main challenge arising when entering this range of channel depths is finding channel substrates which are sufficiently flat to guarantee that the effective channel height is sufficiently reproducible and uniform in space and time.

This is due to the fact that the effective channel depth ($d_{channel}$) of SDF channels equals the sum of the etched spacer height (h_{spacer}) and the thickness of the lubrication layer (δ_{lub}) covering the top of the spacers (see Fig. 6.2a). The thickness of the latter is difficult to control: whereas the layer is initially relatively thick, typically of the order of a few hundreds of nanometer, it continuously decreases (first rapidly, then slowly) under the action of the normal load that is applied to keep the two channel parts in intimate contact. Theoretical considerations show that, under the action of a constant load, the thickness of the excess liquid layer can be expected to decrease according to the square root of the time until the layer becomes so thin that the macroscopic continuity equations (Navier-Stokes equations) cease to hold and the viscosity starts to increase dramatically because of the decreased mobility of the molecules. According to Israelachvili [31] and Gee et al. [32] this occurs when the layer thickness becomes thinner than 5 nm. The thinning of the liquid layer however continues even under these conditions, implying that the application of SDFs inevitably always occurs under conditions of a variable effective channel height.

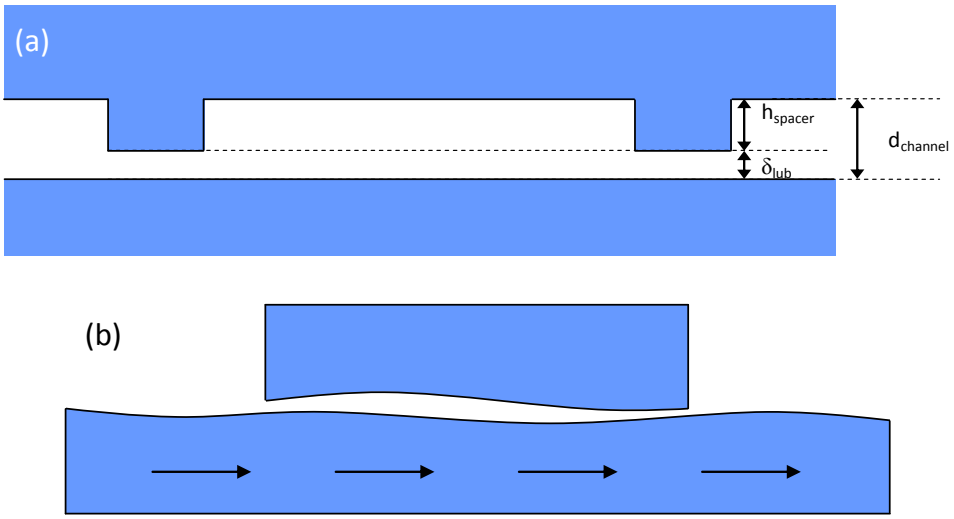

Figure 6.2. (a) Schematic cross-sectional view of an SDF channel (cross-section perpendicular to channel axis; not to scale) showing the stationary wall (top) and the moving wall (bottom) part, the channel spacers (machined into the stationary wall) and the thickness (δ_{lub}) lubrication layer underneath the channel spacers. **(b)** Schematic longitudinal cross-section of the channel showing the large scale waviness of the substrates (not to scale).

The only possibility to escape from this problem is by waiting until the lubrication liquid layer has thinned to a value that is sufficiently small so that it no longer contributes significantly to the total effective channel height (total effective channel height = etched spacer height + thickness of the lubrication layer). In this way, the effect of the ever (albeit very slowly) decreasing lubrication layer thickness on the effective channel depth becomes

insignificant. In previous experiments, using 100 to 400 nm deep channels [25,27], it was found that a wait time of 1 minute was sufficient to achieve this, even though the channel spacers had a width of 500-700µm. This relatively large spacer width, initially selected as such for stability reasons, suffers from the fact that the out-flowing excess liquid needs to travel a relatively large lateral distance. Since the outflow is pressure-driven (originating from the action of the normal load), it is obvious to expect that, the larger the distance that needs to be travelled (i.e., the wider the channel spacer), the slower the outflow velocity of the lubrication layer will be. Considering that the lubrication layer for a channel with a nominal depth of in the order of 40 to 80 nm needs to be made as thin as 2 to 4 nm before its contribution to the total effective channel height drops below 5%, it was anticipated that the wait time needed to achieve this would become impractically long. The spacers used in the present study therefore only had a width of 20µm. To enhance the stability of the stationary wall plate and to keep the local material wear rates as low as possible, the reduction of the individual width of the spacers was compensated by increasing their number (see Fig. 6.3a).

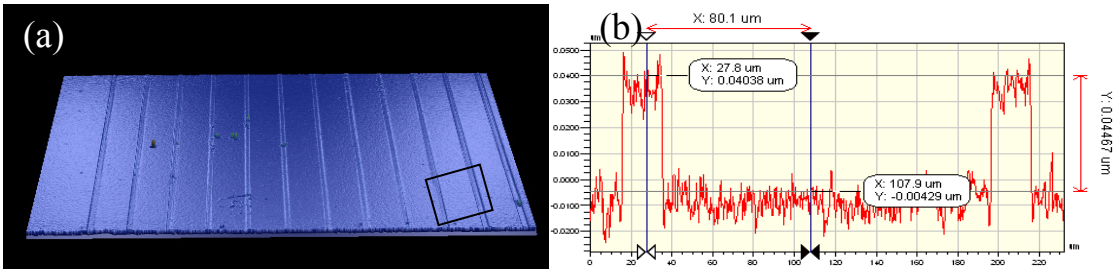

Figure 6.3. (a) 3-D Wyko-scan of one of the employed stationary wall plates carrying the half-open SDF-channels. **(b)** zoom-in of (a): 2-D Wyko-scan of the surface height profile of the stationary wall substrate, showing two protruding spacer regions having a height of 44nm.

6.2. Experimental

6.2.1. Chemicals and samples

The fluorescent dyes Rhodamine 110 (Exiton inc., Dayton, Ohio, USA) and rhodamine 575 (Fluka Chemie GmbH, Buchs, Germany) were used as the analytes in the chromatographic separations. The mobile phase was always a mixture of 50 vol% methanol (LC-MS grade, Biosolve BV, Valkenswaard, The Netherlands) with deionized water.

6.2.2. Microfabrication

The stationary wall part carrying the channel spacer lines were machined in an ultra-flat optical fused silica wafer (1 mm thick, flatness = λ/20 with λ=670 nm, diameter of 4 in.,

Photox Optical Systems, Sheffield, UK). First, mid-UV lithography (mask aligner: EVG 620, EV Group, St. Florian am Inn, Austria) was used to define the spacers in a positive resist layer (Olin 906-12, Arch Chemicals inc, Zwijndrecht, Belgium) with a thickness of 1.2 μm, spinned (spinner Delta 20, SÜSS MicroTec, Garching, Germany) on the wafer surface. After developing the resist (OPD4262, FujiFilm, Japan), the pattern was transferred into the fused silica by deep reactive ion etching (Adixen Alcatel AMS100DE, France). Subsequently, the resist was removed by an oxygen plasma etcher (Tepla 300E, PVA TePla AG, Wettenberg, Germany) and a nitric acid dip (Selectipur: Merck 100453, Germany). Finally, the wafers were diced into chips (Disco DAD321 dicing saw, Japan). Each chip had eight parallel channels with a width of 160μm and separated by continuous spacer lines of 20 μm wide (see also §3.3. for a detailed process flow and mask layout). After their fabrication, the channel wall parts were inspected by making surface height profiles and 3-dimensional profiles using a Wyko NT2000 (Veeco, New York, USA) with a 50X objective and a field of view of 0,5, resulting in an overall magnification of 25X. The C_{18}-stationary phase layer needed to induce the chromatographic retention was induced by silanizing the hydroxyl groups occupying the surface of the half open nano-channels with dimethyl-dodecyl-chlorosilane using the protocol described in [24].

6.2.3. Channel assembly and detection

The main components of the employed set-up have been described in great detail in previous publications [23,27,28]. In brief, the set-up consisted of an inverted epi-fluorescence microscope (IX71, Olympus, Japan) equipped with a mercury vapor lamp (Nikon HB 101-AF, Cetec NV, Belgium) and a high speed EM CCD-camera (electron multiplying charge coupled device camera, Hamamatsu Photonics K.K., Japan) for detection. The movable wall substrate is fixed on the microscope table using a metallic frame holder built in-house. This table could be mechanically moved and positioned using a motorized translation stage (M-TS100DC.5, Newport B.V., The Netherlands), driven by a stepping motor (U611CC, Newport B.V.) and a speed controller (MM 4006, Newport B.V.). Essential for the present study are the high acceleration /deceleration rates of the employed translation stage (max. velocity is 75mm/s and max. acceleration and deceleration is 300mm/s²).

The SDF nano-channels were assembled by putting the diced chip used as the stationary wall inside a precision-milled metal holding frame attached to the microscope head on top of an

ultra flat movable wall substrate (1 mm thick, flatness =λ/20 with λ=670 nm, diameter of 2 in., Photox Optical Systems, Sheffield, UK). During the motion, the moving and stationary part were pressed together using a pneumatic cylinder (PUN-6X1-BL, Festo Belgium NV), positioned directly above the stationary wall plate and contacting it indirectly through a metallic/silicone rubber stack. This force (arising from a typical applied pressure of 1 to 2 bar) is mainly needed to keep both channel parts in close contact and to overcome the natural warp that is present in every unstrained polished material [24].

6.2.4. Band broadening measurements

Similar to the procedures already described elsewhere [24,26,27], band broadening was measured by abruptly stopping the wall movement after this has elapsed a preset distance in order to acquire images with good resolution and S/N ratio. The camera was operated in 8x8 binning mode with a 10x objective (OFR LMU-10x-266, Applied Laser Technology, The Netherlands) yielding a pixel size of 11.75 μm. The binning size was put on maximum (8x8) in order to achieve the lowest possible capture times to minimize the influence of diffusion after the moving wall stopped abruptly. The band broadening (σ^2) and positions (L_{eff}) of the peaks were quantified by analyzing the recorded data using the SigmaPlot software package (Systat software, Richmond, CA, USA) and fitting the peak intensity profiles with a Gaussian curve function with a given spatial peak variance σ^2. Using the classical plate height definition, the measured variances were first corrected by subtracting the contribution of the injection peak width [19,33] ($H_{inj}=w_{inj}^2/12L_{eff}$) and were subsequently converted into experimental plate height values using:

$$H = \frac{\sigma^2}{L_{eff}} - \frac{w_{inj}^2}{12L_{eff}} \qquad (6.2)$$

wherein w_{inj} is the half of the axial displacement distance of the movable wall during injection following the injection procedure described by Desmet et al. [28].

6.3. Results and discussion

Using short etching and long conditioning times on the Adixen DE Bosch-etcher, channel spacers with an average height of respectively 85nm and 40nm were obtained (Fig. 6.3). The cited depth values were obtained after averaging out the average depth profile along 10 equidistant transversal lines covering the entire channel axis. Depth fluctuations along a given

line were of the order of 2 nm. The average depth variations between the different measurement lines were of the same order. This high degree of depth uniformity could be achieved due to the very high etching uniformity of the Adixen DE combined with the fact that all the employed channels were cut out of the central 50% region of the employed 4 inch wafers.

As mentioned in the Introduction, the generation of reproducible SDF's requires a proper control over the lubrication liquid layer thickness. A first assessment of this thickness can be made by checking whether there is a significant fluorescence intensity coming from the regions underneath the channel spacers. Using the currently employed injection method, the injected sample always contacts the entire front face of the stationary wall platelet [26]. As a consequence, the (fluorescently labeled) sample is also injected in the lubrication layer. When the lubrication layer is sufficiently thin, the fluorescence signal coming from this layer should be negligible compared to the intensity originating from the actual separation channel. Whereas this could relatively easily be achieved using channels with a nominal depth in the order of 200 nm and more, the CCD-images collected during the present study nearly always revealed a slight presence of fluorescently labeled sample underneath the channel spacer (see Fig. 6.4). This could not be prevented, not even by respecting very long waiting times, leading to the conclusion that the persistence of a relatively thick lubrication layer is due to the overall waviness of the employed substrate materials (represented schematically in Fig. 6.2b). This waviness prevents the lubrication layer thickness to decrease below a given minimal value.

A second parameter allowing to assess possible differences in the effective channel depth is the effective retention factor k' of the analytes, given by Eq. (6.3).

$$k' = K\frac{V_S}{V_m} = K\frac{\delta_{C18layer}}{d_{channel}} = K\frac{\delta_{C18layer}}{(h_{spacer} + \delta_{lub})} \qquad (6.3)$$

In this expression, δ_{lub} is the only variable parameter. Eq. (6.3) shows that, when δ_{lub} is significant compared to the spacer height, any change in its value will also directly contribute to an appreciable change in k'. In the conducted experiments, it was found that k' varied over a value of about 15% when completely repeating the experiment by disassembling the channel to thoroughly clean both channel parts with methanol and a nitrogen gas jet and reassembling the set-up afterwards. Since the 15%-repeatability of the k'-factor could not be improved by extending the wait time between the application of the normal load and the start of the

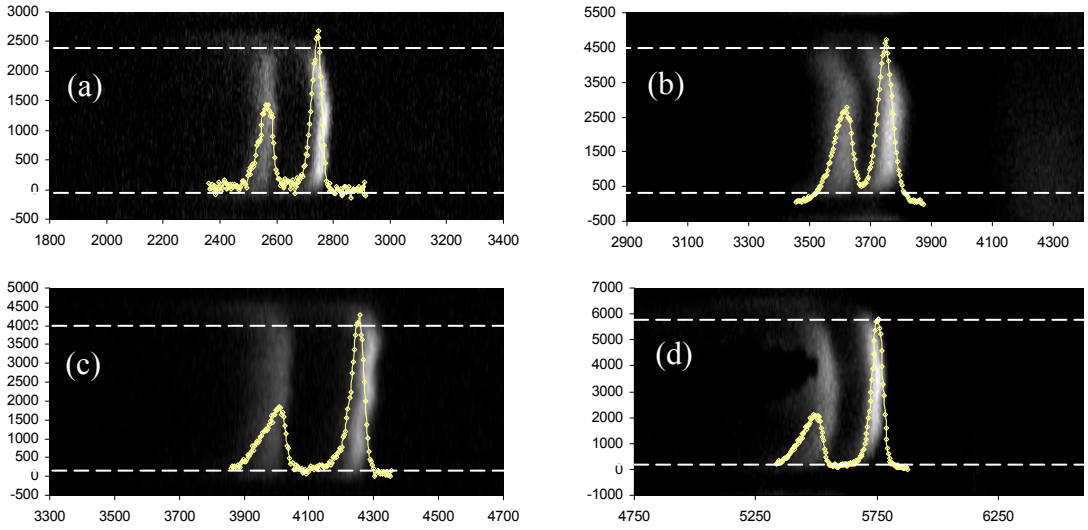

Figure 6.4. CCD-camera images of different separations of Rh110 (least retained peak) and Rh575 (most retained peak) in a 45nm deep channel measured at a mobile phase velocity of 5mm/s (corresponding to a moving wall velocity of 10mm/s). The effective liquid displacement distance in the different cases was respectively: **(a)** 2.75mm, **(b)** 3.75mm, **(c)** 4.25mm and **(d)** 5.75mm. The horizontal dashed lines demarcate the transition between the channel region and the spacers.

separation run, it can be inferred that the run-to-run variations are due to the small differences in the mutual position of the stationary and the moving wall which are inevitable when reassembling the channel. With a spacer height of 45 nm and 85 nm, a change in retention factor of 15% can, according to Eq. (6.3), be calculated to be of the order of some 6 to 12 nm. This is indeed on the same order as the overall surface waviness of the employed channel wall substrates. Despite these substrates had one of the best commercially available flatness values (flatness= $\lambda/20$, with λ=670nm), the cited flatness value still implies that the lowest and highest positions on the surface of the moving wall substrate (diameter = 50mm) can be expected to have a height difference of the order of 30 nm. As schematically represented in Fig 6.2b, the relatively large contact area between the stationary and the moving wall substrate (10 x 20 mm) can, combined with the surface waviness, indeed easily leads to changes in the lubrication layer thickness in the order of a few nanometers and more.

These deviations most probably also explain the variations in band broadening (quantified as the local plate height $H = \Delta\sigma_x^2/\Delta x$ calculated from the difference in spatial variance between two successive axial measurement points) along the channel axis observed in Figures 6.4 and 6.5. The represented measurements are taken from a series of subsequent runs with different moving wall travel lengths. The thus imposed effective liquid displacement distances (L_{eff}) ranged from 2.75 to 5.75 mm. For each displacement distance, five consecutive runs were

made. As can be noted from Fig. 6.5, the measured plate heights vary significantly with the elapsed distance (maximal variation on the order of 50% to 100%), while the variation between runs over the same displacement distance is much smaller than the variation between the different displacement distances. The observed pattern is very similar for both analytes (except for the last measurement point), corroborating the hypothesis that the observed variation is directly related to the surface profile of the employed substrates.

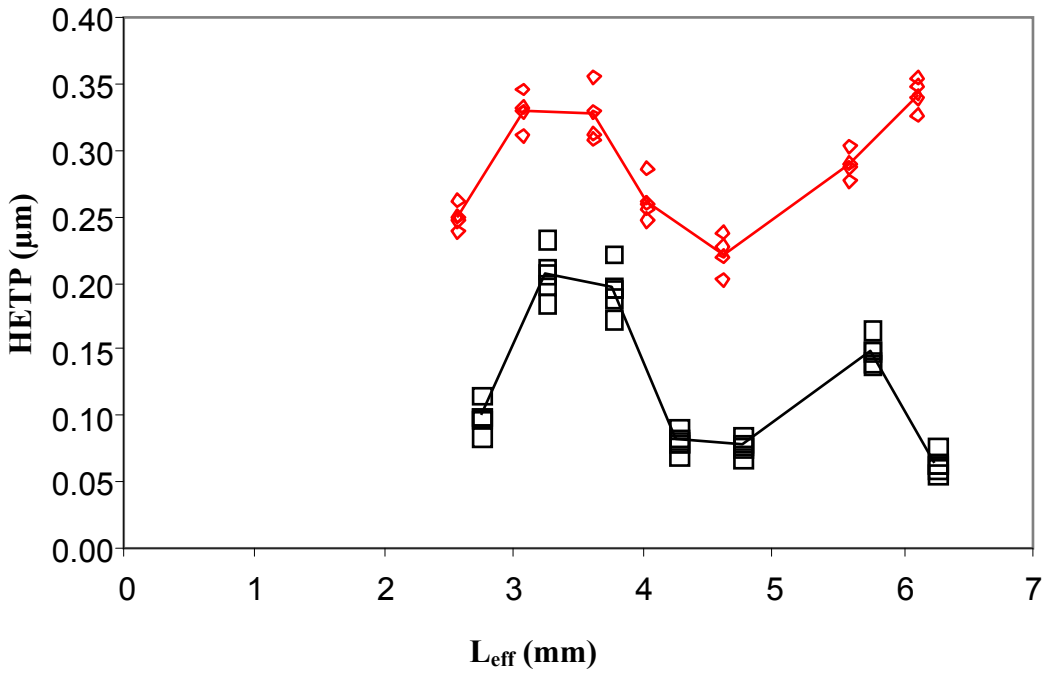

Figure 6.5. Plate heights measured at different axial positions in a 45nm deep SDF-channel. (□ Rh110, ◇ Rh575). The full lines connect the averaged values for each series of experiments at different axial positions.

The different CCD images shown in Fig. 6.4 respectively correspond to a separation efficiency of N= 27,000 and N=10,300 (for Rh110 and Rh575 respectively) for a liquid displacement distance of 2.75 mm (Fig. 6.4a), to a separation efficiency of N= 20,000 and N=11,000 for a distance of 3.75 mm (Fig. 6.4b), N= 51,000 and N=15,600 for a distance of 4.25 mm (Fig. 6.4c), and N= 39,000 and N=19,000 for a distance of 5.75 mm (Fig. 6.4d). In terms of plate heights, these efficiencies translate into values of the order of 0.1-0.2 µm for Rh110 and 0.25-0.3 µm for Rh575 (see Fig, 6.5 for a detailed overview). The highest efficiency value (N=99,000 plates, corresponding to the H=0.06 µm point at 6.25 mm) was measured for the largest travel distance (6.25 mm). Given that the fluid velocity in this experiment equaled 5 mm/s, this corresponds to a plate generation velocity of about 77,000

plates per second. We believe this is among the highest values ever reported in literature for liquid chromatography.

Despite the large variation in plate height observed among the different axial displacement distances, the variability among the values obtained for the same displacement distance is clearly much smaller. This good repeatability also allowed to measure a full Van Deemter curve to quantify the influence of the imposed liquid velocity on the band broadening, collecting all measurement points at the same axial distance (L_{eff} = 4 mm for the data represented in Fig. 6.6) to rule out the axial variation effect.

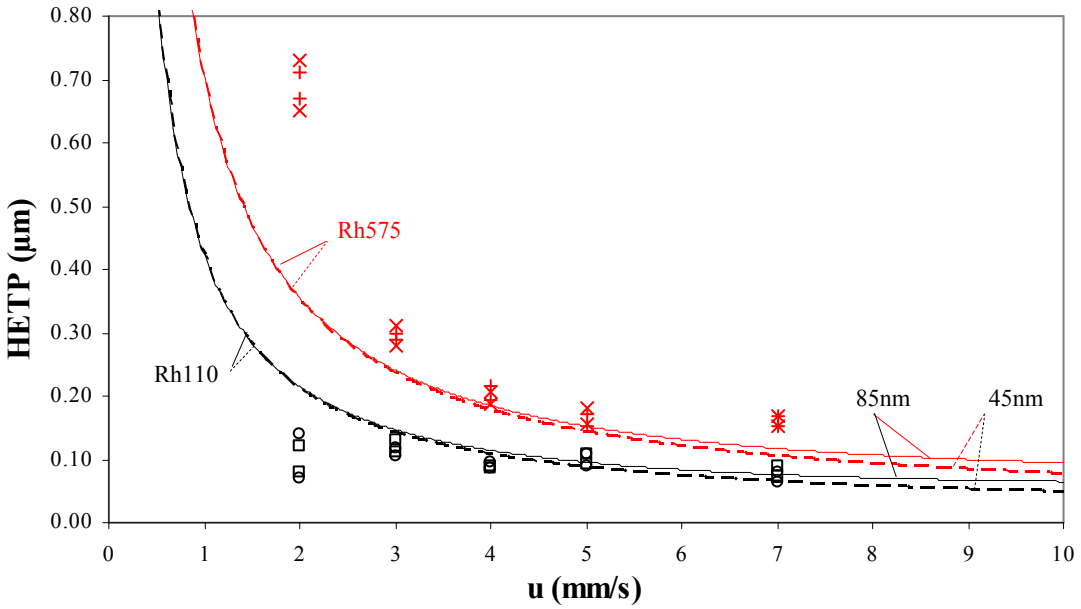

Figure 6.6. Experimental plate height values (red and black data points) measured in 45 and 85 nm deep SDF channels compared to the theoretical expectations (85nm: full lines; 45nm: dashed lines) determined via Eq. (6.4).

At a velocity of u=7 mm/s, the realized separation efficiency measured for a liquid displacement distance of L_{eff}=4 mm was on the order of N=40.000 theoretical plates for Rh110 and N=20,000 for Rh110 and Rh575 respectively. At the given speed, this corresponds to a plate generation of 70,000 to 35,000 plates per second. This is more than one order of magnitude faster than currently achievable with commercial liquid chromatography instruments, where the t_0-times needed to produce 70,000 plates are typically of the order of 1 to 2 minutes (see for example Fig. 7 in Cabooter et al. [34]). This corresponds to a plate generation velocity of "only" 1200 plates per sec (value cited for a pressure-driven packed bed column operated at 1000 bar). Translating the realized shear-driven flow velocities in the nano-channels into their

pressure-driven equivalent, it can be calculated from Poiseuille's law [30] for the pressure-drop in a channel with a flat-rectangular cross-section that a dazzling inlet pressure of 12,000 bar would have been needed in order to achieve the same velocity using the pressure-driven mode in the same 20 mm long and 45 nm deep channel.

The maximal plate generation velocities recorded in the present study are also larger than those obtained by Fekete et al. [25] (39,000-52,000 plates per second) in a 120 nm channel. However, the gain is clearly not in proportion to the roughly three-fold decrease in channel depth (45 versus 120 nm). This smaller-than-expected gain is clearly also related to the fact that no significant difference in separation efficiency can be observed between the two different channels depths (45 and 85 nm) for none of the velocities reported in Fig. 6.5. Although maybe surprising at first sight, this observation can be entirely explained from theory. Eq. (6.4) gives one of the explicit variants of Eq. (6.1), wherein the k'-dependency of f_1 and f_2 has been analytically calculated for the flat-rectangular channel cross-section and the linear flow profile of a SDF [17].

$$H = 2\frac{D_m}{u_m} + \frac{2}{30}\frac{1+7k'+16k'^2}{(1+k')^2}u_m\frac{d_{channel}^2}{D_m} + \frac{2}{3}\frac{k'}{(1+k')^2}u_m\frac{\delta_{C18layer}^{\ 2}}{D_S} \qquad (6.4)$$

In this equation, the single unknown experimental parameter is the liquid phase diffusion coefficient D_{mol}. To determine this value, a separate series of experiments was conducted in relatively deep (d = 1,4 μm), non-coated, channels for which it is known from a separate study [29] that the contribution of the wall or stationary phase diffusion coefficient is negligibly small (time spend in the mobile phase >>> time spent on the surfaces).

The diffusion coefficient experiments were conducted in the so-called peak parking mode [35], wherein a band was injected, transported to a given position in the channel where the flow was stopped and the gradual broadening of the band was then recorded in-situ using the CCD camera. From these measurements, the values for D_{mol} were obtained as one half of the slope of the straight-line relationship between the variation in band broadening ($\Delta\sigma_{band,x}^2$) and the elapsed time interval (Δt). The band diffusion was followed during 60 seconds. An image was captured every 3 s, to minimize the occurrence of photobleaching. The thus obtained values of D_{mol} for the Rh110 and Rh575-species are respectively given by: $D_{mol,Rh110} = (2{,}1 \pm 0{,}3) \cdot 10^{-10}$ m²/s and $D_{mol,Rh575} = (3{,}5 \pm 0{,}4) \cdot 10^{-10}$ m²/s. Using these values in Eq. (6.4), together with the nominal channel depths and the measured k'-values, it is found that the mass

transfer distances in the employed nano-channels are indeed so small in the covered range of velocities (u_m=1 to 7 mm/s) that the band broadening is fully dominated by the molecular diffusion term (first term of Eq. 6.4). As a consequence, the band broadening has become independent of the channel depth and the theoretical curves for the 40 and 85 nm channels nearly coincide perfectly (Fig. 6.6, full lines), hence also explaining why the measured plate heights in the 40 and 85 nm channels perfectly coincide with the measurement error margin.

According to Eq. (6.4), a difference in plate height between both channel depths can only be expected at higher mobile velocities (u_m > 10 mm/s), where the mass transfer contribution between mobile and stationary phase would become significant. Such high velocities are not achievable with the current set-up due to the limited acceleration of the translation stage.

6.4. Conclusions

High speed chromatographic separations have been conducted in nano-channels with two different depths (45 and 85 nm). Using the shear-driven flow principle, velocities as high as 7 mm/s could be realized. When using the conventional pressure-driven flow principle, this would have required an inlet pressure of about 12,000 bar. Due to the extremely small mass transfer distances (i.e., channel depths), the realized chromatographic separations were devoid of any mass transfer resistance, up to the highest realized velocities. As a consequence, the two different investigated channel depths produced very similar plate height values, fully dominated by the molecular diffusion term of the Van Deemter equation. Under these mass transfer resistance-free conditions, the highest realized separation efficiency was of the order of N=50,000 to 70,000 theoretical plates per second.

Given the fact that the channels already operate in mass transfer-free conditions, there is no need for a further reduction of the channel depth. This would practically also be very difficult because the surface variations caused by the large scale (long distance) waviness of the employed channel substrates can, despite their high degree of optical flatness (flatness of $\lambda/20$), no longer be neglected compared to the nominal channel depth.

References

[1] J. C. Giddings, *Dynamics of Chromatography, Part I: Principles and Theory (Chromatographic Science Series, Vol. 1)*, Marcel Dekker, New York, **1965**.

[2] M. J. E. Golay, *Gas Chromatography 1958 (Ed. DH Desty)*, Butterworths, London, **1958**.

[3] R. Aris, *Proceedings of the Royal Society of London. Series A. Mathematical and Physical Sciences* **1959**, *252*, 538–550.

[4] U. D. Neue, *HPLC Columns*, Wiley-VCH, New York, **1997**.

[5] L. D. Menard, J. M. Ramsey, *Analytical chemistry* **2013**, *85*, 1146–53.

[6] M. L. Kovarik, S. C. Jacobson, *Analytical chemistry* **2007**, *79*, 1655–1660.

[7] M. L. Kovarik, S. C. Jacobson, *Analytical chemistry* **2009**, *81*, 7133–7140.

[8] J. P. Kutter, *Journal of Chromatography A* **2012**, *1221*, 72–82.

[9] P. Abgrall, N. T. Nguyen, *Analytical chemistry* **2008**, *80*, 2326–2341.

[10] K. Mawatari, T. Tsukahara, Y. Sugii, T. Kitamori, *Nanoscale* **2010**, *2*, 1588–1595.

[11] M. Kato, M. Inaba, T. Tsukahara, K. Mawatari, A. Hibara, T. Kitamori, *Analytical chemistry* **2010**, *82*, 543–547.

[12] R. Ishibashi, K. Mawatari, T. Kitamori, *Journal of Chromatography A* **2012**, *1238*, 152–155.

[13] B. Wei, B. J. Rogers, M. J. Wirth, *Journal of the American Chemical Society* **2012**, *134*, 10780–10782.

[14] Z. Zhang, S. N. Ratnayaka, M. J. Wirth, *Journal of Chromatography A* **2011**, *1218*, 7196–7202.

[15] B. Wei, D. S. Malkin, M. J. Wirth, *Analytical chemistry* **2010**, *82*, 10216–10221.

[16] R. Singhal, V. N. Mochalin, M. R. Lukatskaya, G. Friedman, Y. Gogotsi, *Scientific reports* **2012**, *2*, 510.

[17] G. Desmet, G. V Baron, *Journal of Chromatography A* **1999**, *855*, 57–70.

[18] G. Desmet, G. V Baron, *Analytical chemistry* **2000**, *72*, 2160–2165.

[19] G. Desmet, N. Vervoort, D. Clicq, G. V Baron, *Journal of Chromatography A* **2001**, *924*, 111–122.

[20] Y. Cai, D. Janasek, J. West, J. Franzke, A. Manz, *Lab on a Chip* **2008**, *8*, 1784–1786.

[21] X. Yang, G. Jenkins, J. Franzke, A. Manz, *Lab on a Chip* **2005**, *5*, 764–771.

[22] M. S. Anderson, *Analytical chemistry* **2005**, *77*, 2907–2911.

[23] D. Clicq, N. Vervoort, R. Vounckx, H. Ottevaere, J. Buijs, C. Gooijer, F. Ariese, G. V Baron, G. Desmet, *Journal of Chromatography A* **2002**, *979*, 33–42.

[24] V. Fekete, D. Clicq, W. De Malsche, H. Gardeniers, G. Desmet, *Journal of Chromatography A* **2007**, *1149*, 2–11.

[25] V. Fekete, D. Clicq, W. De Malsche, H. Gardeniers, G. Desmet, *Journal of Chromatography A* **2008**, *1189*, 2–9.

[26] D. Clicq, K. Pappaert, S. Vankrunkelsven, N. Vervoort, G. V Baron, G. Desmet, *Analytical chemistry* **2004**, *76*, 430A–438A.

[27] D. Clicq, S. Vankrunkelsven, W. Ranson, C. De Tandt, G. V Baron, G. Desmet, *Analytica chimica acta* **2004**, *507*, 79–86.

[28] G. Desmet, N. Vervoort, D. Clicq, A. Huau, P. Gzil, G. V Baron, *Journal of Chromatography A* **2002**, *948*, 19–34.

[29] K. Pappaert, J. Biesemans, D. Clicq, S. Vankrunkelsven, G. Desmet, *Lab on a Chip* **2005**, *5*, 1104–1110.

[30] H. Schlichting, *Boundary-Layer Theory*, McGraw Hill, London, **1958**.

[31] J. N. Israelachvili, *Journal of colloid and interface science* **1986**, *110*, 263–271.

[32] M. L. Gee, P. M. McGuiggan, J. N. Israelachvili, A. M. Homola, *The Journal of Chemical Physics* **1990**, *93*, 1895.

[33] H. Poppe, *Chromatography, Fundamentals and Applications of Chromatograph and Related Differential Methods*, Elsevier, Amsterdam, **1992**.

[34] D. Cabooter, F. Lestremau, F. Lynen, P. Sandra, G. Desmet, *Journal of Chromatography A* **2008**, *1212*, 23–34.

[35] A. Liekens, J. Denayer, G. Desmet, *Journal of Chromatography A* **2011**, *1218*, 4406–4416.

Chapter 7

The Realization of 1.10^6 Theoretical Plates in Liquid Chromatography Using Very Long Pillar Array Columns

Abstract

We report on the possibility to achieve ultra high efficiencies (order of 1 million theoretical plates) in liquid chromatography in a relatively short time of 20 minutes (elution time of unretained marker). This was achieved using a micro-pillar array column with optimized pillar diameter (5 µm) and inter-pillar distance (2.5 µm) to operate close to the Knox & Saleem-limit of micro-pillar array columns in the region of the 1 million theoretical plate mark under the prevailing pressure restriction (350 bar in the present study). The obtained efficiency was slightly affected (some 15 to 20 % around the optimal flow rate) by the turns that were inevitably needed to arrange a 3 meter long column on a 4 inch silicon wafer.

This chapter has been published as:

The Realization of 1.10^6 Theoretical Plates in Liquid Chromatography

Using Very Long Pillar Array Columns

De Malsche W., Op de Beeck J., De Bruyne S., Gardeniers H., Desmet G.

Analytical chemistry **2012**, *84*(3), 1214-1219

DOI: 10.1021/ac203048n

7.1. Introduction

One of the persistent quests marking the history of liquid chromatography is the pursuit of very high separation efficiencies, in an attempt to approach and surpass those achievable in gas chromatography. Nowadays, considering the ever increasing sample complexity in the different "-omics"-fields, the need for high efficiencies is as timely as ever before. In these fields, the samples are so complex that even the most powerful LCxLC techniques [1] could benefit a lot from having one or both dimensions offering plate counts running in the hundreds of thousands or more.

The obvious way to generate extremely high efficiencies in one-dimensional-LC is to create very long separation paths, several meters long if possible. One of the earliest attempts to generate ultra high efficiencies was made by Scott and Kucera in 1979. By constructing a 14 m long (coupled) column filled with 5 μm particles, they demonstrated an impressive efficiency of 650,000 plates in a column dead time (t_0) of 8.3 h, working under non-reained conditions [2]. Using larger particles (7-8 μm) in an even longer column (22 m), Menet et al. [3] were able to produce ~1,000,000 plates in a t_0-time of 18 h and 24 h under non-retained and slightly retained conditions (k'=1.3), respectively. Given their higher permeability, and correspondingly lower separation impedance [4], monolithic columns are better suited to obtain ultra-high efficiencies than packed bed columns [5]. To demonstrate this, Tanaka et al. [6] coupled a number of columns packed with small sized silica skeletons and relatively large flow-through pores to reach a total column length of about 12 m. This column was capable of producing 1,000,000 plates for a retained component (k'=2.4) in only 2.5 h using a pressure of the order of 400-500 bar.

Following upon the seminal work of Regnier [7,8], micro-pillar array columns (PAC's) were introduced during the last decade as a powerful alternative for classical packed bed columns and monoliths [9–13]. While the maximal order of the chromatographic bed in PAC's induces a decrease of the plate height by a factor of 2 or more compared to a packed bed column packed with particles of the same size, also the flow resistance (ϕ) can be drastically reduced compared to what is observed in densely packed channels (for a 40 % porosity cylindrical PAC, the pressure drop is reduced by 32 %; ϕ = 405 for a non-porous packed-bed column whereas ϕ can be easily below 100 for a PAC with a higher external porosity) [14]. These low plate heights have been demonstrated using PAC's containing both porous and non-porous

pillars with diameters between 10-3 μm [15,16], observing dispersion inside the column using fluorescence microscopy. Recently, Lavrik et al pushed the minimal plate height even lower to 0.76 μm by fabricating pillars with diameters of only 1.9 μm and a spacing of about 1 μm, using PECVD deposition of SiO_2 after the etching step to reduce the inter-pillar distance [13]. Whereas the above results were obtained on short channel segments of only a few cm long, hence leading to only relatively small plate numbers, Aoyama et al.[12] published a study on a serpentine PAC with a total length of 110 mm and containing turns filled with micro-pillars and designed according to the work of Griffiths et al. [17]. The square pillars in their columns had a wall-to-wall distance of 3 μm and a spacing of 2 μm. The turns gradually decreased from a channel width of 400 μm to a circular turn with a width of 110 μm. With these turns, the plate height (corrected for injection volume) only increased from 2.7 μm (value measured in a straight part of the column) to 3.5 μm (value incorporating the effect of the turns) for the case of a non-retained component eluting at a mobile phase velocity of ~1.3 mm/s, demonstrating that a serious improvement is obtained as compared to dramatic dispersion that occurs for the constant radius situation (H=510 μm) [12]. In the present study, it was attempted to stretch the efficiency limits of PAC's to the extreme by pursuing the achievement of 1 million theoretical plates. For this purpose, a PAC-chip was designed and optimized to deliver the desired number of plates in the shortest possible time, considering a preset maximal pressure limit.

7.2. Experimental

7.2.1. Chemicals

Coumarin C480 (Cas no. 41267-76-9, Across Organics, Belgium) was dissolved in HPLC-grade methanol at a final concentration of 1×10^{-3} M, after which it was filtered.

7.2.2. Microfabrication

A detailed description of the mask layout and manufacturing of the very long pillar array can be found in §3.5.2.

7.2.3. Injection and detection

The sample injection was performed using an automated valve system, controlled with an in-house written C++ program, as already described in. For the mobile phase propagation an Agilent 1100 series nano-pump (Agilent Technologies, Waldbronn, Deutschland GmbH) was

used. During the sample injection step, the automated valve system ensures that the inlet and the outlet of the mobile phase circuit were closed.

During the subsequent sample separation, the inlet and the outlet of the sample injection circuit were diverted to a high flow resistance capillary, allowing for the existence of a small leakage flow and thus avoiding tailing. A Hg-vapour lamp was used to excite the fluorescent dye in the UV. The peaks were visualized using an air-cooled CCD fluorescence camera (Hamamatsu Photonics K.K., Japan). The peak intensity profiles were subsequently analyzed using the accompanying Simple PCI® image analysis software. On-column chromatograms were obtained by averaging a row of pixels and plotting its values in function of time. For the determination of the peak widths and plate heights, the peak fluorescence intensity was averaged across the channel width. The thus obtained axial concentration distribution was subsequently fitted with a Gaussian function using Sigmaplot®. The concentration profiles and the accompanying variances were determined at 2, 3, 10 and 20 cm downstream the injection H is then obtained as $(\sigma_{x,e}^2 - \sigma_{x,0}^2)/ \Delta x$, wherein $\sigma_{x,e}$ and $\sigma_{x,0}$ are the variance of the injected band at the end and the initial position and wherein Δx is the distance between both positions.

7.3. Results and Discussion

7.3.1. Design and Fabrication

From the kinetic optimization theory of LC [18,19], it is well known that, once the packing format has been decided upon, the fastest way to produce a preset number of theoretical plates is to select the size of the packing elements and the length of the column such that the system produces the required number of theoretical plates when applying a flow rate that simultaneously corresponds to the minimum of the Van Deemter curve, as well as to the maximal allowable pressure. It can be shown that the optimal particle size (pillar diameter in the present case) is given by [20]:

$$d_{pil} = \sqrt{\frac{N\eta D_m h_{min} v_{0,opt} \phi}{\Delta P}} \qquad (8.1)$$

Putting $N = 10^6$, $h_{min} = 0.5$ and $\phi = 100$, based on the results obtained in earlier studies [9,21] and adding a safety margin, Eq. (8.1) returns a value of a $d_{pil} = 4.83$ µm as the optimal pillar size when assuming a pressure drop of 150 bar (set value taken well below the available 350

bar as an additional safety margin). The required column length (calculated via $L=N.h_{min}.d_{pil}$) was subsequently found to lie around L=3 m. A mask was designed aiming for a pillar size with d_{pil}=5 μm and an inter-pillar distance of 2.5 μm and a total column length of 3.1 m. After etching, the pillar sizes turned out to be 5.2 and 2.3 μm respectively, and the column porosity was about ε=0.54. Such small deviations between the original mask drawing and the finally etched structure are difficult to avoid with the currently available lithography techniques. The deviations are however deterministic, so that when the same lithographic procedure is exactly repeated, a very good column-to-column reproducibility can be expected. The deviations between the mask design and the etched PAC unfortunately also occurred for the dimensions characterizing the side-wall. As can be noted from Figure 7.1d, the side-wall was designed as a series connection of embedded semi-pillars, following the design rules established in [22]. The main advantage of the pillar-embedded side wall over the straight sidewalls used in some of our previous work [9,23] is that the optimal distance between the side wall and the nearest row of pillars is larger in the pillar-embedded wall case, thus loosening the required machining tolerances. Despite this advantage, one of the two characteristic side-wall distances was significantly off the mask design in the finally obtained etched column (2.11 μm versus 3.26 μm on the mask). The second characteristic dimension on the other hand was only 0.05 μm off (2.10 μm versus 2.15 μm on the mask). The large deviation for the first characteristic side-wall distance is due to the fact that the cavity formed by the space between subsequent semi-pillars is rather narrow, leading to a poor illumination of that area.

As a consequence, the flow near the side-wall experienced a higher resistance and was therefore slightly slower than in the central part of the bed (about 1.4%), thus giving rise to the type of additional side-wall band broadening visible in for example Figure 2 of De Malsche et al. [9], although the effect was more pronounced in the latter case, as the difference in velocity between the side-wall region and the central part of the bed in that case was of the order of 40%. Since the plate height contribution of this side-wall effect can be expected to be proportional to the square of the channel width [24], it was preferred to keep the column width relatively small (150 μm), i.e., much smaller than the 1 mm wide columns typically used in most our previous work [9,21].

Another critical aspect in the etching is the pillar slope. This should be as vertical as possible in order to avoid any tapering and the creation of a velocity gradient running between the top and bottom plate. Past experiments and theoretical considerations have also learned that the

presence of the top and bottom plate inevitably leads to an extra source of band broadening, increasing with increasing channel depth until it saturates at some maximal value [25,26]. For both reasons it was to limit the depth of the etched column to somewhere between 5 and 10 µm, as a compromise between the mass loadability (needed for detection purposes) and the additional band broadening that may occur if the channels would be too deep.

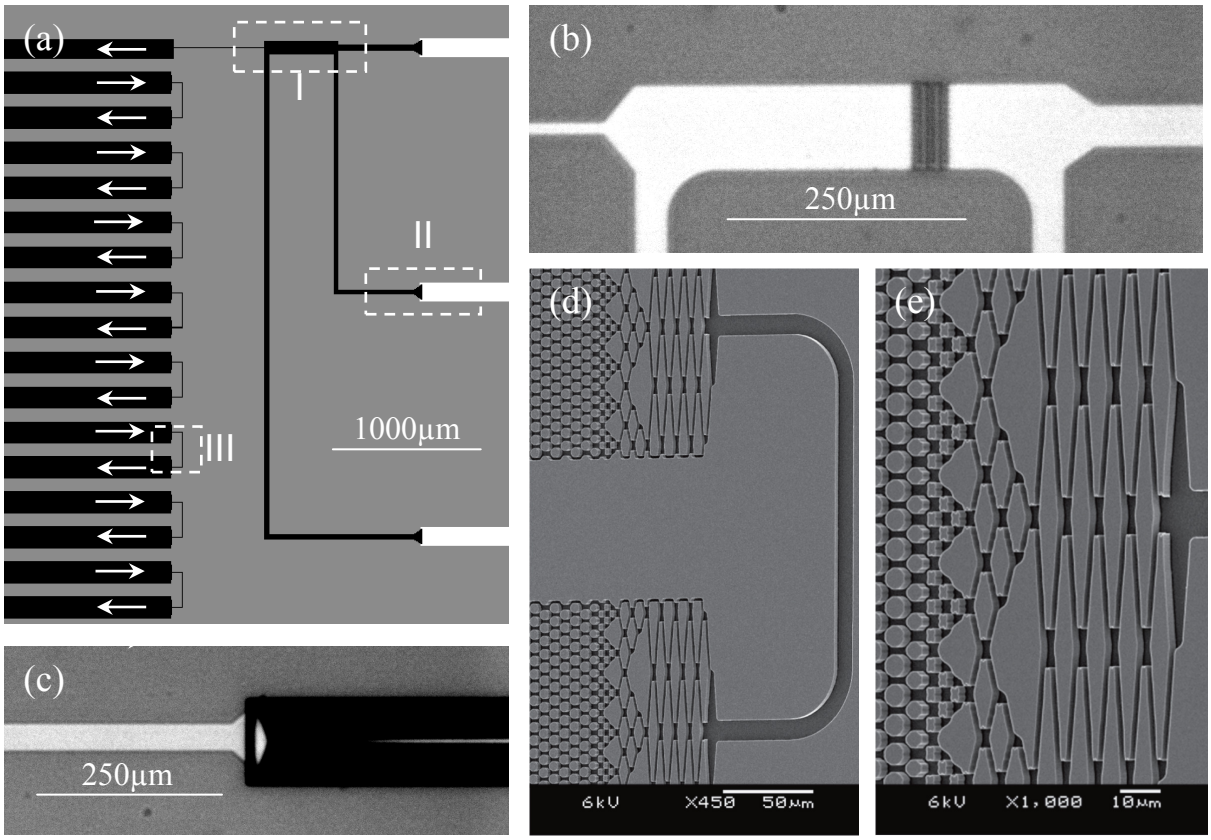

Figure 7.1 (a) Schematic representation of the column design, showing the injection zone (I) and a part of the connected separation lanes. The arrows in the separation lanes indicate the direction of the flow in each lane. Supply channels are preceded by 140 µm deep grooves (II) in which capillaries (108 µm O.D., 40 µm I.D.) are glued. Each pillar lane has a turn segment (III) consisting of a distributor frit and a narrow turn at each side, only one side of the pillar lanes is shown. **(b)** Optical image of the injection zone (I in (a)), **(c)** Optical image depicting the capillary glue channel (II in (a)), **(d)** SEM image showing parallel channel tracks of 150 µm wide connected by a 10 µm wide channel and distributor structures (III in (a)), hence avoiding a race track effect. **(e)** Close-up of the distributor structure.

To arrange the 3 m long column on the surface of the 4 inch silicon wafers employed in the present study, the channel design inevitably needs to include a large number of turns to connect the different bed segments (Figure 7.1a,d). To minimize variations in packing dimensions across the column length, it was preferred to etch the channel only in the central part of the wafer, as it is well known that the etching quality tends to vary when approaching the boundary of the wafer. As a consequence, the length of the different bed lanes was limited to 5 cm. To minimize the losses caused by the turns because of the so-called racetrack effect

[7], the width of the actual turn segments was minimized (10 µm wide, see Figure 7.1d) while the transition between the 150 µm wide the transition between the 150 µm wide separation channels and the turn channels was made via two flow distributors, (see Figure 7.1e for detail) designed according to the optimal design rules obtained in a computational fluid dynamics study [22]. In this optimized design, the aspect ratio of the transversally stretched pillars grows from around unity close to the separation bed to about a factor of 10 at the other end of the distributor.

The turn design recently proposed by Aoyama et al. [12] also appears to be very promising. These authors proposed a design wherein a (asymmetric) transition towards a narrower turn channel is facilitated, however with a continuously bending turn zone. In the design that is used in the current study, there is only a very small region where such an asymmetrical situation is present (i.e. at the turn region, which only extends for some 50 µm per turn). The main advantage of the Aoyama et al.-design [12] appears to be the fact that their turns are filled with pillars, thus reducing the local mass transfer distances and lowering the band spreading in the turn. Obviously, this occurs at the expense of a higher pressure drop. A detailed comparison study of both approaches covering a wide range of mobile phase velocities and channel widths would be needed to identify which one of either approaches (or a combination of both) works best.

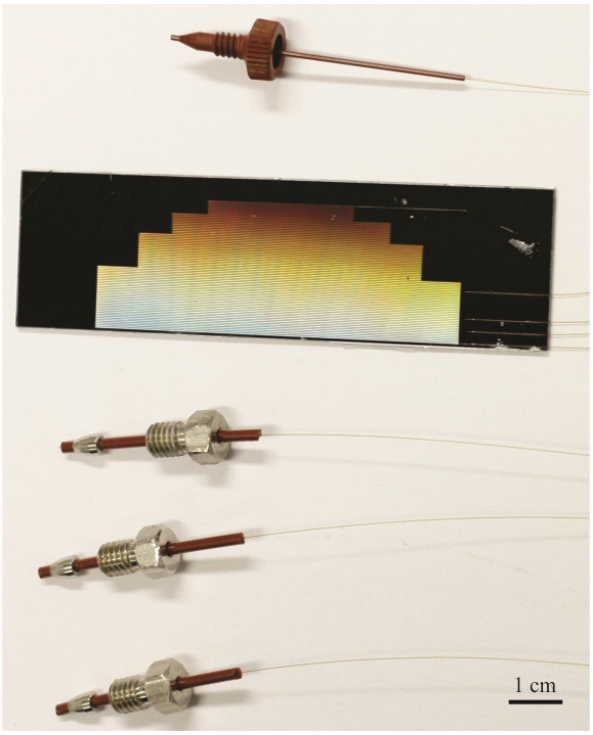

Figure 7.2. Optical image of the 3 m long pillar array columns and the connection capillaries and fittings.

In previous studies the maximum attainable pressure was determined by the limiting operation range of the commercially available Upchurch nanoports, with a maximum leak-free pressure of 50-90 bar. In order to be competitive with traditional HPLC columns, larger operating pressures are required. For this, dedicated connection channels were DRIE etched (120 μm wide and 140 μm deep) ending at the inlet of the PAC (see Figures 7.1 and 7.2). After inserting 108 μm diameter capillaries, epoxy glue was applied at the orifice, where the remaining space ensured an effective capillary action of a few mm, until the glue was hardened. Figure 7.2 depicts the interfacing between the chip and the capillary and the fittings. By applying a mobile phase flow (methanol) through this connection with a capillary HPLC system, it appeared that leakages typically occurred between 350 and 400 bar. Inspection of the leakage revealed a local burst in the glass lid at the inlet zone of the PAC. Besides a mobile phase inlet, also a sample phase inlet and outlet is etched so that very controlled sample plug volumes can be defined (typically smaller than 1 nl). This type of on-chip injection was preferred since the minimal injection volume of commercially available HPLC hardware is typically a few tens of nl, not taking into account the band broadening due to connections and tubing that has to be passed before the separation column is reached.

7.3.2. Column Permeability and Efficiency

Measuring the pressure drop over a wide range of linear velocities (1–7 mm/s, a nearly perfect linear relationship was obtained. From the slope, a bed permeability of $K_v=2.8\ 10^{-13}$ m^2 was calculated. At a linear velocity of 3 mm/s, this for example corresponds to a pressure drop across the bed of about 160 bar, i.e. well below the maximal pressure (350 to 400 bar) that could be delivered by the instrument pump.

In terms of flow resistance (pillar diameter based), the measured flow resistance turns into a value of ϕ=208, which is close to the theoretical expectations calculated numerically by De Smet et al [14], predicting a value of ϕ ranging from ϕ = 274 to ϕ = 121 to ϕ =56 when the external porosity varies from ε = 0.4 to ε = 0.6 to ε =0.8. This result shows that the contribution of the turns and the top- and bottom plates to the flow resistance is negligibly small. This low flow resistance (about 4 times smaller than in a packed bed of non-porous particles) is a crucial factor in the separation speed, since the maximal speed with which a desired number of theoretical plates can be generated is fully determined by Knox' separation impedance number $E_{min} = h_{min}^2\phi$.

By selecting a vertical row of pixels and averaging the values and monitoring this obtained average in function of time, a local chromatogram is obtained. By moving the chip to different positions, local dispersive sources can be studied and assessed.

By moving the microscope lens to different positions along the column, the movement of an injected species band can be followed along the different locations in the column. Figure 7.3 shows an example of such a recording, where first the passage of the band was recorded at some 10 cm downstream of the injector, then a second time at some 20 cm downstream, and finally at the end of the column, where the measured peak standard deviation of σ_t = 1.03 s and the total residence time of 1103 s correspond to some 1.07 10^6 theoretical plates, corresponding to a reduced plate height of h = 0.56 (reduced on the basis of the pillar diameter) or h = 0.38 (reduced on the basis of the domain "size" = "pillar-diameter" + "inter-pillar distance"). These values are somewhat larger than some of the values already reported before [9,21]. The latter values however are only related to the central part of the band (not accounting for the side-wall effect), whereas the currently obtained values incorporate the side-wall effect.

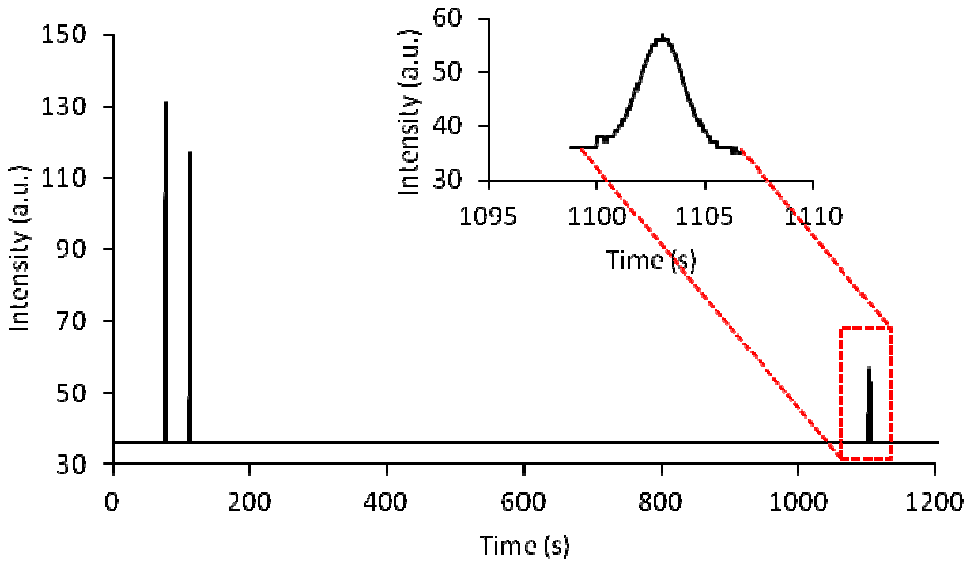

Figure. 7.3. Chromatogram of the same (C480) species band detected at different positions in the channel (10 cm, 20 cm and 308 cm). The y axis reflects the fluorescence emission signal as measured by the CCD camera.

Turning the measured peak width into a volumetric standard deviation (σ_V), it can be calculated that the band elutes from the column with a peak volume of about V_{peak}=4.2 nl ($V_{peak} = (2\pi)^{½}\cdot\sigma_V$). Comparing this to the amount injected (on the order of V_{inj}=0.5 nL), it can be concluded that the contribution to the peak variance caused by band broadening is significantly larger than from the injection volume.

To study the performance in more detail, and more specifically the contribution of the turns, Van Deemter curves were measured within the same track (bottom curve in Figure 7.4), and over a distance covering two tracks and two turns (top curve in Figure 7.4). The van Deemter curve contains also the value obtained at the end of the 3m long column (large circle). For the establishment of large mobile phase velocities of the van Deemter plot, a fraction of the channel tracks was removed in order to reduce the pressure drop. As can be noted from Figure 7.4, the effect of the turns is significant, but acceptable, especially around the optimal velocity, where the turns increase H_{min} by some 10 to 15% from 2.3 µm to 2.7 µm. In the large velocity range, the contribution of the turns is more significant, as the increase in plate height they induce seems to be proportional to the mobile phase velocity. This suggests that the turns induce a C-term like dispersive effect. This is in agreement with theory. Giddings has already addressed the concept of band dispersion at turns in 1960 [27]. Being relevant at the time for coiled GC columns, he calculated the dispersion at a turn showing that the laterally induced concentration gradients can indeed be treated as a non-equilibrium effect.

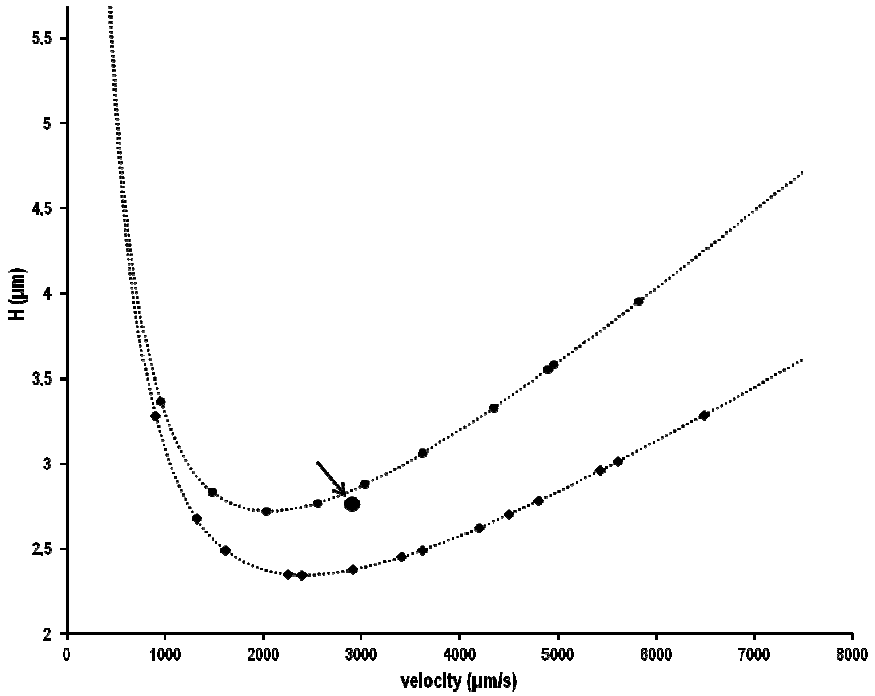

Figure 7.4. Van Deemter curves and fits (dotted lines) of C480 in methanol obtained in a 150 µm (7.2 µm deep) determined over a 2 cm channel length within the same track without turn (bottom curve) and over a 10 cm channel length including two turns (top curve). The arrow indicates the plate height measured at a channel length of 2.9 m.

Repeating our experiments under retained conditions (using 70/30 (v/v) water/methanol as the mobile phase and coumarin C440 and C480 as the analytes) in generally lead to poor performances compared to the theoretical expectations [9] and the excellent performance under non-retained conditions. We believe this is due to the high concentrations that needed

to be injected to rise above the detection limit of the CCD-camera. These high concentrations (1-3 μM) are suspected to lead to mass overloading conditions in the presently employed non-porous pillar array system. Where we theoretically expected a plate height of about 4 to 5 μm, based on the theoretical calculations of De Smet et al. [14], we only measured a minimal plate height of 8 μm. To solve this overloading problem, either fully porous or porous shell micro-pillars would be needed [15,21]. These have a considerably higher (roughly 200 times) mass loadability. Given that the surface to volume ratio in the turns is smaller than in the bed (roughly some 4 times smaller), it can be expected that the effect of the presence of the turns will be smaller under retained than under non-retained conditions, because, when the components will for example have a retention factor of 5 to 10 in the bed, they will only experience a retention factor of the order of 1.3-2.6 in the turns. This reduces the band broadening contribution of the turns compared to that of the bed, an effect which is not present under non-retained conditions.

7.4. Conclusion

Using 10 μm wide turns interconnecting the different separation lanes of a 3 m long micro fabricated column, interfacing the 150 μm wide separation lanes with the turns using flow distributors whose internal structure was optimized using computational flow dynamics, the efficiency losses caused by the turns can be minimized so that a total plate count of over 1 million theoretical plates can be realized in less than 20 minutes (elution time of the t_0-marker). This is significantly faster than previous 1 million plate systems realized using packed bed or monolithic columns. Using on-chip injection and detection to measure the Van Deemter curve of a coumarin dye under non-retained conditions, minimal plate heights between 2.4 (without turns) and 2.7 μm (with turns) were observed. Detecting at the end of the column, 1.07 10^6 theoretical plates were obtained, revealing an enormous separation potential, especially considering that the obtained result is still negatively influenced by an imperfectly etched side-wall region, representing an additional source of band broadening. Unfortunately, the performances under retained conditions were less good (minimal plate heights in the order of 8 μm), most probably due to the fact the present study was conducted under overloading conditions for the retained analytes.

References

[1] S. W. Simpkins, J. W. Bedard, S. R. Groskreutz, M. M. Swenson, T. E. Liskutin, D. R. Stoll, *Journal of Chromatography A* **2010**, *1217*, 7648–7660.

[2] R. P. W. Scott, P. Kucera, *Journal of Chromatography A* **1979**, *169*, 51–72.

[3] H. G. Menet, P. C. Gareil, R. H. Rosset, *Analytical Chemistry* **1984**, *56*, 1770–1773.

[4] N. Tanaka, H. Kobayashi, K. Nakanishi, H. Minakuchi, N. Ishizuka, *Analytical chemistry* **2001**, *73*, 420–429.

[5] J. Billen, G. Desmet, *Journal of chromatography. A* **2007**, *1168*, 73–99.

[6] K. Miyamoto, T. Hara, H. Kobayashi, H. Morisaka, D. Tokuda, K. Horie, K. Koduki, S. Makino, O. Núñez, C. Yang, T. Kawabe, T. Ikegami, H. Takubo, Y. Ishihama, N. Tanaka, *Analytical chemistry* **2008**, *80*, 8741–8750.

[7] B. He, N. Tait, F. Regnier, *Analytical Chemistry* **1998**, *70*, 3790–3797.

[8] B. E. Slentz, N. A. Penner, F. Regnier, *Journal of separation science* **2002**, *25*, 1011–1018.

[9] W. De Malsche, H. Eghbali, D. Clicq, J. Vangelooven, H. Gardeniers, G. Desmet, *Analytical chemistry* **2007**, *79*, 5915–5926.

[10] K. B. Mogensen, F. Eriksson, O. Gustafsson, R. P. H. Nikolajsen, J. P. Kutter, *Electrophoresis* **2004**, *25*, 3788–3795.

[11] X. Illa, W. De Malsche, J. Bomer, H. Gardeniers, J. Eijkel, J. R. Morante, A. Romano-Rodríguez, G. Desmet, *Lab on a Chip* **2009**, *9*, 1511–1516.

[12] C. Aoyama, A. Saeki, M. Noguchi, Y. Shirasaki, S. Shoji, T. Funatsu, J. Mizuno, M. Tsunoda, *Analytical chemistry* **2010**, *82*, 1420–1426.

[13] L. C. Taylor, N. V Lavrik, M. J. Sepaniak, *Analytical chemistry* **2010**, *82*, 9549–9556.

[14] J. De Smet, P. Gzil, N. Vervoort, H. Verelst, G. V Baron, G. Desmet, *Journal of Chromatography A* **2005**, *1073*, 43–51.

[15] W. De Malsche, H. Gardeniers, G. Desmet, *Analytical chemistry* **2008**, *80*, 5391–5400.

[16] N. V Lavrik, L. T. Taylor, M. J. Sepaniak, *Analytica chimica acta* **2011**, *694*, 6–20.

[17] S. K. Griffiths, R. H. Nilson, *Analytical chemistry* **2001**, *73*, 272–278.

[18] J. H. Knox, M. Saleem, *Journal of chromatographic science* **1969**, *7*, 614–622.

[19] J. H. Knox, *Journal of Chromatographic Science* **1980**, *18*, 453–461.

[20] G. Desmet, D. Clicq, P. Gzil, *Analytical chemistry* **2005**, *77*, 4058–4070.

[21] F. Detobel, S. De Bruyne, J. Vangelooven, W. De Malsche, T. Aerts, H. Terryn, H. Gardeniers, S. Eeltink, G. Desmet, *Analytical Chemistry* **2010**, *82*, 7208–7217.

[22] J. Vangelooven, G. Desmet, *Journal of Chromatography A* **2010**, *1217*, 8121–8126.

[23] N. Vervoort, J. Billen, P. Gzil, G. V Baron, G. Desmet, *Analytical chemistry* **2004**, *76*, 4501–4507.

[24] K. Broeckhoven, G. Desmet, *Journal of Chromatography A* **2007**, *1172*, 25–39.

[25] J. De Smet, P. Gzil, G. V Baron, G. Desmet, *Journal of Chromatography A* **2007**, *1154*, 189–197.

[26] H. Eghbali, W. De Malsche, J. De Smet, J. Billen, M. De Pra, W. T. Kok, P. J. Schoenmakers, H. Gardeniers, G. Desmet, *Journal of separation science* **2007**, *30*, 2605–2613.

[27] J. C. Giddings, *J. Chromatog* **1960**, *3*, 520–523.

Chapter 8

Porous-shell pillar array column separations on a capillary LC instrument

Abstract

We investigated the achievable separation performance of a 9 cm long and 1 mm wide pillar array channel (volume=0.6 μL) containing 5 μm diameter Si pillars (spacing 2.5 μm) cladded with a meso-porous silica layer with a thickness of 300 nm when this channel is directly interfaced to a capillary LC instrument. The chip has a small footprint of only 4 cm x 4 mm and the channel consists of three lanes that are each 3 cm long and that are interconnected using low dispersion turns consisting of a narrow U-turn (10 μm), pro- and preceded by a diverging flow distributor. Measuring the band broadening within a single lane and comparing it to the total channel band broadening, the additional band broadening of the turns can be estimated to be of the order of 0.5 μm around the minimum of the van Deemter curve, and around some 1 μm (non-retained species) and 2 μm (retained species) in the C-term dominated regime. The overall performance (chip + instrument) was evaluated by conducting gradient elution separations of digests of cytochrome c and bovine serum albumin. Peak capacities up to 150 could be demonstrated, nearly completely independent of the flow rate.

This chapter has been published as:

Separations using a Porous-shell pillar array column on a capillary LC instrument

De Malsche W., De Bruyne S., Op de Beeck J., Eeltink S., Detobel F., Gardeniers H., Desmet G.

Journal of Separation Science **2012**, *35*, 2010-2017

DOI: 10.1002/jssc.201200279

8.1. Introduction

Since the introduction of the 'micro-total analysis system' (μTAS) concept by Manz [1], it has become apparent that miniaturization offers numerous advantages. Besides the reduction of sample and solvent volumes, also the ability to integrate several functions in series or parallel on a small foot-print, offers undeniable advantages for a large number of applications. A reductionof the critical dimensions of the device using microfabrication technology can result in improved chemical or analytical functions. For the specific case of liquid chromatography, the possibility to create a packing with a high degree of order and a small flow resistance opens the road to produce highly permeable columns that are nearly completely devoid of the eddy-dispersion compromising the separation performance of the conventionally used packed bed columns [2]. In the early years of the μTAS-era, the development of micro-machined separation systems was almost exclusively focused on electrokinetic separation methods such as CE, CEC or MEKC [3]. A large number of problems have prevented the early development of pressure-driven HPLC chips, such as the on-chip application of high pressures and the manufacturing of columns with sufficient sample capacity [3]. The ultimate role of microtechnology could be to tailor the external porosity and packing geometry to the separation specifications at hand while simultaneously providing mass loadability by using an internally porous column material [4].

Simultaneously, also more macroscopic approaches based on polymerization have been pursued to improve the separation performance. The introduction of polymer and silica monolithic columns nearly 2 decades ago created an enormous momentum to develop novel packing structure for HPLC [5–10]. With their high permeability and easy integration into longer columns, monoliths were identified as the best suitable columns to perform high efficiency separations. The lower pressure drop in monoliths is a consequence of the possibility to tune the external porosity to relatively high values, much higher than the characteristic porosity of 40 % in packed bed columns. At the end of the 90's, a similar positional freedom was pursued by introducing the concept of micro-machined fused-silica pillar array columns (PAC's). Initially only being used to conduct CEC separations [11], the idea was picked up a few years later by several groups [12–14] to perform pressure-driven separations as well. Instead of using fused-silica, this new generation of PAC's was produced in Si. Using the well established Bosch® procedure [15], this material allows obtaining pillars with vertical sidewalls, even at extremely high aspect ratios (pillar height/inter-pillar distance) of 20 and more. With these columns, it could be demonstrated that the induced order results in

a reduction of the minimal reduced plate height h_{min} by a factor of 2 or even more. An important bottleneck of these PAC's is however their limited specific surface. A number of strategies have been put forward to tackle this issue. Using an HF-based anodization procedure in highly B-doped Si wafers, our group has generated conformal porous layers on Si pillars. Growing a 1 µm thick layer in a 10 µm diameter PAC (40 % porosity), this resulted in an estimated specific surface increase of a factor of 260 compared to fully solid pillar, while maintaining a minimal reduced plate height of h_{min} ~1, even at retention factors of k'=12 [16].

Other strategies to introduce porous layers in PAC's on chips have been described in the last few years. The Kutter group implemented the 'black silicon method', a process that relies on a competition between passivation and anisotropic etching, to form 5 µm high needles with 0.5 µm flow-through pores [17]. Another interesting approach, adopted by Fonverne et al. [18], consists of applying carbon nanotubes (CNT's) on pillars before bonding them to a glass lid. To ensure proper bonding, a small gap had to be maintained to avoid CNT growth at the bonding surface.

Another strategy to apply the porous layer after bonding in pillar array columns (PAC's) was applied by Detobel et al, merging the well developed sol-gel technology to fabricate silica monoliths with the micro-PAC technology [19]. It was shown that, by tuning the ratio of the domain size of the bulk monolith to the inter-pillar distance, two distinct situations can be obtained. On the one hand (when the domain size/inter-pillar distance approaches unity), it is possible to establish a quasi-ordered 3D network of linear interconnections, with the branches oriented perpendicular to the pillars. On the other hand (high values of domain size/inter-pillar distance), the pillars can be uniformly coated with a meso-porous shell.

In the present study, the latter approach is used to produce micro-pillar array columns with a retention capacity that is sufficiently high to generate broad elution windows in the reverse-phase chromatography mode, as well as to enable a wider dynamic range of detectable concentrations than is possible with non-porous pillars. The main aim of the present study was to investigate the separation performance under practically relevant conditions, i.e., by performing protein digest separations and coupling the chips to the injector and detector of a standard capillary LC instrument (UV-Vis detection). To allow interpreting the results obtained with the cladded chips, a series of non-cladded chips was characterized prior to cladding as well.

8.2. Experimental

8.2.1. Chemicals and instrumentation

Acetonitrile (ACN, HPLC supra-gradient quality) and trifluoroacetic acid (TFA, ULC/MS quality) were purchased from Biosolve B.V. (Valkenswaard, The Netherlands). Poly(ethylene glycol) (PEG, MW 10 000), urea, tetramethoxysilane (TMOS), acetic acid, HPLC-grade methanol, anhydrous toluene, and octyldimethylchlorosilane were purchased at Sigma-Aldrich Inc., St. Louis, MO.

HPLC experiments were performed using an UltiMate 3000 Proteomics MDLC system (Dionex, Germering, Germany) consisting of a dual-ternary gradient pump with membrane degasser, a thermostatted flow-manager module equipped with a 1:300 flow splitter, a well-plate autosampler, and a variable-wavelength detector equipped with a 3-nL z-shaped flow cell. The injection volume was 1 µl, mobile phase A= 0.05% aqueous TFA, mobile phase B = 80:20% ACN:H_2O containing 0.04% TFA. UV detection was performed at 214 nm (10 Hz data collection rate; 0.1 s response time). Cytochrome C digest (lyophilized) was purchased from Dionex (P/N 161089) and dissolved in an aqueous solution (5 % AN, 0.05 TFA) to obtain a final concentration of 125 pmol/µl.

8.2.2. Chip fabrication

A 9 cm long and 1 mm wide pillar-array channel (mask design: 5 µm diameter pillars, inter-pillar distance 2.5 µm) was patterned using broadband UV photolithography (photoresist, Olin 907-12), followed by a dry etching step (Adixen AMS100DE, Alcatel Vacuum Technology, Culemborg, The Netherlands) to etch the 200 nm thick SiO_2 hard mask underneath. The cylindrical shape was chosen because it is theoretically expected to yield porous layers with the highest degree of uniformity. Other shapes with corners and bends are conceivable and can theoretically yield slightly lower plate heights (without the application of a porous layer), but these shapes will inevitably induce differences in local surface to volume ratios and concomitant differences in porous material after deposition. Next, the capillary channels were defined by subsequent broadband UV lithography, etching of the Si layer by a Bosch-type deep-reactive-ion etching step (Adixen AMS100SE) reaching a depth of 115 µm. After this, the resist was removed by oxygen plasma and nitric acid, and the pillars were defined in the SiO_2 mask (also the already defined and partly etched capillary groove was etched further) were subsequently Bosch etched to reach a depth of 15 µm (and the capillary

channel a total depth of about 130 µm). A diverging flow distributor containing an array of radially stretched diamond-shaped pillars [20] with a width-over length aspect ratio of 5 was placed at the capillary-pillar channel interface to ensure a good flow distribution over the entire width of the pillar-array column. The microfluidic channels were subsequently sealed with a Pyrex wafer (thickness 0.5 mm), anodically bonded to the Si substrate using an EV-501 wafer bonder (EV Group Inc., Schaerding, Austria). Next, the chip was diced (100 µm deep) from both sides of the wafer and subsequently cleaved, exposing the channels to insert the interfacing capillaries (108 µm OD and 40 µm ID) into. Then, the capillaries were inserted in the grooves and sealed by epoxy glue (see also §3.5.2.2 for the mask design).

8.2.3. Porous layer deposition

Silica-layer deposition was performed using the TMOS-based sol-gel procedures described by Detobel et al. [21]. First, 0.40 g of PEG was dissolved together with 1.00 g of urea in 10 mL of a 0.01 M aqueous acetic acid solution. Then, 4.50 mL of TMOS was added to the mixture and the solution was stirred for 45 min at 0 °C. The microfluidic pillar-array channels were subsequently filled with the polymerization solution and flushed with solutions contained in a 2 ml volume stainless steel loop that was connected to a capillary HPLC pump that delivered typically a flow rate of 2 µl per min during these steps. The gelation and aging of the polymerization solution inside the microchannels was performed at 40 °C for 24 h. To create mesopores, the wet gel was heated in the oven at a rate of 1 °C per minute and left at 110 °C for 4 h. After cooling down, the channels were dried by opening the channel in- and outlets and leaving the chip for another 24 h at 40 °C. In a final step, the remaining organic moieties in the dried silica layer were pyrolyzed at 400 °C for 72 h. A C8 hydrophobic coating was applied on the porous silica layer by means of a liquid-phase coating procedure. First, the microchannels were flushed with methanol for 1 day and anhydrous toluene for 1day. A solution of 5% octyldimethylchlorosilane in anhydrous toluene was pumped through the channel for 72 h at room temperature. Afterward, the channels were flushed with anhydrous toluene for 1 day and with methanol for 1 day.

8.3. Results and discussion

8.3.1. 3.1 Visual system characterization

Figure 8.1 shows an overall picture of the chip (before applying the porous-shell layer) and the connection tubing (see Figure 8.1a), as well as some SEM-pictures of one of the turns

connecting two adjacent separation lanes (see Figure 8.1b). These turns consist of a narrow connection channel of 10 µm (to minimize the volume of the turn), pro- and preceded by a flow distributor (see Figure 8.1c) generally consisting of 5 µm x 63 µm diamond features, stretched perpendicular to the flow direction (spacing 2.3 µm). The aspect ratio of the transversally stretched pillars grows from around unity close to the separation bed to about a factor of 12 at the other end of the distributor.

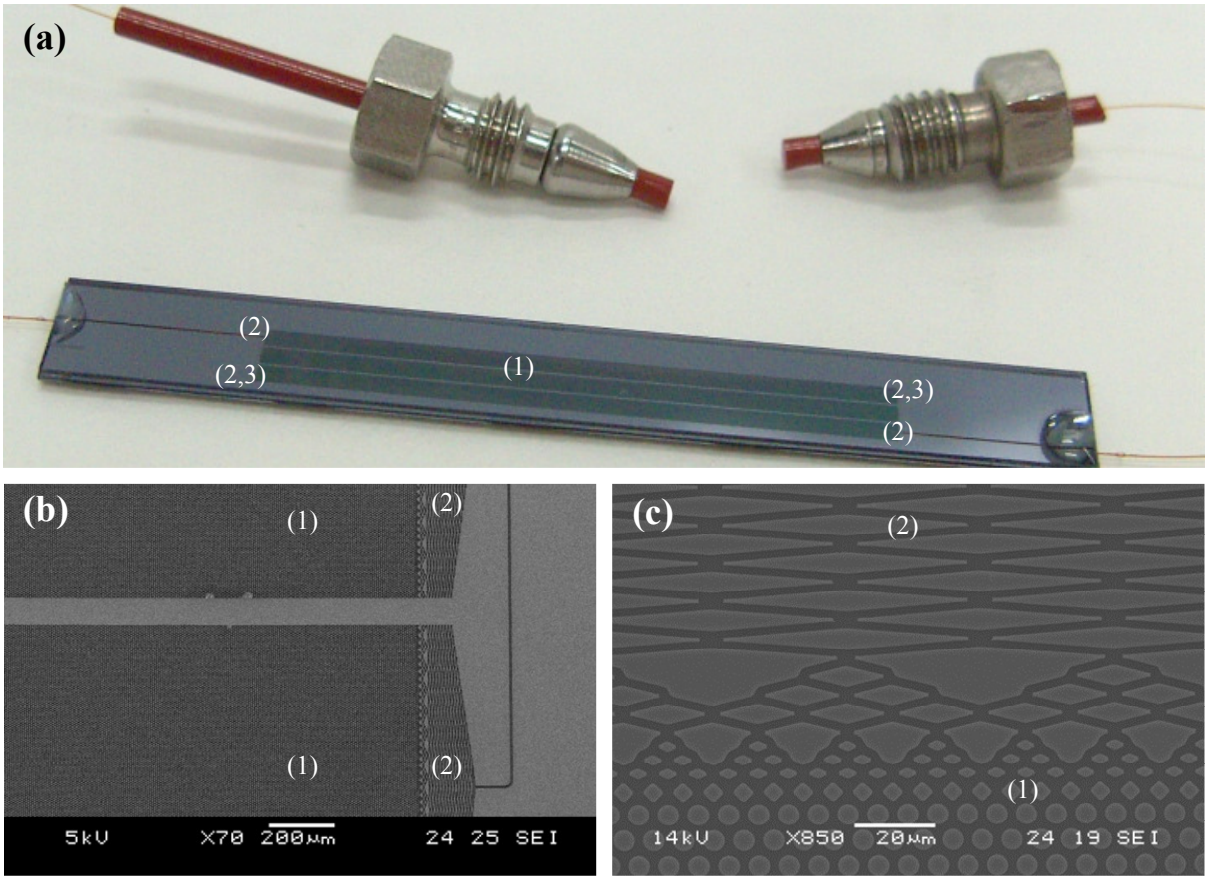

Figure 8.1. (a) Optical picture of PAC chip containing three separation lanes of each 3 cm (depth 16 µm), the connection capillaries and the fittings, (1) is the pillar region, (2) is the distributor region, and (3) is a 10 µm wide turn channel **(b)** overview (SEM) of pillar channel, distributor and turn channel **(c)** close-up (SEM) of the flow distributor containing transition structures towards diamond pillars.

Figure 8.2 shows the pillars after the application of the porous-shell layer. The latter was prepared using the recipe developed by Detobel et al. [21] (see experimental section), resulting in a relatively conformal coating, with the thickness varying on the same scale as the Si substrate roughness (60 nm between largest and smallest dimension). One of the drawbacks mentioned by Detobel et al. was the occurrence of small pieces of monolith at the supply channels and around the injection zone. At these relatively large channel dimensions, the small domain-criterion required to obtain a conformal coating is not met, resulting in uncontrolled (and non-conformal) silica deposition. In the current design, these zones are

omitted as the injection occurs off chip and the supply capillary channels extent to the channel in-and outlet. To avoid uncontrolled deposition in the connection capillaries, they were glued only at the border of the chip, so that after the cladding procedure, the capillary could be removed and replaced by a fresh one. Near the top and bottom part of the pillars, the coating thickness is slightly thicker than in the intermediate region. This is due to the unavoidable differences in local surface to volume ratios between these regions. At a corner area (i.e., where the pillars connect to the top and bottom channel plate), the coating is deposited on the surfaces at each side of the corner, resulting in a thicker layer than in a region without corners.

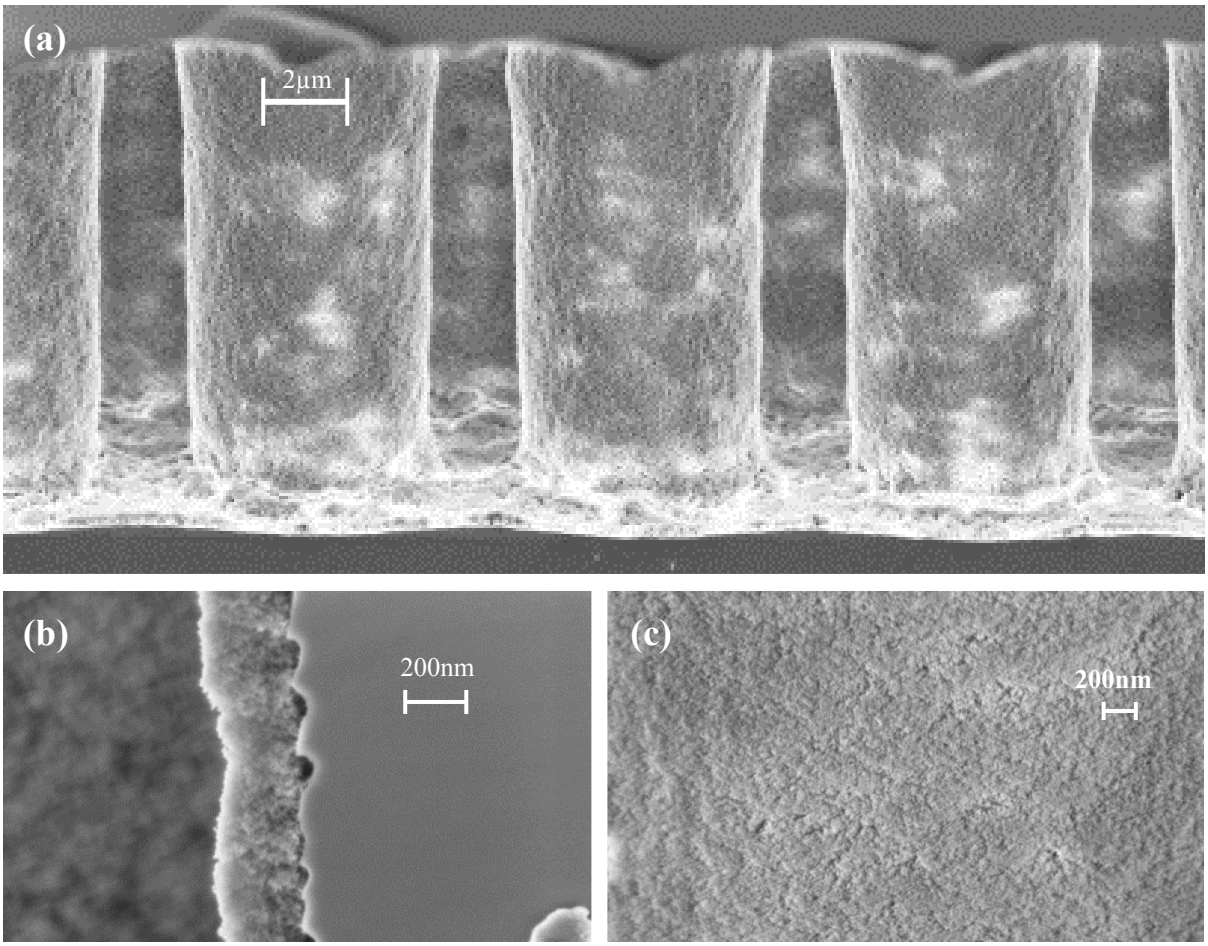

Figure 8.2 (a) Cross section (SEM) of porous PAC **(b)** zoom-in of porous layer at a cross section of pillar after cleaving the pillar. The layer thickness of the layer on the pillar mantle is on the order of 300 nm. **(c)** pillar mantle surface at non-cleaved zone.

In Figure 8.2b, a close-up of a partly cleaved pillar is depicted, revealing a layer thickness on the order of 250-350 nm. This variance is due to the presence of so-called scallops (these are rings as visible of Figure 8.2b, resulting from the cyclic nature of the applied Bosch® etching recipe, which consists of an alteration of deposition and etching steps) and the above mentioned location effect (central pillar region or top/bottom of pillars). Figure 8.2c shows a

SEM-image of the mesoporous layer. The image looks directly to the pillar mantle surface and reveals that no cracks or grooves are present.

8.3.2. On-chip separation performance

To interpret the finally obtained separation performance of the chip when coupled to an external injector and UV detector of a commercial capillary HPLC system , it is of course important to first characterize the performance of the chip alone. This was done using the on-chip injection and detection approach used in our previous work, using on-chip injection and detection of coumarins.

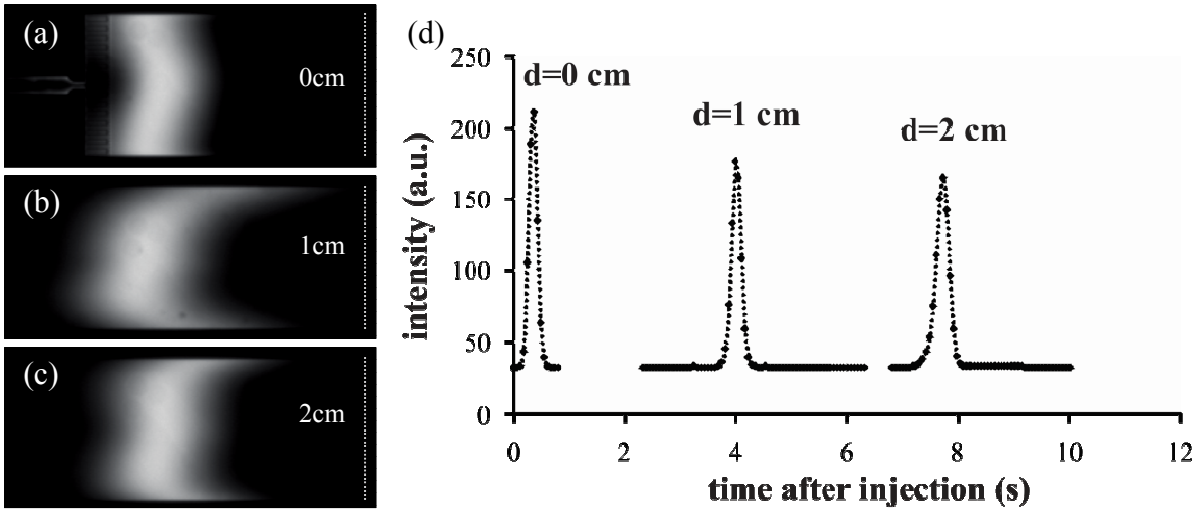

Figure 8.3. CCD images of a coumarin band in methanol at **(a)** channel inlet **(b)** 1 cm downstream **(c)** 2 cm downstream **(d)** intensity plots obtained at the dashed monitor lines (measuring across the entire channel width). The mobile phase velocity is 2.7 mm/s and the plate height is 2.1 μm.

For this purpose, two additional capillaries were inserted to deliver the sample just in front of the distributor (see e.g. [22] for the details of this on-chip injection system). Figure 8.3 shows how a coumarin band (C480) enters the first lane of the separation bed and subsequently flows through the first 2 cm of the bed. It is clearly visible that the sample band is distorted at the sidewall region, as also already experienced in some of our previous designs. This is due to minor deviations (on the order of only some 100 nm) between the finally obtained distance (after etching) between the pillars and the side wall and the target distance which was calculated such that the local flow resistances in the center and side-wall region of the channel would be equal [23]. By selecting a vertical row of pixels and plotting the average value as a function of time, a local chromatogram is obtained. Generally, the bands had a nearly Gaussian shape, despite the spatially deformed peak shape. This is because the fronting part of the band at the sidewall area only represents a minor fraction of the total band. Converting the obtained temporal standard deviation σ_t to the spatial variant σ_x, ($\sigma_x = \sigma_t$ u, with u the

mobile phase velocity), a plate height value H can be obtained ($H=\Delta\sigma_x^2/\Delta x$, with Δx the distance between the observation spots).

Figure 8.4 gives an overview of all obtained plate height values, for the case of a non-retained component (measured at 100% methanol and without coating applied to the pillars) and a retained component (retention factor k=1.3, and with only a C8-monolayer applied to the pillar outer surface). To check the influence of the turns, measurements obtained within 1 channel track (without turns) were compared with those obtained over 3 channel tracks (including 3 turns).

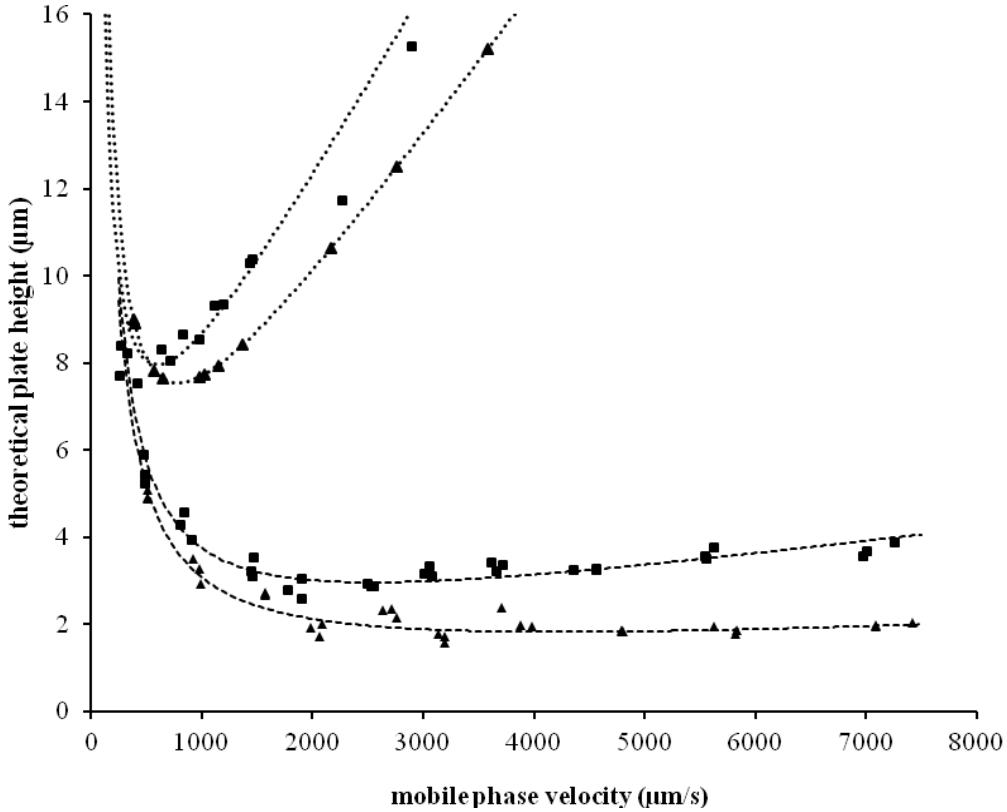

Figure 8.4. Van Deemter curves obtained under retained (upper curves) and non-retained conditions (lower curves) in the same channel track at 2 cm distance and 2 turns later 8 cm further downstream the channel (C480 in 65/35 v% H_20/MeOH , k'=1.3).

Under non-retained conditions, a minimal plate height of 2.0 µm is obtained (u_{opt}=4.0 mm/s) within the same channel track. Measuring over a longer length (3 turns included), a minimal plate height of 3.1 µm was measured (u_{opt}=2.2 mm/s). Under retained conditions, a minimal plate height of 7.6 µm (u_{opt}=0.8 mm/s) is observed without turns and 8.0 µm (u_{opt}=0.6 mm/s) with turns. This loss in efficiency is a direct consequence of the relatively large band broadening induced by the turns, which in turn is linked to the fact that relatively wide channels (1 mm) were used in the present study.

Comparing the slopes of the van Deemter curves in the high velocity range for the case with and without turns, the presence of the turns clearly represents an additional source of band broadening that varies more or less linearly with the velocity. This is in agreement with the fact that the turns are in fact open-tubular capillaries, for which it is well known that their band broadening varies linearly with the velocity in the high velocity range, even when the capillary contains turn structures [23]. This is due to the fact that, at high velocities, the molecules have insufficient time to interchange between the different flow lines and will migrate further relative to each other. The increase in slope between the case with and without turns is a factor of 1.3 for the non-retained case and a factor of 2.8 for the retained case.

The plate height and the slope of the C-term region can be reduced by decreasing the characteristic dimensions. With the applied broadband UV lithography equipment, it is however not possible to produce critical dimensions smaller than 2 μm. This is the smallest dimension in the present chip at the sidewall region, and this cannot be reduced further without inducing dramatic sidewall effects.

8.3.3. Chip performance in capillary LC system

To connect the chip to a commercial capillary LC instrument, the capillaries (108 μm o.d. and 40 μm i.d.) entering and leaving the chip were connected to the injection valve or to the detector capillary using a zero dead volume connection [23,24]. In the present study, pressures of up to 200 bar were applied to the chip by pumping acetonitrile-water mixtures at varying ratios without observing of leakages or sudden pressure drops. Tests on longer (non-porous channels) channels with a larger pressure drop and with another HPLC instrument revealed that the connection failed at 420 bar, witnessed by a sudden pressure drop of the pump.

To enhance the detection sensitivity, large sample volumes (order of 1 μL) were loaded onto the column, by focusing the injected sample on the head of the column at the start of the gradient using initially a large water fraction.

With the measured etch-depth of 15.2 μm and a total channel width of 1 mm and the external porosity of 46 %, the volume of the PAC channel equals about 0.6 μl (neglecting the internal pore volume), with the cross section corresponding to a cylindrical capillary with a diameter of 139 μm. Using a 1 μl injection loop and a total of 45 cm connection tubing with 40 μm i.d.,

the system volume before the column can be estimated to be about 1.6 µl; the system volume after the PAC can be estimated to be 0.6 µl (25 cm connection tubing with 40 µm i.d. glued to the chip, connected with a zero dead volume connection to 35 cm connection tubing with 20 µm i.d. running through the UV-VIS flow cell). Due to the expected focusing of the analytes on top of the column, it is only the after-column volume that can be expected to contribute to the system band broadening.

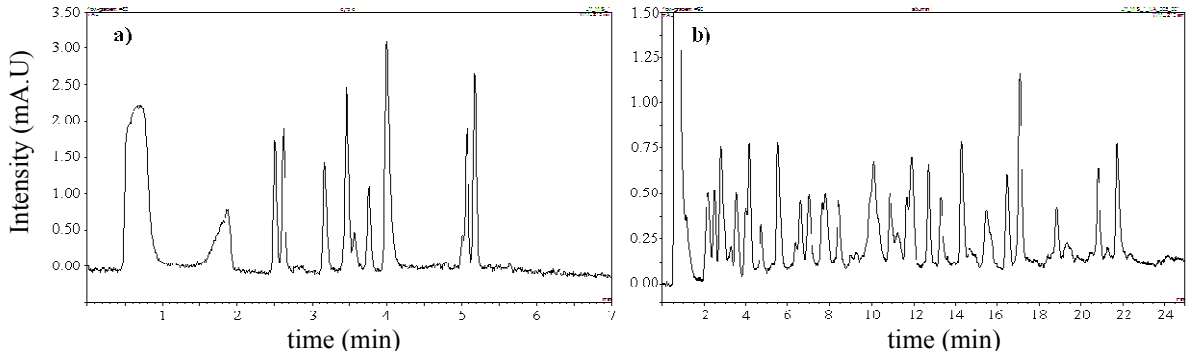

Figure 8.5. (a) Cytochrome c digest separations (gradient running from 0 to 70 % B in 10 min), sample: 1 µl, injected mass: 1 pmol, flow rate=4 µl/min, A:water (0.05 % TFA), B: 50/50 AN/H20 (0.04 % TFA), 30 °C, 4 µl/min, 210 nm **(b)** separation of albumin digest (gradient running from 0 to 50 % B in 30 min), V_{inj}= 1 µl, injected mass 1 µg/µl, other conditions as in (a).

In Figure 8.5, the chromatograms of the separations of cytochrome c and albumin digests are depicted. The first peak originates from the injection, and the baseline is reasonably stable between the follow up peaks. The peak shapes are very good and no fronting or tailing peaks are observed, indicating the absence of severe sidewall effects [12]. The reproducibility was also studied by performing 25 gradient separations under identical conditions (see Figure 8.6), resulting in retention time-based RSD values on the order of 5 %.

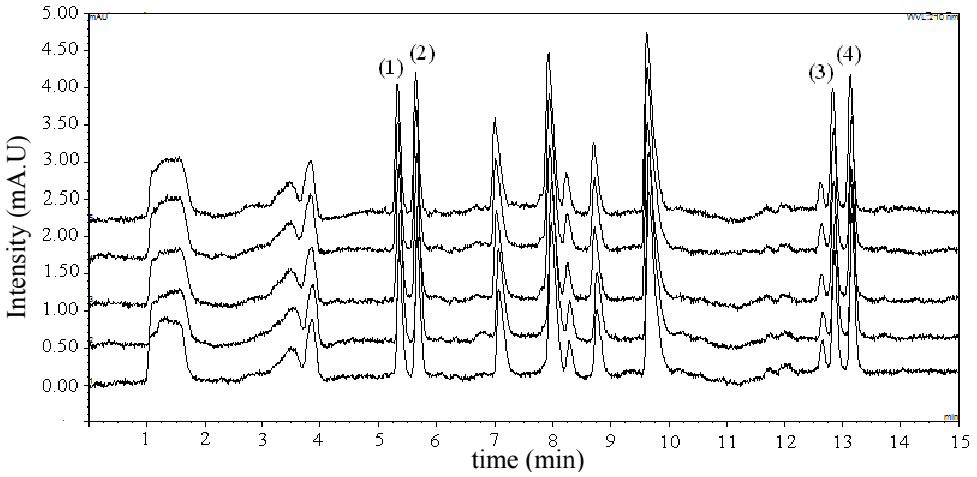

Figure 8.6. Repeated experiments (cytochrome c digest), 30 °C, A: water (0.05 % TFA), B: 50/50 AN/$H_2$0 (0.04 % TFA), 0-70 % B (7.5 min), 70-100 % B (0.1 min), 100 % B (2 min); 100-0% B (0.1 min), sample: 1 µl, injected mass 1 pmol, flow rate=4 µl/min. RSD's (n=25): (1) 5.4 % , (2) 4.8 %, (3) 4.8 %, (4) 4.3 % .

In order to evaluate the performance the peak capacity was determined using [25]:

$$n_p = \frac{t_g}{w_p} + 1 \qquad (8.1)$$

with n_p is the maximum peak capacity that can be obtained, w_p is the average base peak width and t_G the gradient duration.

Measurements of n_p were made for a wide range of gradient times and flow rates. The result is shown in Figure 8.7. It appears from these measurements that the peak capacity is hardly affected by the flow rate at identical gradient times. This indicates that H is nearly independent of the flow rate. In terms of kinetics, it is obvious that the highest flow rate (4 µl/min) is the most interesting.

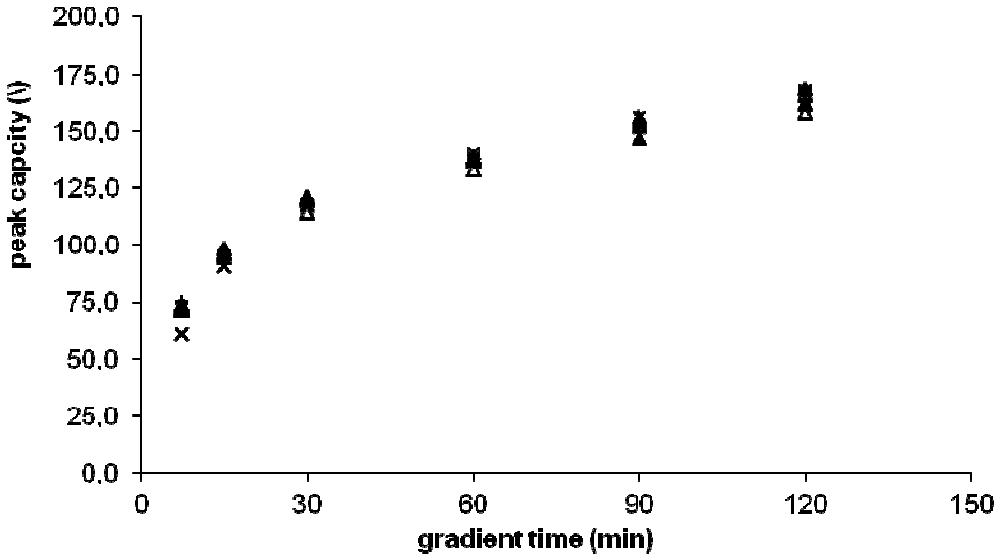

Figure 8.7. Peak capacities of cytochrome c digest (based on the average of peak 3, 4, 8 and 9) at 1 (×), 2 (▲), 3 (+) and 4 (Δ) µl min in function of the gradient time. The other conditions are identical to those in Figure 8.6.

To ensure that injected samples with a concentration of 1 pmol/µl were separated under non-overloading conditions, larger concentrations (up to 4 pmol/µl) were injected as well. The relative standard deviation of the obtained peak widths was less than 5 %, similar to the obtained value for identical injections, hence demonstrating the absence of overloading at the applied conditions. In the future, an on-chip injection system will be developed for the sol-gel cladded pillars. This will allow the injection of tracer components under isocratic conditions, without the need to trap and subsequently elute the injected sample at the head of the column under gradient conditions. This will enable a more fundamental study of the band broadening characteristics of the cladded pillars by the establishment of van Deemter curves of different

porous layer thicknesses and porosities, as well as an accurate determination of the specific surface area.

The dependency of n_p on the gradient time is similar to that of any chromatographic system, showing an initial steep increase of the peak capacity with t_G, after which the curve tends to level off with a further increase of t_G [26]. The maximal peak capacity that could be reached with the system is n_p=150 for a gradient time of 120 min. This is considerably lower than what is obtained on e.g. a state-of the art polymeric monolithic [27], where for a 5 cm column (V_{column}=1.2 µl, V_{sample}=1 µl) a peak capacity of n_p=400 can be obtained separating a digest mix, however operated at a higher and more beneficial temperature of 60 °C and at a smaller concentration to avoid overloading.

Comparing this to an extrapolated performance based on a 5 cm x 0.1 mm fused-core-particle column (2.7 µm, C18, Advanced Materials Technologies, Wilmington, USA), a stationary phase which is more comparable to the silica cladded pillars, operated at 60 °C and with similar gradient times [25], where a peak capacity of Pc ~ 100 was obtained, the obtained result in the current study is similar. Taking into account that the pillars used in the present study (after deposition of the porous layer) are as large as 5.6 µm (spacing 1.9 µm) and that the separations in the present study were conducted at room temperature, the obtained peak capacities are very satisfactory.

8.4. Conclusion

A 9 cm long micro-pillar array chip has been successfully cladded to surround each pillar with a 300 nm thick layer of meso-porous silica to enhance its retention capacity and mass loadability. The chip was tested before cladding after the application of a C8 stationary phase using on-chip detection, revealing some loss of efficiency caused by the turns, but nevertheless showing good minimal plate heights in the order of 3 µm (unretained component) and 8 µm (retained component), respectively corresponding to reduced plate heights of 0.4 and 1.1 when based on the domain size. The cladded chip was successfully connected to a commercial capillary LC system and could be used for the gradient separation of a cytochrome c digest. The obtained peak capacity (150 in 120 minutes) is certainly still amenable to improvement, mainly by reducing the extra-column volume and by using an identical top and bottom wall (to reduce top-bottom differences in migration velocity).

References

[1] A. Manz, Y. Miyahara, J. Miura, Y. Watanabe, H. Miyagi, K. Sato, *Sensors and actuators B: Chemical* **1990**, *1*, 249–255.

[2] J. H. Knox, *Journal of Chromatography A* **1999**, *831*, 3–15.

[3] J. C. T. Eijkel, A. van den Berg, *Electrophoresis* **2006**, *27*, 677–85.

[4] J. C. T. Eijkel, *Lab on a chip* **2007**, *7*, 815–7.

[5] C. Viklund, F. Svec, J. M. J. Fréchet, K. Irgum, *Chemistry of Materials* **1996**, *8*, 744–750.

[6] F. Svec, J. M. J. Frechet, *Macromolecules* **1995**, *28*, 7580–7582.

[7] F. Svec, C. G. Huber, *Analytical chemistry* **2006**, *78*, 2100–2107.

[8] K. Nakanishi, N. Soga, *Journal of the American Ceramic Society* **1991**, *74*, 2518–2530.

[9] K. Nakanishi, N. Soga, *Journal of Non-Crystalline Solids* **1992**, *139*, 1–13.

[10] N. Tanaka, H. Kobayashi, N. Ishizuka, H. Minakuchi, K. Nakanishi, K. Hosoya, T. Ikegami, *Journal of Chromatography A* **2002**, *965*, 35–49.

[11] B. He, N. Tait, F. Regnier, *Analytical Chemistry* **1998**, *70*, 3790–3797.

[12] W. De Malsche, H. Eghbali, D. Clicq, J. Vangelooven, H. Gardeniers, G. Desmet, *Analytical chemistry* **2007**, *79*, 5915–5926.

[13] L. C. Taylor, N. V Lavrik, M. J. Sepaniak, *Analytical chemistry* **2010**, *82*, 9549–9556.

[14] C. Aoyama, A. Saeki, M. Noguchi, Y. Shirasaki, S. Shoji, T. Funatsu, J. Mizuno, M. Tsunoda, *Analytical chemistry* **2010**, *82*, 1420–1426.

[15] M. Elwenspoek, H. V. Jansen, *Silicon Micromachining*, Cambridge University Press, Cambridge, UK, **2004**.

[16] W. De Malsche, H. Gardeniers, G. Desmet, *Analytical chemistry* **2008**, *80*, 5391–5400.

[17] R. C. de Andrade Costa, K. B. Mogensen, J. P. Kutter, *Lab on a chip* **2005**, *5*, 1310–4.

[18] A. Fonverne, C. Demesmay, F. Ricoul, E. Rouvière, J. Dijon, F. Vinet, *Sensors and Actuators A: Physical* **2011**, *167*, 517–523.

[19] F. Detobel, H. Eghbali, S. De Bruyne, H. Terryn, H. Gardeniers, G. Desmet, *Journal of chromatography. A* **2009**, *1216*, 7360–7367.

[20] J. Vangelooven, W. De Malsche, J. O. De Beeck, H. Eghbali, H. Gardeniers, G. Desmet, *Lab on a Chip* **2010**, *10*, 349–356.

[21] F. Detobel, S. De Bruyne, J. Vangelooven, W. De Malsche, T. Aerts, H. Terryn, H. Gardeniers, S. Eeltink, G. Desmet, *Analytical Chemistry* **2010**, *82*, 7208–7217.

[22] W. De Malsche, J. Op De Beeck, H. Gardeniers, G. Desmet, *Journal of chromatography. A* **2009**, *1216*, 5511–5517.

[23] W. De Malsche, J. Op De Beeck, S. De Bruyne, H. Gardeniers, G. Desmet, *Analytical chemistry* **2012**, *84*, 1214–1219.

[24] W. De Malsche, S. De Bruyne, J. Op De Beeck, P. Sandra, H. Gardeniers, G. Desmet, F. Lynen, *Journal of chromatography. A* **2012**, *1230*, 41–47.

[25] A. Vaast, K. Broeckhoven, S. Dolman, G. Desmet, S. Eeltink, *Journal of chromatography. A* **2012**, *1228*, 270–275.

[26] U. D. Neue, *Journal of Chromatography A* **2005**, *1079*, 153–161.

[27] S. Eeltink, S. Dolman, R. Swart, M. Ursem, P. J. Schoenmakers, *Journal of chromatography. A* **2009**, *1216*, 7368–7374.

Chapter 9

General Conclusions

Ultra-rapid chromatographic separation devices can be developed by using the advanced micro-machining methods originally established for the micro-electronics industry. In the present thesis, novel devices for use in shear-driven nano-channel chromatography and pressure-driven pillar array column chromatography have been designed and fabricated. Special attention was also paid to the development of zero-dead volume connection structures to lead the separated fractions to an off chip commercial detector. Separation channels were fabricated in both silicon and glass.

Using the latter, fully transparent separation could be produced. A dedicated optical set-up could be built with which these transparent channels could be used to make very precise measurements of the radial dispersion coefficient in 2-D porous media. This set-up enables optical "injections" (=local activation or uncaging of caged fluorophores) with a spatial resolution down to 5µm. The set-up allows measuring fluid velocities with an accuracy of about 99% at low and high Peclet numbers. The actual radial dispersion coefficient values can be determined from the radial variance of the steady-state dispersion plume formed upon a continuous local "injection" of the fluorophore. The radial intensity cross-section of this fluorescent plume could be fitted with a Gauss distribution function with a $r^2 > 99\%$. Overall the accuracy of the D_{rad}-values was about 96% for the beds with 60% or 80% porosity.

The measurements showed that the advective component helps the species to rapidly disperse over the radial region covered by the group of streamlines the species are initially injected in. Moving over to an adjacent set of streamlines however requires an additional diffusion step which, at high ν, becomes rate limiting. As a consequence, the relation between D_{rad} and ν tends to level off to a constant value at high ν. Depending on the packing density, this leveling off occurs at a value of about $D_{rad}/D_{mol}=10$ ($\varepsilon=0.4$), $D_{rad}/D_{mol}=4$ ($\varepsilon=0.6$) and $D_{rad}/D_{mol}=2{,}5$ ($\varepsilon=0.8$). Interestingly, the effect of the bed order on the observed radial dispersion process (both qualitatively in Section 5.4.1 and quantitatively in Section 5.4.2) is relatively small. All these observations can be represented very well using the series-connection model proposed by Deridder [1]. As also shown by Deridder, even more sophisticated D_{rad}-models can be conceived, based on similar but more complex considerations. Their use however falls outside the scope of the present study, as more accurate measurements would be needed to discriminate them from the presently considered simple series-connection model.

Pursuing the ultimate limit of channel miniaturization, shear-driven nano-channels with a depth of only 40nm and 80nm were produced. To be able to operate such shallow channels in a mechanically stable way, a new type of micro-structured spacers had to be developed. In addition work has been conducted to provide a uniform meso-porous silicon nano-layer to enhance the chromatographic retention and selectivity. Using the shear-driven nano-channels, it was found that the ultra-fast mass transfer kinetics prevailing in this range of small channel depths allow to completely eliminate the C-term contribution to band broadening, at least up to the upper speed limit of our current set-up (7mm/s mobile phase velocity), leaving the inescapable molecular diffusion (i.e., B-term band broadening) as the sole source of band broadening. In the absence of any mass transfer limitations, 50.000 to 100.000 theoretical plates could be generated in the span of 1 to 1.5 seconds. This is nearly two orders of magnitude faster than the best performing commercial pressure-driven UHPLC-systems. With the employed channel depths, we appear to have struck a practical lower limit for the channel miniaturization of shear-driven flows. Despite the use of channel substrates with the highest grades of optical flatness, the overall substrate waviness (order of some 5 to 10 nm) can no longer be neglected compared to the etched channel depth, which in turn significantly influenced the local retention factor and band broadening.

Using the newly produced pressure-driven micro-pillar array columns, connection together with the newly developed zero-dead volume capillary connection methods, we could demonstrate the possibility to achieve ultra high efficiencies (order of 1 million theoretical plates) in liquid chromatography in a relatively short time of 20 minutes (elution time of unretained marker). This was achieved using a micro-pillar array column with optimized pillar diameter (5 μm) and inter-pillar distance (2.5 μm) to operate close to the Knox & Saleem-limit of micro-pillar array columns in the region of the 1 million theoretical plate mark under the prevailing pressure restriction (350 bar in the present study). The obtained efficiency was slightly affected (some 15 to 20 % around the optimal flow rate) by the turns that were inevitably needed to arrange a 3 meter long column on a 4 inch silicon wafer.

Finally, also considerable progress was made in the direct coupling of microfabricated micro-pillar array columns to commercial capillary LC instruments. For this purpose we investigated the achievable separation performance of a 9 cm long and 1 mm wide pillar array channel (volume=0.6 μL) containing 5 μm diameter Si pillars (spacing 2.5 μm) cladded with a meso-porous silica layer with a thickness of 300 nm when this channel is directly interfaced to a

capillary LC instrument. The chip had a small footprint of only 4 cm x 4 mm and the channel consists of three lanes that are each 3 cm long and that are interconnected using low dispersion turns consisting of a narrow U-turn (10 μm), pro- and preceded by a diverging flow distributor. Measuring the band broadening within a single lane and comparing it to the total channel band broadening, the additional band broadening of the turns could be estimated to be of the order of 0.5 μm around the minimum of the van Deemter curve, and around some 1 μm (non-retained species) and 2 μm (retained species) in the C-term dominated regime.

The analysis of liquid mixtures,
as e.g. encountered in environmental monitoring,
food safety analysis, the development of novel
pharmaceutical compounds, etc… is usually carried out
using chromatographic separation techniques.

Theoretical calculations have shown that
the efficiency of these techniques can be strongly
enhanced if they would be carried out in
perfectly ordered chromatographic beds, in stead
of the randomly packed tubes filled with spherical
particles as used today.

In the present work, the various details of the fabrication
processes needed to produce such perfectly ordered
chromatographic beds (on-chip HPLC columns) have
been analyzed and solutions have been proposed.
Lithographic etching protocols, based on the use of
Bosch-etching process have been optimized to produce
ordered arrays of micro-pillars over long column lengths.

Optimized turn structures were developed to arrange very long
(up to 3m) columns on the surface of a 4 inch wafer.
Various coupling techniques, to connect the on-chip
HPLC columns with a minimum of coupling losses were developed.

In addition, a novel experimental set-up and procedure
were developed to study the flow processes,
and especially the radial dispersion process in on-chip
HPLC-columns in great detail. This work lead to a novel
correlation for the velocity dependency of the radial dispersion in
ordered and disordered beds of cylindrical micro-pillars.

ISBN: 978-90-365-3562-5